UNIVERSITÉ DU QUÉBEC À MONTRÉAL

APERÇU DE L'HISTOIRE GLACIAIRE/INTERGLACIAIRE DE L'OCEAN ARCTIQUE AU COURS DU QUATERNAIRE RECENT À PARTIR DES ISOTOPES DES SERIES URANIUM-THORIUM ET DU NEODYME

THÈSE

PRÉSENTÉE

COMME EXIGENCE PARTIELLE

DU DOCTORAT EN SCIENCES DE LA TERRE ET DE L'ATMOSPHÈRE

PAR

TENGFEI SONG

SEPTEMBRE 2023

UNIVERSITÉ DU QUÉBEC À MONTRÉAL

INSIGHTS INTO THE LATE QUATERNARY GLACIAL/INTERGLACIAL HISTORY OF THE ARCTIC OCEAN FROM URANIUM-THORIUM SERIES AND NEODYMIUM ISOTOPES STUDIES

DISSERTATION

PRESENTED

AS PARTIAL REQUIREMENT

OF THE DOCTORATE OF EARTH AND ATMOSPHERIC SCIENCES

BY

TENGFEI SONG

SEPTEMBER 2023

REMERCIEMENTS

First of all, I would like to express my appreciation to Prof. Claude Hillaire-Marcel and Anne de Vernal. Without their trust and invaluable help, this thesis could not have been accomplished. I am grateful for all the support and encouragement that my supervisor, Claude Hillaire-Marcel, provided throughout my doctoral study. His critical and thoughtful comments on either the design of laboratory approaches or the structure of the manuscripts were always helpful and made this doctoral project significantly improve. Our meetings and discussions together have undoubtedly helped to develop my scientific mind. "One can not be more serious with the original datasets and their statistical analyses anymore" and "One should show the highest respect for nature and fact", are the two most important things I learned from him. I am deeply grateful for having the opportunity to work with him over the past five years.

Thanks to all the support and help from my co-supervisor, Prof. Anne de Vernal. Anne is such a nice person who helped me resolve all the difficulties I met during my studies and living in Montreal. Her suggestions for this doctoral program in a Paleoceanographic view and careful reading and editing of each manuscript are highly appreciated.

I thank Dr. Bassam Ghaleb for his technical support in the Radiochronology Laboratory at Geotop-UQAM. He never minds giving a hand to me during my work at the laboratory even at midnight. With Bassam's unconditional help, I have learned systematic skills in dealing with the U-Th series analyses. His accompany and assistance made the lab work to be enjoyable.

I also thank Dr. André Poirier for his assistance with the chemical extraction and MC-ICP-MS analyses of the Nd isotopes. Special thanks to Dr. Jean-François Hélie and Mrs. Agnieszka Adamowicz for their support in the organic matter and stable carbon isotopic composition analyses; to Mr. Michel Preda for his solid help in the clay mineral and bulk mineral XRD measurements; to Dr. Martin Roy, Dr. François Hardy, and Mr. Philippe Roberge for their assistance in the particle size analyses.

Prof. Yanguang Liu is thanked for the research materials supply and the full trust in me. Each marine sediment sample from the Arctic Ocean is priceless. His material support makes this project achievable.

Great thanks to my colleagues and office mates, Xiner Wu, Tiffany Audet, Vladislav Carnero-Bravo, Jade Falardeau, and Jena Zumaque for providing a friendly work environment. Special acknowledgment to Xiner Wu and Tiffany Audet for their English-to-French translation help.

Thanks to the Germany-Canada Arctrain program allowing me to meet so many friends during the annual meeting. The field trip to northern Quebec in the Autumn of 2019 was amazing.

Financial support for my overseas study from the China Scholarship Council is highly appreciated.

At last, thanks to the understanding and support from my parents. Sorry that I can't go back to China to visit you during the pandemic period. I would like to thank my wife Yufen Rong. Thanks for your accompany over the past eleven years, especially during those hard times. You are always there whenever I need you.

AVANT-PROPOS

This thesis is written in the form of three chapters in English, each corresponding to a scientific article published in a peer-reviewed journal. For this reason, the format of the reference lists is slightly different between chapters to remain consistent with the instructions of the journals in which they have been published. Following the *Guide de présentation des mémoires et thèse* of Université du Québec à Montréal, the introduction and conclusion are also written in English whereas a French abstract is provided.

The first chapter entitled “A reassessment of Nd-isotopes and clay minerals as tracers of the Holocene Pacific water flux through Bering Strait”, has been published in the Journal of *Marine Geology* (DOI: 10.1016/j.margeo.2021.106698), with the collaboration of Claude Hillaire-Marcel, Anne de Vernal, Yanguang Liu, Weiguo Wang, and Yuanhui Huang. The second chapter named “A resilient ice cover over the southernmost Mendeleev Ridge during the late Quaternary” has been published in the Journal of *Boreas* (DOI: 10.1111/bor.12632). This article is written with the support of co-authors Claude Hillaire-Marcel, Anne de Vernal, and Yanguang Liu. The third article was published in the Journal of *Earth-science Reviews* (DOI: 10.1016/j.earscirev.2023.104514), with the title of "Cycling and behavior of ^{230}Th in the Arctic Ocean: Insights from sedimentary archives". It is written in collaboration with Claude Hillaire-Marcel, Yanguang Liu, Bassam Ghaleb, and Anne de Vernal.

My contribution to the three scientific papers that make up the main body of this thesis first covers the collection and analysis of the major part of the entire dataset. I carried out the particle size separation, grain-size analysis, X-ray clay mineral analysis, organic carbon and its stable isotopic measurements, neodymium isotope measurements on distinct particle size fractions, and uranium-thorium-radium-lead analyses. The X-ray diffraction analyses of bulk minerals were made at the X-ray diffraction laboratory in UQAM with the help of Mr. Michel Preda. The Accelerator Mass Spectrometry ^{14}C measurements, part of the grain-size measurements were made in collaboration with the teams from the First Institute of Oceanography and Third Institute of Oceanography, China. I am responsible for the compilation and statistical analyses of all datasets. The interpretation of these data and writing of the three scientific papers are under the supervision of my research directors, Claude Hillaire-Marcel and Anne de Vernal.

TABLE DES MATIÈRES

LISTE DES FIGURES

LISTE DES TABLEAUX

RÉSUMÉ

L'océan Arctique diffère des autres océans en raison de sa couverture saisonnière de glace de mer, de la surface disproportionnée de ses plateaux continentaux, et de sa connexion limitée avec l'océan Pacifique via le détroit de Béring, dont la profondeur maximale est de l'ordre de 50 m. Le niveau de la mer et les conditions d'insolation, déterminant les bilans thermiques et la croissance ou la fonte de la glace, sont ainsi les principaux facteurs régissant les processus de sédimentation dans l'océan Arctique. Le niveau de la mer, en particulier, détermine la profondeur du détroit de Béring, donc les flux d'eau relativement chaude, peu salée et riche en nutriments, du Pacifique, jouant ainsi un rôle sur le bilan d'eau douce, l'étendue de la glace de mer et la productivité primaire dans l'océan Arctique. Cependant, en l'absence d'une chronostratigraphie fiable et de traceurs univoques, les processus de sédimentation dans l'océan Arctique, sous différentes conditions climatiques et de flux d'eau du Pacifique à travers le détroit de Bering, restent peu documentés. Dans cette thèse, parallèlement aux approches sédimentologiques courantes, les isotopes de l'uranium (U), du Thorium (Th) et du néodyme (Nd) de différents carottes sédimentaire de l'océan Arctique ont été utilisés pour fournir des repères chronologiques et retracer les processus de sédimentation au cours des derniers cycles glaciaires/interglaciaires, ainsi que pour estimer l'impact des flux d'eau du Pacifique via le détroit de Béring en réponse à la hausse du niveau de la mer après la dernière glaciation.

Le chapitre 1 présente une réévaluation de l'utilisation des isotopes du Nd et de la distribution de la smectite comme traceurs potentiels des flux d'eau du Pacifique par le détroit de Bering. Les résultats montrent que les teneurs en smectite et la composition isotopique Nd (εNd) des lixiviats dans les argiles, toutes deux liées à l'altération des roches volcaniques dans la mer de Béring, constituent de bons traceurs des flux d'eau pacifique. La composition isotopique du néodyme (εNd) des lixiviats des fractions argileuses d'une carotte par gravité Arc4-R09 provenant du plateau central de la mer des Tchouktches, a évolué vers des compositions plus radiogéniques depuis le début de l'Holocène, suivant l'augmentation du niveau moyen global de la mer, et donc l'approfondissement du détroit de Béring. Au site d'étude, les flux de smectite provenant du plateau sibérien et de l'archipel arctique canadien sont importants. Par suite, dans la mer de Chukchi, la présence de smectite d'origine sibérienne et l'archipel arctique canadien masque ou dilue les apports de la mer de Béring et du Pacifique, via le détroit de Bering. Ainsi, seule, la composition isotopique du néodyme (εNd) des lixiviats dans la fraction argileuse constitue un seul traceur fiable des flux d'eau du Pacifique à travers le détroit de Béring. Cependant, au-delà de la mer de Chukchi, le signal

Nd du Pacifique disparaît rapidement, limitant ainsi l'utilisation du traceur aux séquences du plateau continental.

Dans le chapitre 2, les résultats des analyses d'une carotte par gravité (Arc7-E25), prélevée au sud de la dorsale Mendeleev, permettent de retracer les processus sédimentaires après la transition du Pleistocene moyen dans l'ouest de l'océan Arctique. Les mesures de la série U-Th dans les 163 cm supérieurs de la carotte suggèrent un intervalle d'âge allant du stade isotopique marin (MIS) 1 au stade 11. Le sédiment contient très peu de matière organique et de sable mais se caractérise par un contenu élevé en argile, notamment dans la partie inférieure de la carotte. Nous interprétons ces caractéristiques comme l'indication de la présence d'une plate-forme glaciaire ou d'un inlandsis résilient, globalement entre les transitions MIS 11/10 et MIS 6/5e. Des conditions de glace de mer ouverte saisonnièrement ont cependant peut-être prévalu pendant l'intervalle couvrant le la Terminaison III et le MIS 7, comme l'indiquent des proportions élevées de sable et faibles d'argile, ainsi que des teneurs en ^{13}C de la matière organique élevées suggérant des flux résultant d'une productivité primaire effective au cours de l'intervalle.

Dans le troisième chapitre, nous avons compilé tous les enregistrements de $^{230}Th_{xs}$ de séquences sédimentaires de l'océan Arctique qui ont été publiés. La distribution et les inventaires des excès de ^{230}Th sédimentaires ($^{230}Th_{xs}$), vs la fraction minérale de cet isotope, confirment la fiabilité du $^{230}Th_{xs}$ en tant qu'outil chronostratigraphique pour l'étude des séquences marines du Quaternaire tardif de l'océan Arctique caractérisées par un faible taux de sédimentation. L'estimation des flux de ^{230}Th dans la colonne d'eau, au cours de conditions climatiques glaciaires vs interglaciaires, indique que le taux de production du ^{230}Th était réduit d'environ 40% pendant les glaciations, par comparaison à celui des interglaciaires. La diminution des flux de ^{230}Th serait à l'origine de la faible accumulation du $^{230}Th_{xs}$ sur les crêtes océaniques peu profondes au cours des épisodes glaciaires. Elle serait liée au développement d'épaisses plates-formes de glace sur l'océan Arctique surmontant une couche d'eau de très faible salinité. Les faibles taux de production et le faible dépôt de sédiments grossiers pendant les glaciations ont pu conduire à l'exportation de ^{230}Th vers les mers nordiques et une accumulation partielle dans les bassins profonds de l'océan Arctique. Notre étude a également permis de conclure que les flux sédimentaitres de $^{230}Th_{xs}$, dans l'océan Arctique, dépendent non seulement des flux de matière organique, mais aussi de la bathymétrie, avec un transfert de $^{230}Th_{xs}$ des crêtes vers les bassins profonds via des processus de vannage induits par l'accumulation de la saumure dans la partie occidentale de l'Océan Arctique, et son évacuation vers le

détroit de Fram. Les flux de carbone organique seraient liés d'une part aux apports fluviatiles de composés organiques dissous d'origine terrestre et, d'autre part, à la productivité primaire régie par l'ouverture saisonnière de la couverture de glace de mer, mais dissociée des flux de particules grossières.

Dans l'ensemble, les contributions principales de cette thèse sont i) la vérification de la zone géographique permettant de tracer les flux de Nd radiogénique (εNd) de la mer de Bering, via les lixiviats des sédiments du plateau intérieur de la mer des Tchouktches; ii) un essai de leur quantification en relation avec le niveau de la mer et la bathymétrie du détroit de Béring; iii) une meilleure appréciation des paramètres gouvernant les flux sédimentaires à partir d'une stratigraphie basée sur le $^{230}Th_{xs}$; iv) la mise en évidence d'une plate-forme de glace résiliente, depuis la Sibérie orientale jusqu'à la crête de la ride de Mendeleïev la plus méridionale; v) un examen circonstancié du cycle et du comportement du ^{230}Th dans l'océan Arctique.

Mots clés : Océan Arctique, Quaternaire, isotopes radiogéniques, Eau du Pacifique, sédimentation

ABSTRACT

The Arctic Ocean is unique among the world's oceans because of its seasonal sea ice cover, disproportional continental shelf area, and limited connection to the Pacific Ocean via the shallow Bering Strait presently ~50 m deep. Sea level in addition to solar insolation that drives the heat budget and plays a role in ice formation and melt are major parameters governing sedimentation processes in the Arctic Ocean. Sea level, in particular, plays a determinant role in regulating the fluxes of low-salinity, relatively warm, and nutrient-rich Pacific Water through Bering Strait, thus governing the freshwater budget, sea ice extent, and primary productivity in the Arctic Ocean. Due to the lack of reliable chronostratigraphy and effective tracers, sedimentation processes in the Arctic Ocean under different climate conditions as well as the role of variation in Pacific Water fluxes through Bering Strait are debated and altogether not well documented. In this thesis, Uranium (U)-Thorium (Th) series and Neodymium (Nd) isotopes in cored sequences were used to provide chronological constraints in selected sedimentary cores and to evaluate sedimentation processes in the Arctic Ocean during the last few glacial/interglacial cycles, as well as to estimate the Pacific Water fluxes through Bering Strait in response to sea level rise following the last glaciation.

In chapter 1, a reassessment of Nd isotopes and smectite abundance as potential tracers of Pacific Water inflowing through Bering Strait was made. Results show that smectite content and the Nd isotopic composition (εNd) of leachates in clays, both relating to the weathering of volcanic rocks in the Bering Sea, constitute sensitive tracers of the inflowing Pacific Water. The εNd values of leachates in clay fractions of a gravity core Arc4-R09 from the central Chukchi Sea shelf, increased progressively since the early Holocene until ca 4 ka BP, in accordance with the rising global mean sea level and the consequent deepening of Bering Strait. In the study site, the Siberian and Canadian Arctic Archipalego-sourced smectite affects the unequivocal usage of this mineral as a tracer of Bering Sea/Pacific water sources. Thus, the εNd-values of leachates in clay fraction appear to be the only reliable tracer of Pacific Water fluxes through the Bering Strait. However, beyond the Chukchi Sea, dilution of this signal by other Nd sources limits the use of this tracer.

In chapter 2, a gravity core Arc7-E25 collected from the southern Mendeleev Ridge was used to document the late Pleistocene sedimentation in the western Arctic Ocean. U-Th series measurements in the upper 163 cm of core Arc7-E25 suggest an age range from marine isotope stage (MIS) 1 to 11. Based on this

stratigraphy, sedimentation patterns remained broadly similar between glacial/interglacial climatic scales. The core has an overall very low organic matter and sand contents, and high clay contents notably in the lower part of the core. We interpret these features as resulting from resilient ice shelf/ice sheet, at least throughout MIS 11 to 5e. Open sea ice conditions may have prevailed during the MIS 7-Termination III interval, as documented by relatively high sand and low clay contents, and relatively high $\delta^{13}C$-values of organic matter relating to primary productivity within the interval.

In chapter 3, we compiled all published $^{230}Th_{xs}$ records from Arctic Ocean sedimentary sequences. $^{230}Th_{xs}$ distributions and inventories confirm the reliability of $^{230}Th_{xs}$ as a chronostratigraphic tool for the study of low-sedimentation rate, late Quaternary marine sequences of the Arctic Ocean. Estimation of ^{230}Th production in the water column under distinct climate conditions suggests that its production rate was reduced by about 40% during glacials relative to the interglacials. This reduction was thought to be responsible for the nil $^{230}Th_{xs}$ accumulation over shallow ridges and related to the development of thick ice shelves over the Arctic Ocean overlying a low-salinity/freshwater layer. Low production rates and scarce coarse sediment deposition during glacials led to ^{230}Th export towards the Nordic seas and/or its partial built up in the deep basins of the Arctic Ocean. It is concluded that $^{230}Th_{xs}$-burial in the Arctic Ocean depends on the bathymetry, with $^{230}Th_{xs}$ transfer from ridges to deep basins by the accumulation of brine in the western part of the Arctic Ocean and its evacuation towards the Fram Strait, and organic matter fluxes. The latter is linked to i) riverine discharge of terrestrial dissolved organic compounds and ii) primary productivity, which is governed by the seasonal sea ice opening, but dissociated with coarse particle fluxes.

Overall, the main contribution of this thesis is i) the verification of Nd isotopes of leachates in sediments from the inner Chukchi Sea Shelf as a tracer of Pacific Water fluxes through Bering Strait; ii) the support of a sediment-starved Arctic Basin using $^{230}Th_{xs}$-based stratigraphy; iii) the proposal of a resilient East Siberian Ice Shelf over the southernmost Mendeleev Ridge; iv) the review of the cycling and behavior of ^{230}Th in the Arctic Ocean.

Keywords: Arctic Ocean, Quaternary, radiogenic isotopes, Pacific Water, sedimentation

INTRODUCTION

0.1 Research subject and motivation

The Arctic Ocean is a small basin of the global oceans surrounded by the world's largest continental shelf areas (Jakobsson, 2002), which are a major source of detrital particles to the deep central Arctic Ocean. Its seasonal sea-ice cover is another remarkable and unique feature of the Arctic Ocean. There, under the influence of tide, wind, and waves, abundant suspended particles can be trapped in sea ice and transported with surface currents toward the central Arctic Ocean. It has been estimated that ice-rafting materials account for two-thirds of the sediments accumulated in the deep Arctic Ocean (cf. Stein, 2008). The sea ice also governs the primary productivity in the Arctic Ocean by controlling nutrient supply and sunlight penetration to the underlying water column (Lewis et al., 2020). Other factors, such as the advection of Atlantic and Pacific waters and the upwelling of nutrient-rich deep water towards the surface water, could also influence phytoplanktonic productions (e.g., Lewis et al., 2020; Stein et al., 2017a). As an example, in the western Arctic Ocean, the inflowing of nutrient-rich, relatively warm, and low-salinity Pacific Water through Bering Strait not only carries significant amounts of detrital particles and nutrients (e.g., Asahara et al., 2012) but also promotes sea ice melting (e.g., Woodgate et al., 2010), leading Chukchi Sea to be one of the most productive areas of the world (Grebmeier et al., 2005). Several studies reported that primary productivity in the western Arctic Ocean was likely associated with the Pacific Water fluxes, at least, during the Holocene (e.g., Khim et al., 2018; Stein et al., 2017a; Polyak et al., 2016). It was also estimated that the inflowing Pacific Water contributes to one-third of the freshwater budget of the Arctic Ocean (Woodgate & Aagaard, 2005).

Under low sea levels during glacial periods, the Arctic continental shelves were exposed. It is considered that two ice sheets, the Eurasian Ice Sheet and Laurentide Ice Sheet, and a possible East Siberian Ice Shelf /Ice Sheet directly influenced the Arctic Ocean during the “cold” period (Stein et al., 2017b). Their dynamics led to seafloor scouring at a maximum water depth of ~1200 m (e.g., Jakobsson et al., 2016; Niessen et al., 2013). Based on the geophysical, sedimentological, and geochemical investigations, a 1 km thick ice shelf was thought to have existed in the Arctic Ocean during, at least, the last two glacial periods (e.g., Geibert et al., 2021; Jakobsson et al., 2016). The glacial sediments were then mainly delivered by ice-streaming/icebergs (e.g., Darby et al., 2009; Deschamps et al., 2018; Purcell et al., 2022) or bottom currents (e.g., Deschamps et al., 2019; Ye et al., 2020).

As the only gateway that connects the Pacific and Arctic oceans, the Bering Strait (depth of ~50 m) was closed during glacial periods (Jakobsson et al., 2017), preventing the Pacific Water fluxes toward the Arctic Ocean. Hence, the closing and the opening of the Strait play an important role in governing the Arctic freshwater budget and the export of freshwater toward the North Atlantic Ocean, even influencing the global oceanic circulation by regulating the formation of North Atlantic Deep Water (Hu et al., 2015).

Several approaches have been used to evaluate the Pacific Water input through Bering Strait and its influences on the paleoceanographic and sedimentological changes of the western Arctic Ocean. Geochemical archives (biogenic opal content, stable carbon isotopic composition of organic matter, stable nitrogen isotopic composition of foraminifers, etc.) in sedimentary sequences from the western Arctic Ocean suggested that the latest opening of Bering Strait started at ~11 cal. ka BP (e.g., Deschamps et al., 2018; Farmer et al., 2021; Khim et al., 2018), with enhanced nutrient supply through the inflowing Pacific Water since 8 kyr ago only (e.g., Khim et al., 2018; Stein et al., 2017a). However, aside from the Pacific Water, solar insolation and sea ice conditions also influence surface-water productivity in the Chukchi Sea (e.g., Stein et al., 2017a). The organic matter content and its stable isotope composition in marine sediments although influenced by the early diagenetic processes (e.g., Farmer et al., 2021; Khim et al., 2018), still remain relatively good indicators of sea ice opening and warm intervals, with high primary productivity and high fluxes of terrestrial carbon (e.g., Kang et al., 2007).

Using chlorite and muscovite abundances in a core sequence (HLY0501-06JPC) from the Alaskan margin, Ortiz et al. (2009) suggested enhanced Pacific Water input toward the western Arctic Ocean from ~6 to 4 cal. ka BP. This proxy was also applied by Stein et al. (2017a) to decipher the Pacific Water influences on the sea ice evolution and primary productivity changes in the Chukchi Sea. Based on X-ray diffraction analyses of 58 surface sediment samples from the western Arctic Ocean, Kobayashi et al. (2015) recommended the use of (chlorite + kaolinite)/illite ratio to document the Pacific Water inflow. Subsequently, this ratio was applied in several studies to reconstruct Holocene Pacific Water fluxes (e.g., Swärd et al., 2018; Yamamoto et al., 2017). However, the high variability of chlorite and muscovite abundances and (chlorite + kaolinite)/illite ratios in the cored sequences from the Chukchi Sea points to large uncertainties in its use to estimate the fluxes of the northward Pacific Water (e.g., Stein et al., 2017a; Yamamoto et al., 2017) but has been used to track changes in sediment provenance and deep water circulation in the western Arctic Ocean (Deschamps et al., 2018, 2019). In the case of the smectite

abundance gradients in surface sediments from the Bering Sea to the Chukchi Sea, Naidu et al. (1982) and Stein (2008) suggested that the smectite content in clay fractions of sediments from the Chukchi Sea shelf could be a potential indicator of the Pacific Water (Figure 0-1).

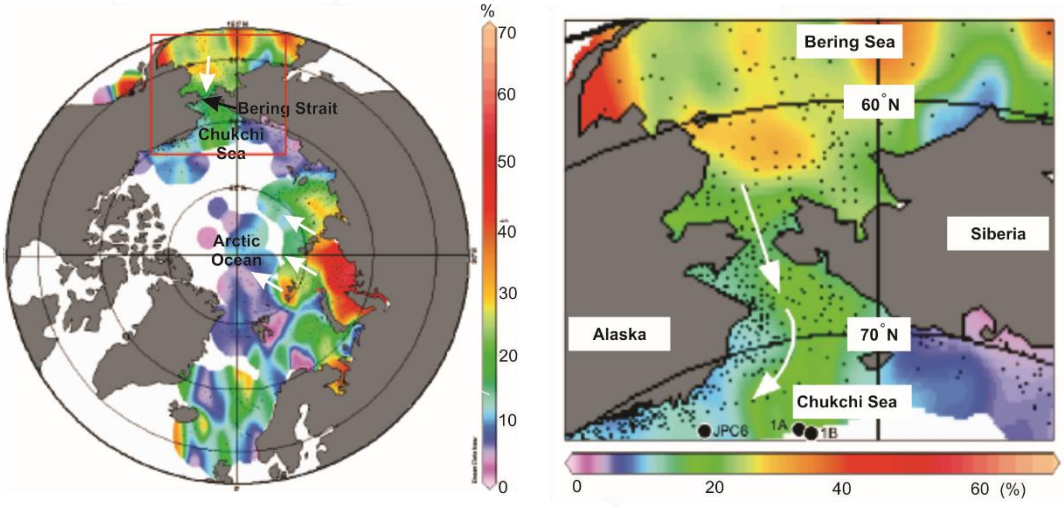

Figure 0-1 Smectite content (%) in surface sediments from the Arctic Ocean, modified from Stein et al. (2017a). White arrows: potential smectite dispersal routes.

In this thesis, the major tracer expected to record the Pacific Water inputs through the Bering Strait is the neodymium (Nd) isotopic composition of authigenic Fe-Mn oxides (i.e., leachate fractions) in sediments. The Nd isotopic composition is generally expressed in the εNd notation, following the equation as follows: $\varepsilon Nd = \{[(^{143}Nd/^{144}Nd)_{sample}/(^{143}Nd/^{144}Nd)_{CHUR}]-1\}*10^4$; where CHUR stands for the Chondritic Uniform Reservoir, with a modern $^{143}Nd/^{144}Nd$ value of 0.512638 (Wasserburg et al., 1981).

The εNd values of leachates in sediments from the Arctic Ocean have been notably used to document the deep-water circulation which is related to the brine cascading at the Siberian shelves and Atlantic-sourced water exchanges between different basins (e.g., Meinhardt et al., 2016). However, the use of Nd isotopes to trace the influx of Pacific Water back in time is still lacking. Based on the Nd isotope measurements on seawater samples from the western Arctic Ocean, Porcelli et al. (2009) reported that the radiogenic Nd signatures (εNd value up to ~ -6) in the halocline layer are linked to the Pacific Water diffusion, whereas deep waters depict lower εNd values of less than ~ -9 due to the intrusion of the unradiogenic Atlantic Water (εNd value of ~ -10.8; Andersson et al., 2008). Later, Haley & Polyak (2013) demonstrated that the εNd value of leachates could be used to track the Pacific Water masses based on the Nd isotopic analyses on leachates in bulk surface sediments from the western Arctic Ocean (Figure 0-2). The relatively high εNd

values of leachates in sediments from the Alaskan margin area, inherited from the Pacific Water, were thought to relate to the brine penetration or sediment redistribution (Haley & Polyak, 2013; Figure 0-2).

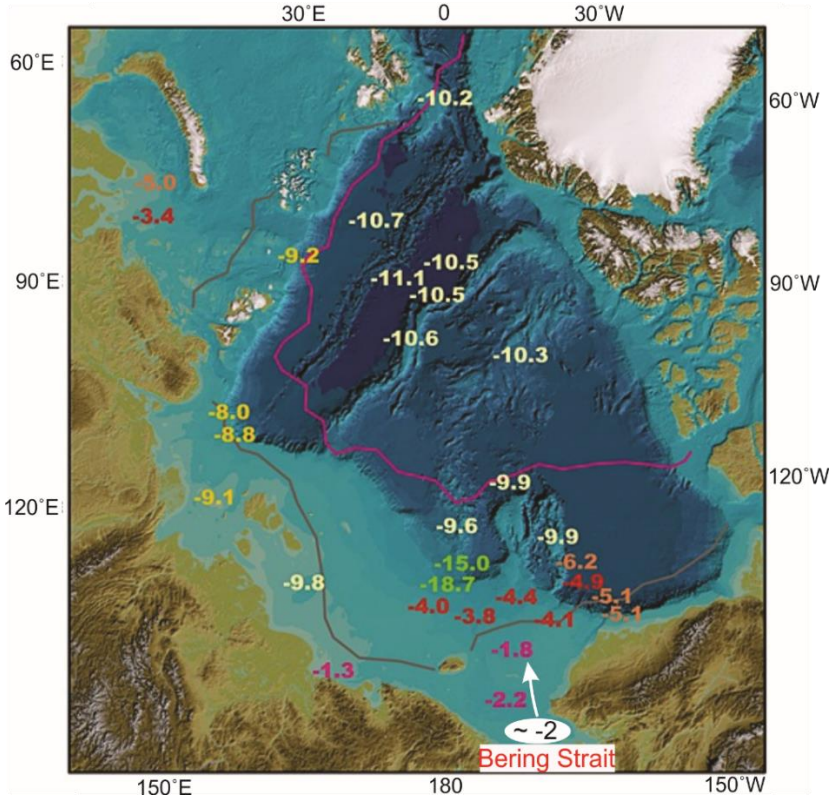

Figure 0-2 εNd values of leachates in surface sediments from the Arctic Ocean, modified from Haley and Polyak, (2013). The εNd values of the inflowing Pacific Water through Bering Strait are estimated to be ~ -2 based on the analyses of Nd isotopes in carbonates from surface sediments of the northern Bering Sea shelf (Asahara et al., 2012).

Following these works, Deschamps et al. (2019) reconstructed the Pacific Water inflowing history over the past 6 ka based on Nd isotope measurements on a core (HLY0501-01JPC) raised from the Chukchi–Alaskan margin. Unfortunately, because the core was collected at a water depth of ~1200 m, the influence of the intermediate Atlantic Water on the geochemical properties of the sediment is probably important. In addition, the bottom age of this core was dated to ~6 ka ago. A long-term record, particularly from the Chukchi Sea shelf dominated by the northward Pacific Water, would be needed to better document the history of Pacific Water inputs and its influence on the sedimentology and paleoceanography changes in the western Arctic Ocean.

Quaternary sedimentation in the Arctic Ocean has been investigated using the particle size distribution as well as mineralogical and geochemical archives in several research papers (e.g., Joe et al., 2020; Not & Hillaire-Marcel, 2010; Deschamps et al., 2018; Xu et al., 2021). Most of these studies were based on an age framework setup using the Mn-cyclostratigraphy (Jakobsson et al., 2000), ecostratigraphic markers (e.g., Backman et al., 2009), and the correlation of Pink-White layers (i.e., dolomite rich layers; Stein, 2008), which led the authors to suggest high sedimentation rate scenario of the order of cm.kyr^{-1}, thus much different from the scenario of a "sediment-starved Arctic Basin" with sedimentation rates of the order of mm.kyr^{-1} as suggested by Clark et al. (1980). The issues of the Mn-cyclostratigraphy were recently reviewed by Hillaire-Marcel et al. (2017) and Hillaire-Marcel & de Vernal (2022). The earlier assigned ages of the Pink-White layers were challenged in reference to the thorium-230 (^{230}Th) based chronostratigraphy (Geibert et al., 2021). The use of microfossils as stratigraphic indices should also be cautious in the central Arctic Ocean, not only because of the discontinuous microfossil records but also due to the fact that microfossils from two adjacent layers of interglacial/interstadial might be mixed due to low sedimentation rates (Hillaire-Marcel et al., 2022a). Considering the uncertainties of these three approaches, in this thesis, the ^{230}Th distribution and decay age are designed as a means to build the late Pleistocene chronostratigraphy of the Arctic Ocean.

Thorium is a particle-reactive element, with a residence time of a few decades (Figure 0-3). It is rapidly adsorbed onto the surface of fine particles and accumulated at the seafloor after its production from its parent isotope uranium-234 (^{234}U) in the seawater, i.e., the scavenging process (Anderson et al., 1983). The measured ^{230}Th in the marine sediment, therefore, includes three components: the lithological fractions, the authigenic fractions, and the scavenged fractions (i.e., the excess in ^{230}Th ($^{230}Th_{xs}$)). By the subtraction of the activity of measured ^{230}Th from that of its parent isotopes (^{234}U or ^{238}U), the activity of $^{230}Th_{xs}$ can be estimated as the authigenic ^{230}Th content is negligible in sediments from the Arctic Ocean (e.g., Geibert et al., 2021; Hillaire-Marcel et al., 2017).

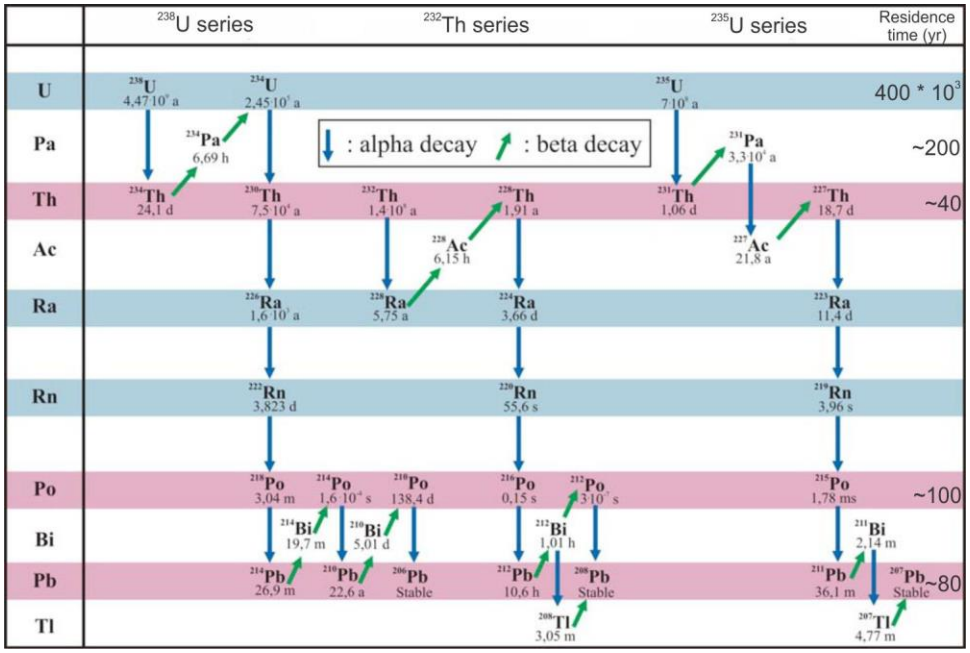

Figure 0-3 U-Th decay series with half-lives and major residence times, modified from Ghaleb (2009). The low-solubility isotopes are highlighted in pink, while the soluble ones (excluding radon which is a radioactive noble gas) are highlighted in light blue.

Regarding its high adsorption efficiency onto fine particles, ^{230}Th has been applied for assessing sedimentation processes in the deep oceans using a constant ^{230}Th flux model (e.g., Costa et al., 2020). However, this constant model could not be simply used in the Arctic Ocean (e.g., Not & Hillaire-Marcel, 2010). Under high sea levels during the interglacial/interstadial periods, fine particles delivered by sea ice rafting are responsible for the significant ^{230}Th scavenging in the deep Arctic Ocean (Figure 0-4; e.g., Geibert et al., 2021; Hillaire-Marcel et al., 2017; Not & Hillaire-Marcel, 2010; Spielhagen et al., 1997). Whereas reduced or even nil ^{230}Th scavenging occurred in the glaciated Arctic either due to the coarse particles supplied by ice streaming or iceberg-rafting (Figure 0-4; Hillaire-Marcel et al., 2022b; Purcell et al., 2022) or to the weakened ^{230}Th production assuming a freshwater filled Arctic Basin (Geibert et al., 2021), a scenario however challenged by Spielhagen et al. (2022) and Hillaire-Marcel et al. (2022b). The ^{230}Th scavenging in the Arctic Ocean is thus discontinuous and highly linked to the climate cycles. The high abundance of $^{230}Th_{xs}$ in sedimentary sequences from the Arctic Ocean is then used to identify interglacial/interstadial layers, whereas layers with deficits in $^{230}Th_{xs}$ are correlated with glacial/stadial intervals (e.g., Geibert et al., 2021; Hillaire-Marcel et al., 2017; Not & Hillaire-Marcel, 2010; Purcell et al., 2022). Assuming constant decay, a $^{230}Th_{xs}$ extinction age of ~350 kyr could be estimated based on the half-

life of the isotope (Figure 0-3; e.g., Hillaire-Marcel et al., 2017; Not & Hillaire-Marcel, 2010; Purcell et al., 2022).

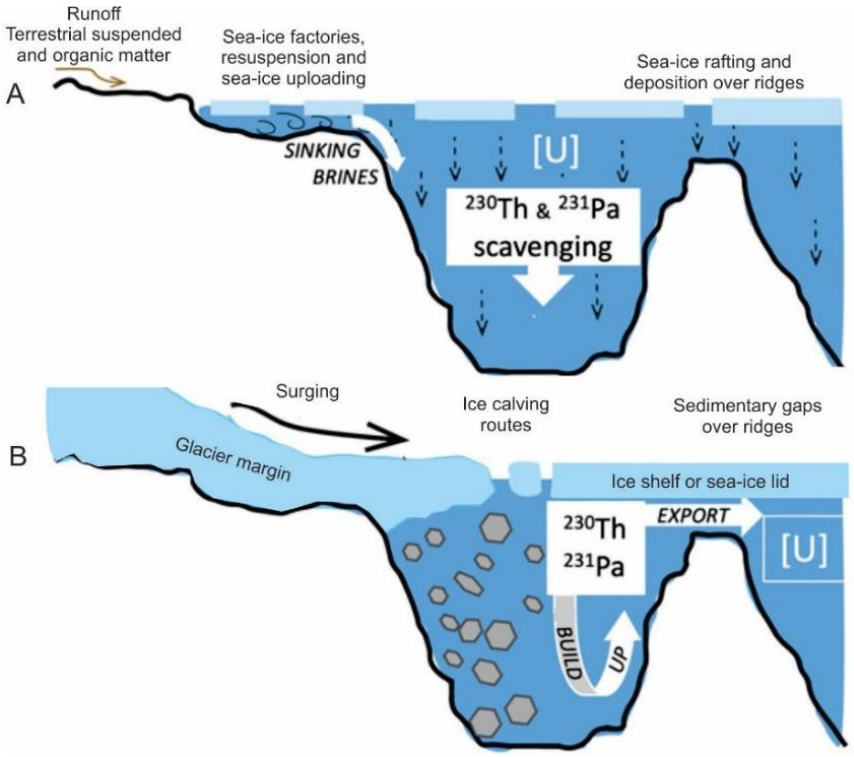

Figure 0-4 Sketch of the sedimentation process related to the ^{230}Th scavenging under distinct climate conditions in the Arctic Ocean (Modified from Hillaire-Marcel et al., 2022b).

So far, $^{230}Th_{xs}$ profiles have been used to date and evaluate the sedimentation processes in the northern Mendeleev, Alpha, Northwind, and Lomonosov ridges of the Arctic Ocean (e.g., Geibert et al., 2021; Gusev et al., 2013; Hillaire-Marcel et al., 2017; Not & Hillaire-Marcel, 2010; Purcell et al., 2022; Spielhagen et al., 1997; Xu et al., 2021). However, there are still rare applications of the approach in the East Siberian margin area. In the case of the nil $^{230}Th_{xs}$ contents during the Marine Isotope Stage (MIS) 4 and 6, a 1 km-thick ice shelf covering the central Arctic Ocean was hypothesized by Geibert et al. (2021). The existence of the thick ice shelf has been evidenced by the glacial scouring over the seafloor ridges and plateaus (e.g., Jakobsson et al., 2016; Niessen et al., 2013). In the western Arctic Ocean, features related to glacial erosion and landforms from the East Siberian–Chukchi Plateau area suggest a resilient East Siberian Ice Sheet/Ice Shelf (e.g., Niessen et al., 2013; O'Regan et al., 2017). However, the duration of the East Siberian Ice Sheet/Ice Shelf is still under debate. Based on the eco-stratigraphy and Mn-based cyclostratigraphy, the East Siberian Ice Sheet/Ice Shelf was considered to be active, at least, during MIS 4, and possibly MIS 6

(Joe et al., 2020; O'Regan et al., 2017). With suitable cored sediment sequences from the East Siberian–Chukchi Plateau area, distinct views of the long-term existence of the East Siberian Ice Sheet/Ice Shelf could be provided using the $^{230}Th_{xs}$-based stratigraphy of Geibert et al. (2021) and Purcell et al. (2022).

At last, despite the consensual $^{230}Th_{xs}$ -chronostratigraphy proposed since Not and Hillaire-Marcel (2010), the mechanism related to the weak ^{230}Th scavenging in the glaciated Arctic is still open to discussion (Geibert et al., 2021; Hillaire-Marcel et al., 2022b). To figure out the major factors governing the ^{230}Th burial in the Arctic Ocean, a compilation of the published U-Th series datasets seems thus relevant.

0.2 Objectives and outline of the thesis

The general objectives of this thesis include i) estimating the Pacific Water fluxes through Bering Strait during the present interglacial interval; ii) verifying the reliability of the $^{230}Th_{xs}$-based chronostratigraphy of the Arctic Ocean; iii) reconstructing the Arctic paleoceanographic and sedimentological history under different climate conditions. In detail, the first goal of this thesis is to reassess smectite abundance and Nd isotopes in leachates of sediments as potential tracers of the Pacific Water through the Bering Strait. Then, on this ground, to establish the Holocene changes in the inflow of Pacific Water based on the εNd values of leachates in clays from core ARC4-R09. The second objective is to reconstruct the sedimentation history of the western Arctic Ocean, with special attention to its relationship with the dynamics of the East Siberian Ice Sheet/Ice Shelf, using sedimentological, geochemical (organic matter and its stable carbon composition, $^{230}Th_{xs}$), and mineralogical properties of core Arc7-E25, whose chronostratigraphy is built by the $^{230}Th_{xs}$ distribution and distinction age downcore. The final aim is to evaluate the $^{230}Th_{xs}$ distribution and decay downcore as a robust chronostratigraphic tool and to infer paleoceanographic and sedimentological changes in the Arctic Ocean under glacial/interglacial cycles by the compilation of published U-Th series datasets.

Chapter 1 thus presents the distribution of clay mineral abundances and εNd values of leachate and residue phases of different fractions in the five surface samples from the Chukchi Sea. In comparison with the published datasets, their relationships with the Pacific Water inflowing and the terrestrial sources were evaluated. Assuming that sea level was the major parameter controlling the Holocene Pacific Water fluxes through the Bering Strait, correlations of smectite contents, and εNd values of clay leachates of core R09 with the global mean sea level rise were made to assess the reliable tracer of Pacific Water. Using two

εNd-value endmembers, i.e., the Arctic Water endmember and Pacific Water endmember, Pacific Water fluxes through the Bering Strait could be estimated. In addition, the sedimentary environment changes corresponding to the sea level rise were determined using the grain size distribution, clay mineral variation, and εNd values of residues records.

Chapter 2 re-examines the late Pleistocene sedimentation history of the western Arctic Ocean based on grain size, geochemistry, and mineralogy measurements in sediment from core E25. The age model was previously set up by Zhao et al. (2022) using Mn-cyclostratigraphy and Pink-White layers. In this study, the chronostratigraphy of core E25 was rebuilt from the $^{230}Th_{xs}$ distribution and distinction age downcore, thus providing distinct stratigraphical patterns compared to the ones of Zhao et al. (2022). Our study indicates that a few centimeters of "interglacial/interstadial" sediments were deposited within a few thousand years, consistent with the hypothesis of a “sediment-starved” Arctic basin. Aside from this, the PW layers were re-assigned using the $^{230}Th_{xs}$-based chronostratigraphy. By the correlations with the published sedimentological and geochemical archives, the sea ice conditions on the East Siberian-Chukchi Sea margin, possibly related to the resilience of the East Siberian Ice Sheet/Shelf, were investigated.

Chapter 3 reviews the $^{230}Th_{xs}$ distribution and inventory of available sedimentary sequences from the Arctic Ocean, confirming the reliability of using $^{230}Th_{xs}$ to set up the chronostratigraphy of the Arctic Ocean. It evaluates the parameters related to the ^{230}Th scavenging in the Arctic Ocean based on the correlations of the post-glacial $^{230}Th_{xs}$ inventory with the physical (bathymetry and distance from the continental shelf to the coring site), geochemical (organic matter content), and sedimentological (clay and coarse particles content) archives. Furthermore, sedimentological processes governing the ^{230}Th burials and redistributions were examined by comparing the $^{230}Th_{xs}$ inventory with its production in the water column and the $^{230}Th_{xs}$ inventory differences at adjacent sites.

CHAPITRE 1

A reassessment of Nd-isotopes and clay minerals as tracers of the Holocene Pacific Water flux through Bering Strait

Tengfei Song[a], Claude Hillaire-Marcel[a,*], Anne de Vernal[a], Yanguang Liu[b,c,*], Weiguo Wang[d] and Yuanhui Huang[b,c]

a Geotop, Université du Québec à Montréal, C.P. 8888, Montréal, QC H3C 3P8, Canada;
b Key Laboratory of Marine Geology and Metallogeny, First Institute of Oceanography, Ministry of Natural Resources, Qingdao 266061, China;
c Laboratory for Marine Geology, Qingdao National Laboratory for Marine Science and Technology, Qingdao 266061, China;
d Laboratory of Coastal and Marine Geology, Third Institute of Oceanography, Ministry of Natural Resources, Xiamen 361026, China;

Article published in 2022 at the Journal of *Marine Geology*, 443: 106698, https://doi.org/10.1016/j.margeo.2021.106698.

Abstract

The flux of low-salinity Pacific Water (PW) through Bering Strait (BS) weighs on the freshwater budget of the Arctic Ocean, which, in turn, impacts the Atlantic Meridional Overturning Circulation (AMOC). Through time, this PW flux has been tightly controlled by the bathymetry of the Strait (~50 m water depth at present), thus by sea-level (SL) changes and documented in several papers based on a large array of sedimentological and geochemical tracers. The present study aimed at reassessing the robustness of these tracers of the PW-flux, based on five surface samples collected along a south-north transect from BS to Chukchi Plateau, within the bathymetric range of the PW-mass dispersal. We also estimated their variation in relation to the post-glacial SL-rise in a sedimentary core (ARC4-R09), from the Chukchi shelf, spanning the last ~ 10 kyr. Potential indicators of PW-flux include sortable silt, clay minerals, and the particulate and exchangeable Nd-isotope composition of specific grain-size fractions. The results indicate that εNd-values in leachates, and to a lesser extent, the smectite abundance, both relating to volcanic rocks of the Bering Sea, are sensitive indicators of the PW-flux, whereas sortable silts and other clay minerals relative abundances are also influenced by other processes (e.g., west-east shelf currents, sea-ice rafting). The modern distributions of εNd-value and smectite abundance illustrate mixing between two endmembers: i) a northern Bering Sea endmember, characterized by ~ 14 % of smectite (vs all clay minerals) and a εNd-

value of the exchangeable fraction of ~ -2; ii) a Chukchi Sea endmember, characterized by ~ 8 % of smectite and a εNd-value ranging from -7 to -8. The Holocene sedimentary record from the study core indicates a progressive increase in the Bering Sea supplies through time, linked to an enhanced inflow of PW, which we associate with the deepening of the Strait due to the rising SL. Following a major reorganization of the Arctic Ocean circulation at ~ 8 ka BP, a steady increase in PW flux prevailed until ~ 4 cal. ka BP. A tenuous but continuous positive trend towards modern εNd values followed during the late Holocene. The middle Holocene steep increase of warm, low salinity PW-flux through BS, led to important changes in the Arctic Ocean, in particular of its salinity budget. Assuming that the BS bathymetry is the main parameter governing the PW-flux towards the Arctic Ocean, a first-order estimate of PW-flux under a higher than modern SL can be made using the SL-elevation-εNd relationship of the major middle Holocene shift.

1.1 Introduction

The Arctic Ocean is an important component of the climate system as its sea-ice albedo feedback could regulate the atmospheric pressure gradients in the Northern Hemisphere (Proshutinsky et al., 2015). Its freshwater export into the North Atlantic also affects the surface ocean density and stratification, thus the Atlantic Meridional Overturning Circulation (AMOC) (Broecker, 1991; Shaffer and Bendtsen, 1994; Yang et al., 2016). Two-thirds of the modern freshwater budget of the Arctic Ocean are linked to runoff and precipitations, the remaining is related to the inflow of low-salinity Pacific water (PW) through Bering Strait (BS) (Woodgate and Aagaard, 2005). PW fluxes also impact the sea-ice cover and the surface circulation in the Arctic Ocean, which, aside from wind regimes, influence the strength of the Beaufort Gyre (BG) and pathway of Transpolar Drift (Renssen et al., 2002; Prange and Lohmann, 2004). As a consequence, the freshwater export towards the North Atlantic would directly impact the AMOC (Shaffer and Bendtsen, 1994; Keigwin and Cook, 2007; Hu et al., 2015; Zhang et al., 2021).

PW is also a significant source of heat and nutrients, in particular, silicon (Cooper et al., 1997) which promotes primary productivity in the Chukchi Sea and the southern Beaufort shelf (Grebmeier et al., 2006; Lewis et al., 2020). The heat content of the PW inflow is also assumed to be one of the drivers of the present decline in the sea-ice cover of the Chukchi Sea (Woodgate et al., 2010; Serreze et al., 2016).

Several studies have been published concerning the evolution of PW fluxes through time, in particular, since the last deglaciation and in relation to the opening and deepening of BS, using a large array of

sedimentological and geochemical tracers, in particular, clay minerals and Nd-isotopes (e.g., Stein et al., 2017; Yamamoto et al., 2017; Khim et al. 2018; Deschamps et al., 2018, 2019, and references therein). In the present study, we intend to reassess the relative robustness of these tracers, based on sediments collected along an S-N transect, north of the BS, and try to further document potential linkages between sea-level (SL) changes, BS deepening, and PW fluxes from a gravity core record raised near the edge of the Chukchi Sea shelf.

Two parameters mostly control the PW flux through BS: the bathymetry of the sill and the wind regime. On one hand, any high-frequency variability linked to steric effects cannot be captured in samples representing hundreds of years of sedimentation. On another hand, recent records suggest that interseasonal to interannual variability linked to wind variability should remain within about ±20% of the mean pluriannual flux (Nguyen et al., 2020). Therefore, we assume here that the bathymetry of the BS has been the major parameter controlling mean PW inflow secular changes through time. With a sill depth of ~ 50 m, the Strait has been closed during most glacial intervals under low SL conditions. During terminations, the rising SL (e.g., Lambeck et al., 2014) led to reopenings of BS with a final "interglacial" status determined by the continental ice sheet melting. As an example, during Termination 1, BS flooding started at ~ 11.5 cal. ka BP (Jakobsson et al. 2017; Pico et al., 2020) and the Strait continued to deepen during the Holocene. Yamamoto et al. (2017) investigated the evolution of BS based on mineralogical analyses of three cores from the northern Chukchi Sea. Mostly based on chlorite/illite (C/I) records, Yamamoto et al. (2017) concluded that an intensified flow from the Bering Sea occurred during the middle Holocene, which they attributed primarily to the effect of an overall weaker Aleutian Low with a coeval intense subpolar gyre circulation in the North Atlantic. Several other authors have used clay minerals as tracers of PW inputs, with investigations about chlorite and muscovite abundances, C/I ratios, chlorite+kaolinite/illite ((C+K)/I) ratios, smectite/illite (S/I) ratios (Ortiz et al., 2009; Kobayashi et al., 2016; Stein et al., 2017; Deschamps et al., 2018; Khim et al., 2018; Swärd et al., 2018). For example, Ortiz et al. (2009) inferred an enhanced PW influx from 6 to 3.2 cal. ka BP, based on chlorite and muscovite abundances in size fractions of less than 4 µm. Smectite content was underestimated in their study as their X-ray diffraction analysis also included fine silt fractions. Aside from methodology issues (cf. Kobayashi et al., 2016; Khim et al., 2017), clay mineral relative abundances also depend on other parameters, for instance, the large array of circum-Arctic source supplies, their variability through time (coastal erosion,

shelf bathymetry…), and particularly their transport mechanism (e.g., sea-ice, icebergs, currents). Most of these processes are subject to changes with SL rises and falls.

A general feature of sediments from the southern Chukchi Sea is their high smectite content (~ 20%) in contrast to those from the adjacent northern, eastern, and western areas (Wahsner et al., 1999; Viscosi-Shirley et al., 2003; Stein, 2008). Hence, smectite is thought to be carried with water masses and sea-ice from the Bering Sea (Naidu et al., 1982), and its abundance could thus be used as a potential tracer of PW inputs (Stein, 2008). The neodymium isotope composition (εNd) of exchangeable fractions (sediment leachates) have also been applied to track PW inflow (Haley and Polyak, 2013; Deschamps et al., 2019), as this Nd bears a distinctive radiogenic εNd signature, acquired in the Bering Sea (Piepgras and Jacobsen, 1988; Asahara et al., 2012; Maccali et al., 2018) in comparison with the Arctic Ocean water (Porcelli et al., 2009).

In the present study, we paid special attention to all clay minerals, including kaolinite and smectite, and looked deeper into parameters governing their distributions along the S-N PW route in the Chukchi Sea, following earlier works by Naidu et al. (1982), Viscosi-Shirley et al. (2003), Stein (2008), and Swärd et al. (2018). In conjunction with the smectite content, the Nd isotope compositions of exchangeable and detrital fractions were also analyzed as they have often been used as direct tracers of the Bering Sea water inflow (Haley and Polyak, 2013; Deschamps et al., 2019).

1.2 Regional setting

The low salinity (around 32.5 psu) and relatively warm (up to 12 ℃) PWs (Woodgate and Aagaard, 2005) flow north through BS as the result of the steric difference between the western Arctic Ocean and the Bering Sea (Aagaard et al., 2006), with rare reversals in winter (Woodgate et al., 2005; Danielson et al., 2014). The current velocity in the Strait varies from ~ 20 to ~ 30 cm. s^{-1}, peaking exceptionally at 100 cm. s^{-1} under extreme wind regimes (Woodgate et al., 2005; Danielson et al., 2014). The measurements made over the last decade indicate that the PW flux ranges from 0.7 to 1.2 Sv (Sv = 10^6 $m^3.s^{-1}$), with a mean value of ~ 1.0 Sv (Woodgate, 2018). Presently, PW contributes an average of 30% of the freshwater budget of the Arctic Ocean (Serreze et al., 2006), possibly up to 40%, according to Yamamoto-Kawai et al., (2008). The PW includes two water masses: the Bering Sea Water (BSW) and the Alaskan Coastal Water (ACW) (Fig. 1-1A). After entering the Chukchi Sea, the BSW divides into three branches: one turns west around

Herald Shoal, the second is diverted through the Central Channel, and the third flows east of Hanna Shoal into the Barrow Canyon (Fig. 1-1A; Grebmeier et al., 2006; Hunt et al., 2013). The ACW is entrained into the Chukchi and Beaufort seas along the Alaskan coast (Fig. 1-1A). Given the bathymetry of the Chukchi Sea, the Herald Canyon was probably the major conduit of the PW flow during the early Holocene, when SL started rising above the BS sill (Fig. 1-1B).

Major contributors to the freshwater budget of the Arctic Ocean are all the northern Russian rivers and the Mackenzie, on the Canadian side. The three important rivers that directly influence the Chukchi Sea and adjacent areas are the Yukon, Mackenzie, and Kolyma rivers (Fig. 1-1A), which contribute not only to the freshwater budget but also to the Nd isotope budget of the Arctic Ocean.

Several shelf and coastal currents flow essentially eastward in the Chukchi Sea and its adjacent areas, including the East Siberian Sea, and the southern Beaufort Sea as described by Li et al. (2019) (Fig. 1-1A). Modern sediments of the western Chukchi Sea may derive from different sources that include: i) Bering Sea supplies through BS; ii) the Russian shelves through the Siberian Coastal Current (SCC); iii) occasional inputs linked to sea-ice, rafting westward, under enhanced BG circulation (e.g., Petty, 2016; Maccali et al., 2018). In the eastern Chukchi Sea, the sediments originate mostly from the BS inflow and the Alaskan/Canadian margin supplies (Fig. 1-1A; Pfirman et al., 1997; Darby, 2003; Maccali et al., 2018).

1.3 Materials and Methods

1.3.1 Sampling sites and sediment sampling

Five surface sediments were recovered by multi-corers, from the northern BS to the Chukchi Plateau, during the 6th Chinese Arctic expedition on the R/V *Xue Long* in 2014 (Table 1.1). To verify that recent sediments were not lost during coring, ^{210}Pb-measurements were performed (see ANNEXE A Supplementary Fig. 1). During the 4th cruise of the *Xue Long* in 2010, a gravity core (ARC4-R09, hereafter named core R09; 168.9 °W, 72.0 °N; 51 m deep) has been recovered close to the Chukchi shelf edge (Table 1.1, Fig. 1-1). The site of core R09 is located within a channel that was probably submerged rapidly at the opening of the BS (Fig. 1-1B). The site is under the combined influence of seasonally variable currents and water masses that include the warm and moderately saline BSW in summer-early fall, and the cold waters either locally formed or carried by the SCC in winter (e.g., Weingartner et al., 2005; Pisareva et al., 2015).

Core R09 was continuously sampled at 1 cm intervals. In this study, a total of 24 samples were analyzed for their sedimentological, mineralogical, and Nd-isotope properties (see ANNEXE A Supplementary Table 1). A tighter sampling spacing has been selected in the middle core section to achieve a better resolution for the interval spanning the transition that accompanied the deepening of the BS.

1.3.2 Analytical methods

1.3.2.1 ^{210}Pb in surface sediment samples

As a means to ascertain the recovery of surface sediments, ^{210}Pb measurements were performed on core top sediments (Geotop-UQAM laboratory). About 0.2 g-aliquots of all samples were dried and ground for this purpose. Chemical extraction and counting efficiencies were determined using a ^{209}Po-spike (see details in Not and Hillaire-Marcel, 2010). An HCl–HNO_3–HF ^{210}Po-extraction method was performed following Baskaran and Naidu (1995). Elution was deposited on a silver disk (Flynn, 1968). The ^{209}Po and ^{210}Po activities were measured using a silicon surface barrier α spectrometer (EGG and ORTEC type 576A). Uncertainties were estimated as ±1σ standard deviations from counting statistics; they average 3% of the value obtained. The excess ^{210}Pb-fraction ($^{210}Pb_{xs}$) was estimated assuming a supported fraction corresponding to the mean ^{226}Ra activity measured by Baskaran and Naidu (1995), in surface sediments from the same area: 1.10 ± 0.25 dpm. g^{-1} (±1σ; n = 10; see ANNEXE A Supplementary Table 2).

1.3.2.2 Grain size and sortable silt measurements

Grain-size measurements of the bulk surface sediment samples are performed in the laboratory at UQAM. Grain-size data are reported as the weight percentages of fractions separated through wet-sieving (> 10 µm fractions) and suctioning (< 10 µm fractions). Suctioning separations of the 2–10 µm and < 2 µm fractions were based on Stokes's Law. These fractions include sand (> 63 µm), coarse silt (10–63 µm), fine silt (2–10 µm) and clay (< 2 µm). Results are reported in ANNEXE A Supplementary Table 3.

Grain-size analyses in samples from core R09 were performed on carbonate-, opal-, and organic-free samples at the Third Institute of Oceanography, Ministry of Natural Resources, China following a protocol described in McCave et al. (1995). Measurements were made with a Malvern MasterSizer 2000™ laser particle analyzer over the 0.02–2000 µm size range, with a reproducibility better than 3% (Wang et al., 2020). The sortable silt fraction used for current velocity estimates ranges from 10 to 63 µm (McCave et

al., 2017). To make the appropriate grain-size correction (Kissel et al., 2013), sortable silt fractions were amended downcore using a correction factor determined from density data calibrated with core top value, i.e.:

$SS_i = SS_i^m * \rho_i/\rho_0$,

where:

SS_i^m = sortable silt fraction measured at the core depth i

ρ_i = density of the core depth i

ρ_0: density of the core top.

The density data of core R09 was inferred from the nearby core ARA2B-1A (site 2 of Fig. 1-1A; Stein et al., 2017) based on their magnetic susceptibility correlations. All sedimentological data are reported in ANNEXE A Supplementary Table 1.

1.3.2.3 X-ray clay mineral analysis

About 2 g-aliquots of bulk sediment were used for clay mineral studies. The sediment was wet rinsed through 63 and 10 µm sieves. Clay fractions were separated by suctioning according to Stokes' Law. X-ray clay mineral analyses were made using the method of Moore and Robert Jr. (1989) and following the procedures adopted at the UQAM X-ray laboratory (Fagel et al., 2004). Smear slides of the clay fraction were prepared after the following treatments: (1) air-dried sample; (2) ethylene-glycol solvation during 24 hours to estimate the smectite peak area at 17 Å; (3) heating to 325℃ for 4 hours to check the collapse of smectite. The smear slides were automatically loaded on the goniometer of a Siemens D-5000™ diffractometer (CoKα 1, 2 radiation; silicon detector). Semi-quantitative estimates of the main clay minerals, including smectite, illite, chlorite, and kaolinite, were made based on the DIFFRAC-EVA™ software. Further corrections followed Biscaye (1965), i.e., a weight factor of 4 for illite, a factor of 2 for chlorite and kaolinite, and 1 for smectite. This method was widely used in the Arctic Ocean, allowing comparison with reference materials (e.g., Wahsner et al., 1999; Viscosi-Shirley et al., 2003). Uncertainties average 5 to 10% for clay mineral abundances, based on Fagel et al. (2004). The clay mineral composition is reported in dry weight percent (%) of the four major clay minerals in ANNEXE A Supplementary Tables 1 and 4. Results from site R03 are unfortunately missing due to their loss during laboratory procedures.

1.3.2.4 Nd-isotope measurements

Nd isotopic measurements were performed at Geotop-UQAM on different grain-size fractions (sand, coarse silt, fine silt, and clay) of the surface sediment samples as well as on the clay fraction in sediment samples from core R09. About 0.3 g of each subsample was treated for Nd extraction and isotopic measurements, following Chen et al. (2012). Minor differences in chemical extraction of exchangeable Nd may be found in the literature (e.g., Gutjahr et al., 2007; Asahara et al., 2012; Chen et al., 2012; Maccali et al., 2013; Wilson et al. et al., 2013; Blaser et al., 2016; Deschamps et al., 2019; Huang et al., 2021); they are discussed in the ANNEXE A Supplementary Material. In the first step, a Na acetate buffer (1M, sodium acetate and acetic acid in a ratio of 1:1) treatment, at room temperature, slightly shaking the Teflon™ tube for 3 hours, was used to remove calcite. Dolomite is resistant to the Na acetate buffer but appears negligible in the sediments from the Chukchi shelf south of 75º (Kobayashi et al., 2016). After rinsing three times with Milli-Q water, the residues were dried and ground. Powders were subsequently leached and slightly shaken at room temperature for approximately 3 hours with a solution of 0.005 M hydroxylamine hydrochloride (HH)-1.5% acetic acid-0.03 M Na-EDTA, buffered to pH 4 with sodium hydroxide (NaOH). This second leaching is designed to specifically dissolve Fe-Mn oxides. The solutions of acetic acid and HH used here are highly diluted compared with those used by Asahara et al. (2012), to avoid any leaching of Nd from the detrital minerals (Chen et al., 2012). Residues were rinsed again as described above and the solution was transferred into the supernatant. Henceforth, the recovered supernatant is referred to as the Fe-Mn leachate that contains the exchangeable Nd-fraction (Bayon et al., 2002; Gutjahr et al., 2007). The final residues, thought to represent exclusively the inherited, non-exchangeable Nd-fraction, were digested in concentrated HF, HNO_3 mixtures on a 110°C-hot plate for more than 3 days to ensure complete dissolution.

After drying and redissolution, the Fe-Mn leachates and residues were separately loaded successively on two sets of columns in distinct clean fume hoods to extract Nd isotopes. Briefly, samples were firstly loaded on a column of TRU Spec© resin, rare earth elements were separated using dilute HNO_3. Nd was then isolated using an LN Spec© resin column with HCl and collected in a Teflon™ beaker. Details could be seen in Pratte et al. (2017). The Nd fractions from Fe-Mn leachates and residues were analyzed on a VG Sector-54™ mass spectrometer in dynamic collection mode. Nd isotopic compositions are expressed as:

$\varepsilon Nd = \{(^{143}Nd/^{144}Nd)\ sample/\ (^{143}Nd/^{144}Nd)_{CHUR} - 1\} * 10^4$

i.e., in reference to the Chondritic Uniform Reservoir (CHUR) composition.

Replicated analyses of reference material JNdi-1 show a mean value of $^{143}Nd/^{144}Nd$ = 0.512095 ± 0.000032 (±2σ; n=25), which agrees with the uncertainties of its certified value of 0.512115 ± 0.000007 (Tanaka et al., 2000). The external reproducibility was better than 0.6 ε units (±2σ). Results are reported in ANNEXE A Supplementary Tables 1 and 4.

1.3.2.5 Radiocarbon measurements and calibrated age determination in core R09

Biogenic carbonates used for ^{14}C measurements consist of mollusk shell fragments that were recovered in seven layers of core R09. Shells were sent to the Beta Analytic Testing Laboratory for measurements by accelerator mass spectrometry. The shells' pre-treatments consisted of mechanical abrasion and leaching with dilute hydrochloric acid to remove any surface contaminations. Radiocarbon ages ("conventional" ^{14}C years) were calibrated using the Marine13 calibration curve (Reimer et al., 2013; Heaton et al., 2020). The correction for the marine reservoir effect was estimated from the CALIB database (http://calib.org/calib/) indicating an ΔR-value of 465 ± 95 yr, in addition to the conventional 400 yr of the air-sea reservoir offset. This correction fits with estimates from Pearce et al. (2017) and Reuther et al. (2020) for the Chukchi Sea. Results are reported in Table 2. The age-depth relationship was established using the *Bacon* package (Blaauw and Christen, 2011).

1.4 Surface sample results

1.4.1 Sedimentology

Total ^{210}Pb activities in surface samples from the Chukchi shelf range 2.3–2.7 dpm. g^{-1}, with a northward trend for slightly increasing values (see ANNEXE A Supplementary Fig. 1). They fall in the upper range of ^{210}Pb activities reported for surface sediments of the Chukchi shelf by Baskaran and Naidu (1995): 1.0 to 2.5 dpm. g^{-1} (n = 10), but below the mean value of those from the same area analyzed by Kuzyk et al. (2013): ~ 3.8 ± 0.2 dpm. g^{-1} (n = 3). Using the Baskaran and Naidu (1995) ^{226}Ra measurements as a first estimate of the supported ^{210}Pb-activity, shelf sediment $^{210}Pb_{xs}$ values would average ~ 1.5 dpm. g^{-1}. We thus assume that material from the last decades is present in all core tops. The deeper Chukchi Plateau site yielded a much higher ^{210}Pb activity in the core top (~ 8.2 dpm. g^{-1}), due to sediment focusing as already documented by Lepore et al. (2009).

Sediments are poorly sorted (see ANNEXE A Supplementary Table 3). Silt size particles dominate in all samples. The sand fraction is very high (~ 30 to ~ 40%) in samples from the shallowest sites at the proximity of BS and still represents ~ 20% in the sample of the deepest site (SR14), suggesting high ice-rafting contributions. Most samples from the Chukchi shelf contain ~ 10% of clay, except at site SR11 where the sample contains clay fraction up to 23%. At the deepest site SR14, there is only ~ 3% of clay. This site is under the influence of slope current flowing eastward, which might explain its lower clay content (Stabeno and McCabe, 2020).

1.4.2 Clay mineralogy

All sites show a relatively well-clustered clay mineral distribution. Illite is dominant in all samples, with percentages of ≥ 60 % (Fig. 1-2a). Chlorite comes second, with percentages ranging between ~ 10 and ~ 20 % (Fig. 1-2b). Smectite and kaolinite represent respectively ~ 8 to ~ 17 % (Fig. 1-2c) and ~ 7 to ~ 13 % (Fig. 1-2d). No clear trend in relative abundances can be inferred from this transect. Normalizing clay abundances to $^{210}Pb_{xs}$ to estimate relative fluxes northward would not modify the observed pattern, at least over the shelf, where the ^{210}Pb activity is almost uniform.

1.4.3 Nd-isotopes

The εNd values of residues range from -5.4 to -8.2 on the Chukchi shelf, with a trend towards more negative values northward. Coarse silts and sands depict slightly more radiogenic values than fine silts and clays (Fig. 1-3a–d). Significantly less radiogenic εNd values, -13 to -11, are observed at the deeper site SR14 from the Chukchi Plateau. The εNd-values of leachates from the shelf samples range from a highly radiogenic value near BS (~ -2) towards slightly more negative values northward (~ -3 to ~ -4) (Fig. 1-3e–h). This is true for all fractions. The εNd values in leachates from the deeper Chukchi Plateau sample SR14 fall in a -7 to -8 range, i.e., close to that observed by Porcelli et al. (2009) in the Canada Basin.

1.5 Gravity core results

1.5.1 Age model

The age model of core R09 (Fig. 1-4) is not well constrained due to the low number of dated layers (see Blaauw et al., 2018), especially within the middle Holocene interval (~ 8 to 4 cal. ka BP). A smoothed probabilistically weighted interpolation is illustrated in Figure 1-4. Linear interpolations between age

clusters of the upper and lower parts of the core that are relatively well-dated suggest three phases with distinct sedimentation rates:

i) ~ 40 cm. kyr^{-1} from core bottom to ~ 195 cm (i.e., from ~ 10 to ~ 8 cal. ka BP; henceforth the second part of the "early Holocene");

ii) ~ 15 cm. kyr^{-1} between ~ 195 and ~ 130 cm (i.e., from ~ 8 to ~ 4 cal. ka BP; henceforth the "middle Holocene");

iii) ~ 36 cm. kyr^{-1} from ~ 130 cm to core top (i.e., from ~ 4 cal. ka BP to the Present; henceforth the "late Holocene").

1.5.2 Sedimentary regimes

The sedimentary sequence of core R09 varies from sandy silt in the lower and middle part of the core below 130 cm (> 4 cal. ka BP) to clayey silt in the late Holocene overlying section (Fig. 1-5c–e; ANNEXE A Supplementary Table 1). Silt and sand contents are anti-correlated (R^2 = 0.95; see ANNEXE A Supplementary Fig. 2), suggesting significant changes in current velocity during the recorded interval. The grain size data also indicate an increasing clay abundance through time and broadly define two distinct regimes: an early and middle Holocene transitional regime characterized by a decrease in sediment coarseness, and a late Holocene almost steady regime. However, sortable silt values slightly depart from this pattern, with a progressive evolution from ~ 40 µm, at the bottom of the core, to ~ 25 µm in the upper 60 cm section corresponding to the last ~ 1500 yr (Fig. 1-5b).

1.5.3 Clay mineralogy

Illite dominates throughout the sequence with a small decreasing trend from ~ 77% at the bottom of the core down to ~ 60% at the core top (Fig. 1-5h). Accordingly, the clay mineral ratio (C+K)/I is broadly anticorrelated to the illite content (R^2 = 0.45). Similarly, the smectite content is anticorrelated with that of illite (R^2 = 0.84, see ANNEXE A Supplementary Fig. 3). Therefore, the driver of trends depicted in the clay mineral content could be either a slight increase in chlorite, kaolinite, and more importantly of smectite, or a decrease in the relative flux of illite. Overall, clays depict complex variations, with a broad increasing trend for smectite (Fig. 1-5j) and a decreasing one for illite throughout the middle and late Holocene (Fig.

1-5h). The chlorite and kaolinite contents do not show a clear trend but a high variability through time (Fig. 1-5f, g), relating probably to variable erosion rates, shelf currents, and ice-rafting.

1.5.4 Nd-isotopes

With a mean of -9.4, εNd values of clay-sized residues from core R09 vary little (Fig. 1-5k). Minor excursions (± 0.6 εNd units) are recorded during the transition between the early/middle and middle/late Holocene. The early/middle Holocene shifts are worth noticing as they correlate with excursions in the exchangeable fraction as well.

The εNd values of leachates increase in two steps, from ~ -5.9 at the base of the core in the latest part of the early Holocene to ~ -3.3 at the middle/late Holocene transition. This increase is marked by short oscillations at the transition between the early/middle Holocene. The leachate εNd value remains broadly stable around -3.0 throughout the late Holocene (Fig. 1-5l). Hence, with a major trend from unradiogenic to radiogenic values from the base to the upper part of the core, the pattern of downcore changes in the εNd values of leachates resembles that of the sortable silts (Fig. 1-5b).

1.6 Discussion

The major objective of the present study was to assess the robustness of clay minerals and Nd-isotopes as tracers frequently used for documenting PW inflow changes during the present interglacial. Earlier studies revealed that clay minerals were somewhat equivocal tracers of PW fluxes due to their high-frequency variability (e.g., Kobayashi et al., 2016; Yamamoto et al., 2017; Deschamps et al. 2018; Swärd et al., 2018). Nd-data from Deschamps et al. (2019) is also equivocal as they are based on a core from a relatively deep site (HLY0501-01JPC; water depth: 1163 m; site 1 in Fig. 1-1A), marked by the influence of slope currents (Li et al., 2019). Hence, uncertainties remain for both categories of tracers. Based on our results, we will first discuss the sedimentary fluxes, north of BS, then, the reliability of clay minerals and Nd isotopes as tracers of modern PW fluxes. At last, we will make attempts at estimating PW fluxes through time, at least, during the last 10 kyr interval recorded in core R09.

1.6.1 Particulate transport, bottom currents, and sediment deposition

1.6.1.1 Sediment grain size and depositional processes

Sand content in surface sediments exceeds 30% in samples from the Chukchi shelf, whereas it decreases to about 20% in the sample from the Chukchi Plateau (Fig. 1-6; ANNEXE A Supplementary Table 3). In comparison, sites from the deep western Arctic Ocean, where sea-ice rafting is the main sediment source, contain rarely more than a few percent of sand (Not and Hillaire-Marcel, 2010; Park et al., 2014). Observations from Darby et al. (2011) about materials carried by sea ice also suggest that the coarse fraction content of the Chukchi Sea shelf surface sediment is mostly linked to the shelf and/or tidal currents (Wang et al., 2016; Cooper and Grebmeier, 2018), whereas dust deposition seems negligible (Stein, 2008). Based on Li et al. (2005) and Woodgate et al. (2005), tidal currents would not be significant in the Chukchi Sea. Thus, shelf currents could be seen as the major players, aside from some wave actions during the open sea-ice season (Francis et al., 2011). Mean current velocity ranges from 1 to 12 cm. s^{-1} on the shelf and reaches up to about 30 cm. s^{-1} in BS (Woodgate et al., 2005, Wang et al., 2016). Such velocities are within the transport/deposition range of sands (Voogt et al., 1991). Seasonal patterns in sedimentary dynamics (Kipp et al., 2020; Lalande et al., 2020) may account for finer fraction deposition, notably during summer characterized by lesser current velocities (Kim et al., 2021). This probably explains the presence of up to ~ 23% of clay in the sample of site SR11, collected near the shelf edge (Fig. 1-6). These results show a northward trend towards finer sedimentation from BS to the shelf edge. This trend is consistent with slightly increasing concentrations of ^{210}Pb (ANNEXE A Supplementary Fig. 1).

Mechanisms of particulate transport and deposition on the Chukchi Plateau are distinct from those on the shelf. At site SR14, located below the Chukchi Slope Current that extends down to 900 m, the annual average bottom current velocity is practically nil (Stabeno and McCabe, 2020), explaining the low clay content of this site (Fig. 1-6). Low clay contents are also reported around the Chukchi slope area, where they are associated with relatively coarse ice-rafted debris (IRD) from the sea ice, mostly carried along with the BG. The Plateau itself, where the clays remain in the 12–24% range (Park et al., 2014), thus depicts a distinct signature.

1.6.1.2 Evolution of sedimentation at site R09 during the Holocene

The coring site R09 is located in a channel under the combined influence of the BSW flow and coastal current from the East Siberian Sea (Fig. 1-1A). The sortable silt index decreases from the base of the core to ~ 1500 cal. yr BP. A steeper slope is observed during the early Holocene (up to ~ 8 kyr BP; Fig. 1-5b), which corresponds to the early submergence stage of the inner Chukchi shelf, thus an interval marked by the weakening of the wave actions. Below, the overall sortable silt trend follows quite closely the mean global SL curve (Fig. 1-5a, b), suggesting a reduction of bottom current velocity and reduced wave influences in response to the deepening of the site. This is consistent with the reducing trend in sand content, thus with the decrease of sediment coarseness throughout the recorded interval. Lesser and steadier current velocities characterized the late Holocene interval (Fig. 1-5b) when SL was close to its present position (Fig. 1-5a; Jordan and Mason, 1999). In contrast to mineralogical and geochemical parameters, the grain size distribution does not show any major oscillations at about 8 cal. ka BP. This suggests that the bottom current velocity did not change significantly during this interval, despite the reorganization of the Arctic Ocean circulation.

1.6.2 Clay minerals as PW tracers

1.6.2.1 Clay mineral distribution in the surface samples

Illite is an abundant clay mineral in cold/arid areas, particularly in the glacial environment. It is abundant throughout the Arctic Ocean, except in some areas of the Kara Sea (Wahsner et al., 1999). The chlorite content varies between 14% and 25%, except in some areas of the Chukchi Sea and the American coast (Wahsner et al., 1999). Kaolinite, a rare clay mineral in the Arctic area, is thought to derive from kaolinite-bearing paleosols. Its content is generally < 10% (Viscosi-Shirley et al., 2003). Smectite, a product of the erosion and weathering of the young volcanic rocks, is abundant in the Kara and western Laptev seas (Wahsner et al., 1999), as well as in the Bering Sea (Naidu et al., 1982). Its distribution in surface sediments from the East Siberian Sea to the Chukchi Sea shows a limited eastward dispersal, notably east of the Kolyma River (Fig. 1-7; Wahsner et al., 1999; Viscosi-Shirley et al., 2003). Thus, it is assumed to be essentially transported into the Chukchi Sea through the BS (e.g., Khim, 2003; Stein, 2008).

As illustrated in Figure 1-7, the smectite relative abundances decrease, from ~ 14 % in the northern Bering Sea to ~ 8 % on the Chukchi Sea shelf edge. Smectite content can be assumed to trace PW-sourced

sediment dispersal in the Chukchi Sea (cf. also Stein, 2008). However, the most abundant clay mineral remains illite (averaging 60 %). Hence, any minor changes in illite flux, for example, linked to some variability of the W-E flowing SCC, would unavoidably impact the relative abundance of other clay minerals, including smectite (Fig. 1-7; cf. also Khim, 2003). Variations in the SCC could thus impact the relative abundance of smectite in surface sediments from the Chukchi Sea and invalidate any attempts at using changes in the relative abundance of smectite as recording exclusively PW fluxes. So far, information about potential Holocene instabilities of the SCC is missing. However, some changes probably occurred in response to the SL rise of the early to middle Holocene.

1.6.2.2 Holocene clay mineral changes recorded at site R09

Broad mineralogical trends are observed in core R09 with increasing smectite and decreasing illite relative abundances upcore (Fig. 1-5h, j). Accordingly, the S/I ratio increases from the early to late Holocene. Chlorite and kaolinite show some variations through time (Fig. 1-5f, g). As they are not abundant, minor changes in their relative supply may induce variations in their respective proportions. They can be due to slight changes in erosion rates, bottom currents and/or ice-rafting drift patterns, and deposition rates (e.g., Stein et al., 2017).

Some broad features are observed for all clay minerals, particularly their high variability in the early Holocene part of the record, indicating that shoreface processes, wave, and sea-ice actions were then major factors of the sedimentary dynamics. Although clay mineral fluxes could not be determined precisely, as explained above, their mean fluxes of the middle Holocene interval were broadly lower than those recorded during the early and late Holocene intervals (Fig. 1-8). The only clear feature of the Arctic Ocean within this time window is its reduced sea-ice cover (e.g., de Vernal et al., 2020). Nevertheless, the increasing trend of smectite during the late Holocene in most records from the western Arctic published so far is more pronounced than that of other clay minerals (Darby and Bischof, 2004). One may thus assume increasing smectite supplies from the Bering Sea. In previous studies, the smectite content and some clay mineral ratios (C/I, (C+K)/I) have been used as indices of PW fluxes (e.g., Kobayashi et al., 2016; Yamamoto et al., 2017; Deschamps et al., 2018). Clay mineral data from core R09 do not seem as conclusive from this viewpoint (Figs. 1-5, 8): whereas smectite proportions and fluxes seem somewhat

linked to PW inflow, the increase of all clay mineral fluxes during the late Holocene mostly relates to the decreasing grain size and finer sediment deposition linked to the deepening of the study site (Fig. 1-5c–e).

1.6.3 εNd-values of detrital minerals vs sediment sources

1.6.3.1 Surface sediments and their source

A large difference is observed between εNd-values of coarse silt fractions from the Chukchi Sea shelf (mean = -6.6±1.0; ±1σ; n = 4) vs that from the Chukchi Plateau, which depicts a significantly lesser radiogenic value (~ -12.5; Fig. 1-6). The εNd values of different grain-size fractions follow a similar pattern. Moreover, there seems to be an apparent relationship between grain size and εNd value, notably near BS, where the coarse fractions (sand ~ -5.9; coarse silts ~ -5.4) seem slightly more radiogenic than the fine fractions (fine silt ~ -7.0; clay ~ -7.7; Fig. 1-6). They could relate to some IRD supplies from the northern Bering Sea, based on the nearly similar values (~ -5.8) measured by Maccali et al. (2018) in sediments from sea-ice rafts in the northern Bering Sea. Aside from this minor feature, the εNd values in the Chukchi Sea shelf sediment suggest mixing of radiogenic material from the Bering Sea (mean = -7.4±0.7; ±1σ; n = 5; Asahara et al., 2012) with less radiogenic material from the East Siberian Sea (mean = -9.5±1.4; ±1σ; n = 7) and Alaskan coast (~ -9.5; Maccali et al., 2018). The single sample from the Chukchi Plateau is characterized by the lowest mean εNd-value (-11.5±0.7; ±1σ; n = 4). Similar values in downcore and surface sediments were also reported over the Mendeleev Ridge, where they were assigned to IRD supplies from the Canadian Arctic margin, along with the BG (Fagel et al., 2014; Meinhardt et al., 2016). The influence of Bering Sea sediment supply seems thus mostly restricted to the Chukchi Sea shelf.

1.6.3.2 Sediment source changes through time

The εNd values of residues from clay fractions in core R09 average -9.4 ± 0.2 (±1σ; n = 24), within the range of the reproducibility of the JNdi-1 reference material. When compared to the mean εNd-value of residues from clays in surface sediment from the inner Chukchi shelf (-7.9 ± 0.3; ±1σ; n = 4), site R09, located close to the shelf edge, depict a statistically significant less radiogenic signature. This site is characterized by mineral sources slightly distinct from those of sites closer to the BS, with possibly some mixing of Bering Sea sources with i) long-distance transported clay-sized sediments by the eastward-flowing shelf currents, or ii) sea-ice carried materials from the Mackenzie River and coastal Alaska (Asahara et al., 2012; Maccali et al., 2018).

As mentioned earlier, both clay residues and leachates show isotopic excursions at cal. 8 kyr BP, the inception of the middle-Holocene, and also at 5 cal. ka BP (Fig. 1-5k). Whereas, the middle Holocene Nd isotopic composition of residues averages -9.5±0.1 (±1σ; n = 10) when discarding the 4 radiogenic excursions, samples from these excursions yielded a mean value of -9.0±0.1 (±1σ). The difference is statistically significant and points toward short pulses of more radiogenic supplies likely from the BS/Bering Sea area. Discarding these excursions, the εNd-values in residues from the clay fractions do not record any trends that could be associated with either the Holocene SL rise, the BS deepening, and/or any enhanced PW sedimentary supplies. This would suggest that the sources of fine particulate material accumulated at site R09 varied little throughout the interval, as also suggested by the near parallel evolution of clay mineral fluxes (Fig. 1-8).

1.6.4 εNd-values of exchangeable Nd-fractions

1.6.4.1 Spatial distribution inferred by the surface samples

εNd values in leachates from surface sediments depict similar trends regardless of the grain-size fractions analyzed (Fig. 1-6). This is a fair indication of the reliability of the extraction of exchangeable fractions considered to be representative of εNd values in ambient water masses (see Fig. 1-7 and also the ANNEXE A Supplementary Material). Leachate data follow a spatial trend resembling that of detrital fractions, with a radiogenic signal increasing southward, from ~ -8 to ~ -2 (vs from ~ -12 to ~ -7 in detrital fractions), as also observed in previous studies (e.g., Lacan et al., 2012; Robinson et al., 2021). Thus, the εNd values of leachates may be seen as sensitive and robust tracers of PW fluxes toward the Chukchi Sea.

The northward decrease of εNd values in leachates relates to increasing mixing with unradiogenic Nd from the western Arctic Ocean waters (~ -8; Porcelli et al., 2009). In detail, leachates from coarse materials show more radiogenic mean values (-1.9±0.3; ±1σ; n = 4) vs fine fractions (-2.2±0.1; ±1σ; n = 4), in the southernmost sites (Fig. 1-6). Conversely, fine fractions bear a more radiogenic signature (~ -7) than the coarser fractions (~ -8) towards the Chukchi Sea endmember. This behavior can be explained in several ways. First, the exchangeable Nd-content of sand grains is much lower than that of fine fractions (Jeandel et al., 1995). Sand may thus exchange more rapidly trace metals (e.g., Jain and Ram, 1997), and acquire more rapidly the Nd-isotope signature of ambient waters. Moreover, the residence time of particles in the water column may also interfere with their final εNd signature (Jeandel et al., 2015). The coarse fraction

carried from the Bering Sea by sea ice (Maccali et al., 2018), and rapidly deposited north of the Strait, is unlikely to exchange much of its leachable-Nd during its sinking in such a shallow water setting. Whereas, this is a parameter not easily controlled in a marine environment such as the Chukchi shelf, characterized by highly variable current velocities (Woodgate et al., 2005).

1.6.4.2 Exchangeable εNd value changes during the Holocene

In core R09, the overall increase in εNd-values of leachates from core bottom to its top is interpreted as the most robust recorder of an increasing PW-flux linked to the deepening of the BS (Fig. 1-5a). This εNd shift occurred in three distinct steps. From about 10 to 8 cal. ka BP, it increased from ~ -6 to ~ -5, suggesting a minor but steadily increasing influence of PW influx. This trend was interrupted at the early to middle Holocene transition, exactly between two layers dated ~ 8.4 and 7.9 cal. ka BP (Table 1.2) respectively. This interval, marked here by εNd oscillations, between ~ -5 and ~ -6, is known for large-amplitude climate oscillations elsewhere, often linked to the so-called "8.2 ka event" (Thomas et al., 2007). A possible factor explaining the εNd instability recorded at that time is the interaction of increasing PW-inflow with the strong North Atlantic Water (NAW) intrusion in the Arctic Ocean, reported to have occurred between 9 and 7 cal. ka BP (Andrews and Dunhill, 2004; Hillaire-Marcel et al., 2004; Polyakova and Stein, 2004). This major reorganization of the large-scale circulation in the Arctic Ocean may also relate to the catastrophic opening of Nares Strait, channeling a substantial part of the Arctic Ocean outflow towards the Baffin Bay at that time (Madaj et al., 2021). Above the layer assigned to this event, a more steady evolution of the BS-Chukchi Sea paleoceanography resumed, marked in particular by an εNd-value trend from ~ -6 to ~ -3. It will be discussed further below.

1.6.5 Inferences about the middle to late Holocene paleoceanography of the BS to Chukchi Sea area

Combining all information from clay minerals and εNd data, the strongest shift toward modern conditions occurred during the middle Holocene, from about 8 to 4 cal. ka BP. This feature is particularly well recorded by the εNd-value of the exchangeable Nd fraction (Fig. 1-5l). The middle Holocene interval also stands out with its low sedimentation rates in comparison with those of the early and late Holocene intervals. Similar changes in sedimentation rates have been observed westward in core PS72/350-2 from the East Siberian Sea (site 3 in Fig. 1-1A; Stein et al., 2017). Site PS72/350-2 is located within the same deep channel as R09, and approximately at a similar depth. The similarity in sedimentation rate changes at both sites suggests

some common influences of an eastward-flowing shelf current, carrying Siberian coastal water; a situation still observed today, east of Herald Canyon, in the R09 area (Pisareva et al., 2015). According to Broadman et al. (2020), the mean Holocene interval was characterized by a distinct wind regime with a strengthened Aleutian Low, leading to an enhanced PW inflow and a wetter climate over Arctic Alaska, as well as to a lesser summer sea-ice cover in the Chukchi Sea (Polyak et al., 2016). And more generally, in the Arctic Ocean (de Vernal et al., 2020). These features could have been responsible for reduced particulate fluxes, in particular, a lesser sea-ice rafting sediment deposition.

The high sedimentation rates of the early Holocene interval were probably due to depositional conditions in shallow waters, thus under foreshore-type conditions. During the late Holocene, we could not identify a specific sedimentary parameter that would account for the relatively high sedimentation rate, except perhaps, the establishment of a tide-dominated system following the earlier wave/sea-ice-dominated system. This interval nonetheless corresponds to a lesser variability in current and turbulence in the water column. Such conditions, favorable for fine sediment deposition, are consistent with the finer grain-size particles that characterize the late Holocene sedimentation (see Fig. 1-5e). High marine primary production in the Chukchi Sea might have also contributed to the high sedimentation rates of the late Holocene (e.g., Stein et al., 2017; Khim et al., 2018).

Intending to estimate quantitative relationships between PW fluxes and clay minerals, εNd tracers at the coring site, we used the mean SL values from Lambeck et al. (2014) and assumed that PW fluxes primarily depend upon the depth of the BS (see Fig. 1-9). We would have expected smectite abundance to be a good indicator of PW fluxes (e.g., Stein, 2008), but it is not the case here as illustrated by the absence of correlation between SL and smectite percentages (Fig. 1-9b). Even when estimating absolute fluxes of clays (Fig. 1-8), there is no clear linkage between smectite and SL as all clays depict nearly similar changes during the middle and late Holocene interval, in relation to grain size and sedimentation rates. This observation also applies to the clay mineral ratios (Fig. 1-5i and Fig. 1-9c, d), which had been previously proposed as a potential tracer of PW supplies (e.g., Kobayashi et al., 2016; Yamamoto et al., 2017). Therefore, if linkages can be made between sedimentological features and the deepening of the water column in general terms, they do not apply at our coring site.

So far, Nd-isotopes from exchangeable fractions seem the best tracer of PW flux as suggested from the excellent correlation with SL and deepening of the BS during the mid-Holocene (Fig. 1-9a). The best fit is found with a 2nd-order polynomial relationship between εNd and SL; it yields an R^2 value of 0.98. Adding the late Holocene values, the correlation coefficient does not change ($R^2 = 0.97$) significantly. We interpret this polynomial fit as a response to the relationship between the depth of the Strait and the surface of its transect (e.g., Clement-Kinney et al., 2014). This relationship seems robust, likely because waters from the Bering Sea constitute the exclusive radiogenic Nd source in this area.

Whereas the relationship between εNd in core R09 and SL is significant since 8 cal. ka BP, its variability during the transition between the early and middle Holocene must be addressed (Fig. 1-5l). The variations observed suggest changes in the respective fluxes of PW vs SCC or any isotopically similar water mass, in addition to potential changes in the isotopic composition of both water masses. The present SCC flux (~ 0.1 Sv; Weingartner et al., 1999) may be seen as negligible in comparison with the PW flux (~ 1.0 Sv; Woodgate et al., 2018). We assume that the SCC flux should not have been stronger back in time, especially when SL was still below its present elevation. On this ground, we infer that the primary parameter governing the εNd value of exchangeable Nd-fraction at site R09 is the fluxes of PW, which plays a determinant role on the mixing rate between the Arctic Ocean surface water and the PW that respectively bear distinct isotopic signatures. On the Pacific side, the coastal Bering Sea system, with its currents and Nd sources, has not changed since the inception of the Alaskan Coastal Current some 8000 years ago (Sancetta, 1979; Katsuki et al., 2009). Thus, we hypothesize a relatively invariable Nd isotope composition and concentration of PW, at least since 8 kyr BP. The only estimate of the εNd value of PW entering the BS is derived from the analyses of Nd-isotopes in carbonates from surface sediments of the northern Bering Sea shelf that yielded a value of ~ -2 (Asahara et al., 2012). The contribution of Arctic Ocean surface water masses may have varied considerably with the evolution of the circum-Arctic circulation, relating to NAW fluxes, Arctic river runoffs, and PW inflows through BS (Woodgate and Aagaard, 2005). As a first estimate for the Arctic water endmember, we can use the modern εNd-value in surface waters from the southern Canadian Basin, which averages -8, based on Porcelli et al. (2009). This means that today, the R09-core top value of -3 would reflect the mixing of ~ 17% Arctic water with ~ 83% PW. At ~ 8 cal. ka BP, at the onset of the transition between the early and middle Holocene, when SL was still about 12 m below the Present (Lambeck et al., 2014), the εNd value was about -5.7. Using the same endmember values of -2 for PW inflow through BS and -8 for Arctic waters, the PW would have already represented about ~ 38% of the

mixing system. However, it is unlikely that the Arctic Ocean surface water had an isotopic composition identical to the present one because the overall influence of radiogenic supplies from PW on the Arctic surface water was probably much reduced. Thus, the above 38% estimate must be considered with some caution. At the transition between the early and middle Holocene, the NAW circulation was already well set with εNd-value of -10.6±0.2 (Jang et al., 2013), comparable with the modern εNd-value averaging -10.8 (Andersson et al., 2008). Using εNd-value of -10.6 for the 8 cal. ka BP Arctic Ocean endmember would move the contribution of the PW up to 57%. We may here assume that the influence of the dissolved Nd from Arctic rivers did not change significantly since ~ 7000 years ago based on the work of Wagner et al. (2011). Thus, the εNd-value of -10.6 could be seen as an acceptable lower range value for the Arctic Ocean endmember at the transition between the early and middle Holocene, while the εNd-value of -8 measured by Porcelli et al. (2009) is the most likely recent Arctic Ocean endmember.

One could be tempted to use εNd-values as a quantitative proxy of PW flux. However, two unknowns prevent doing this with confidence. First, we do not precisely know the PW flux at ~ 8 cal. ka BP. Second, we cannot assess the stability of the signature and fluxes of the other mixing member, the Arctic Ocean water. Nonetheless, taking into consideration a direct proportionality between εNd gradients and PW flux, the modern value of ~ 1 Sv (Woodgate et al., 2018) and the ~ 83% contribution of PW to the water column at site R09, at ~ 8 cal. ka BP, a flux of about 0.5 Sv at this time could be proposed as a rough estimate.

1.6.6 PW-fluxes

The most immediate large-scale impact of changes in PW fluxes during the Holocene concerns its freshwater contribution to the salinity budget of the Arctic Ocean (Prange and Lohmann, 2004). Near steady-state conditions for the PW flux were only achieved by about 4 cal. ka BP (Fig. 1-5). Therefore, the freshwater flux from the Arctic Ocean towards the convection sites of the AMOC (Piron et al., 2017), in the Norwegian, Greenland, and Labrador seas and the Irminger basin, only stabilized about 4000 years ago (Renssen et al., 2005), as well. This suggests a late Holocene relative stabilization of the AMOC, at the time of the onset of the trend towards the Neoglacial, marked by cooler conditions in middle and high latitudes of the Northern Hemisphere. Summing up, one may infer the final inception of a modern-like AMOC at about 4 kyr BP (e.g., Ayache et al., 2018; Klus et al., 2018), notwithstanding its high-frequency variability at interannual to interdecadal time-scales (Friedman et al., 2017).

Another aspect that could attract some attention is the fate of the PW-flux under high global SL, such as the one estimated during the optimum of the last interglacial (~ +9 m; Dutton et al., 2015). Assuming all parameters governing the PW flux through BS would behave conservatively, extrapolating the Holocene curve to a +9 m SL leads to an estimate of 1.5 Sv. However, considering all other parameters governing PW fluxes through BS, in particular, the sea-ice cover and wind regime, a more realistic estimate would require experiments from a fully coupled regional model.

Finally, assessing the near-future impact of changes in PW fluxes on the Pacific-Arctic-Atlantic system requires looking deeper into the freshwater budget of the Arctic Ocean and sub-Arctic seas. Freshwater discharge from the Greenland Ice Sheet, riverine runoff, and PW-fluxes related to the future SL rising (e.g., ~ +9 m), would contribute to freshening surface water in the subarctic North Atlantic, where convection occurs. Assuming warmer and fresher surface water conditions, thus more stratified surface water, the formation of the present North Atlantic Deep Water might be hampered, at least significantly reduced (Shaffer and Bendtsen, 1994; Lohmann and Ditlevsen, 2021; Zhang et al., 2021).

1.7 Conclusion

The first objective of this study was to reassess the potential of clay minerals and Nd-isotopes as tracers of PW fluxes. Surface sediment data show a gradient in smectite relative abundance from the BS to the Chukchi Sea shelf edge. Similarly, εNd-values of exchangeable Nd-fraction from all grain-size fractions show a northward decreasing trend that we assign to enhanced mixing of PW with an unradiogenic-Nd bearing Arctic Ocean water. Therefore, smectite abundances and exchangeable εNd-values could be seen as potential proxies of PW inflow. However, analyses of core R09, which spans most of the Holocene, indicate that, back in time, these tracers do not behave conservatively vs PW-fluxes. Even the εNd-value of exchangeable fractions, which significantly correlated with SL elevation during the middle Holocene, presents some peculiarities, in particular a return to initial εNd-values at about 8 cal. ka BP, possibly linked to the penetration of a modern-like NAW component into the western Arctic Ocean. Moreover, clay minerals are not as conclusive as they could have been expected based on earlier studies, at least in our working area. Smectite, chlorite, and kaolinite abundances are highly influenced by the relative flux of illite, which is the dominant clay mineral in the Chukchi Sea. As illite is also transported by the eastward-flowing Siberian shelf current, clay minerals variability does not relate unequivocally to PW fluxes. In the study

core, quantitative fluxes of clay minerals, including smectite, depict nearly similar trends which mostly relate to the core site deepening and subsequent finer sedimentation. Nevertheless, some minor departures of smectite flux from this trend could perhaps be linked to PW flux changes, but a more robust age model would be needed to ascertain this statement.

The εNd-values in leachates of clay fraction correlated well with SL rise since 8 kyr BP. They could be seen as a robust proxy for PW fluxes during this interval, but several parameters govern the relationship between SL and the flux of PW. Thus, estimates of PW flux from εNd-values are at best, tentative. More reliable estimates, for the 8 cal. ka BP to Present interval, would require the support of a high-resolution regional coupled model, using boundary conditions close to modern conditions. Adding more records could certainly help understand better the short events recorded in the studied core R09 but confronting data with model experiments would probably be the next step to consider.

1.8 Acknowledgments

This work was supported by the Natural Sciences and Engineering Research Council (NSERC) of Canada, the Fonds de Recherche du Québec Nature et Technologies (FQRNT), and the National Natural Science Foundation of China [grant number: 42176245]. This work is a contribution to the 4th and 6th Chinese National Arctic Research Expeditions conducted by R/V Xuelong. Thanks for the three anonymous reviewers' constructive suggestions, which make this paper highly improved. T.-F. Song acknowledges the financial support from the China Scholarship Council for his overseas study. Thanks to André Poirier, Michel Preda, Vladislav Carnero-Bravo, and François Hardy (UQAM), for their support in the laboratory, and to Jenny Maccali (Bergen Univ.) and Ross Stevenson (UQAM) for providing their protocols for Nd chemistry.

1.9 Data availability

All the data used in this study are available in Appendix files.

1.10 References

Aagaard, K., et al., 2006. Some controls on flow and salinity in Bering Strait. Geophys. Res. Lett. 33.19, L19602.

Andersson, P. S., et al., 2008. Neodymium isotopes in seawater from the Barents Sea and Fram Strait Arctic–Atlantic gateways. Geochim. Cosmochim. Acta 72.12, 2854-2867.

Andrews, J. T., and Dunhill, G., 2004. Early to mid-Holocene Atlantic water influx and deglacial meltwater events, Beaufort Sea slope, Arctic Ocean. Quat. Res. 61.1, 14-21.

Asahara, Y., et al., 2012. Provenance of terrigenous detritus of the surface sediments in the Bering and Chukchi Seas as derived from Sr and Nd isotopes: Implications for recent climate change in the Arctic regions. Deep Sea Res. Part II Top. Stud. Oceanogr. 61, 155-171.

Ayache, M., et al., 2018. Multi-centennial variability of the AMOC over the Holocene: A new reconstruction based on multiple proxy-derived SST records. Glob. Planet Change 170, 172-189.

Baskaran, M., and Naidu, A. S., 1995. ^{210}Pb-derived chronology and the fluxes of ^{210}Pb and ^{137}Cs isotopes into continental shelf sediments, East Chukchi Sea, Alaskan Arctic. Geochim. Cosmochim. Acta. 59.21, 4435-4448.

Bayon, G., et al., 2002. An improved method for extracting marine sediment fractions and its application to Sr and Nd isotopic analysis. Chem. Geol. 187.3-4, 179-199.

Biscaye, P. E., 1965. Mineralogy and sedimentation of recent deep-sea clay in the Atlantic Ocean and adjacent seas and oceans. Geol. Soc. Am. Bull. 76.7, 803-832.

Blaauw, M., and Christen, J. A., 2011. Flexible paleoclimate age-depth models using an autoregressive gamma process. Bayesian Anal. 6.3, 457-474.

Blaauw, M., et al., 2018. Double the dates and go for Bayes—Impacts of model choice, dating density and quality on chronologies. Quat. Sci. Rev. 188, 58-66.

Blaser, P., et al., 2016. Extracting foraminiferal seawater Nd isotope signatures from bulk deep sea sediment by chemical leaching. Chem. Geol. 439, 189-204.

Broadman, E., et al., 2020. Coupled impacts of sea ice variability and North Pacific atmospheric circulation on Holocene hydroclimate in Arctic Alaska. Proc. Natl. Acad. Sci. 117.52, 33034-33042.

Broecker, W. S., 1991. The great ocean conveyor. Oceanography 4.2, 79-89.

Chen, T., et al., 2012. Variations of North Atlantic inflow to the central Arctic Ocean over the last 14 million years inferred from hafnium and neodymium isotopes. Earth Planet. Sci. Lett. 353, 82-92.

Clement-Kinney, et al., 2014. On the flow through Bering Strait: A synthesis of model results and observations, in: Grebmeier, J. M., Maslowski, W. (Eds), The Pacific Arctic Region. Springer Science+Business Media, Dordrecht, pp. 167-198.

Cooper, L. W., and Grebmeier, J. M., 2018. Deposition patterns on the Chukchi shelf using radionuclide inventories in relation to surface sediment characteristics. Deep Sea Res. Part II Top. Stud. Oceanogr. 152, 48-66.

Cooper, L. W., et al., 1997. The nutrient, salinity, and stable oxygen isotope composition of Bering and Chukchi Seas waters in and near the BS. J. Geophys. Res. Oceans 102.C6, 12563-12573.

Danielson, S. L., et al., 2014. Coupled wind-forced controls of the Bering-Chukchi shelf circulation and the Bering Strait throughflow: Ekman transport, continental shelf waves, and variations of the Pacific–Arctic sea surface height gradient. Prog. Oceanogr. 125, 40-61.

Darby, D. A., 2003. Sources of sediment found in sea ice from the western Arctic Ocean, new insights into processes of entrainment and drift patterns. J. Geophys. Res. Oceans 108.C8, 13.

Darby, D. A. and Bischof, J.F. (2004). A Holocene record of changing Arctic Ocean ice drift analogous to the effects of the Arctic Oscillation. Paleoceanography, 19(1), PA1027.

Darby, D. A., et al., 2011. Modern dirty sea ice characteristics and sources: The role of anchor ice. J. Geophys. Res. Oceans 116.C9, C09008.

Deschamps, C. E., Montero-Serrano, J. C., and St‐Onge, G., 2018. Sediment provenance changes in the western Arctic Ocean in response to ice rafting, sea level, and oceanic circulation variations since the last deglaciation. Geochem. Geophys. Geosyst. 19.7, 2147-2165.

Deschamps, C. E., et al., 2019. Holocene changes in deep water circulation inferred from authigenic Nd and Hf isotopes in sediment records from the Chukchi‐Alaskan and Canadian Beaufort margins. Paleoceanogr. Paleoclimatol. 34.7, 1038-1056.

de Vernal, A., et al., 2020. Natural variability of the Arctic Ocean sea ice during the present interglacial. Proc. Natl. Acad. Sci. 117.42, 26069-26075.

Dutton, A., et al., 2015. Sea-level rise due to polar ice-sheet mass loss during past warm periods. Science 349.6244, aaa4019.

Fagel, N., et al., 2004. Nd and Pb isotope signatures of the clay-size fraction of Labrador Sea sediments during the Holocene: Implications for the inception of the modern deep circulation pattern. Paleoceanography 19.3, PA3002.

Fagel, N., et al., 2014. Late Quaternary evolution of sediment provenances in the Central Arctic Ocean: mineral assemblage, trace element composition and Nd and Pb isotope fingerprints of detrital fraction from the Northern Mendeleev Ridge. Quat. Sci. Rev. 92, 140-154.

Flynn, W. W., 1968. The determination of low levels of polonium-210 in environmental materials. Anal. Chim. Acta 43, 221-227.

Francis, O. P., Panteleev, G. G., and Atkinson, D. E., 2011. Ocean wave conditions in the Chukchi Sea from satellite and in situ observations. Geophys. Res. Lett. 38.24, L24610.

Friedman, A. R., et al., 2017. A new record of Atlantic sea surface salinity from 1896 to 2013 reveals the signatures of climate variability and long-term trends. Geophys. Res. Lett. 44.4, 1866-1876.

Grebmeier, J. M., et al., 2006. Ecosystem dynamics of the Pacific-influenced northern Bering and Chukchi Seas in the Amerasian Arctic. Prog. Oceanogr. 71.2-4, 331-361.

Gutjahr, M., et al., 2007. Reliable extraction of a deepwater trace metal isotope signal from Fe-Mn oxyhydroxide coatings of marine sediments. Chem. Geol. 242.3-4, 351-370.

Haley, B. A., and Polyak, L., 2013. Pre-modern Arctic Ocean circulation from surface sediment neodymium isotopes. Geophys. Res. Lett. 40.5, 893-897.

Heaton, T. J., et al., 2020. Marine20—the marine radiocarbon age calibration curve (0–55,000 cal BP). Radiocarbon 62.4, 779-820.

Hillaire-Marcel, C., et al., 2004. Size-dependent isotopic composition of planktic foraminifers from Chukchi Sea vs. NW Atlantic sediments-implications for the Holocene paleoceanography of the western Arctic. Quat. Sci. Rev. 23.3-4, 245-260.

Hu, A., et al., 2015. Effects of the Bering Strait closure on AMOC and global climate under different background climates. Prog. Oceanogr. 132, 174-196.

Huang, H., et al., 2021. Efficient extraction of past seawater Pb and Nd isotope signatures from Southern Ocean sediments. Geochem. Geophys. Geosyst. 22.3, e2020GC009287.

Hunt, Jr. G. L., et al., 2013. The Barents and Chukchi Seas: comparison of two Arctic shelf ecosystems. J. Mar. Syst. 109, 43-68.

Jain, C. K. and Ram, D., 1997. Adsorption of metal ions on bed sediments. Hydrol. Sci. J. 42.5, 713-723.

Jakobsson, M., et al., 2017. Post-glacial flooding of the Bering Land Bridge dated to 11 cal ka BP based on new geophysical and sediment records. Clim. Past 13.8, 991.

Jang, K., et al., 2013. Glacial freshwater discharge events recorded by authigenic neodymium isotopes in sediments from the Mendeleev Ridge, western Arctic Ocean. Earth Planet. Sci. Lett. 369, 148-157.

Jeandel, C., et al., 1995. Exchange of neodymium and its isotopes between seawater and small and large particles in the Sargasso Sea. Geochim. Cosmochim. Acta 59.3, 535-547.

Jeandel, C., et al., 2015. What did we learn about ocean particle dynamics in the GEOSECS–JGOFS era?. Prog. Oceanogr. 133, 6-16.

Jordan, J. W., and Mason, O. K., 1999. A 5000 year record of intertidal peat stratigraphy and sea level change from northwest Alaska. Quat. Int. 60.1, 37-47.

Katsuki, K., et al., 2009. Land—sea linkage of Holocene paleoclimate on the Southern Bering Continental Shelf. The Holocene 19.5, 747-756.

Keigwin, L. D., and Cook, M. S., 2007. A role for North Pacific salinity in stabilizing North Atlantic climate. Paleoceanography 22.3, PA3102.

Khim, B. K., 2003. Two modes of clay-mineral dispersal pathways on the continental shelves of the East Siberian Sea and western Chukchi Sea. Geosci. J. 7.3, 253-262.

Khim, B. K., et al., 2018. Surface water productivity and sediment transport by BS throughflow in the Chukchi Shelf (the western Arctic Ocean) during the Holocene. The Holocene 28.5, 814-826.

Kim, H. J., et al., 2021. Temporal and spatial variations in particle fluxes on the Chukchi Sea and East Siberian Sea slopes from 2017 to 2018. Front. Mar. Sci. 7, 609748.

Kipp, L. E., et al., 2020. Observational and modeling evidence of seasonal trends in sediment-derived material inputs to the Chukchi Sea. J. Geophys. Res. Oceans 125.5, e2019JC016007.

Kissel, C., et al., 2013. Variations in the strength of the North Atlantic bottom water during Holocene. Earth Planet. Sci. Lett. 369, 248-259.

Klus, A., et al., 2018. Abrupt cold events in the North Atlantic Ocean in a transient Holocene simulation. Clim. Past 14.8, 1165-1178.

Kobayashi, D., et al., 2016. Distribution of detrital minerals and sediment color in western Arctic Ocean and northern Bering Sea sediments: Changes in the provenance of western Arctic Ocean sediments since the last glacial period. Polar Sci. 10.4, 519-531.

Kuzyk, Z. Z. A., Gobeil, C., and Macdonald, R. W., 2013. ^{210}Pb and ^{137}Cs in margin sediments of the Arctic Ocean: Controls on boundary scavenging. Global Biogeochem. Cycles 27.2, 422-439.

Lacan, F., et al., 2012. Neodymium isotopic composition of the oceans: A compilation of seawater data. Chem. Geol. 300, 177-184.

Lalande, C., et al., 2020. Annual cycle of export fluxes of biogenic matter near Hanna Shoal in the northeast Chukchi Sea. Deep Sea Res. Part II Top. Stud. Oceanogr. 177, 104730.

Lambeck, K., et al., 2014. Sea level and global ice volumes from the Last Glacial Maximum to the Holocene. Proc. Natl. Acad. Sci. 111.43, 15296-15303.

Lepore, K., Moran, S. B. and Smith, J. N., 2009. ^{210}Pb as a tracer of shelf–basin transport and sediment focusing in the Chukchi Sea. Deep Sea Res. Part II Top. Stud. Oceanogr. 56.17, 1305-1315.

Lewis, K. M., Van Dijken, G. L., and Arrigo, K. R., 2020. Changes in phytoplankton concentration now drive increased Arctic Ocean primary production. Science 369.6500, 198-202.

Li, M., et al., 2019. Circulation of the Chukchi Sea shelfbreak and slope from moored time series. Prog. Oceanogr. 172, 14-33.

Lohmann, J., and Ditlevsen, P. D., 2021. Risk of tipping the overturning circulation due to increasing rates of ice melt. Proc. Natl. Acad. Sci. 118.9, e2017989118.

Maccali, J., et al., 2013. Geochemical signatures of sediments documenting Arctic sea-ice and water mass export through Fram Strait since the Last Glacial Maximum. Quat. Sci. Rev. 64, 136-151.

Maccali, J., et al., 2018. Radiogenic isotope (Nd, Pb, Sr) signatures of surface and sea ice-transported sediments from the Arctic Ocean under the present interglacial conditions. Polar Res. 37.1, 1442982.

Madaj, L., et al., 2021. Radiogenic Isotope Signatures of Holocene Sediments from Kane Basin: Linkage with the Re-opening and Evolution of Nares Strait. EGU General Assembly 2021, online, 19–30 Apr 2021, EGU21-9301.

McCave, I. N., Manighetti, B., and Robinson, S. G., 1995. Sortable silt and fine sediment size/composition slicing: parameters for palaeocurrent speed and palaeoceanography. Paleoceanography 10.3, 593-610.

McCave, I. N., Thornalley, D. J. R., and Hall, I. R., 2017. Relation of sortable silt grain-size to deep-sea current speeds: Calibration of the 'Mud Current Meter'. Deep Sea Res. Part I Oceanogr. Res. Pap. 127, 1-12.

Meinhardt, A. K., et al., 2016. Climate change and response in bottom water circulation and sediment provenance in the Central Arctic Ocean since the Last Glacial. Chem. Geol. 427, 98-108.

Moore, D. M., and Reynolds Jr, R. C, 1989. X-ray Diffraction and the Identification and Analysis of Clay Minerals. Oxford University Press (OUP), New York.

Moser, F. C., and Hein, J. R., 1984. Distribution of clay minerals in the suspended and bottom sediments from the Northern Bering Sea shelf area, Alaska. US Government Printing Office.

Naidu, A. S., Creager, J. S., and Mowatt, T. C., 1982. Clay mineral dispersal patterns in the north Bering and Chukchi Seas. Mar. Geol. 47.1-2, 1-15.

Nguyen, A. T., Woodgate, R. A., and Heimbach, P., 2020. Elucidating Large‐Scale Atmospheric Controls on Bering Strait Throughflow Variability Using a Data‐Constrained Ocean Model and Its Adjoint. J. Geophys. Res. Oceans 125.9, e2020JC016213.

Not, C., and Hillaire-Marcel, C., 2010. Time constraints from ^{230}Th and ^{231}Pa data in late Quaternary, low sedimentation rate sequences from the Arctic Ocean: an example from the northern Mendeleev Ridge. Quat. Sci. Rev. 29.25-26, 3665-3675.

Ortiz, J. D., et al., 2009. Provenance of Holocene sediment on the Chukchi-Alaskan margin based on combined diffuse spectral reflectance and quantitative X-Ray Diffraction analysis. Glob. Planet. Change 68.1-2, 73-84.

Park, Y., et al., 2014. Distribution, source and transportation of glycerol dialkyl glycerol tetraethers in surface sediments from the western Arctic Ocean and the northern Bering Sea. Mar. Chem. 165, 10-24.

Pearce, C., et al., 2017. The 3.6 ka Aniakchak tephra in the Arctic Ocean: a constraint on the Holocene radiocarbon reservoir age in the Chukchi Sea. Clim. Past 13.4, 303-316.

Petty, A. A., et al., 2016. Sea ice circulation around the Beaufort Gyre: The changing role of wind forcing and the sea ice state. J. Geophys. Res. Oceans 121.5, 3278-3296.

Pfirman, S. L., et al., 1997. Reconstructing the origin and trajectory of drifting Arctic sea ice. J. Geophys. Res. Oceans 102.C6, 12575-12586.

Pico, T., et al., 2020. Sea level fingerprinting of the Bering Strait flooding history detects the source of the Younger Dryas climate event. Sci. Adv. 6.9, eaay2935.

Piepgras, D. J., and Jacobsen, S. B., 1988. The isotopic composition of neodymium in the North Pacific. Geochim. Cosmochim. Acta 52.6, 1373-1381.

Piron, A., et al., 2017. Gyre-scale deep convection in the subpolar North Atlantic Ocean during winter 2014–2015. Geophys. Res. Lett. 44.3, 1439-1447.

Pisareva, M. N., et al., 2015. Flow of Pacific water in the western Chukchi Sea: Results from the 2009 RUSALCA expedition. Deep Sea Res. Part I Oceanogr. Res. Pap. 105, 53-73.

Polyak, L., et al., 2016. Holocene sea-ice conditions and circulation at the Chukchi-Alaskan margin, Arctic Ocean, inferred from biomarker proxies. The Holocene 26.11, 1810-1821.

Polyakova, Y. I., and Stein, R., 2004. Holocene paleoenvironmental implications of diatom and organic carbon records from the southeastern Kara Sea (Siberian Margin). Quat. Res. 62.3, 256-266.

Porcelli, D., et al., 2009. The distribution of neodymium isotopes in Arctic Ocean basins. Geochim. Cosmochim. Acta. 73.9, 2645-2659.

Prange, M., and Lohmann, G., 2004. Variable freshwater input to the Arctic Ocean during the Holocene: Implications for large-scale ocean-sea ice dynamics as simulated by a circulation model, in: Fischer, H., et al. (Eds), The Climate in Historical Times. Springer, Berlin, Heidelberg, pp. 319-335.

Pratte, S., De Vleeschouwer, F., and Garneau, M., 2017. Geochemical characterization (REE, Nd and Pb isotopes) of atmospheric mineral dust deposited in two maritime peat bogs from the St. Lawrence North Shore (eastern Canada). J. Quat. Sci. 32.5, 617-627.

Proshutinsky, A., et al., 2015. Arctic circulation regimes. Philos. Trans. A Math. Phys. Eng. Sci. 373.2052, 20140160.

Reimer, P. J., et al., 2013. IntCal13 and Marine13 radiocarbon age calibration curves 0-50,000 years cal BP." Radiocarbon 55.4, 1869-1887.

Renssen, H., Goosse, H., and Fichefet, T., 2002. Modeling the effect of freshwater pulses on the early Holocene climate: The influence of high ‐ frequency climate variability. Paleoceanography 17.2, 10-1.

Renssen, H., Goosse, H., and Fichefet, T., 2005. Contrasting trends in North Atlantic deep ‐ water formation in the Labrador Sea and Nordic seas during the Holocene. Geophys. Res. Lett. 32.8, L08711.

Reuther, J., et al., 2020. Marine Reservoir Effects in Seal (Phocidae) Bones in the Northern Bering and Chukchi Seas, Northwestern Alaska. Radiocarbon 63.1, 1-19.

Robinson, S., et al., 2021. Global continental and marine detrital εNd: An updated compilation for use in understanding marine Nd cycling. Chem. Geol. 567, 120119.

Sancetta, C., 1979. Use of semiquantitative microfossil data for paleoceanography. Geology 7.2, 88-92.

Serreze, M. C., et al., 2006. The large ‐ scale freshwater cycle of the Arctic. J. Geophys. Res. Oceans 111, C11010.

Serreze, M. C., et al., 2016. Variability, trends, and predictability of seasonal sea ice retreat and advance in the Chukchi Sea. J. Geophys. Res. Oceans 121.10, 7308-7325.

Shaffer, G., and Bendtsen, J., 1994. Role of the Bering Strait in controlling North Atlantic ocean circulation and climate. Nature 367.6461, 354-357.

Stabeno, P. J., and McCabe, R. M., 2020. Vertical structure and temporal variability of currents over the Chukchi Sea continental slope. Deep Sea Res. Part II Top. Stud. Oceanogr. 177, 104805.

Stein, R., 2008. Arctic Ocean sediments: processes, proxies, and paleoenvironment. Elsevier, 592 pp.

Stein, R., et al., 2017. Holocene variability in sea ice cover, primary production, and Pacific-Water inflow and climate change in the Chukchi and East Siberian Seas (Arctic Ocean). J. Quat. Sci. 32.3, 362-379.

Swärd, H., et al., 2018. Sedimentary proxies for Pacific water inflow through the Herald Canyon, western Arctic Ocean. Arktos 4.1, 19.

Thomas, E. R., et al., 2007. The 8.2 ka event from Greenland ice cores. Quat. Sci. Rev. 26.1-2, 70-81.

Viscosi-Shirley, C., et al., 2003. Clay mineralogy and multi-element chemistry of surface sediments on the Siberian-Arctic shelf: implications for sediment provenance and grain size sorting. Cont. Shelf Res. 23.11-13, 1175-1200.

Voogt, L., van Rijn, L. C. and van den Berg, J. H., 1991. Sediment transport of fine sands at high velocities. J. Hydraul. Eng. 117.7, 869-890.

Wagner, A., Lohmann, G., and Prange, M., 2011. Arctic river discharge trends since 7 ka BP. Glob. Planet. Change 79.1-2, 48-60.

Wahsner, M., et al., 1999. Clay-mineral distribution in surface sediments of the Eurasian Arctic Ocean and continental margin as indicator for source areas and transport pathways-a synthesis. Boreas 28.1, 215-233.

Wang, H., et al., 2016. Tide and current observations in the central Chukchi Sea during the summer of 2012. J. Ocean Univ. China 15.2, 201-208.

Wang, W., et al., 2020. Spatial variation in grain-size population of surface sediments from northern Bering Sea and western Arctic Ocean: implications for provenance and depositional mechanisms. Adv. Polar Sci. 31.3, 192-204.

Weingartner, T., et al., 2005. Circulation on the north central Chukchi Sea shelf. Deep Sea Res. Part II Top. Stud. Oceanogr. 52.24-26, 3150-3174.

Weingartner, T. J., et al., 1999. The Siberian Coastal Current: A wind-and buoyancy-forced Arctic coastal current. J. Geophys. Res. Oceans 104.C12, 29697-29713.

Wilson, D. J., et al., 2013. Reactivity of neodymium carriers in deep sea sediments: Implications for boundary exchange and paleoceanography. Geochim. Cosmochim. Acta 109, 197-221.

Woodgate, R. A., Aagaard, K., and Weingartner, T. J., 2005. Monthly temperature, salinity, and transport variability of the Bering Strait through flow. Geophys. Res. Lett. 32.4, L04601.

Woodgate, R. A., and Aagaard, K., 2005. Revising the Bering Strait freshwater flux into the Arctic Ocean. Geophys. Res. Lett. 32.2, L02602.

Woodgate, R. A., 2018. Increases in the Pacific inflow to the Arctic from 1990 to 2015, and insights into seasonal trends and driving mechanisms from year-round BS mooring data. Prog. Oceanogr. 160, 124-154.

Woodgate, R. A., Weingartner, T., and Lindsay, R., 2010. The 2007 BS oceanic heat flux and anomalous Arctic sea-ice retreat. Geophys. Res. Lett. 37.1, L01602.

Yamamoto, M., et al., 2017. Holocene dynamics in the BS inflow to the Arctic and the Beaufort Gyre circulation based on sedimentary records from the Chukchi Sea. Clim. Past 13.9, 1111-1127.

Yamamoto-Kawai, M., et al., 2008. Freshwater budget of the Canada Basin, Arctic Ocean, from salinity, $\delta^{18}O$, and nutrients. J. Geophys. Res. Oceans 113.C1, C01007.

Yang, Q., et al., 2016. Recent increases in Arctic freshwater flux affects Labrador Sea convection and Atlantic overturning circulation. Nat. Commun. 7.1, 1-8.

Zhang, J., et al., 2021. Labrador Sea freshening linked to Beaufort Gyre freshwater release. Nat. Commun. 12.1, 1-8.

Table 1.1 Core locations.

Site	Longitude (°W)	Latitude (°N)	Water Depth (m)
Surface samples			
ARC6-R03	168.9	68.6	46.4
ARC6-SR03	168.9	67.7	42.4
ARC6-SR09	168.9	71.0	35.5
ARC6-SR11	169.0	73.0	64.9
ARC6-SR14	169.0	78.0	609
Gravity core			
ARC4-R09	168.9	72.0	51

Table 1.2 AMS^{14}C dates of samples from core R09.

No.	Depth (cm)	^{14}C conventional age (yr BP)	error	Delta R	Median calibrated age (yr BP)
1	4	830	30	465 ± 95	101
2	85	2940	30	465 ± 95	2206
3	100	3490	30	465 ± 95	2780
4	141	4660	30	465 ± 95	4331
5	195	7930	30	465 ± 95	7888
6	212	8450	30	465 ± 95	8417
7	245	8920	30	465 ± 95	9168

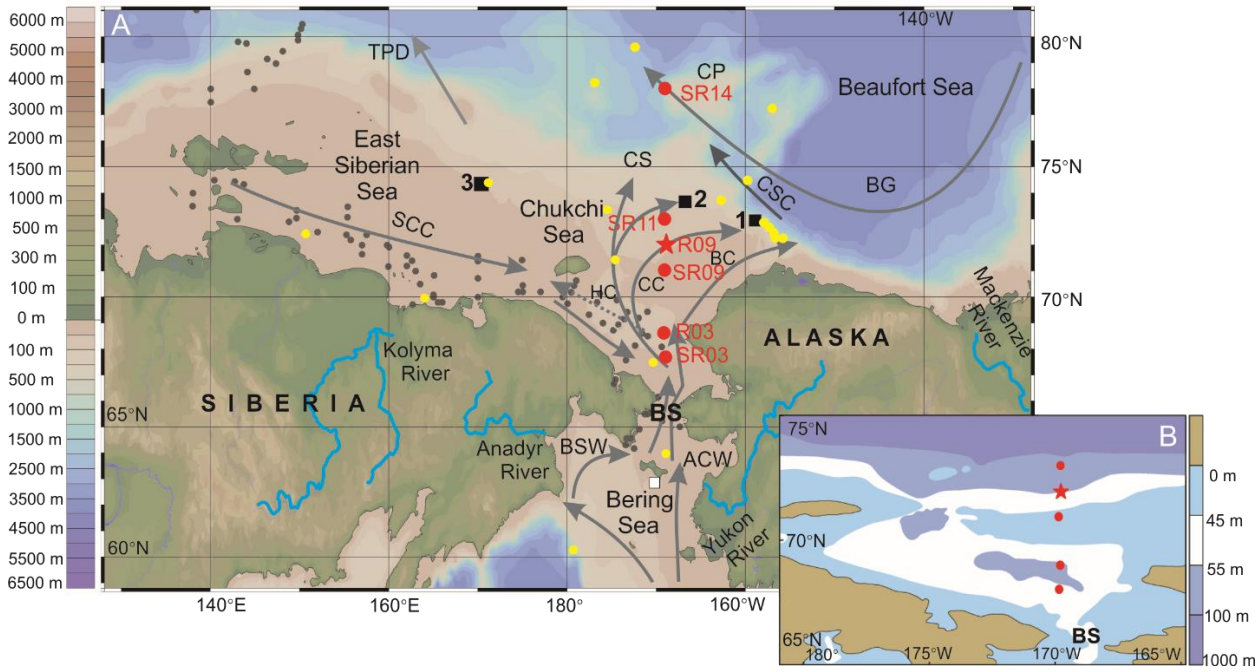

Figure 1-1 A) Bathymetric map with major currents and core locations. Red circles: surface samples (this study); red star: core R09; black squares: sites mentioned in the text with references to the literature (1-Deschamps et al., 2019; 2-Stein et al., 2017; Yamamoto et al., 2017; 3-Stein et al., 2017); grey circles: locations of clay mineralogical data from surface sediments (cf. Wahsner et al., 1999; Viscosi-Shirley et al., 2003); yellow circles: locations of exchangeable Nd-isotope data from surface sediments (cf. Asahara et al., 2012; Hadley and Polyak, 2013); white square: location of Nd isotopes data from sea-ice sediment (Maccali et al., 2018); grey arrows illustrate the main current paths (from Grebmeier et al., 2006; Hunt et al., 2013): ACW = Alaskan Coastal Water; BG = Beaufort Gyre; BSW = Bering Sea Water; CSC = Chukchi Slope Current; CS: Chukchi Slope; SCC = Siberia Coastal Current; TPD = Transpolar Drift; BC = Barrow Canyon; BS = Bering Strait; CC = Central Channel; CP = Chukchi Plateau; HC = Herald Canyon; bathymetry from GEBCO world map (2014). B) Sketch of the paleogeography at ~ 11 to 10.5 cal. ka BP: major submerged channels (about -55 to -45 m deep) are indicated in white (sea-level estimated from Lambeck et al., 2014). Red cycles and the star correspond to the symbols mentioned in 1A.

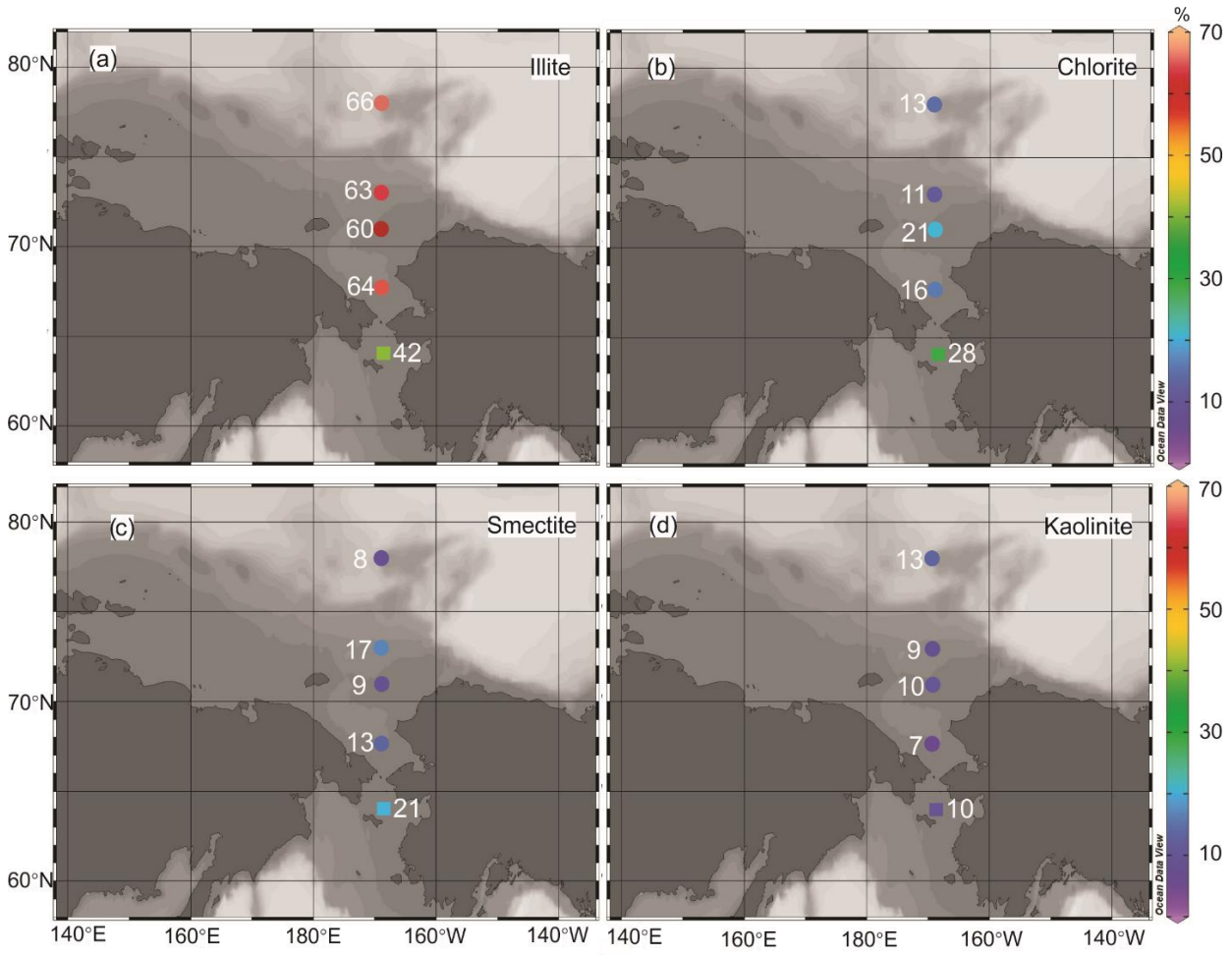

Figure 1-2 Clay mineral percentages in surface sediment samples. (a) illite; (b) chlorite; (c) smectite; (d) kaolinite. Dots: present study; square: from Moser and Hynes (1984).

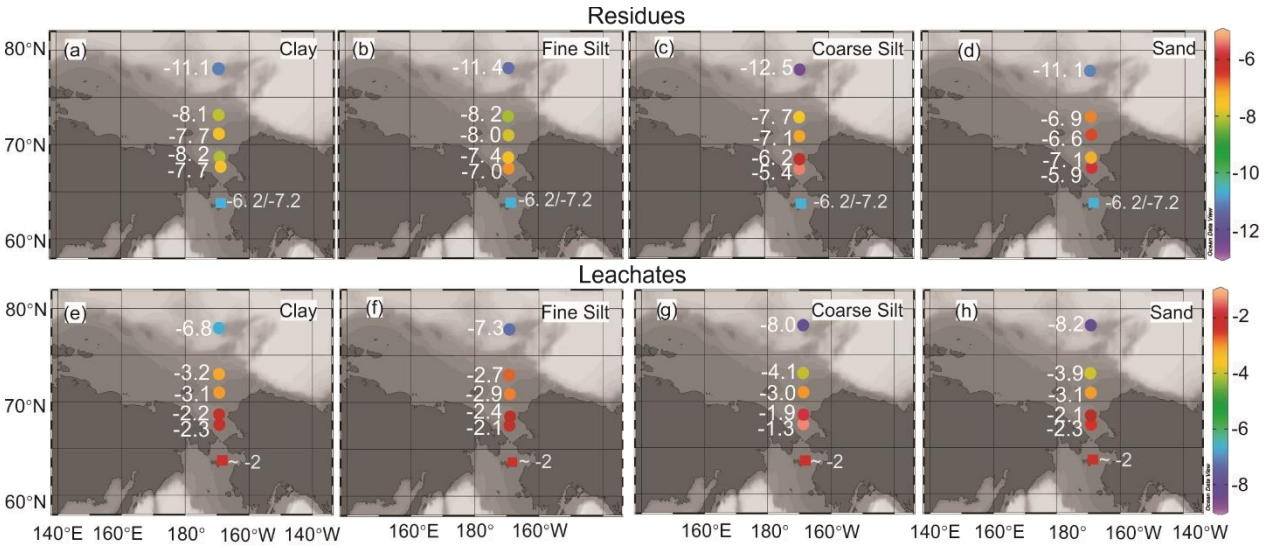

Figure 1-3 Nd-isotope compositions. Dots: residues (top) and leachates (bottom) vs size fractions of surface sediment samples from the present study: (a, e) clay; (b, f) fine silt; (c, g) coarse silt; (d, h) sand. Squares: bulk/silicate εNd-values (top row) and carbonate εNd-values (bottom row) at site MC18 (Asahara et al., 2012).

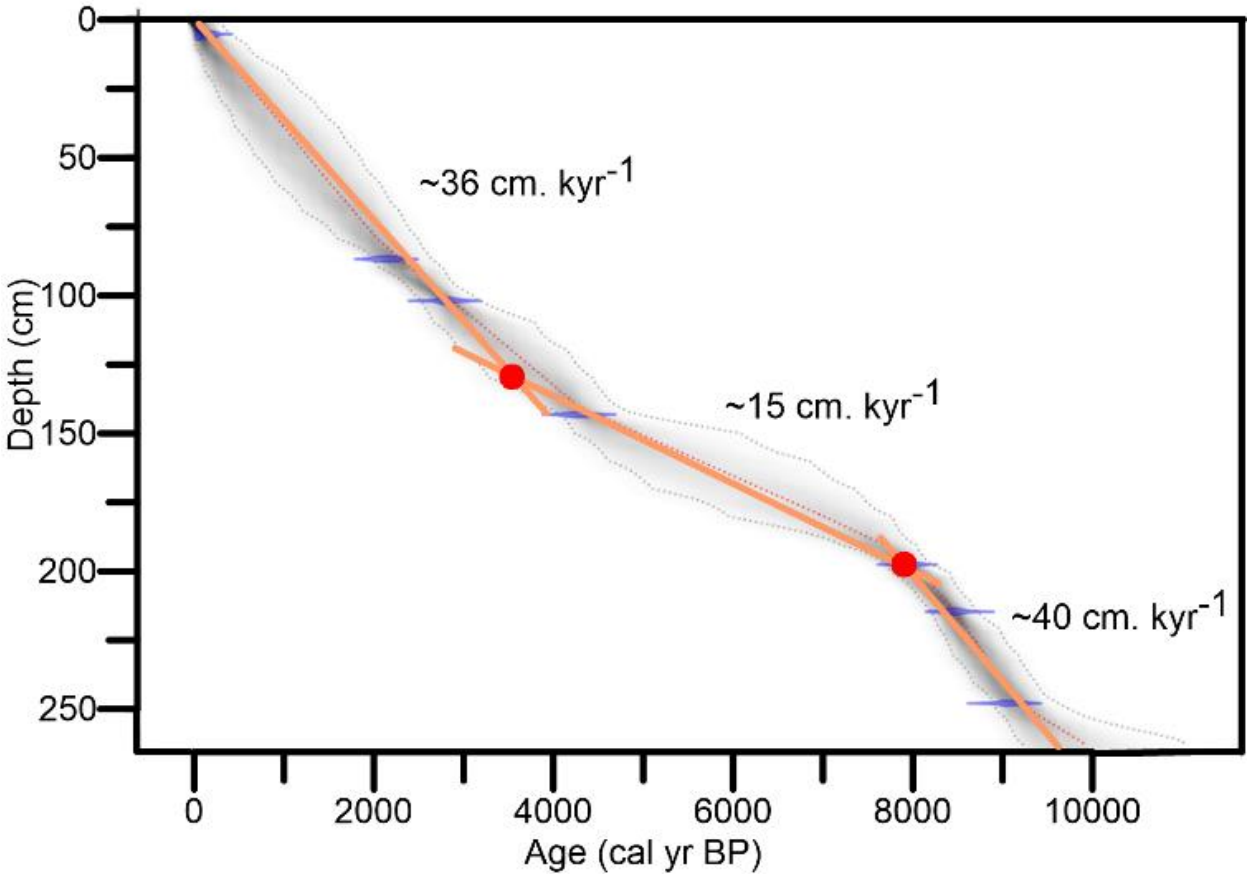

Figure 1-4 Age-depth relationship in core R09. The red circles represent intercepts of linear regressions through the 3 clusters, including two relatively well-dated layers (lower and upper part of the core), and the less-constrained middle Holocene. They allow estimating sedimentation rates of ~ 40 cm. kyr^{-1} (early Holocene), ~ 15 cm. kyr^{-1} (middle Holocene), ~ 36 cm. kyr^{-1} (late Holocene).

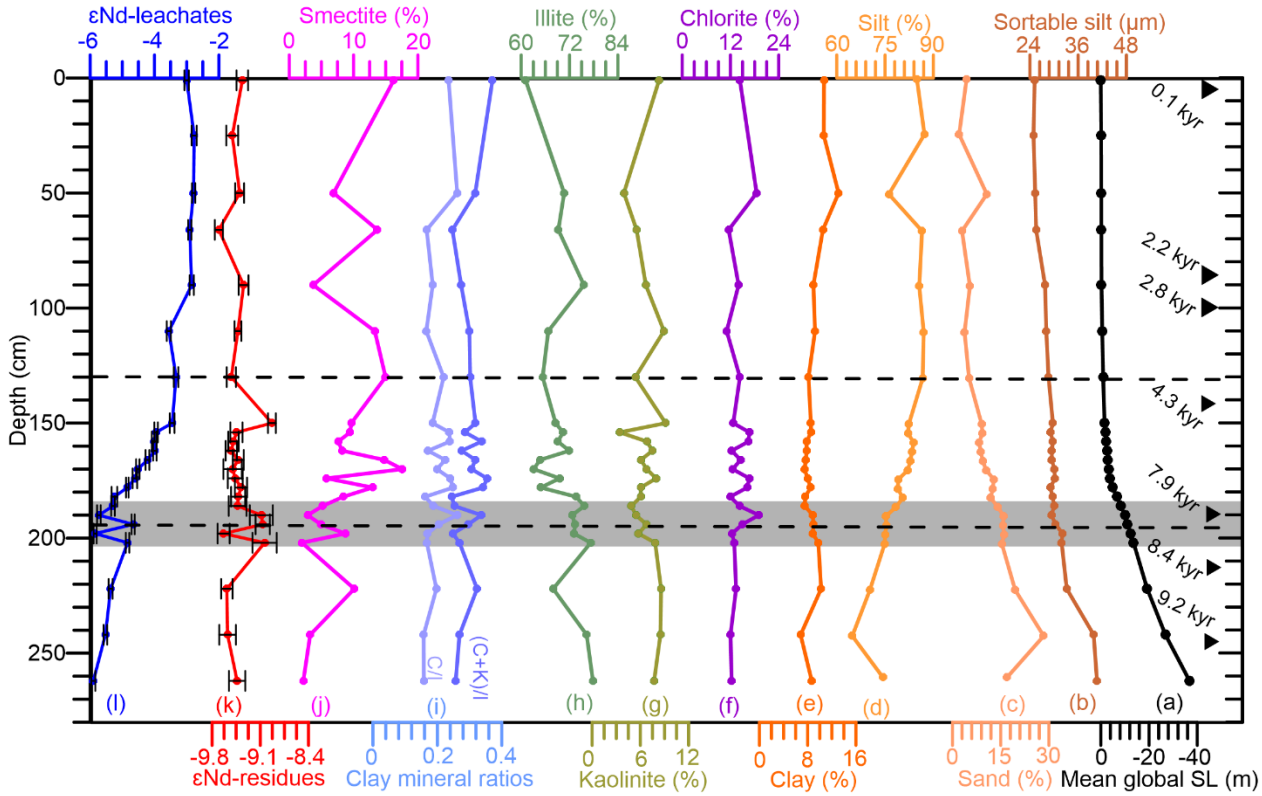

Figure 1-5 Sedimentological and geochemical properties of core R09 vs the mean global SL curve (from Lambeck et al., 2014). The three phases of suggested sedimentation rates are separated by dashed lines at ~ 195 and 130 cm. Black triangles: ^{14}C-dated layers. Grey area: εNd-value oscillations during the early to middle Holocene transition. The darkened transition at ~ 200 cm (~ 8 cal. ka BP) corresponds to a two steps-return of εNd-values to the initial bottom core value of ~ -6, the trend towards more radiogenic values resuming above.

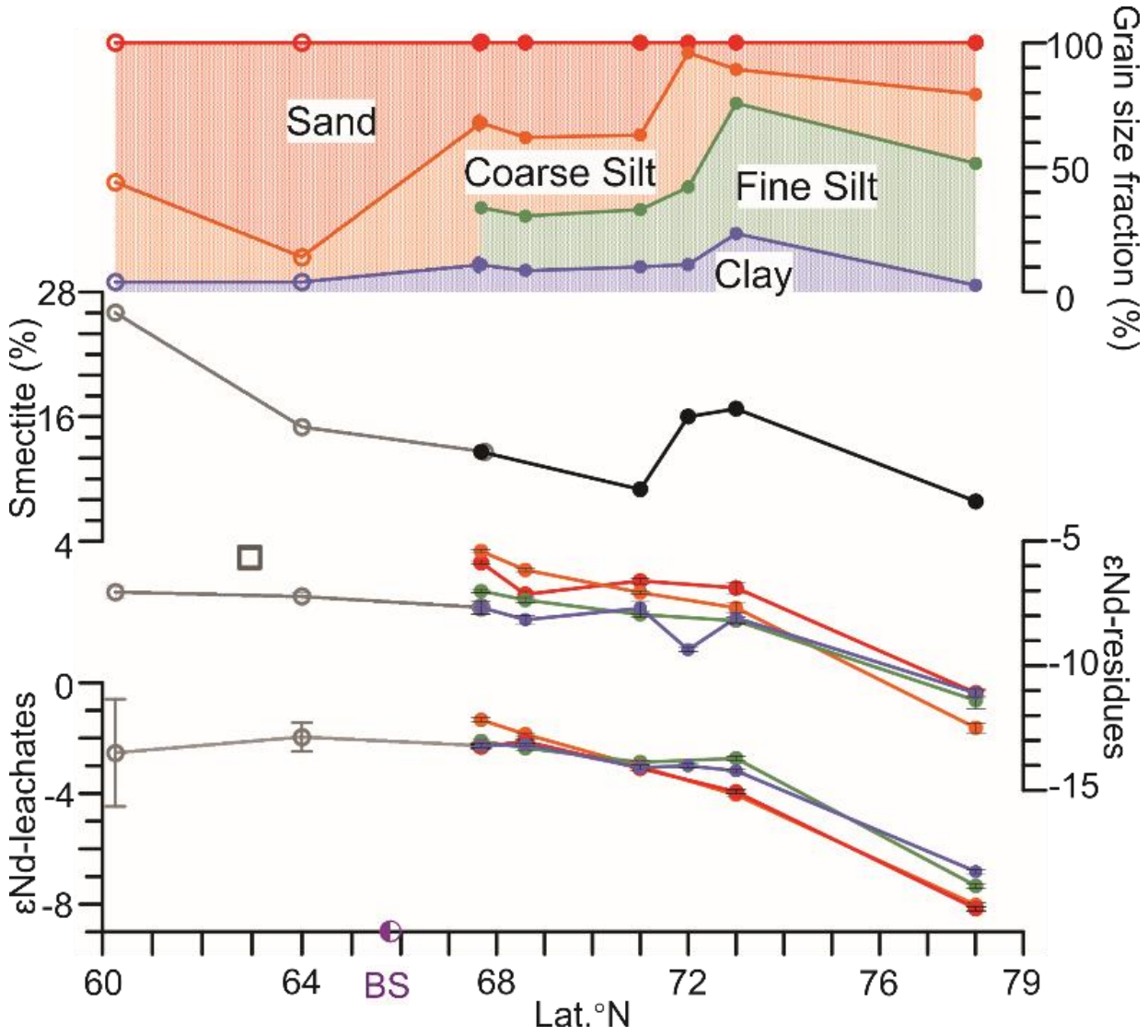

Figure 1-6 A) Map of surface sample locations. Black circles: present study; red star: core top sediments of R09 (present study); white squares: Asahara et al. (2012); black cross: sea-ice rafting data from Maccali et al. (2018). B) Sediment grain size, smectite relative abundance, and Nd-isotope data along the S-N transect from the Bering Sea to the Chukchi Plateau. Color codes: red = sand; orange = coarse silt; green = fine silt; blue = clay. BS: Bering Strait; purple circle: location of the BS; circle data are from present study; star data are from the core top samples of R09; square data are from Park et al. (2014), Moser and Hein (1984), Asahara et al. (2012), and Maccali et al. (2018).

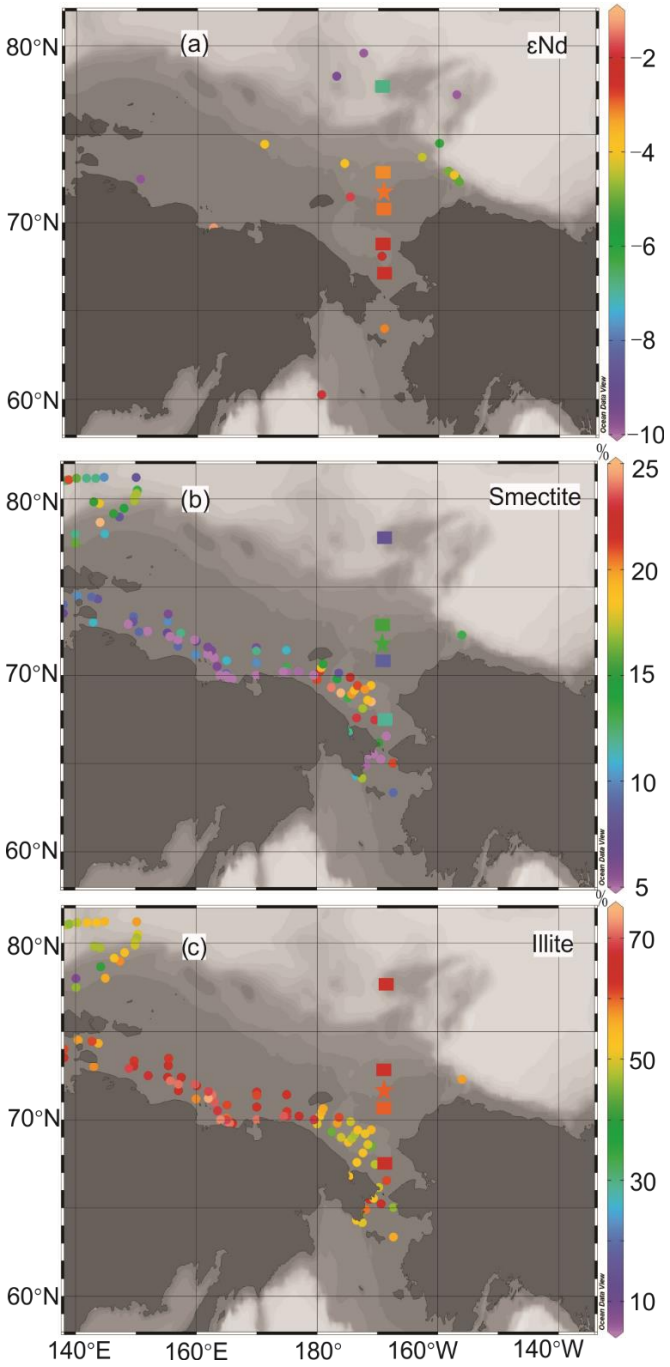

Figure 1-7 Maps of surface sediment properties. a) εNd-values in leachates. Circles: bulk sediments after Asahara et al. (2012) and Hadley and Polyak (2013); squares: clay fractions of surface samples from this study; star: clay fractions of core top sediments of R09 from this study; maps b & c-smectite and illite abundances; circles: from

Wahsner et al., (1999); Viscosi-Shirley et al., (2003); squares: surface sediments from this study; star: core top sediments of R09 from this study.

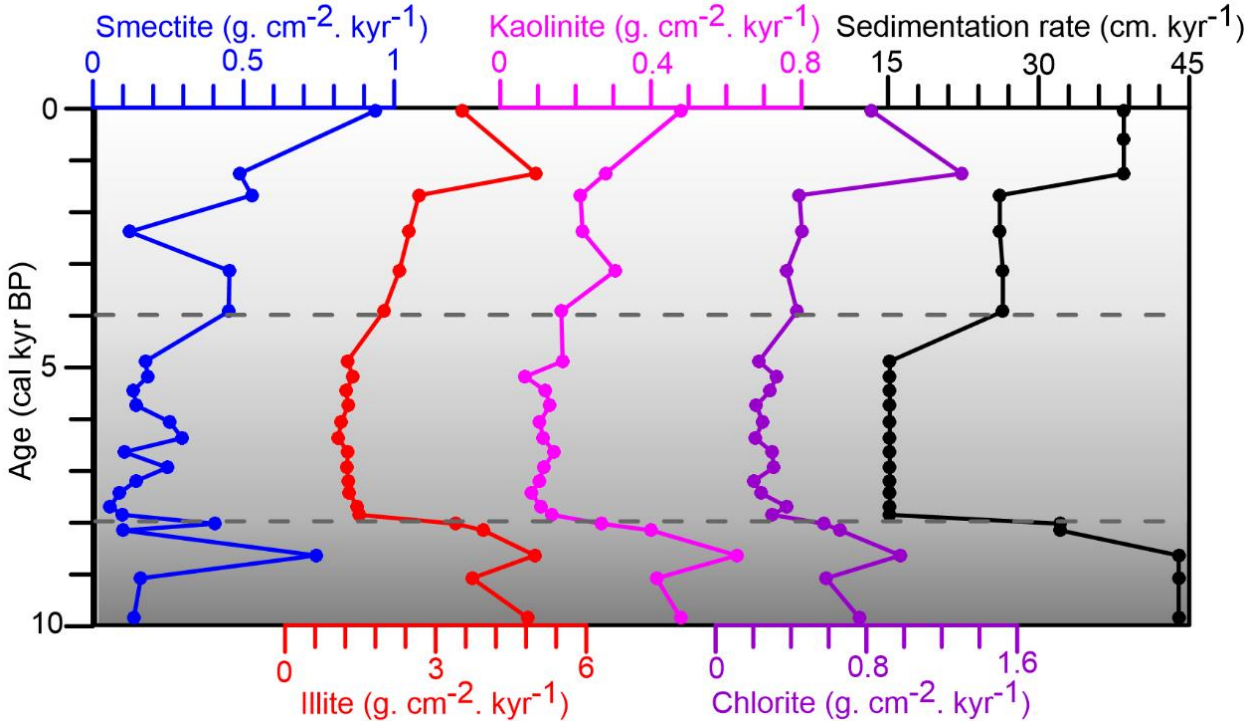

Figure 1-8 Fluxes of clay minerals at site R09. Horizontal dashed lines correspond to transitions in sedimentation rates as in Fig. 1-5.

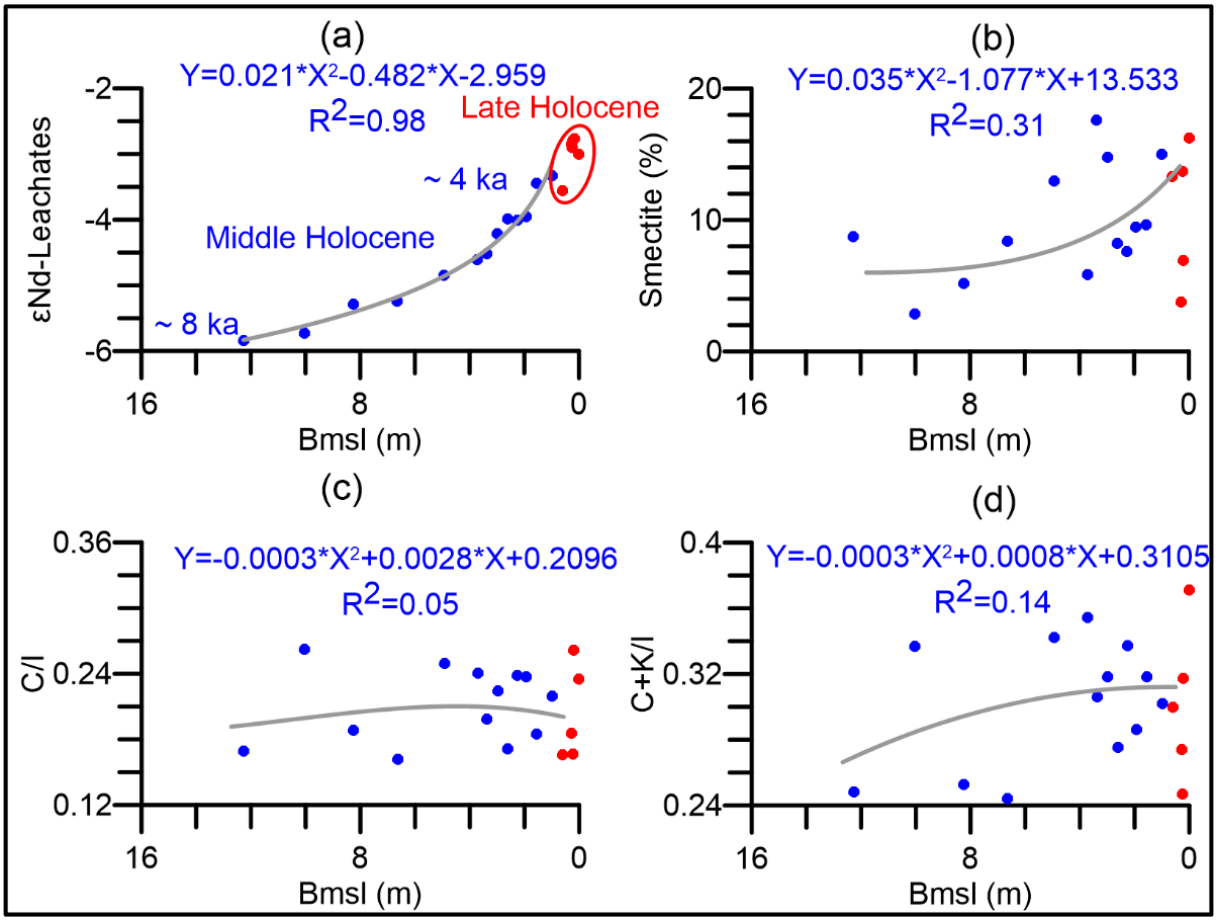

Figure 1-9 εNd and mineralogical tracer vs BS depth at site R09, inferred from the SL curve of Lambeck et al. (2014). Bmsl: water depth below modern sea-level (m); blue and red dots correspond to the middle Holocene and late Holocene data points, respectively. The correlation coefficients (R^2) are reported for data points encompassing the middle Holocene.

CHAPITRE 2

A resilient ice cover over the southernmost Mendeleev Ridge during the late Quaternary

TENGFEI SONG, CLAUDE HILLAIRE-MARCEL, ANNE DE VERNAL, YANGUANG LIU

The article was published in 2023 in the Journal of *Boreas*, https://doi.org/10.1111/bor.12632.

The presence of a late Quaternary ice sheet/ice shelf over the East Siberian Sea has been proposed in several papers. Here, we further document its duration/resilience based on the sedimentary, bulk mineralogical, and geochemical (organic matter content and its stable isotopic composition, U-Th series) properties of a core raised from the southernmost Mendeleev Ridge. The chronostratigraphy of the studied core was mainly built from the ^{230}Th excess ($^{230}Th_{xs}$) distribution and decay downcore. At the core-top, peaking-$^{230}Th_{xs}$ values during the early MIS 3 and mid-MIS 1 encompassing an MIS 2 hiatus were observed. As documented in several papers, these peaks suggest seasonally open ice conditions over proximal continental shelves. Below, the interval spanning MIS 4 and possibly MIS 5d records major ice rafting events illustrated by overall high coarse-fraction contents. Underlying MIS 5e, down to MIS 11, the sediment depicts relatively low sand (1.7±2.5 dw%), high clay (33.5±4.7 dw%), and very low organic carbon (0.10±0.06 dw%) contents, and low $\delta^{13}C_{org}$ values (-24.3±0.9‰). This section is interpreted as recording fine sediment transport by deep currents and/or meltwater plumes below a resilient ice cover, only interrupted by a few short-duration events. These events include i) detrital carbonate pulses assigned to deglacial events along the NW Laurentide Ice Sheet margin (Termination -T- III); ii) intervals with some planktonic foraminifer occurrences, likely relating to their advection from open areas of the Arctic Ocean (MIS 5e, 9 and 11). All Terminations, but TII and the early MIS 3, show peaking Mn/Al values linked to the submergence of Arctic shelves, under a rising sea level. We conclude that the resilient ice cover, likely an ice shelf, has been present over the southern Mendeleev Ridge during most of the interval after the Mid-Pleistocene Transition and was favoured by the low summer insolation of the MIS 14 to 10 interval.

Tengfei Song (song.tengfei@outlook.com), Claude Hillaire-Marcel and Anne de Vernal, Geotop, Université du Québec à Montréal, C.P. 8888, Montréal, QC H3C 3P8, Canada; Yanguang Liu, Key Laboratory of Marine Geology and Metallogeny, First Institute of Oceanography, Ministry of Natural Resources, Qingdao 266061,

China and College of Earth Science and Engineering, Shandong University of Science and Technology, Qingdao 266590, China;

2.1 Introduction

The existence of ice shelves in the Arctic Ocean has been proposed for more than one century (e.g., Thomson, 1888). Based on the observations of glacial scouring and glacigenic landforms on the seafloor of the Lomonosov Ridge, Northwind Ridge, Chukchi Plateau, and Chukchi Rise, Polyak et al. (2001) proposed that a 1 km-thick ice shelf covered the Arctic Ocean during the Pleistocene ice ages. This finding was supported by the sea floor mapping at the Arlis Plateau and southern Mendeleev Ridge (e.g., Jakobsson et al., 2010, 2016). Recently, the presence of an ice sheet anchored over the East Siberian shelves was further proposed based on the observations of glacial scours with multiple orientations (e.g., Niessen et al., 2013; Dove et al., 2014) and a glacial trough on the East Siberian-Chukchi Seas margin (O'Regan et al., 2017), with supporting ice model simulations (Gasson et al., 2018; Batchelor et al., 2019). Using a 3D thermo-mechanical ice sheet model, Colleoni et al. (2016) suggested that the hypothesized ice body that expanded over the East Siberian continental margin might have been an ice shelf. Although the East Siberian Ice Sheet scenario has been adopted in several studies to decipher the environmental and sedimentation changes in the western Arctic Ocean (e.g., Dong et al., 2017, 2020; Ye et al., 2020; Wang et al., 2021; Alatarvas et al., 2022; Zhao et al., 2022), arguments against the presence of a grounded ice sheet over the East Siberian shelves have been posed in several studies (e.g., Sher, 1995; Brigham-Grette, 2013) and have been supported by field investigations (Gualtieri et al., 2003; Nørgaard et al., 2023). Considering the low precipitation rate over the Arctic during glacials (Kageyama et al., 2021), which did not allow the formation of an ice sheet over the areas around the East Siberian Sea (Brigham-Grette, 2013), the East Siberian Ice Shelf (henceforth ESIS) scenario appears more likely and is accepted in this study. The presence of an ESIS, either as an extension of the Beringia ice cap (Colleoni et al., 2016) or an ice body fed by the ice floes from the Laurentide Ice Sheet (LIS) (Engels et al., 2008; Jakobsson et al., 2008), could have led to the glacial scouring over the Northwind Ridge and Chukchi Sea Borderland areas (Polyak et al., 2001; Niessen et al., 2013).

The age and duration of the ESIS, with or without being related to an ice sheet, have not been determined with certainty yet. Its prevalent assignment to Marine Isotope Stage (MIS) 6 and/or MIS 4 (e.g., O'Regan

et al., 2017; Alatarvas et al., 2022) was mainly based on equivocal ecostratigraphic inferences (e.g., Jakobsson et al., 2001; Backman et al., 2009). One of the ecostatigraphical markers is the coccolith *Emiliania huxleyi*, used with an MIS 5e assignment (Backman et al., 2009; Jakobsson et al., 2010, 2016), although the first appearance of this species dates from MIS 8 (Thierstein et al., 1977), and probably earlier (Guballa & Pelleo-Alampay, 2020). The other ecostratigraphical marker is the benthic foraminifer *Bulimina aculeata* used as the datum for the MIS 5a in several studies (e.g., Baumann, 1990; Jakobsson et al., 2001; Backman et al., 2004; Polyak et al., 2004; Nørgaard-Pedersen et al., 2007), despite the common occurrence of the species since the Miocene (Hayward et al., 2004; Tzevahirtzian et al., 2023). Besides, discontinuous microfossil records (Backman et al., 2009) and potential benthic mixing processes (Hillaire-Marcel et al., 2022b) can lead to some biases in the interpretation of microfossil records. The usage of microfossils as stratigraphical tools in the central Arctic Ocean is then questionable.

Recent geophysical investigations from the East Siberian Sea, Chukchi Sea Rise, and the Northwind Ridge have documented the existence of several glacial erosion phases during the Quaternary (Dove et al., 2014; Kim et al., 2021). The latest deep ice grounding event was assumed to date back to the MIS 4/3 transition based on the Mn-based cyclostratigraphy time frame and the identification of Pink-White (PW) layers (Schreck et al., 2018; Joe et al., 2020). With a similar age model, clay mineral and geochemical studies of sedimentary sequences from the Mendeleev and Northwind ridges, and the Canada Basin also illustrated the development of the ESIS during the last two glacial episodes (e.g., Dong et al., 2017, 2020; Ye et al., 2020). However, radiometric-based chronostratigraphies (Not and Hillaire-Marcel, 2010; Dipre et al., 2018; Geibert et al., 2021) led to considering a drastically distinct time frame for the Arctic Ocean events beyond the radiocarbon time scale (see Hillaire-Marcel and de Vernal, 2022). Therefore, the question about the resilience or recurrence of the ESIS during the glaciations after the Mid-Pleistocene Transition is still open.

In the present study, we intend to document further the ESIS history, mostly based on the study of a core raised from the southernmost Mendeleev Ridge (Arc7-E25; hereafter referred to as E25). Its location at the northern edge of the ESIS, slightly below ice-scouring features, was seen as suitable for this purpose. This core was analyzed by Zhao et al. (2022) who used the Mn-cyclostratigraphy with ages constrained based on a paleomagnetic inclination reversal/excursion at ~285 cm interpreted as the Biwa II event, thus leading to the assignment of the base of the core to MIS 7 (Jakobsson et al., 2000). However, the interpretation of the paleomagnetic inclination reversal/excursion stratigraphy in the Arctic Ocean is

under discussion (e.g., Liu et al., 2019; Dong et al., 2022) and the chronological assignments of Zhao et al. (2022) are subject to debate. Herein, we revised the chronostratigraphy of core E25 mainly based on uranium (U)-series measurements and, for the lower part of the core, on the tentative assignment of the inclination reversal at the core bottom to the Brunhes/Matuyama boundary. Whenever needed, we complemented the existing sedimentological, mineralogical, and geochemical data, with new measurements. Our key objectives were i) to outline the history of the ESIS, within the frame of the thorium-230 excess ($^{230}Th_{xs}$)-based stratigraphy, with special attention paid to its age and duration, ii) to document the paleoceanography at the southern tip of Mendeleev Ridge, and iii) to identify remote sedimentary signals from the northwestern LIS.

2.2 Background setting

The shallow continental shelves of the Arctic Ocean represent more than 50% of its total area (Jakobsson et al., 2003; Fig. 2-1). It acts as a major source of dissolved elements (e.g., Mn, Fe) and detrital particles for the deeper central Arctic Ocean (Macdonald & Gobeil, 2012; Rogalla et al., 2021). Under high sea levels, i.e., during interglacials and/or interstadials, the shelves are submerged; and thus the coastal erosion, tidal and wind mixing result in the upload of particles by seasonal sea ice (Charette et al., 2020). Sediments are then redistributed by currents and slope processes, and through sea-ice rafting deposition along the Transpolar Drift (TPD) and Beaufort Gyre (BG) routes (Fig. 2-1). During glacials, marked by low sea levels and glaciated shelves, streaming pulses from surrounding ice sheets released iceberg fleets, dispersing ice-rafted debris (IRD) with a high content in sand and coarse fractions (see Polyak et al., 2010) as far as the Nordic seas (Dowdeswell et al., 1999). In comparison, IRD transported by sea ice is generally composed of finer detrital particles, with a smaller fraction of sand (see Polyak et al., 2010). Lastly, during deglaciations, major drainage events of glacial lakes in the northwestern LIS sector (e.g., Not and Hillaire-Marcel, 2012), result in sedimentary pulses of deposition of fine dolomite-rich detrital material (Vogt, 1997) throughout most of the Arctic Ocean (e.g., Hanslik et al., 2013), often referred to as "PW layers" in the literature (cf. Polyak and Jakobsson, 2011).

During glacial periods, two major ice sheets directly influenced the Arctic Ocean: the Eurasian Ice Sheet, and the LIS on the North American side (Stein et al., 2017). A hypothesized ESIS was thought to be present over the East Siberian Shelf-Chukchi Sea Borderland (Colleoni et al., 2016). Unlike the relatively well-known

Eurasian and Laurentide ice sheets, the formation of the ESIS anchored over the East Siberian margin is far from clear. It could have resulted from the extension of the Eurasian Ice Sheet (Gasson et al., 2018) or of the Beringia ice cap (Colleoni et al., 2016), or from ice stream feedings by the LIS (Engels et al., 2008; Jakobsson et al., 2008). Recently, a glacially scoured trough discovered on the outer continental shelf of the East Siberian Sea (O'Regan et al., 2017) and the absence of large Late Pleistocene ice masses in northeastern Siberia (Nørgaard et al., 2023) make the first assumption more likely. However, the presence of a local ice cap, a Eurasian Ice Sheet extension, or a very thick ice shelf (Grosswald and Hughes, 1999; Colleoni et al., 2016; Gasson et al., 2018) cannot be deciphered based on the core collected above a water depth of ~1 km, which is the depth from where ice-scouring traces were documented (e.g., Polyak et al., 2001; Niessen et al., 2013; Dove et al., 2014; Kim et al., 2021). Besides, in respect of the fact that our study core is located at the northern tip of the hypothesized ESIS, where ice thickness was only ~200 m during MIS 6 according to model simulations (Colleoni et al., 2016), we will thus refer to the presence of an ESIS complex, likely an ice shelf, when evidence for perennial and thick ice cover is found at the area of the studied site.

2.3 Material and method

2.3.1 Material

Gravity core E25 (latitude 78° 57′ 33″ N, longitude 179° 26′ 11″ W; water depth of ~1200 m) was retrieved from the southernmost Mendeleev Ridge during the 7th cruise of the Chinese Arctic expedition on the R/V *Xue Long* in 2016. After splitting into two sections, no obvious unconformity was observed in the 320 cm-long core (Zhao et al., 2022). The core was continuously subsampled at 1 cm intervals and analyzed for colour reflectance, dry bulk density, XRF element content, coarse sediment fraction (>63 μm), planktonic foraminifera abundance (>154 μm), and their stable isotopic composition ($\delta^{18}O$), paleomagnetic inclination, and mineralogy, at the First Institute of Oceanography (FIO), MNR, China and other laboratories mentioned in Zhao et al. (2022).

As $^{230}Th_{xs}$ records cannot provide any robust stratigraphy beyond the last four climatic cycles due to its decay within this time frame, complementary measurements were undertaken at Geotop-UQAM, initially down to 163 cm, i.e., at the depth expected to reach MIS 11 based on our initial stratigraphic estimate from FIO data. To assess any potential surface sediment loss, ^{210}Pb and ^{226}Ra measurements were

performed in the upper 10 cm of the core. Below, subsampling at variable intervals ranging from 2 to 16 cm was carried out to obtain a better resolution for critical intervals. Our initial datasets were obtained from the sampling interval of 0 to 163 cm for U-Th series measurements. The Mn/Al ratio, planktonic foraminifera (>154 µm) abundance, and three AMS^{14}C dates are from Zhao et al. (2022). In addition, AMS^{14}C measurements on a fish otolith recovered from the surface sample (0–1 cm), and on a planktonic foraminifera assemblage between 2 and 3 cm were conducted at Alfred Wegener Institute (Bremerhaven, Germany), and the Andre E. Lalonde AMS Laboratory of the University of Ottawa (Ottawa, Canada), respectively. They yielded conventional ^{14}C ages of ~3.28 ± 0.08 ka and ~6.58 ± 0.03 ka, respectively. Contrary to Zhao et al. (2022), we only used the top five ^{14}C ages to estimate recent (MIS 1 to MIS 3) sedimentation rates, as ^{14}C activities in foraminifera shells from deep-sea sediments are not reliable beyond ~35 ka (e.g., Broecker et al., 2006; Haynert, 2011). Examples of ^{14}C-chronological inversions in Arctic Ocean cores can be found in many papers (e.g., Clark et al., 1986; Darby et al., 1997; Adler et al., 2009). See Hillaire-Marcel et al., (2022a) for a deeper examination of ^{14}C-based chronologies in low sedimentation rate sites of the Arctic Ocean.

2.3.2 Method

All methods described below refer to measurements performed at Geotop-UQAM. The methods used for measurements by Zhao et al. (2022) are described in the original paper.

2.3.2.1 Grain-size analysis

A total of 36 subsamples of ~0.3 g each subsampled at intervals of 2–20 cm in the upper 167 cm of the core were selected to conduct the grain size measurement using laser-diffraction equipment. The uneven sampling depths are due to insufficient sample quantity for the grain size measurements. Below 167 cm, the grain size measurements were taken at 4 cm intervals. The subsamples were treated with 30% H_2O_2 and 3% HCl to remove organic matter and calcite, in particular foraminifera shells. After drying and rinsing, Na-hexametaphosphate was then added to disperse the sediments for more than 24 h. Subsamples were treated in an ultrasound bath for 30 seconds, followed by rotated agitation. The disaggregated sediment samples were then analyzed with a laser-diffraction particle-size analyzer (LS13320, Beckman-Coulter™) for the fractions smaller than 2000 µm. The grain size data and granulometric statistics were processed

using GRADISTAT software (Blott and Pye, 2001). The analytical reproducibility is better than 1%, according to Daubois et al. (2015).

2.3.2.2 X-Ray diffraction measurement

About 0.2 g of ground bulk sediments were used for X-Ray diffraction measurement with a Siemens D-5000™ diffractometer (CoKα 1, 2 radiation and a silicon detector). Semi-quantitative estimates of the main mineral species were based on their main diffraction peak height (in counts per second) with automatically applied correction factors using the Bruker DIFFRAC-EVA™ software. The percentage of each mineral was estimated from its relative peak height corrected for quartz and normalized to 100%. Analytical errors are estimated to be below 5% (Not and Hillaire-Marcel, 2010).

2.3.2.3 Organic carbon and $^{13}C_{org}$ measurements

Bulk sediments were dried in the oven at ~50°C for more than 24 h. Two aliquots of ~15 mg dry ground subsamples were acidified with concentrated HCl for more than 24 h to make sure that any detrital dolomite was totally removed. The organic carbon (C_{org}) and $^{13}C_{org}$ measurements were performed using a Carlo Erba^{TM} elemental analyzer and an Isoprime-100^{TM} mass spectrometer, respectively. The results of $^{13}C_{org}$ measurements are expressed using the standard δ notation in comparison with the Vienna Pee Dee Belemnite (VPDB). The analytical precision is estimated at ±0.05% for C_{org} and better than ±0.1‰ for $\delta^{13}C_{org}$ based on replicate analyses of the study samples.

2.3.2.4 U-series isotopes

Lead-210 (^{210}Pb): About 0.2 g-aliquots of the core top samples were dried and ground for ^{210}Pb measurement at 1-cm intervals, excluding between 6 and 8 cm (samples lost). Details related to the ^{210}Pb extraction and analysis could be found in Song et al. (2022). The standard deviation from alpha counting statistics averages 3% of the value obtained.

Radium-226 (^{226}Ra): ^{226}Ra activity was measured by gamma-ray using an EGG-Ortec gamma well detector (pure germanium) spectrometer. Pre-weighed sediment samples were sealed in 10-cm^3 glass vials for at least 21 days to ensure the secular equilibrium between ^{226}Ra and ^{222}Rn. Only five samples of the top 10 cm were large enough to allow for ^{226}Ra measurements. The ^{226}Ra-activities were determined from the

measurement of the daughter ^{214}Pb (295.2, and 351.9 keV) and ^{214}Bi (609.3 keV) decay products. Counting continued until reaching an uncertainty of less than 10%.

U-Th series: Analyses of ^{230}Th, ^{234}U, and ^{238}U were performed on dried and ground bulk sediment samples (~0.15 g). Powdered samples were spiked using a mixed ^{233}U-^{236}U-^{229}Th solution of known ratios and dissolved by a series of concentrated acids (HF-HNO_3-HCl-H_3BO_4). Digested samples were loaded onto AG® 1-X8 anionic exchange resin for U-Th separation. Th and U were further purified through AG® 1-X8 and UTEVA® resins, respectively. Both Th and U fractions were then analyzed on a Nu Plasma™ multi-collector inductively coupled plasma mass spectrometer (MC-ICP-MS) by peak jumping on a filtered ion counter. Mass bias was corrected by the exponential law using the ^{236}U/^{233}U ratio. All results were quoted at ±2σ standard deviation uncertainty level. The HU-1 solution was used as a standard solution to monitor analytical sessions. Duplicated analyses of the HU-1 solution yielded a mean activity ratio of ^{234}U versus ^{238}U of 1.0022 ± 0.0049 (±1σ; n = 7). For the present study, estimates of the excess in ^{230}Th ($^{230}Th_{xs}$) activity were obtained from the equation: $A^{230}Th_{xs} = A^{230}Th - A^{234}U_{mean}$, where A is the activity in disintegrations per minute and per gram (dpm. g^{-1}). Details about the calculation of $^{230}Th_{xs}$ can be found in Purcell et al. (2022) and the discussion below.

Analytical data are reported with one standard deviation except for U and Th isotopes data which are reported with two standard deviations. All mean estimates are reported with one standard deviation.

2.4 Results

2.4.1 Sedimentology properties

Laser-based grain size measurements indicate that core E25 is mostly composed of silty clay, with some intervals containing up to ~14.2 dry weight per cent (dw%) of sand (Fig. 2-2). The bottom layer, from 55 to 167 cm, shows a low sand content (1.7 ± 2.5 dw%), low mean grain size (Φ) values (6.2 ± 2.8 μm), and a high clay fraction content (33.5 ± 4.7 dw%). The intermediate layer, from 38 to 55 cm, depicts a much higher sand content (7.1 ± 5.1 dw%,) and higher Φ-values (15.8 ± 5.8 μm), but a lower clay content (20.7 ± 3.2 dw%). The upper layer is characterized by a low sand content (0.6 ± 0.9 dw%), low Φ-values (6.0 ± 2.4 μm), and an intermediate clay content (29.5 ± 6.7 dw%).

2.4.2 Major mineralogical features

Mineralogical data from bulk sediments indicate that quartz (45 ± 4%), albite (18 ± 3%), and illite (12 ± 2%) are the three dominant minerals. Dolomite shows peaking values from ~118 to 94 cm (up to ~9%) and from ~34 to 18 cm (up to ~13%) and does not show any significant relationships with the sand content, thus suggesting distinct depositional mechanisms. Three major calcite peaks are observed. They correlate with the foraminifer abundance (R^2 = 0.59; see ANNEXE B Supplementary Material Fig. S1). In these intervals, the calcite/dolomite ratio averages 2.9 ± 0.8 vs 1.7 ± 0.4 in other intervals. Smectite, which is often used as a tracer of the Laptev Sea and/or the Bering Sea sediment sources (Wahsner et al., 1999; Viscosi-Shirley et al., 2003; Song et al., 2022), records low abundance. It does not exceed 0.5% in the upper 115 cm and raises to ~1.5% below 122 cm. Due to the uncertainties in semi-quantitative estimates of clay minerals through bulk X-ray mineralogy measurement, this difference must be interpreted with caution.

2.4.3 Organic carbon content and its isotopic composition

The C_{org} content in core E25 is very low, less than 0.33 dw%. It shows an overall decreasing trend downcore (Fig. 2-2). From the core top to 29 cm, it averages 0.29 ± 0.02 dw% with two excursions towards lower values, notably one at ~9 cm, where it falls below 0.09 dw%. Deeper downcore, down to ~71 cm, it averages 0.19 ± 0.02 %. Below, from 71 to 163 cm, it averages 0.07 ± 0.02 dw%.

$\delta^{13}C_{org}$ values vary from -25.3‰ to -22.3‰. A similar range was reported for the Chukchi Sea rise (Park et al., 2017). From the core top to ~71 cm, the mean $\delta^{13}C_{org}$ value is -23.2 ± 0.5‰. Below, it decreases to -24.3 ± 0.9‰. Worthy of mention is the fact that the upper two samples from the core top record the maximum $\delta^{13}C_{org}$ values (~ -22.4 ‰), pointing to a prominent contribution of marine carbon (Schubert and Calvert, 2001). Downcore, slight oscillations towards higher $\delta^{13}C_{org}$ values characterize several intervals. They may similarly relate to enhanced marine carbon supplies.

2.4.4 Radiocarbon ages

The radiocarbon ages range from ~3.3 to ~34.5 ka from the core top to 26 cm (Fig. 2-2; Table 2.1). However, such ages should be used with caution as mixing by benthic fauna may result in smoothing. This is particularly critical at sites characterized by low sedimentation rates (e.g., Adler et al., 2009), where the mixing of Holocene and pre-LGM populations may occur (Hillaire-Marcel et al., 2022a).

2.4.5 U-series isotopes

There is no measurable excess in ^{210}Pb ($^{210}Pb_{xs}$) at the core top vs its parent ^{226}Ra isotope (see ANNEXE B Supplementary Material Table S1). Most Arctic Ocean sites show some $^{210}Pb_{xs}$ at the sediment surface, even those with very low sedimentation rates (i.e., <1 cm.kyr^{-1}; e.g., Not et al., 2008; Not and Hillaire-Marcel, 2010). However, some other sites, notably from the Lomonosov Ridge, seem also deprived of any $^{210}Pb_{xs}$ at the very surface of the sediment (e.g., PS87/023-2; Le Duc, 2018).

The ^{238}U and ^{232}Th contents vary between 1.38 and 1.98 ppm, and 7.81 to 12.21 ppm, respectively (Fig. 2-2). The AR($^{238}U/^{232}Th$) value averages 0.53 ± 0.05, a value in the lower range of those reported elsewhere in the Arctic Ocean (e.g., Not and Hillaire-Marcel, 2010; Gusev et al., 2013; Hillaire-Marcel et al., 2017). The AR($^{234}U/^{238}U$) has a mean value of 1.00 ± 0.04, suggesting a near-secular equilibrium between these two isotopes. A high AR($^{234}U/^{238}U$) value (~1.12) is observed at the interval of 162 to 163 cm, which may relate to the U relocation driven by late diagenetic processes (Purcell et al., 2022), but as it concerns an insignificant U concentration change, its impact on the $^{230}Th_{xs}$ estimate should remain within error bars.

The $^{230}Th_{xs}$ profile of core E25 follows closely those reported for most Arctic Ocean sites (Not and Hillaire-Marcel, 2010; Hillaire-Marcel et al., 2017; Geibert et al., 2021). Peaking $^{230}Th_{xs}$ values were thus assigned to specific marine isotope stages (MIS 1, 3, 5e, 7, 9, 11) and their corresponding Ts, as shown in Fig. 2-2.

2.5 Discussion

2.5.1 The $^{230}Th_{xs}$-based chronostratigraphy of core E25

2.5.1.1 U-Th series isotopes in core E25

All parameters that can affect a reliable estimate of $^{230}Th_{xs}$, i.e., of the ^{230}Th-fraction strictly inherited from the ^{230}Th produced in the water column and accumulated in sediments through scavenging processes, were summarized by Purcell et al. (2022). These parameters include i) any potential marine U-uptake in surface sediments, ii) any late diagenetic U-mobility driven by redox gradients in the sedimentary column. In both cases, the C_{org} concentration is critical for the development of low Eh horizons driving U-precipitation, either from the water column or from detrital minerals of over/underlying oxidized layers in the U^{4+} state, with preferential uptake of ^{234}U in the case of diagenetic processes (Gariépy et al., 1994; McManus et al., 2005; Wall and Krumholz, 2006; Purcell et al., 2022).

Here, core E25 is featured in low C_{org} content and oxidizing conditions, unlikely to result in early or late diagenetic U uptake. If any, U losses from the sedimentary column towards the water column should have been modest as indicated by the near secular equilibrium between ^{230}Th and ^{234}U in layers deprived of any $^{230}Th_{xs}$.

Similarly, any significant enrichment in ^{234}U (vs ^{238}U) can be discarded as indicated by the mean $\delta^{234}U$ value observed (0 ± 4‰). Any uptake of marine U at the water/sediment interface or any late diagenetic U-relocation downcore should result in excesses vs deficits in ^{234}U as, in the first case, the marine U shows a $\delta^{234}U$ value of ~114‰ (e.g., Chen et al., 1986; Not et al., 2012); in the second case, even greater excesses in ^{234}U could be expected (e.g., $\delta^{234}U$ of ~149 ‰ in C_{org}-rich layers of Lomonosov Ridge core PS2757-8; Purcell et al., 2022).

At last, U concentrations in the cored sequence (mean [U] = 1.72 ± 0.13 ppm) are much less variable than those of thorium ([Th] = 9.94 ± 1.13 ppm) and the overall variability of the $^{238}U/^{232}Th$ mass ratio is mostly driven by ^{232}Th variability (see ANNEXE B Supplementary Material Fig. S2). Altogether, this suggests that the minor changes in U concentrations observed are linked to variable detrital sediment sources.

The correlations between AR($^{238}U/^{232}Th$), and sedimentological and mineralogical properties indicate that the AR($^{238}U/^{232}Th$) value is relatively high in intervals with enhanced IRD supplies and high quartz contents (see ANNEXE B Supplementary Material Fig. S3). High AR($^{238}U/^{232}Th$) seems to be linked either to high coastal erosion and sea-ice rafting under high sea level (i.e., interglacials and MIS 3) or to glacial advances during stadials (cf. Purcell et al., 2022).

2.5.1.2 Calculation of the $^{230}Th_{xs}$ extinction depth

In the present study, we followed the approach of Purcell et al. (2022) for the calculation of the extinction depth and age of ^{230}Th vs its parent ^{234}U. Even under the sporadic sedimentation regime of the Arctic Ocean (e.g., Hillaire-Marcel et al., 2017, 2022b), $^{230}Th_{xs}$ broadly follows a negative exponential decay downcore. As illustrated in Fig. 2-3, the linear trend of $\ln(A^{230}Th)$ downcore illustrates an R^2-value of 0.57. Its intercept with the mean $A^{234}U$ value, yields a ^{230}Th "extinction" age of 402 ± 20 kyr, at a depth of 166 + 64/- 45 cm, taking into consideration the uncertainties on the slope of the $\ln(A^{230}Th)$ line and mean ^{234}U activity.

2.5.1.3 The $^{230}Th_{xs}$-based stratigraphy

As documented previously by Huh et al. (1997), $^{230}Th_{xs}$ profiles in the Arctic Ocean depict a strong "sub-surface" peak. It has been assigned to the early MIS 3, based on sequences with sedimentation rates high enough to decipher the MIS 3 peak from that of MIS 1(see Hillaire-Marcel et al., 2017 and Purcell et al., 2022). These two peaks sometimes overlap at sites with very low sediment accumulation, often characterized by an MIS 2 hiatus (Fig. 2-4; Not and Hillaire-Marcel, 2010; Hillaire-Marcel et al., 2017). So far, there is no well-documented explanation for the peaking $^{230}Th_{xs}$ values of MIS 3. Hillaire-Marcel et al. (2022b) proposed that this $^{230}Th_{xs}$ peak results from its build-up in the water column during the preceding MIS 5d–4 interval, followed by its rapid scavenging during the early MIS 3 sea level rise (e.g., Siddal et al., 2008). The high MIS 3 sea-level likely led to the opening of Bering Strait (Farmer et al., 2021) and the submergence of the Arctic Ocean shelves, possibly accompanied by seasonal sea ice openings and sea-ice rafting deposition of $^{230}Th_{xs}$ scavenging compounds (organic matter and clays; cf. Purcell et al., 2022). Note that Geibert et al. (2022) associated the high $^{230}Th_{xs}$ values of samples in MIS 3 interval with continuous but low sedimentary fluxes, considering that "*Even a short particle pulse would be enough to remove ^{230}Th from the water column*".

Below the MIS 3 $^{230}Th_{xs}$ peak, two intervals with measurable peaking $^{230}Th_{xs}$ values are identified. They are usually assigned to the MIS 5 and 7 and their corresponding Ts (TII, TIII; Not and Hillaire-Marcel, 2010; Hillaire-Marcel et al., 2017; Purcell et al., 2022). As documented by Geibert et al. (2021), reduced $^{230}Th_{xs}$ values mark the MIS 4 and MIS 6, possibly pointing to very low sediment accumulation rates, and even to a sedimentary hiatus in some areas of the central Arctic Ocean during MIS 6 (Fig. 2-4), not unlike those of MIS 2 (see also Hillaire-Marcel et al., 2017). Regardless of the consensus about the assignment to MIS 6, the identification of the MIS 4 layer is still under debate. Purcell et al. (2022) suggested that the low $^{230}Th_{xs}$ interval between the last interglacial (MIS 5e) and MIS 3 $^{230}Th_{xs}$ peaking layers should be assigned to MIS 5d–4 considering the overall low summer season insolation and sea level conditions during this period (Hillaire-Marcel et al., 2021). As shown in Fig. 2-4, $^{230}Th_{xs}$ peaks during MIS 5a and 5c could not be recognized, leading us to adopt the advanced stratigraphy proposed by Purcell et al. (2022) for this study.

Following Not and Hillaire-Marcel (2010) and Purcell et al. (2022), the two lower minor peaks of measurable excesses in ^{230}Th illustrated in Fig. 2-4 could be assigned to MIS 9 (~120 to 145 cm) and 11

(~163 cm). This stratigraphy would support the assignment of the major long-duration magnetic reversal observed at a depth of ~285 cm (Zhao et al., 2022), to the Brunhes/Matuyama boundary (~780 kyr; deMenocal et al., 1990) thus fitting with the magnetostratigraphy proposed in early papers (e.g., Herman, 1970; Clark et al., 1980; Aksu and Mudie, 1985), and supporting the concept of a "sediment starved" glacial Arctic Ocean.

2.5.2 Sedimentary regimes

2.5.2.1 Sedimentological features: sea-ice vs iceberg rafting

Coarse particles in the sediments are often used to track the ice-rafting events in the Arctic Ocean (Polyak et al., 2010), as they are delivered by either sea ice or icebergs. To recognize these two distinct transport processes from grain size measurements, several approaches have been applied (Lisitzin, 2002). For example, Spielhagen et al. (2004) proposed that icebergs were the predominant carrier of particles larger than 63 µm, whereas Dowdeswell et al. (1999) considered the fractions larger than 250 µm as being transported by icebergs. Adler et al. (2009) and Polyak et al. (2009) considered that larger than 63 µm fractions were compatible with sea ice rafting. However, sea ice anchored over the continental shelf could entrain all particle-size materials and transport them toward the deep sea (Reimnitz et al., 1987). Later on, Polyak et al. (2010) suggested that sediments with a high sand content, larger than 10–20 dw%, were more likely transported by icebergs, whereas sediments with less than 5–10 dw% of sands were rather delivered by sea ice. In addition, dry weight data should be used with care as one single gravel- or pebble-sized particle could significantly bias the content of coarse fractions. At last, other processes, such as current winnowing, turbidity, etc., could also affect the grain size distribution (see Stein, 2008).

In core E25, the sand content is low, varying between 0 and ~14 dw% with a median below 2 dw%. In opposition, the clay content varies between ~17 to ~44 dw% with a median of about 31 dw%. These data point to the unlikeness of any long-duration IRD deposition by icebergs except possibly for the ~14 and ~10 dw% peaking sand contents at ~50 cm and ~105 cm, respectively. The corresponding intervals could be assigned here to the late MIS 4 and MIS 8 glacial stages. However, the grain size data fit better with sea ice or deep current transport mechanisms throughout most of the recorded interval of core E25, except for the MIS 4/3 transition. Indeed, grain-size measurements in "dirty" seasonal sea ice and shelf sediments from the Laptev Sea by Dethleff (2005) depict a distribution similar to that generally characterizing core

E25 (~30 dw% of clay; ~63 dw% of silt; ~7 dw% of sand). Worthy of mention here is the fact that ^{14}C ages surface sediments from sites that are presently covered by perennial sea ice vary from ~8 to 5 ka (e.g., Spielhagen et al., 2004; Not and Hillaire-Marcel, 2010; Hillaire-Marcel et al., 2017; de Vernal et al., 2020; Xiao et al., 2020), implying very little sedimentation in the central Arctic Ocean under perennial sea ice, which is almost sediment free.

During glacial intervals, with the development of ice shelves (e.g., Dowdeswell and Jeffries, 2017), sedimentation was mostly linked to meltwater plumes (e.g., Reilly et al., 2016), resulting in a high content of fine silt-clay particles (<11 µm; ~82 dw%) and almost nil sand deposition (~1 dw%; cf. Jennings et al., 2022).

Whenever ice advance or retreat occurred, sporadic coarse particle deposition by icebergs would be expected. According to Clark and Hanson (1983), it should be characterized by low clay (~7 dw%) and high sand (up to 27 dw%) contents. On these grounds, using both coarse and fine fractions seems an appropriate means to assess the ice-rafting transport process. The ϕ-value, whose variation has been associated with the coarse fraction content (e.g., Not and Hillaire-Marcel, 2010), could additionally be used to reflect ice condition changes in the Arctic Ocean.

As illustrated in Fig. 2-2, two intervals depict Φ-values >10: the MIS 8/7 and MIS 4/3 transitions, the latter one being the most important. The Φ-values may suggest some ice streaming or open sea-ice conditions, possibly related to the dislocation of the ESIS (Dove et al., 2014; O'Regan et al., 2017; Schreck et al., 2018; Kim et al., 2021). With the exception of the above intervals marked by coarser sediment, the interval encompassing the MIS 11 to MIS 4/3 transition is characterized by low sand content (0.7 ± 0.5 dw%), high clay (34.4 ± 4.7 dw%) and fine silt-clay (84.8 ± 5.6 dw%) contents, and a low Φ-value (5.0 ± 1.1 µm), suggesting lateral transport of fine sediments, possibly through subglacial drainage systems (Jennings et al., 2022).

2.5.2.2 Sediment fluxes

Sediment accumulation in the central Arctic Ocean was low during glacials, almost nil during MIS 2 (Not and Hillaire-Marcel, 2010), and possibly MIS 6 (Hillaire-Marcel et al., 2017; Geibert et al., 2021). Moreover, during glacial stages or transitions, coarse sediments were deposited whenever ice retreat or ice advance

occurred as suggested by Purcell et al. (2022). Thus, inferences about effective sedimentation rates for such sequences would be misleading.

In core E25, sediment accumulation mostly occurred during depositional windows of early/middle interglacial (or interstadial in the case of MIS 3) intervals. These accumulations cannot be assigned to a specific time-span, as they were linked to high sea-ice rafting rates and/or lateral transportation, thus to intervals with submerged shelves, and high summer insolation values (Hillaire-Marcel et al., 2021). For example, during the present interglacial, sedimentation resumed at ~8 ka in the central Arctic but decreased rapidly during the Neoglacial starting at about 4 ka (e.g., Darby et al., 1997; Adler et al., 2009; de Vernal et al., 2020). Thus, the few cm of "interglacial/interstadial" sediment accumulated at sites, such as the one of core E25, were deposited within a few thousand years. Nonetheless, we have tentatively outlined a stratigraphic scheme for core E25 in Fig. 2-5, with possible depositional time windows. Except for the interval assigned to MIS 3, the sedimentary regime would have led to an overall near-linear age-depth trend for these time windows throughout the whole record. The outlined stratigraphy based on $^{230}Th_{xs}$ distribution and decay downcore is of course different from that proposed by Zhao et al. (2022), mainly set from the Mn-based cyclostratigraphy and the PW layer depths, pointing to a significantly lower overall sediment accumulation during relatively short time windows in opposition to the higher sedimentation rates proposed by Zhao et al. (2022) (see Hillaire-Marcel and de Vernal, 2022).

2.5.3 Terrestrial supplies during the late Quaternary

2.5.3.1 Detrital carbonate pulses from the Canadian Arctic Archipelago

Dolomite in sediments from the Arctic Ocean represents supplies from the Canadian Arctic Archipelago (CAA) and northern Greenland, where source rocks outcrop. Dolomite is thus a tracer of ice-rafting (Bischof et al., 1996; Vogt, 1997) and/or glacial lake drainage events (Not and Hillaire-Marcel, 2012; Swärd et al., 2022) from the Mackenzie region. At site E25, dolomite peaks at about 13% during MIS 7/late TIII and MIS 3, when it reaches up to ~40% at two sites from northern Mendeleev Ridge investigated by Not and Hillaire-Marcel (2010), about 250 nautical miles northward (Figs. 2-1, 6). Another distinct feature of the dolomite record from core E25 is that the MIS 5e/late TII pulse is missing whereas the northernmost Mendeleev sites recorded systematically such pulses for all deglaciations including the MIS 5e/late TII interval (Fig. 2-6; Not and Hillaire-Marcel, 2010). The sheltered situation of coring site E25 and/or its

isolation from the western Arctic Ocean margin due to the existence of ESIS (Ye et al., 2020), could explain these discrepancies. However, the fact that sites from the central Lomonosov Ridge (PS2185-3/6 and PS2200-5; Fig. 2-6), as well as Amerasian Basin (PS72/396-3/5) and Alpha Ridge (PS51/038-4), also recorded a reduced, even negligible, dolomite pulse during MIS 5e/late TII (Geibert et al., 2021) suggests a weak discharge/drainage event from the northwestern LIS toward the Arctic Ocean (Dalton et al., 2022).

The detrital carbonate layers referred to as “PW III” and "PW II" were tentatively assigned to MIS 3 and 5d respectively, based on the records of stable carbon and oxygen isotopes of planktonic foraminifer and planktonic foraminifer abundances (e.g., Polyak et al., 2004; Spielhagen et al., 2004; Stein, 2008). However, the "PW II" should be re-assigned to the early MIS 7/late TIII (Fig. 2-6), following the present $^{230}Th_{xs}$-based stratigraphy and the chronostratigraphy proposed initially by Spielhagen et al. (1997). Different from Spielhagen et al. (1997), who assigned the three ^{10}Be peaks at the interval of ~120–200 cm of core PS2185-3/6 to MIS 7, 9, and 11, we interpret the corresponding $^{230}Th_{xs}$ peaks to MIS 7 following Hillaire-Marcel et al. (2021) (Fig. 2-6) as $^{230}Th_{xs}$ could not be detected at MIS 11, even MIS 9, layer using the low-precision alpha counting analyses.

The fine-detrital dolomite peaks of MIS 7/late TIII and early MIS 3, i.e., the so-called “PW II” and "PW III”, observed systematically in deep Arctic Ocean sequences, likely relate to some important meltwater outbursts from the northwestern LIS (Not and Hillaire-Marcel, 2012; Fagel et al., 2014; Dalton et al., 2019; Swärd et al., 2022). Such outbursts rarely lasted more than a few hundred years (e.g., Clarke et al., 2004, 2009; Kleman and Applegate, 2014). The spreading of detrital dolomite over relatively thick layers (up to about 20 cm at site E25; Fig. 2-6) suggests mixing by physical or biological processes as illustrated by the dating of biogenic carbonate from low sedimentation rate sites of the Lomonosov Ridge (Hillaire-Marcel et al., 2022a).

2.5.3.2 Silicate supplies from the East Siberian Shelf

Amphiboles and pyroxenes are two common heavy minerals of the East Siberian Shelf (Behrends et al., 2009). Their abundances in sedimentary sequences from the Lomonosov Ridge have been considered as supporting an East Siberian Ice Sheet advance hypothesis (e.g., Alatarvas et al., 2022). However, these two minerals are undetectable in core E25 (see also Zhao et al., 2022), possibly due to the overall low sand content downcore (Fig. 2-2). The occurrence of quartz grains has been proposed as an alternative indicator

of glacial activity over the East Siberian Shelf (Bazhenova, 2012; Dong et al., 2020). Quartz is abundant in core E25, but mostly in fine fractions. Its variations might be compatible with some deglacial pulses in the critical area (Fig. 2-2).

Illite, the most abundant clay mineral of the sequence, has been proposed as a primary indicator of sea-ice rafting deposition and meltwater plumes and current transportations at the Chukchi–Alaskan margin (Ye et al., 2020; Koo et al., 2021; Wang et al., 2021). At site E25, the illite/quartz ratio records peak values during glacial intervals of MIS 5d–4, 8, 10 (Fig. 2-2), thus fitting better with deep current transportation at the site than with sea-ice rafting. As the illite/quartz ratio is proportional to illite abundance (R^2 = 0.90; ANNEXE B Supplementary Material Fig. S5), it seems likely that variations in illite fluxes throughout the studied interval are effective tracers of deep-current transported fine particles from the East Siberian Sea (Wang et al., 2021).

2.5.4 Resilient ice cover off the East Siberian Shelf during the late Quaternary

Several sedimentological features of core E25 can help document further the nature and resilience of the ice overlying the site during a substantial part of the recorded interval. They include i) the relative thicknesses of sedimentary layers deposited within discontinuous time windows; ii) the grain size properties of the sediment; iii) the C_{org} content; iv) the geochemical and isotopic properties ($^{230}Th_{xs}$ in particular); iv) the microfaunal content.

In the first step, we used high clay, low sand, and low C_{org} contents, as major discriminants to define conditions pointing to the presence of a perennial and thick ice cover at the study site, i.e. a situation when sedimentation was mainly governed by deep currents and/or meltwater plumes beneath the ESIS, a situation when primary productivity was extremely low. Unfortunately, aside from our study core E25, only two sites (MC11 and MA01; Not and Hillaire-Marcel, 2010; Xiao et al., 2020; Xu et al., 2021; Park et al. 2022) from the northern Mendeleev Ridge provide information about sedimentological and organic matter properties, in addition to $^{230}Th_{xs}$ profiles allowing for the set up of similar chronostratigraphies. As illustrated in Fig. 2-7, most core E25 data fall within the domain of perennial and thick ice, thus the resilient ESIS. The five outliers correspond to the coarse pulses we assigned to the MIS 8/7 and 4/3 transitions, with a retreating ESIS, leading to intervals with open sea-ice conditions during MIS 7 and the early MIS 3. Other northern sites from the Mendeleev Ridge area (sites MA01 and MC11), likely far from the ESIS margin (Fig.

2-1) and with a thinner ice cover (Colleoni et al., 2016), record overall coarser sedimentation and higher organic carbon fluxes linked to either iceberg-rafting events or seasonally open sea ice conditions. Hence, a resilient ESIS cover likely prevailed in the E25 core area from MIS 11 to MIS 4, with some opening during MIS 7, while the northern sites (e.g., site MA01) show distinct features pointing to alternations of ice-streaming to sea-ice rafting events.

We should mention here that using different stratigraphic tools, distinct age models were proposed for some of the cores mentioned above (see Fig. 2-5). For core MA01, using the Mn-based cyclostratigraphy and the interpretation of the first paleomagnetic inclination event to the boundary of MIS 8/7, Xiao et al. (2020) assigned the interval from core top to ~240 cm to the MIS 1 to 7 period. As this layer is characterized by a relatively high abundance of foraminifer shells, this feature was assigned to enhanced biogenic preservation under extensive sea ice cover conditions (Xiao et al., 2020). Of course, based on the $^{230}Th_{xs}$-stratigraphy, the MIS 7 layer of core MA01 should be strictly assigned to the interval of 35 to 50 cm (Fig. 2-6). Within this framework, the prevalent severe ice conditions hypothesized by Xiao et al. (2020) should then persist for a much longer time and are not inconsistent with our findings.

Based on the stratigraphy constrained from the $^{230}Th_{xs}$ profiles, data from earlier studies of core E25 (Zhao et al., 2022) provide clues about conditions before MIS 11. As illustrated in Fig. 2-8, the resilient ESIS cover may have been initiated during the late Quaternary after the Mid-Pleistocene Transition (Bischof and Darby, 1997; Dipre et al., 2018), following the abrupt orbital forcing changes (Tziperman & Gildor, 2003), thus the low summer insolation interval that makes unlikely any major ice cover opening in the Arctic Ocean (Hillaire-Marcel et al., 2021).

Resilient ESIS conditions at the study site probably persisted throughout MIS 5e as there is no evidence of sea-ice rafting deposition. We hypothesize that the short duration of the high summer insolation peak of MIS 5e (Hillaire-Marcel et al., 2021) failed to lead to the full melt of the ESIS inherited from MIS 6 (Colleoni et al., 2016). The low Mn/Al ratio observed during this interval (Figs. 2-2, 8) could relate to the presence of some ice over the East Siberian-Chukchi seas shelves, preventing the formation of Mn-oxides or their transportation toward the deep Arctic Ocean, or to complex diagenetic processes (Sundby et al., 2015). Furthermore, the stable isotopic composition ($\delta^{18}O$, δD) and pollen records of a layered ice/peat complex on the southern coast of the Bol'shoy Lyakhovsky Island, led Wetterich et al. (2016) to conclude that winter

conditions during MIS 5 were colder than during MIS 3 while summer conditions during MIS 5 were harsher than during MIS 3. As the Bol'shoy Lyakhovsky Island is adjacent to the postulated ESIS area (Fig. 2-1B), cold "glacial" conditions over the island linked to some residual ESIS would make sense. Such cold climate conditions might have been limited to the East Siberian continental margin area, as several studies suggest summer temperatures in other areas of the Arctic Ocean are up to ~5˚C higher than at present (e.g., Miller et al., 2010).

Harsh conditions during MIS 5e are also suggested by the low foraminiferal abundance in the corresponding interval (less than 32 per gram; Figs. 2-2, 8), adding that these few tests might have been carried along the lower halocline from open sea-ice settings off the ESIS potential area (Zamelczyk et al., 2021).

During glacial stages MIS 5d–4 and earlier stadials of the Quaternary, one can hypothesize i) a $\geqslant$800 m thick ice-shelf (Jakobsson et al., 2010, 2016; Geibert et al., 2021), ii) an underlying freshwater layer of a few hundred meters (Hillaire-Marcel et al., 2022b) or possibly deeper (Geibert et al., 2021), iii) a thinner but normal salinity layer below (Hillaire-Marcel et al., 2022b); iv) rare and coarse detrital fluxes linked to iceberg rafting, thus a lesser fine particles supply (Hillaire-Marcel et al., 2022b). During such intervals, ^{230}Th scavenging and deposition at the sea floor were likely very low (Fig. 2-4; Geibert et al., 2021; Hillaire-Marcel et al, 2022b).

During the late Ts/early interglacials preceding the MIS 5d–4 cold spell and within the $^{230}Th_{xs}$ time-span (i.e., MIS 5e/TII, MIS 9/TIV, possibly MIS 11 in core E25), more significant $^{230}Th_{xs}$ scavenging and deposition occurred. However, this does not necessarily imply open sea-ice conditions in the area. Fine particle supplies by mesoscale eddies, deep currents, and down-slope nepheloid processes (e.g., Darby et al., 2009; Xiang and Lam, 2020; Schulz et al., 2021; Watanabe et al., 2022) could have been responsible for $^{230}Th_{xs}$ advection at the study site.

Resuspended sediment could have also adsorbed Mn-oxides from the shelves, leading to the high Mn/Al ratio characterizing the early interglacial/late termination transitions (Figs. 2-2, 8). This process has already been reported in cores from the Lomonosov Ridge and Yermak Plateau, where large amounts of reworked materials rich in terrestrial organic matter, were recovered (Kremer et al., 2018; Purcell et al., 2022).

2.6 Conclusion

Using $^{230}Th_{xs}$ distribution and decay downcore, a distinct chronostratigraphy of core E25 merges out from the earlier one which was based on the Mn-cyclostratigraphy and PW layers age assignments (cf. Zhao et al., 2022). It leads to inferring paleoceanographic changes compatible with those proposed recently by Hillaire-Marcel et al. (2017), Geibert et al. (2021), and Purcell et al. (2022). It is also consistent with the orbitally tuned parameters governing sea-ice dynamics in the Arctic Ocean, which are the summer cumulative insolation and the sea level (Hillaire-Marcel et al., 2021).

As in earlier studies proposing the advance of a thick ice shelf or an ice sheet over the East Siberian Sea, our data from core E25 are in line with the presence of a resilient ice shelf extending slightly beyond the East Siberian Sea slope. Its northern tip did not extend much beyond 79.0°N (the latitude of site E25), as the northern core MA01 located at 82.0°N suggests seasonal sea ice activity during intervals that could be assigned to interglacials or interstadials (Xiao et al., 2020; Xu et al., 2021). The inception of such a resilient ice shelf could have been linked to the MIS 14–10 low insolation interval, thus possibly marking the MIS 14 glacial inception. This thick ice seems to have been a resilient feature in the area until MIS 2 with a few episodes of ice retreat. Among those, the early MIS 3 and MIS 7, in particular, are characterized by high $^{230}Th_{xs}$ and foraminiferal counts suggesting some open ice conditions in the western Arctic. However, both tracers could have been linked to advective processes along slopes and do not ascertain the full disappearance of resilient ice over the study area.

2.7 Acknowledgements

This work was supported by the Natural Sciences and Engineering Research Council (NSERC) of Canada, the Fonds de Recherche du Québec Nature et Technologies (FQRNT), and the National Natural Science Foundation of China [grant numbers: 41876070, 42176245]. Thanks to all scientists and crews for their help with the sampling of core E25 during the 7th Chinese National Arctic Research Expeditions (CHINARE 2016). The financial support from China Scholarship Council is highly appreciated by T.-F. Song. Thanks to André Poirier for his kind support in the MC-ICP-MS laboratory of Geotop-UQAM. We also appreciate all technical support from Agnieszka Adamowicz, Jean-François Hélie, Julien Gogot, François Hardy, Michel Preda, and Philippe Roberge. Reviews from Walter Geibert (Marum, Bremen) and Matt O'Regan (Stockholm University) helped to clarify several aspects of the manuscript.

2.8 Data availability

All the data used in this study are available in the ANNEXE B Supplementary files and the Pangaea database (https://doi.org/10.1594/PANGAEA.94984).

2.9 Declaration of interests

The authors declare that they have no known competing financial interests or personal relationships that could have appeared to influence the work reported in this paper.

2.10 References

Adler, R. E., Polyak, L., Ortiz, J. D., Kaufman, D. S., Channell, J. E., Xuan, C., Grottoli, A. G., Sellén, E. & Crawford, K. A. 2009: Sediment record from the western Arctic Ocean with an improved Late Quaternary age resolution: HOTRAX core HLY0503-8JPC, Mendeleev Ridge. *Global and Planetary Change 68*, 18–29.

Alatarvas, R., O'Regan, M. & Strand, K. 2022: Heavy mineral assemblages of the De Long Trough and southern Lomonosov Ridge glacigenic deposits: implications for the East Siberian Ice Sheet extent. *Climate of the Past 18*, 1867–1881.

Aksu, A. E. & Mudie, P. J. 1985: Magnetostratigraphy and palynology demonstrate at least 4 million years of Arctic Ocean sedimentation. *Nature 318*, 280–283.

Backman, J., Jakobsson, M., Løvlie, R., Polyak, L. & Febo, L. A. 2004: Is the central Arctic Ocean a sediment starved basin?. *Quaternary Science Reviews 23*, 1435–1454.

Backman, J., Fornaciari, E. & Rio, D. 2009: Biochronology and paleoceanography of late Pleistocene and Holocene calcareous nannofossil abundances across the Arctic Basin. *Marine Micropaleontology 72*, 86–98.

Baumann, M. 1990: Coccoliths in sediments of the eastern Arctic Basin. *Geological history of the polar oceans: Arctic versus Antarctic 308*, 437–445.

Behrends, M., Hoops, E. & Peregovich, B. 1999: Distribution patterns of heavy minerals in Siberian Rivers, the Laptev Sea and the eastern Arctic Ocean: An approach to identify sources, transport and pathways of terrigenous matter. *In* Kassens, H., Bauch, H. A., Dmitrenko, I., Eicken, H., Hubberten, H.-W., Melles, M., Thiede, J. & Timokhov, L. (eds.): *Land-Ocean Systems in the Siberian Arctic*, 265–286. Springer-Verlag, Berlin.

Batchelor, C. L., Margold, M., Krapp, M., Murton, D. K., Dalton, A. S., Gibbard, P. L., Stokes, C. R., Murton, J. B. & Manica, A. 2019: The configuration of Northern Hemisphere ice sheets through the Quaternary. *Nature communications 10*, 3713, https://doi.org/10.1038/s41467-019-11601-2.

Bazhenova, E. 2012: *Reconstruction of late Quaternary sedimentary environments at the southern Mendeleev Ridge (Arctic Ocean).* Ph.D. thesis, Universität Bremen, 49–50 pp.

Bischof, J. & Darby, D. A. 1997: Mid-to Late Pleistocene ice drift in the western Arctic Ocean: evidence for a different circulation in the past. *Science 277*, 74–78.

Bischof, J., Clark, D. L. & Vincent, J. S. 1996: Origin of ice-rafted debris: Pleistocene paleoceanography in the western Arctic Ocean. *Paleoceanography 11*, 743–756.

Blott, S. J. & Pye, K. 2001: GRADISTAT: a grain size distribution and statistics package for the analysis of unconsolidated sediments. *Earth Surface Processes and Landforms 26*, 1237–1248.

Brigham-Grette, J. 2013: A fresh look at Arctic ice sheets. *Nature Geoscience 6*, 807–808.

Broecker, W., Barker, S., Clark, E., Hajdas, I. & Bonani, G. 2006: Anomalous radiocarbon ages for foraminifera shells. *Paleoceanography 21*, PA2008, https://doi.org/10.1029/2005PA001212.

Chen, J. H., Edwards, R. L. & Wasserburg, G. J. 1986: ^{238}U, ^{234}U and ^{232}Th in seawater. *Earth and Planetary Science Letters 80*, 241–251.

Clark, D. L. & Hanson, A. 1983: Central Arctic Ocean sediment texture: a key to ice transport mechanisms. *In* Molnia, B. F. (eds.): *Glacial-Marine Sedimentation*, 301–330. Springer, Boston, MA.

Clark, D. L., Whitman, R. R., Morgan, K. A. & Mackey, S. D. 1980: Stratigraphy and glacial-marine sediments of the Amerasian Basin, central Arctic Ocean. *Special paper of the Geological Society of America 181*, 1–57.

Clark, D. L., Andree, M., Broecker, W. S., Mix, A. C., Bonani, G., Hofmann, H. J., Morenzoni, E., Nessi, M., Suter, M. & Woelfli, W. 1986: Arctic Ocean chronology confirmed by accelerator ^{14}C dating. *Geophysical Research Letters 13*, 319-321.

Clarke, G. K., Leverington, D. W., Teller, J. T. & Dyke, A. S. 2004: Paleohydraulics of the last outburst flood from glacial Lake Agassiz and the 8200BP cold event. *Quaternary Science Reviews 23*, 389–407.

Clarke, G. K. C., Bush, A. B. G. & Bush, J. W. M. 2009: Freshwater discharge, sediment transport, and modeled climate impacts of the final drainage of glacial Lake Agassiz. *Journal of Climate 22*, 2161–2180.

Charette, M. A., Kipp, L. E., Jensen, L. T., Dabrowski, J. S., Whitmore, L. M., Fitzsimmons, J. N., Williford, T., Ulfsbo, A., Jones, E., Bundy, R. M. & Vivancos, S. M. 2020: The transpolar drift as a source of riverine and shelf ‐ derived trace elements to the central Arctic Ocean. *Journal of Geophysical Research: Oceans 125*, e2019JC015920, https://doi.org/10.1029/2019JC015920.

Colleoni, F., Kirchner, N., Niessen, F., Quiquet, A. & Liakka, J. 2016: An East Siberian ice shelf during the Late Pleistocene glaciations: Numerical reconstructions. *Quaternary Science Reviews 147*, 148–163.

deMenocal, P. B., Ruddiman, W. F. & Kent, D. V. 1990: Depth of post-depositional remanence acquisition in deep-sea sediments: a case study of the Brunhes-Matuyama reversal and oxygen isotopic Stage 19.1. *Earth and Planetary Science Letters 99*, 1–13.

Darby, D. A., Bischof, J. F. & Jones, G. A. 1997: Radiocarbon chronology of depositional regimes in the western Arctic Ocean. *Deep Sea Research Part II: Topical Studies in Oceanography 44*, 1745–1757.

Darby, D. A., Ortiz, J., Polyak, L., Lund, S., Jakobsson, M. & Woodgate, R. A. 2009: The role of currents and sea ice in both slowly deposited central Arctic and rapidly deposited Chukchi–Alaskan margin sediments. *Global and Planetary Change 68*, 58–72.

Daubois, V., Roy, M., Veillette, J. J. & Ménard, M. 2015: The drainage of Lake Ojibway in glaciolacustrine sediments of northern Ontario and Quebec, Canada. *Boreas 44*, 305–318.

de Vernal, A., Hillaire-Marcel, C., Le Duc, C., Roberge, P., Brice, C., Matthiessen, J., Spielhagen, R. F. & Stein, R. 2020: Natural variability of the Arctic Ocean sea ice during the present interglacial. *Proceedings of the*

National Academy of Sciences of the United States of America 117, 26069-26075, https://doi.org/10.1073/pnas.2008996117.

Dethleff, D. 2005: Entrainment and export of Laptev Sea ice sediments, Siberian Arctic. *Journal of Geophysical Research: Oceans 110*, C07009, https://doi.org/10.1029/2004JC002740.

Dalton, A. S., Finkelstein, S. A., Forman, S. L., Barnett, P. J., Pico, T. & Mitrovica, J. X. 2019: Was the Laurentide Ice Sheet significantly reduced during marine isotope stage 3?. *Geology 47*, 111–114.

Dalton, A. S., Stokes, C. R. & Batchelor, C. L. 2022: Evolution of the Laurentide and Innuitian ice sheets prior to the Last Glacial Maximum (115 ka to 25 ka). *Earth-Science Reviews 224*, 103875, https://doi.org/10.1016/j.earscirev.2021.103875.

Dipre, G. R., Polyak, L., Kuznetsov, A. B., Oti, E. A., Ortiz, J. D., Brachfeld, S. A., Xuan, C., Lazar, K. B. & Cook, A. E. 2018: Plio-Pleistocene sedimentary record from the Northwind Ridge: new insights into paleoclimatic evolution of the western Arctic Ocean for the last 5 Ma. *Arktos 4*, 54, https://doi.org/10.1007/s41063-018-0054-y.

Dong, L., Liu, Y., Shi, X., Polyak, L., Huang, Y., Fang, X., Liu, J., Zou, J., Wang, K., Sun, F. & Wang, X. 2017: Sedimentary record from the Canada Basin, Arctic Ocean: implications for late to middle Pleistocene glacial history. *Climate of the Past 13*, 511–531.

Dong, L., Polyak, L., Liu, Y., Shi, X., Zhang, J. & Huang, Y. 2020: Isotopic fingerprints of ice‐rafted debris offer new constraints on middle to late quaternary arctic circulation and glacial history. *Geochemistry, Geophysics, Geosystems 21*, e2020GC00901, https://doi.org/10.1029/2020GC009019.

Dong, L., Polyak, L., Xiao, X., Brachfeld, S., Liu, Y., Shi, X., Fang, X., Bai, Y., Zhu, A., Li, C. & Zhao, S. 2022: A Eurasian Basin sedimentary record of glacial impact on the central Arctic Ocean during MIS 1–4. *Global and Planetary Change 219*, 103993, https://doi.org/10.1016/j.gloplacha.2022.103993.

Dowdeswell, J. A. & Jeffries, M. O. 2017: Arctic ice shelves: An introduction. *In* Copland, L. & Mueller, D. (eds.): *Arctic Ice Shelves and Ice Islands*, 3–21. Springer Polar Sciences. Springer, Dordrecht.

Dowdeswell, J. A., Elverhøi, A., Andrews, J. T. & Hebbeln, D. 1999: Asynchronous deposition of ice-rafted layers in the Nordic seas and North Atlantic Ocean. *Nature 400*, 348–351.

Dove, D., Polyak, L. & Coakley, B. 2014: Widespread, multi-source glacial erosion on the Chukchi margin, Arctic Ocean. *Quaternary Science Reviews 92*, 112–122.

Engels, J. L., Edwards, M. H., Polyak, L. & Johnson, P. D. 2008: Seafloor evidence for ice shelf flow across the Alaska–Beaufort margin of the Arctic Ocean. *Earth Surface Processes and Landforms 33*, 1047–1063.

Fagel, N., Not, C., Gueibe, J., Mattielli, N. & Bazhenova, E. 2014: Late Quaternary evolution of sediment provenances in the Central Arctic Ocean: mineral assemblage, trace element composition and Nd and Pb isotope fingerprints of detrital fraction from the Northern Mendeleev Ridge. *Quaternary Science Reviews 92*, 140–154.

Farmer, J. R., Pico, T., Underwood, O. M., Cleveland Stout, R., Granger, J., Cronin, T. M., Fripiat, F., Martínez-García, A., Haug, G. H. & Sigman, D. M. 2023: The Bering Strait was flooded 10,000 years before the Last Glacial Maximum. *Proceedings of the National Academy of Sciences 120*, e2206742119, https://doi.org/10.1073/pnas.2206742119.

Gariépy, C., Ghaleb, B., Hillaire-Marcel, C., Mucci, A. & Vallieres, S. 1994: Early diagenetic processes in Labrador Sea sediments: uranium-isotope geochemistry. *Canadian Journal of Earth Sciences 31*, 28–37.

Gasson, E. G., DeConto, R. M., Pollard, D. & Clark, C. D. 2018: Numerical simulations of a kilometre-thick Arctic ice shelf consistent with ice grounding observations. *Nature communications 9*, 1510, https://doi.org/10.1038/s41467-018-03707-w.

Geibert, W., Matthiessen, J., Stimac, I., Wollenburg, J. & Stein, R. 2021: Glacial episodes of a freshwater Arctic Ocean covered by a thick ice shelf. *Nature 590*, 97–102.

Geibert, W., Matthiessen, J., Wollenburg, J. and Stein, R. 2022: Reply to 'Challenging the hypothesis of an arctic ocean lake during recent glacial episodes' by Hillaire‐Marcel, *et al. Journal of Quaternary Science 37*, 568–571.

Grosswald, M. G. & Hughes, T. J. 1999: The case for an ice shelf in the Pleistocene Arctic Ocean. *Polar Geography 23*, 23–54.

Gualtieri, L., Vartanyan, S., Brigham-Grette, J. & Anderson, P. M. 2003: Pleistocene raised marine deposits on Wrangel Island, northeast Siberia and implications for the presence of an East Siberian ice sheet. *Quaternary Research 59*, 399–410.

Guballa, J. D. & Peleo-Alampay, A. M. 2020: Pleistocene Calcareous Nannofossil Biostratigraphy and Gephyrocapsid Occurrence in Site U1431D, IODP 349, South China Sea. Geosciences *10*, 388, https://doi.org/10.3390/geosciences10100388.

Gusev, E. A., Maksimov, F. E., Kuznetsov, V. Y., Basov, V. A., Novikhina, E. S., Kupriyanova, N. V., Levchenko, S. B. & Zherebtsov, I. E. 2013: Stratigraphy of bottom sediments in the Mendeleev Ridge area (Arctic Ocean). *Doklady Akademii Nauk 450*, 602–606.

Hanslik, D., Löwemark, L. & Jakobsson, M. 2013: Biogenic and detrital-rich intervals in central Arctic Ocean cores identified using x-ray fluorescence scanning. *Polar Research 32*, 18386, https://doi.org/10.3402/polar.v32i0.18386.

Haynert, K., Schönfeld, J., Riebesell, U. & Polovodova, I. 2011: Biometry and dissolution features of the benthic foraminifer Ammonia aomoriensis at high pCO2. *Marine Ecology Progress Series 432*, 53–67.

Hayward, B. W., Grenfell, H. R., Carter, R. & Hayward, J. J. 2004: Benthic foraminiferal proxy evidence for the Neogene palaeoceanographic history of the Southwest Pacific, east of New Zealand. *Marine Geology 205*, 147–184.

Herman, Y. 1970: Arctic paleo-oceanography in late Cenozoic time. *Science 169*, 474–477.

Hillaire-Marcel, C., Ghaleb, B., de Vernal, A., Maccali, J., Cuny, K., Jacobel, A., Le Duc, C. & McManus, J. 2017: A new chronology of late Quaternary sequences from the central Arctic Ocean based on "extinction ages" of their excesses in ^{231}Pa and ^{230}Th. *Geochemistry, Geophysics, Geosystems 18*, 4573–4585, https://doi.org/10.1002/2017GC007050.

Hillaire-Marcel, C., de Vernal, A. & Crucifix, M. 2021: Sea-level and summer season orbital insolation as drivers of Arctic sea-ice. *arXiv 2102*, 02067, https://doi.org/10.48550/arXiv.2102.02067.

Hillaire-Marcel, C. & de Vernal, A. 2022: A comment about" A sedimentary record from the Makarov Basin, Arctic Ocean, reveals changing middle to Late Pleistocene glaciation patterns"(Quat. Sci. Rev., 270 (2021), p. 107176) from W. Xiao, L. Polyak, R. Wang, C. Not, L.

Dong, Y. Liu, T. Ma, T. Zhang. *Quaternary Science Reviews 279*, 107239, https://doi.org/10.1016/j.quascirev.2021.107239.

Hillaire-Marcel, C., de Vernal, A., Rong, Y., Roberge, P. & Song, T. 2022a: Challenging radiocarbon chronostratigraphies in central Arctic Ocean sediment. *Geophysical Research Letters 49*, e2022GL100446, https://doi.org/10.1029/2022GL100446.

Hillaire-Marcel, C., Myers, P. G., Marshall, S., Tarasov, L., Purcell, K., Not, C. & de Vernal, A. 2022b: Challenging the hypothesis of an Arctic Ocean lake during recent glacial episodes. *Journal of Quaternary Science 37*, 559–567.

Huh, C. A., Pisias, N. G., Kelley, J. M., Maiti, T. C. & Grantz, A. 1997: Natural radionuclides and plutonium in sediments from the western Arctic Ocean: sedimentation rates and pathways of radionuclides. *Deep Sea Research Part II: Topical Studies in Oceanography 44*, 1725–1743.

Jakobsson, M., Løvlie, R., Al-Hanbali, H., Arnold, E., Backman, J. & Mörth, M. 2000: Manganese and color cycles in Arctic Ocean sediments constrain Pleistocene chronology. *Geology 28*, 23–26.

Jakobsson, M., Løvlie, R., Arnold, E. M., Backman, J., Polyak, L., Knutsen, J. O. & Musatov, E. 2001: Pleistocene stratigraphy and paleoenvironmental variation from Lomonosov Ridge sediments, central Arctic Ocean. *Global and Planetary change 31*, 1–22, https://doi.org/10.1016/S0921-8181(01)00110-2.

Jakobsson, M., Grantz, A., Kristoffersen, Y. & Macnab, R. 2003: Physiographic provinces of the Arctic Ocean seafloor. *Geological Society of America Bulletin 115*, 1443–1455.

Jakobsson, M., Polyak, L., Edwards, M., Kleman, J. & Coakley, B. 2008: Glacial geomorphology of the central Arctic Ocean: the Chukchi Borderland and the Lomonosov Ridge. *Earth Surface Processes and Landforms 33*, 526–545.

Jakobsson, M., Nilsson, J., O'Regan, M., Backman, J., Löwemark, L., Dowdeswell, J. A., Mayer, L., Polyak, L., Colleoni, F., Anderson, L. G. & Björk, G. 2010: An Arctic Ocean ice shelf during MIS 6 constrained by new geophysical and geological data. *Quaternary Science Reviews 29*, 3505–3517.

Jakobsson, M., Nilsson, J., Anderson, L., Backman, J., Björk, G., Cronin, T. M., Kirchner, N., Koshurnikov, A., Mayer, L., Noormets, R. & O'Regan, M. 2016: Evidence for an ice shelf covering the central Arctic Ocean during the penultimate glaciation. *Nature Communications 7*, 10365, https://doi.org/10.1038/ncomms10365.

Jennings, A., Reilly, B., Andrews, J., Hogan, K., Walczak, M., Jakobsson, M., Stoner, J., Mix, A., Nicholls, K. W., O'Regan, M. & Prins, M. A. 2022: Modern and early Holocene ice shelf sediment facies from Petermann Fjord and northern Nares Strait, northwest Greenland. *Quaternary Science Reviews 283*, 107460, https://doi.org/10.1016/j.quascirev.2022.107460.

Joe, Y. J., Polyak, L., Schreck, M., Niessen, F., Yoon, S. H., Kong, G. S. & Nam, S. I. 2020: Late Quaternary depositional and glacial history of the Arliss Plateau off the East Siberian margin in the western Arctic Ocean. *Quaternary Science Reviews 228*, 106099, https://doi.org/10.1016/j.quascirev.2019.106099.

Kageyama, M., Harrison, S. P., Kapsch, M. L., Lofverstrom, M., Lora, J. M., Mikolajewicz, U., Sherriff-Tadano, S., Vadsaria, T., Abe-Ouchi, A., Bouttes, N. & Chandan, D. 2021: The PMIP4 Last Glacial Maximum experiments: preliminary results and comparison with the PMIP3 simulations. *Climate of the Past 17*, 1065–1089.

Kim, S., Polyak, L., Joe, Y. J., Niessen, F., Kim, H. J., Choi, Y., Kang, S. G., Hong, J. K., Nam, S. I. & Jin, Y. K. 2021: Seismostratigraphic and geomorphic evidence for the glacial history of the northwestern Chukchi margin, Arctic Ocean. *Journal of Geophysical Research: Earth Surface 126*, e2020JF006030, https://doi.org/10.1029/2020JF006030.

Kleman, J. & Applegate, P. J. 2014: Durations and propagation patterns of ice sheet instability events. *Quaternary Science Reviews 92*, 32–39.

Koo, H., Jin, Y. & Cho, H. 2021: Change in Sediment Provenance on the Inner Slope of the Chukchi Rise and Their Paleoenvironmental Implications. *Applied Sciences 11*, 6491, https://doi.org/10.3390/app11146491.

Kremer, A., Stein, R., Fahl, K., Ji, Z., Yang, Z., Wiers, S., Matthiessen, J., Forwick, M., Löwemark, L., O'Regan, M. & Chen, J. 2018: Changes in sea ice cover and ice sheet extent at the Yermak Plateau during the last 160 ka–Reconstructions from biomarker records. *Quaternary Science Reviews 182*, 93–108.

Le Duc, C. 2018: *Flux sédimentaires le long de la ride de Lomonosov, Ocean Arctique*. Mémoire MSc, UQAM, 49 pp.

Lisitzin, A. P. 2002: *Sea-ice and Iceberg Sedimentation in the Ocean: Recent and Past*. 563 pp. Springer-Verlag, Berlin.

Liu, J., Shi, X., Liu, Y., Liu, Q., Liu, Y., Zhang, Q., Ge, S. & Li, J. 2019: A thick negative polarity anomaly in a sediment core from the central arctic ocean: geomagnetic excursion versus reversal. *Journal of Geophysical Research: Solid Earth 124*, 10687–10703, https://doi.org/10.1029/2019JB018073.

Macdonald, R. W. & Gobeil, C. 2012: Manganese sources and sinks in the Arctic Ocean with reference to periodic enrichments in basin sediments. *Aquatic Geochemistry 18*, 565–591.

McManus, J., Berelson, W. M., Klinkhammer, G. P., Hammond, D. E. & Holm, C. 2005: Authigenic uranium: relationship to oxygen penetration depth and organic carbon rain. *Geochimica et Cosmochimica Acta 69*, 95–108.

Miller, G. H., Alley, R. B., Brigham-Grette, J., Fitzpatrick, J. J., Polyak, L., Serreze, M. C. & White, J. W. 2010: Arctic amplification: can the past constrain the future?. *Quaternary Science Reviews 29*, 1779–1790.

Niessen, F., Hong, J. K., Hegewald, A., Matthiessen, J., Stein, R., Kim, H., Kim, S., Jensen, L., Jokat, W., Nam, S. I. & Kang, S. H. 2013: Repeated Pleistocene glaciation of the East Siberian continental margin. *Nature Geoscience 6*, 842–846, https://doi.org/10.1038/ngeo1904.

Nørgaard, J., Margold, M., Jansen, J. D., Kurbanov, R., Szuman, I., Andersen, J. L., Olsen, J., Knudsen, M. F. 2023: Absence of large-scale ice masses in central Northeast Siberia during the Late Pleistocene. *Geophysical Research Letters 50*, e2023GL103594, https://doi.org/10.1029/2023GL103594.

Nørgaard-Pedersen, N., Mikkelsen, N. & Kristoffersen, Y. 2007: Arctic Ocean record of last two glacial-interglacial cycles off North Greenland/Ellesmere Island—Implications for glacial history. *Marine Geology 244*, 93–108.

Not, C., Brown, K., Ghaleb, B. & Hillaire-Marcel, C. 2012: Conservative behavior of uranium vs. salinity in Arctic sea ice and brine. *Marine Chemistry 130*, 33–39.

Not, C. & Hillaire-Marcel, C. 2010: Time constraints from ^{230}Th and ^{231}Pa data in late Quaternary, low sedimentation rate sequences from the Arctic Ocean: an example from the northern Mendeleev Ridge. *Quaternary Science Reviews 29*, 3665–3675.

Not, C. & Hillaire-Marcel, C. 2012: Enhanced sea-ice export from the Arctic during the Younger Dryas. *Nature Communications 3*, 647, https://doi.org/10.1038/ncomms1658.

Not, C., Hillaire-Marcel, C., Ghaleb, B., Polyak, L. & Darby, D. 2008: ^{210}Pb–^{226}Ra–^{230}Th systematics in very low sedimentation rate sediments from the Mendeleev Ridge (Arctic Ocean). *Canadian Journal of Earth Sciences 45*, 1207–1219.

O'Regan, M., Backman, J., Barrientos, N., Cronin, T. M., Gemery, L., Kirchner, N., Mayer, L. A., Nilsson, J., Noormets, R., Pearce, C. & Semiletov, I. 2017: The De Long Trough: a newly discovered glacial trough on the East Siberian continental margin. *Climate of the Past 13*, 1269–1284.

Park, K., Ohkushi, K. I., Cho, H. G. & Khim, B. K. 2017: Lithostratigraphy and paleoceanography in the Chukchi Rise of the western Arctic Ocean since the last glacial period. *Polar Science 11*, 42–53.

Park, K., Wang, R., Xiao, W., Polyak, L., Cho, H. G. & Khim, B. K. 2022: Increased Terrigenous Input from North America to the Northern Mendeleev Ridge (Western Arctic Ocean) Since the Mid-Brunhes Event. *Scientific reports 12*, 15189, https://doi.org/10.1038/s41598-022-19082-y.

Polyak, L., Alley, R. B., Andrews, J. T., Brigham-Grette, J., Cronin, T. M., Darby, D. A., Dyke, A. S., Fitzpatrick, J. J., Funder, S., Holland, M. & Jennings, A. E. 2010: History of sea ice in the Arctic. *Quaternary Science Reviews 29*, 1757–1778.

Polyak, L., Bischof, J., Ortiz, J. D., Darby, D. A., Channell, J. E., Xuan, C., Kaufman, D. S., Løvlie, R., Schneider, D. A., Eberl, D. D. & Adler, R. E. 2009: Late Quaternary stratigraphy and sedimentation patterns in the western Arctic Ocean. *Global and Planetary Change 68*, 5–17.

Polyak, L., Curry, W. B., Darby, D. A., Bischof, J. & Cronin, T. M. 2004: Contrasting glacial/interglacial regimes in the western Arctic Ocean as exemplified by a sedimentary record from the Mendeleev Ridge. *Palaeogeography, Palaeoclimatology, Palaeoecology 203*, 73–93.

Polyak, L., Edwards, M. H., Coakley, B. J. & Jakobsson, M. 2001: Ice shelves in the Pleistocene Arctic Ocean inferred from glaciogenic deep-sea bedforms. *Nature 410*, 453–457.

Polyak, L. & Jakobsson, M. 2011: Quaternary sedimentation in the Arctic Ocean: Recent advances and further challenges. *Oceanography 24*, 52–64.

Purcell, K., Hillaire-Marcel, C., de Vernal, A., Ghaleb, B. & Stein, R. 2022: Potential and limitation of ^{230}Th-excess as a chronostratigraphic tool for late Quaternary Arctic Ocean sediment studies: An example from the Southern Lomonosov Ridge. *Marine Geology 448*, 106802, https://doi.org/10.1016/j.margeo.2022.106802.

Reilly, B. T., Natter Jr, C. J. & Brachfeld, S. A. 2016: Holocene glacial activity in Barilari Bay, west Antarctic Peninsula, tracked by magnetic mineral assemblages: L inking ice, ocean, and atmosphere. *Geochemistry, Geophysics, Geosystems 17*, 4553–4565.

Reimnitz, E., Kempema, E. W. & Barnes, P. W. 1987: Anchor ice, seabed freezing, and sediment dynamics in shallow Arctic seas. *Journal of Geophysical Research: Oceans 92*, 14671–14678.

Rogalla, B., Allen, S. E., Colombo, M., Myers, P. G. & Orians, K. J. 2022: Sediments in sea ice drive the Canada Basin surface Mn maximum: insights from an Arctic Mn ocean model. *Global Biogeochemical Cycles 36*, e2022GB007320, https://doi.org/10.1029/2022GB007320.

Schreck, M., Nam, S. I., Polyak, L., Vogt, C., Kong, G. S., Stein, R., Matthiessen, J. & Niessen, F. 2018: Improved Pleistocene sediment stratigraphy and paleoenvironmental implications for the western Arctic Ocean off the East Siberian and Chukchi margins. *arktos 4*, 21, https://doi.org/10.1007/s41063-018-0057-8.

Schubert, C. J. & Calvert, S. E. 2001: Nitrogen and carbon isotopic composition of marine and terrestrial organic matter in Arctic Ocean sediments: implications for nutrient utilization and organic matter composition. *Deep Sea Research Part I: Oceanographic Research Papers 48*, 789–810.

Schulz, K., Büttner, S., Rogge, A., Janout, M., Hölemann, J. & Rippeth, T. P. 2021: Turbulent mixing and the formation of an intermediate nepheloid layer above the Siberian continental shelf break. *Geophysical Research Letters 48*, e2021GL092988, https://doi.org/10.1029/2021GL092988.

Sher, A. 1995: Is there any real evidence for a huge shelf ice sheet in East Siberia?. *Quaternary International 28*, 39–40.

Siddall, M., Rohling, E. J., Thompson, W. G. & Waelbroeck, C. 2008: Marine isotope stage 3 sea level fluctuations: Data synthesis and new outlook. *Reviews of Geophysics 46*, RG4003, https://doi.org/10.1029/2007RG000226.

Song, T., Hillaire-Marcel, C., de Vernal, A., Liu, Y., Wang, W. & Huang, Y. 2022: A reassessment of Nd-isotopes and clay minerals as tracers of the Holocene Pacific water flux through Bering Strait. *Marine Geology 443*, 106698, https://doi.org/10.1016/j.margeo.2021.106698.

Spielhagen, R. F., Baumann, K. H., Erlenkeuser, H., Nowaczyk, N. R., Nørgaard-Pedersen, N., Vogt, C. & Weiel, D. 2004: Arctic Ocean deep-sea record of northern Eurasian ice sheet history. *Quaternary Science Reviews 23*, 1455–1483.

Spielhagen, R. F., Bonani, G., Eisenhauer, A., Frank, M., Frederichs, T., Kassens, H., Kubik, P. W., Mangini, A., Nøgaard Pedersen, N., Nowaczyk, N. R. & Schäper, S. 1997: Arctic Ocean evidence for late Quaternary initiation of northern Eurasian ice sheets. *Geology 25*, 783–786.

Strobl, C. 1998: *Datierung von Sedimentkernen und Rekonstruktion der Transportwege der Radionuklide ^{10}Be, ^{230}Th und ^{231}Pa in hohen nördlichen Breiten*. Ph.D. thesis, *PhD dissertation*, Universität Heidelberg, 183 pp.

Stein, R. 2008: Arctic Ocean sediments: processes, proxies, and paleoenvironment. *In* Chamley, H. (eds.): *Developments in Marine Geology*, 142–146. Elsevier, Oxford.

Stein, R., Fahl, K., Gierz, P., Niessen, F. & Lohmann, G. 2017: Arctic Ocean sea ice cover during the penultimate glacial and the last interglacial. *Nature communications 8*, 373, https://doi.org/10.1038/s41467-017-00552-1.

Sundby, B., Lecroart, P., Anschutz, P., Katsev, S. & Mucci, A. 2015: When deep diagenesis in Arctic Ocean sediments compromises manganese-based geochronology. *Marine Geology 366*, 62–68.

Swärd, H., Andersson, P., Hilton, R., Vogt, C. & O'Regan, M. 2022: Mineral and isotopic (Nd, Sr) signature of fine-grained deglacial and Holocene sediments from the Mackenzie Trough, Arctic Canada. *Arctic, Antarctic, and Alpine Research 54*, 346–367.

Thierstein, H. R., Geitzenauer, K. R., Molfino, B. & Shackleton, N. J. 1977: Global synchroneity of late Quaternary coccolith datum levels: validation by oxygen isotopes. *Geology 5*, 400–404.

Thomson, W. 1888: Polar Ice-caps and their Influence in Changing Sea Levels. *Transactions of the Geological Society of Glasgow 8*, 322–340.

Tzevahirtzian, A., Caruso, A., Andreetto, F., Bonomo, S. & Krijgsman, W. 2023: A bio-chronostratigraphic study of the upper Miocene from the northern Caltanissetta Basin, Sicily (core 3AGN2S04). Implications for dating the Messinian Salinity Crisis onset. *Sedimentary Geology 445*, 106330, https://doi.org/10.1016/j.sedgeo.2023.106330.

Tziperman, E. & Gildor, H. 2003: On the mid-Pleistocene transition to 100-kyr glacial cycles and the asymmetry between glaciation and deglaciation times. *Paleoceanography 18*, 1001, https://doi.org/10.1029/2001pa000627.

Viscosi-Shirley, C., Mammone, K., Pisias, N. & Dymond, J. 2003: Clay mineralogy and multi- element chemistry of surface sediments on the Siberian-Arctic shelf: implications for sediment provenance and grain size sorting. *Continental Shelf Research 23*, 1175–1200.

Vogt, C. 1997: *Zeitliche und räumliche Verteilung von Mineralvergesellschaftungen in spätquartären Sedimenten des Arktischen Ozeans und ihre Nützlichkeit als Klimaindikatoren während der Glazial/Interglazial-Wechsel*. Berichte zur Polarforschung, AWI, Bremerhaven, 251 pp.

Wahsner, M., Müller, C., Stein, R., Ivanov, G., Levitan, M., Shelekhova, E. & Tarasov, G. 1999: Clay-mineral distribution in surface sediments of the Eurasian Arctic Ocean and continental margin as indicator for source areas and transport pathways—A synthesis. *Boreas 28*, 215–233.

Wall, J. D. & Krumholz, L. R. 2006: Uranium reduction. *Annual review of microbiology 60*, 149–166.

Wang, R., Polyak, L., Zhang, W., Yu, X., Ye, L., Dong, L., Liu, Y., Wang, W. & Diekmann, B. 2021: Glacial-interglacial sedimentation and paleocirculation at the Northwind Ridge, western Arctic Ocean. *Quaternary Science Reviews 258*, 106882, https://doi.org/10.1016/j.quascirev.2021.106882.

Watanabe, E., Onodera, J., Itoh, M. & Mizobata, K. 2022: Transport processes of seafloor sediment from the Chukchi shelf to the western Arctic basin. *Journal of Geophysical Research: Oceans 127*, e2021JC017958, https://doi.org/10.1029/2021JC017958.

Wetterich, S., Tumskoy, V., Rudaya, N., Kuznetsov, V., Maksimov, F., Opel, T., Meyer, H., Andreev, A. A. & Schirrmeister, L. 2016: Ice complex permafrost of MIS5 age in the Dmitry Laptev Strait coastal region (East Siberian Arctic). *Quaternary Science Reviews 147*, 298–311.

Wiers, S., Snowball, I., O'Regan, M., Pearce, C. & Almqvist, B. 2020: The Arctic Ocean Manganese Cycle, an Overlooked Mechanism in the Anomalous Palaeomagnetic Sedimentary Record. *Frontiers in Earth Science 8*, 75, https://doi.org/10.3389/feart.2020.00075.

Xiang, Y. & Lam, P. J. 2020: Size-Fractionated Compositions of Marine Suspended Particles in the Western Arctic Ocean: Lateral and Vertical Sources. *Journal of Geophysical Research: Oceans 125*, e2020JC016144, https://doi.org/10.1029/2020JC016144.

Xiao, W., Polyak, L., Wang, R., Löwemark, L., Mei, J., You, D., Wang, W., Wu, L. & Jin, X. 2020: Middle to Late Pleistocene Arctic paleoceanographic changes based on sedimentary records from Mendeleev Ridge and Makarov Basin. *Quaternary Science Reviews 228*, 106105, https://doi.org/10.1016/j.quascirev.2019.106105.

Xu, Q., Xiao, W., Wang, R., Süfke, F., Lippold, J. & Not, C. 2021: Driving Mechanisms of Sedimentary ^{230}Th and ^{231}Pa Variability in the Western Arctic Ocean Through the Last Glacial Cycle. *Paleoceanography and Paleoclimatology 36*, e2020PA004039, https://doi.org/10.1029/2020PA004039.

Xuan, C. & Channell, J. E. T. 2010: Origin of apparent magnetic excursions in deep‐sea sediments from Mendeleev‐Alpha Ridge, Arctic Ocean. *Geochemistry, Geophysics, Geosystems 11*, Q02003, https://doi.org/10.1029/2009GC002879.

Ye, L., Zhang, W., Wang, R., Yu, X. & Jin, L. 2020: Ice events along the East Siberian continental margin during the last two glaciations: Evidence from clay minerals. *Marine Geology 428*, 106289, https://doi.org/10.1016/j.margeo.2020.106289.

Zamelczyk, K., Fransson, A., Chierici, M., Jones, E., Meilland, J., Anglada-Ortiz, G. & Hodal Lødemel, H. 2021: Distribution and abundances of planktic foraminifera and shelled pteropods during the polar night in the sea-ice covered northern Barents Sea. *Frontiers in Marine Science 8*, 644094, https://doi.org/10.3389/fmars.2021.644094.

Zhao, S., Liu, Y., Dong, L., Shi, X., Polyak, L., Zou, X., Wang, W. & Wu, D. 2022: Sedimentary record of glacial impacts and meltwater discharge off the East Siberian Continental Margin, Arctic Ocean. *Journal of Geophysical Research: Oceans 127*, e2021JC0176, https://doi.org/10.1029/2021JC017650.

Table 2.1 Radiocarbon ages of core E25. The ^{14}C ages are uncalibrated as they are in part mixed between populations of distinct ages (see Hillaire-Marcel et al., 2022a).

Interval (cm)	Depth (cm)	Material	Conventional age (year)	error (±2σ)	Source
0–1	0.5	Fish otolith	3277	76	This study
2–3	2.5	Planktonic Foraminifer	6578	29	This study
6–8	7	Planktonic Foraminifer	8670	30	Zhao et al. (2022)
18–20	19	Planktonic Foraminifer	12540	40	Zhao et al. (2022)
24–26	25	Planktonic Foraminifer	34500	260	Zhao et al. (2022)

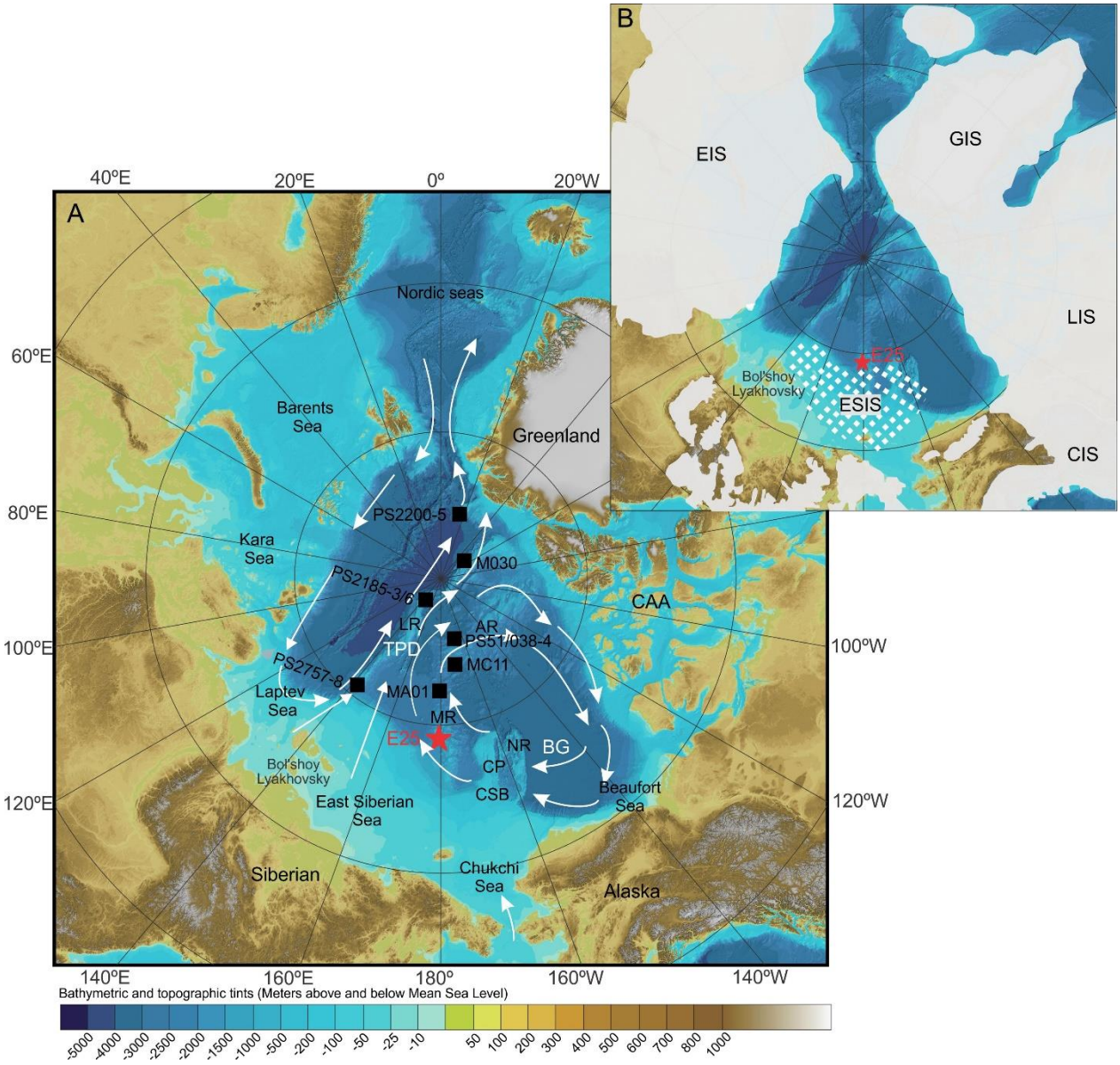

Figure 2-1 Bathymetric map of the Arctic Ocean. A) Ocean circulation and site location. The white arrows: surface circulation paths; red star: the location of the study core E25; black squares: other sites mentioned in the text (from Vogt, 1997; Strobl, 1998; Behreds et al., 1999; Not and Hillaire-Marcel, 2010; Hillaire-Marcel et al., 2017; Geibert et al., 2021; Xu et al., 2021; Purcell et al., 2022); B) The ice sheet/ice shelf extents. The shadow area represents the maximum ice sheet-covered areas during glaciations, as simulated by Batchelor et al. (2019); the red star: location of core E25; AR: Alpha Ridge; BG: Beaufort Gyre; CAA: Canadian Arctic Archipelago; CIS: Cordilleran Ice Sheet; CP: Chukchi Plateau; CSB: Chukchi Sea Borderland; EIS: Eurasian Ice Sheet; ESIS: the hypothesized location of the East Siberian Ice Shelf/Ice Sheet; GIS: Greenland Ice Sheet; LIS: Laurentide Ice Sheet; LR: Lomonosov Ridge; MR: Mendeleev Ridge; NR: Northwind Ridge; TPD: Transpolar Drift.

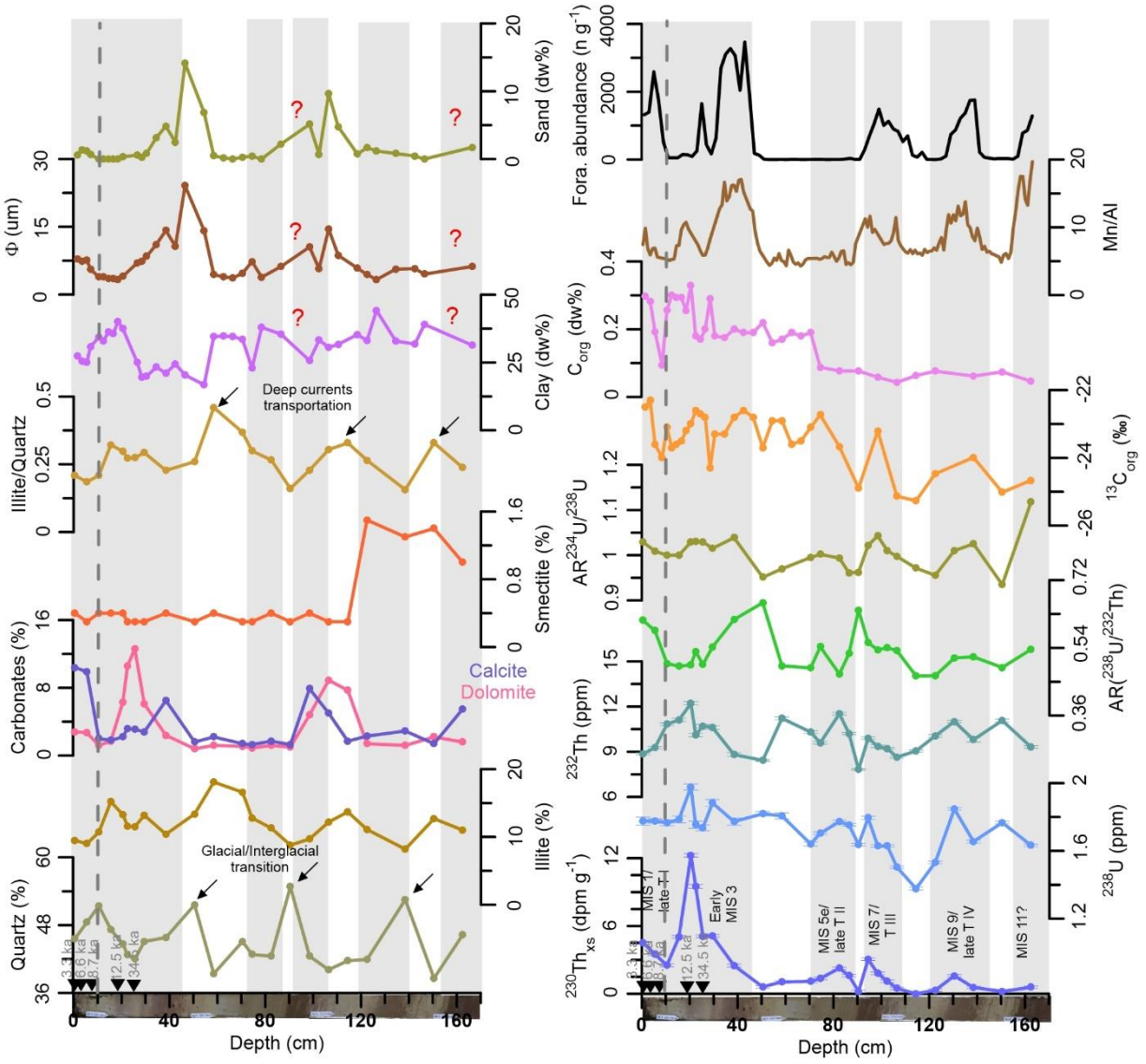

Figure 2-2 Major sedimentological, mineralogical (left), and geochemical (right) features of the 0 to ~167 cm section of core E25 (see Tables in the ANNEXE B Supplementary Material for details). The dashed dark grey lines correspond to the Last Glacial Maximum (LGM) sedimentary gap (see text); light grey shadows highlight layers assigned to early/middle interglacial/interstadial (odd MIS numbers) or late Termination (T) intervals; red question marks point to intervals of insufficient sedimentological data. Photos of the studied core section, Mn/Al ratio and foraminifer abundance are from Zhao et al., (2022); all other measurements are from the present study.

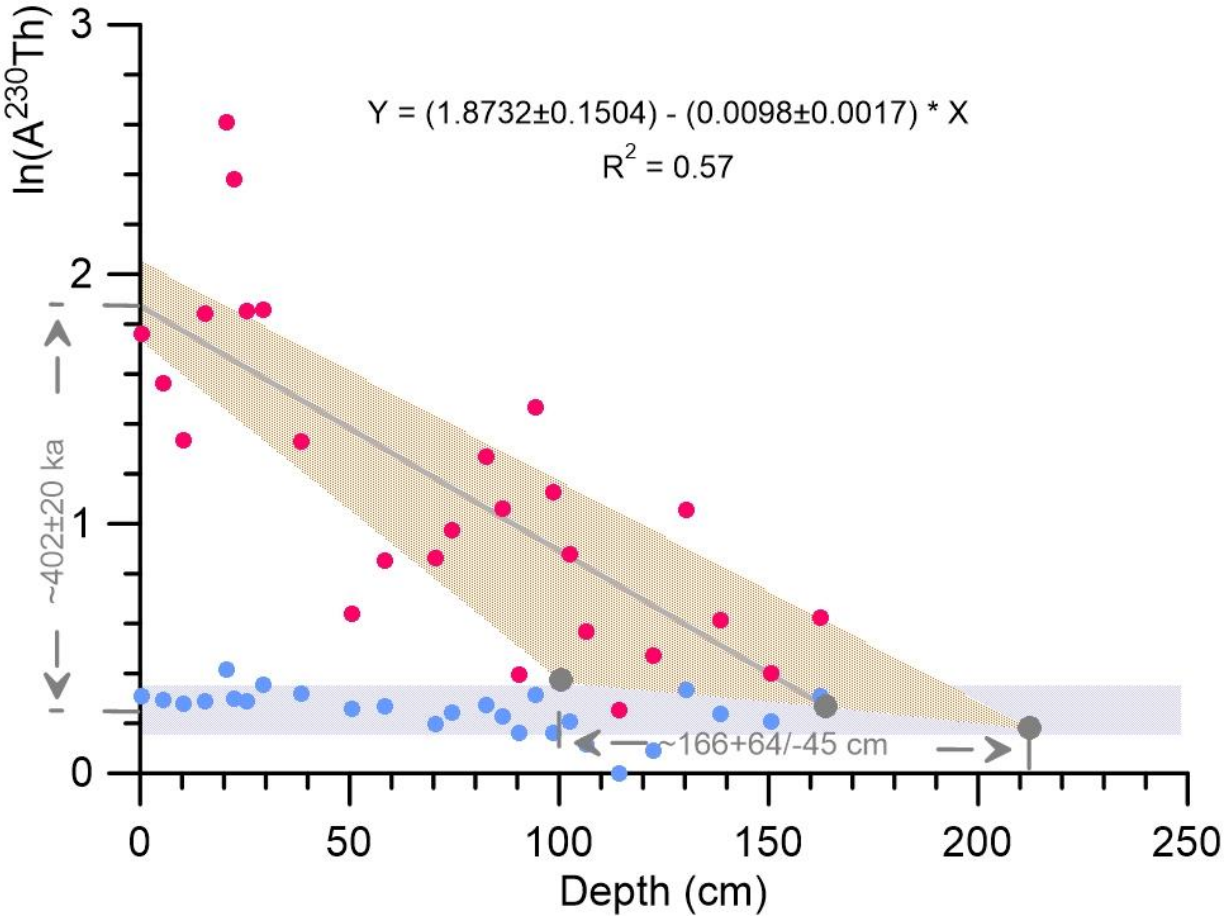

Figure 2-3 Linear correlation of ln($A^{230}Th$) value vs core depth. Blue dots: ln($A^{234}U$); light blue area: the uncertainty envelopes are ±1σ; red dots: ln($A^{230}Th$). The intercept of ln($A^{230}Th$) vs ln($A^{234}U$) corresponds to a $^{230}Th_{xs}$ extinction age of 402 ± 20 ka, reached at a depth of 166 + 64/- 45 cm.

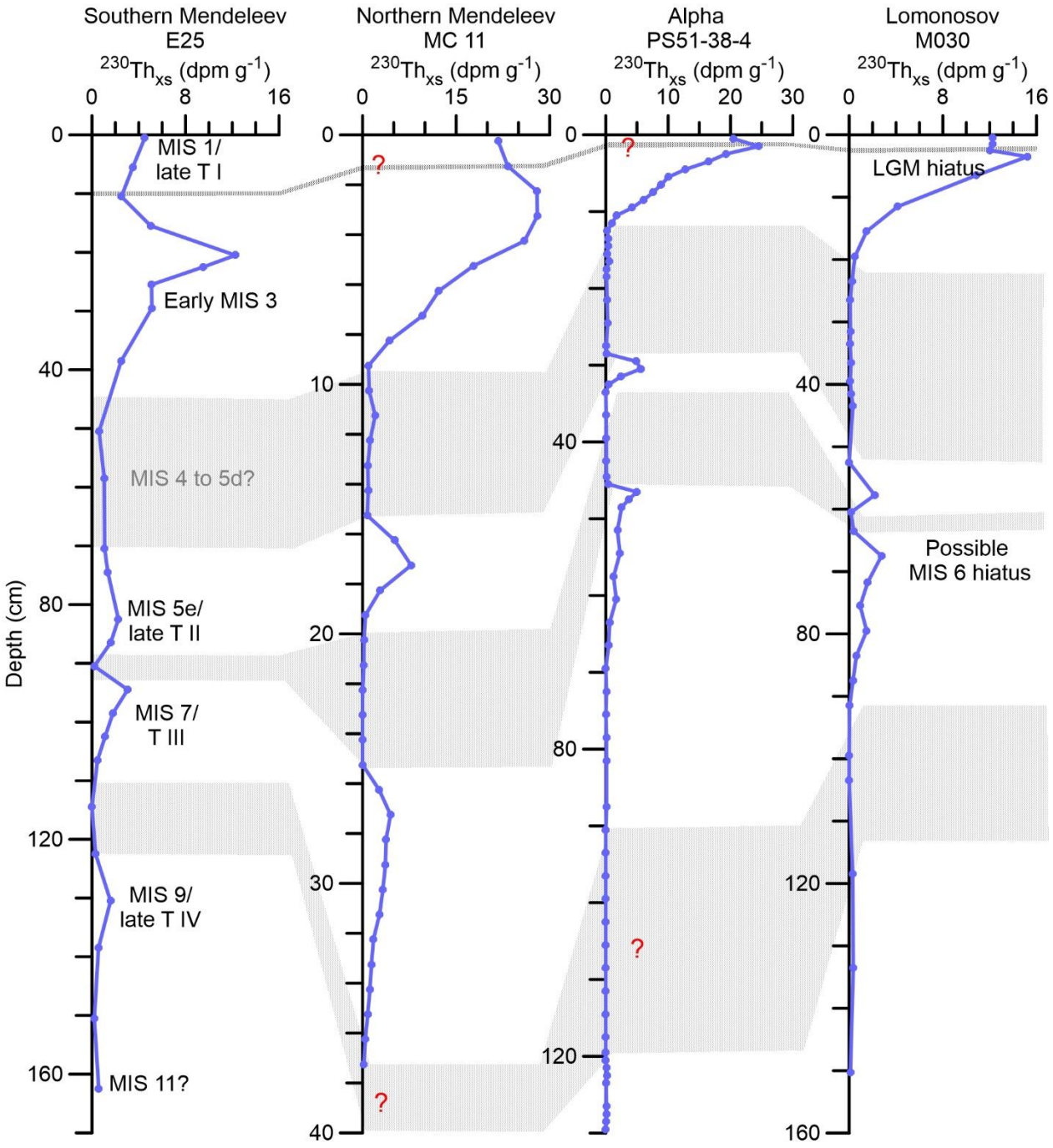

Figure 2-4 $^{230}Th_{xs}$ distributions in a few sites from the Arctic Ocean ridges. The grey shadow area: sedimentations during glacials, including the LGM and possible MIS 6 hiatuses; red question marks: equivocal depth of LGM hiatus and interval of MIS 8. The raw U-Th series data are from the present study (E25), Not and Hillaire-Marcel (2010) for MC11, Hillaire-Marcel et al. (2017) for M030, and Geibert et al. (2021) for PS51/038-4.

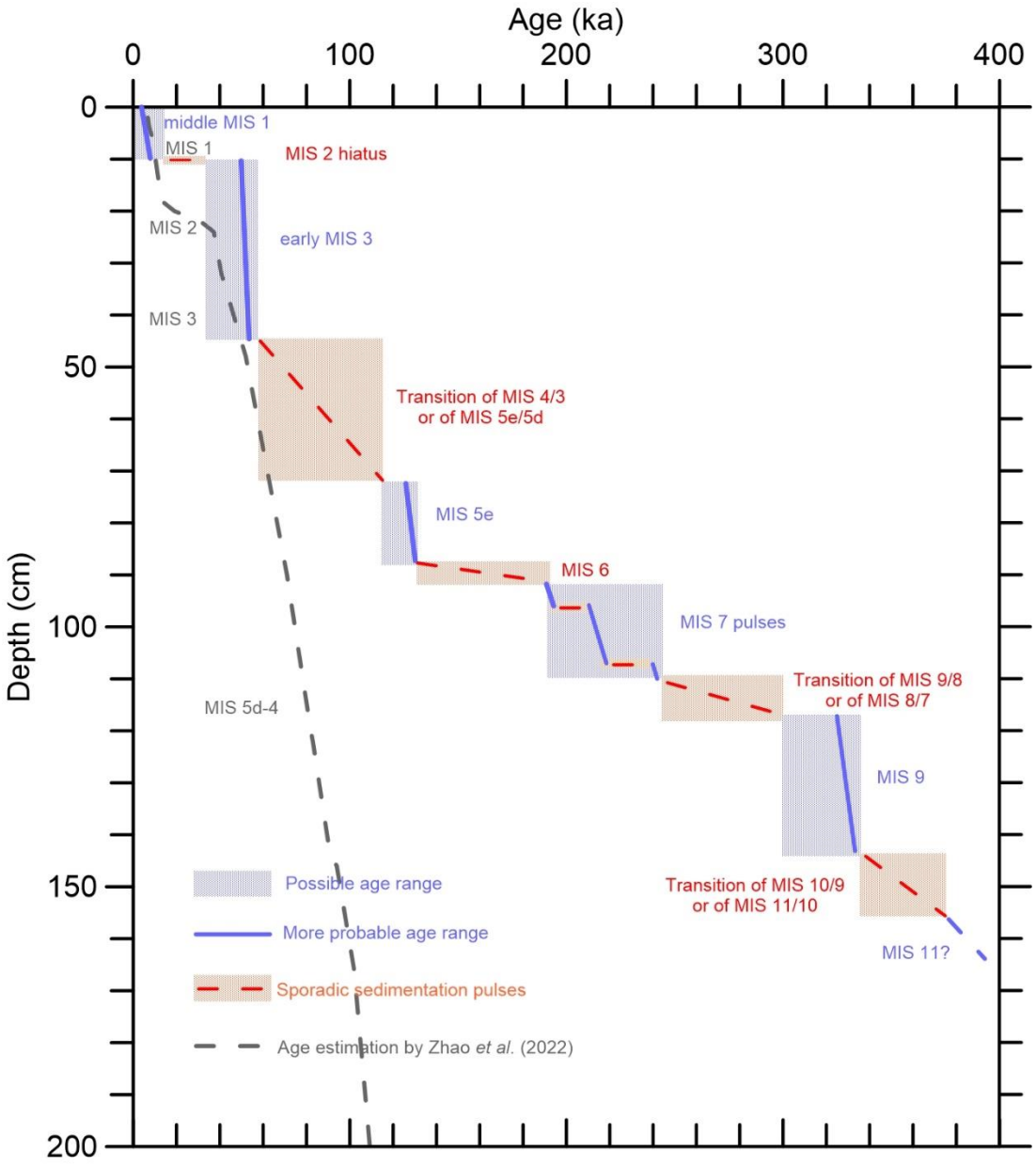

Figure 2-5 Outline of a tentative chronostratigraphy in core E25 based on 230Thxs distribution. The effective duration of sedimentary pulses is open to discussion, but probable sedimentary windows are indicated by thick lines, blue for sea-ice rafting deposition during "warm" intervals (i.e., with a high sea-level/high insolation for sea-ice rafting deposition; see text), and red dashed, for sediments deposited during late or early transitions. Grey dashed line: chronostratigraphy proposed by Zhao et al. (2022) using the Mn-based cyclostratigraphy. Shadow areas mark the maximum duration of the intervals. deposition; see text), and red dashed, for sediments deposited during late or early transitions. Shadow areas mark the maximum duration of the intervals.

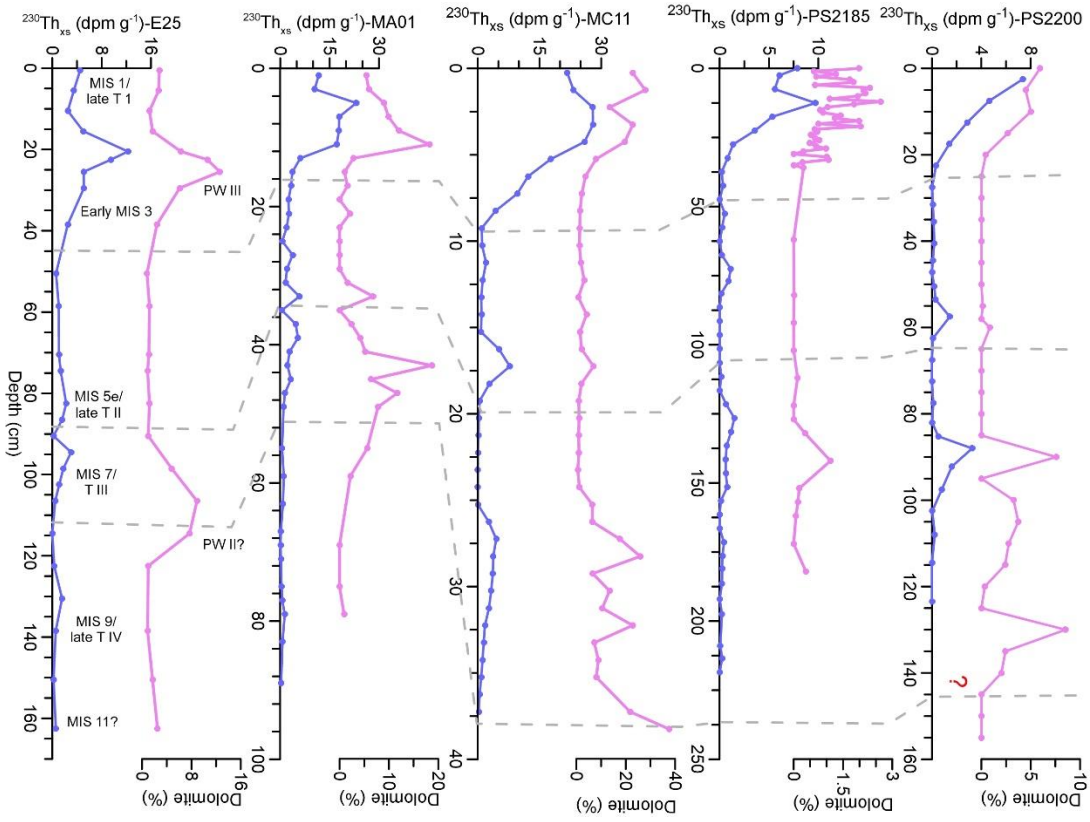

Figure 2-6 Dolomite content distributions in the Arctic Ocean using the $^{230}Th_{xs}$-based chronostratigraphy. Core MA01: from Xu et al., (2021); core MC11: from Not and Hillaire-Marcel (2010); cores PS2185-3/6 and PS2200-5: from Vogt, 1977; Strobl, 1998, Behrends, 1999. Dash lines correspond to the inception of MIS 7/T III, 5e/late T II, and 3, respectively. The age model of core MA01 was revised here based on the $^{230}Th_{xs}$ extinction age using our method (see ANNEXE B Supplementary Material Fig. S4). The re-interpretation of $^{230}Th_{xs}$ profiles of cores PS2185-3/6 and PS2200-5 was according to Not and Hillaire-Marcel (2010) and Geibert et al. (2021). The assignment of the bottom depth of the MIS 7/T III layer in core PS2200-5 was based on the ^{10}Be profile (Strobl, 1998).

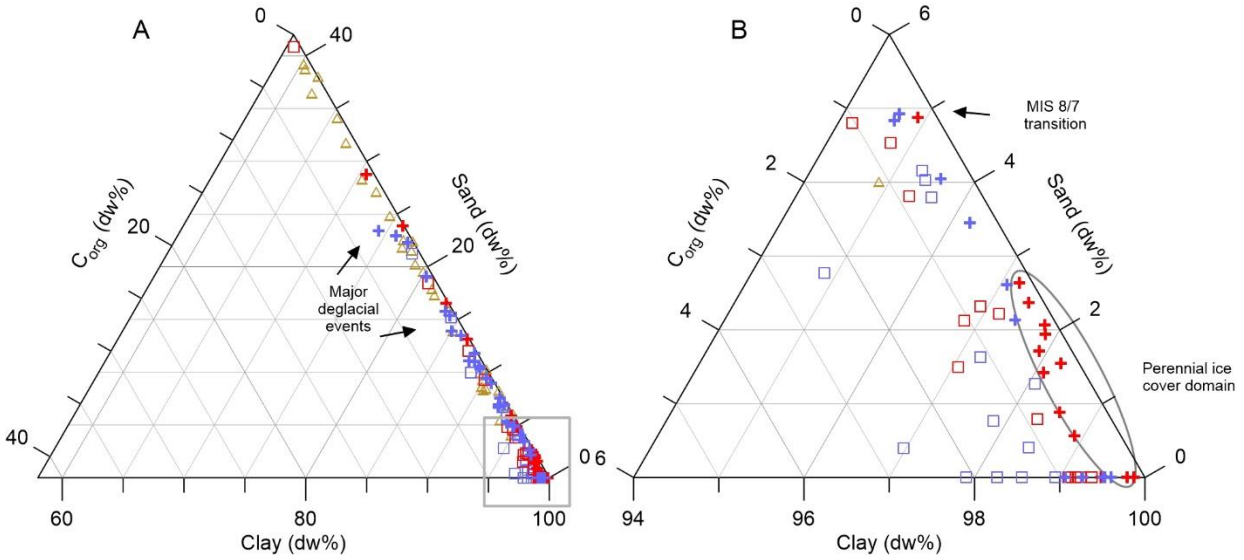

Figure 2-7 Ternary analysis of clay, sand, and C_{org} contents in cores from the Mendeleev Ridge area (A) and zoom-in on the perennial ice cover cluster (B). These three components were plotted as relative percentages. Red: data from the study core E25; blue: data from core MA01 (Xu et al., 2021; Park et al. 2022); olive: data from core MC11 (Not and Hillaire-Marcel, 2010). For site E25, the perennial and thick ice cover (resilient ESIS) domain includes data from MIS 11 to MIS 4 (cross symbols), MIS 8/7 transition excluded, whereas data from the MIS 4/3 transition to the present (square symbols) and MIS 8/7 fall into the seasonal sea-ice domain. It seems that perennial and thick ice extended northward to the area of site MA01 during MIS 6 and 5d–4.

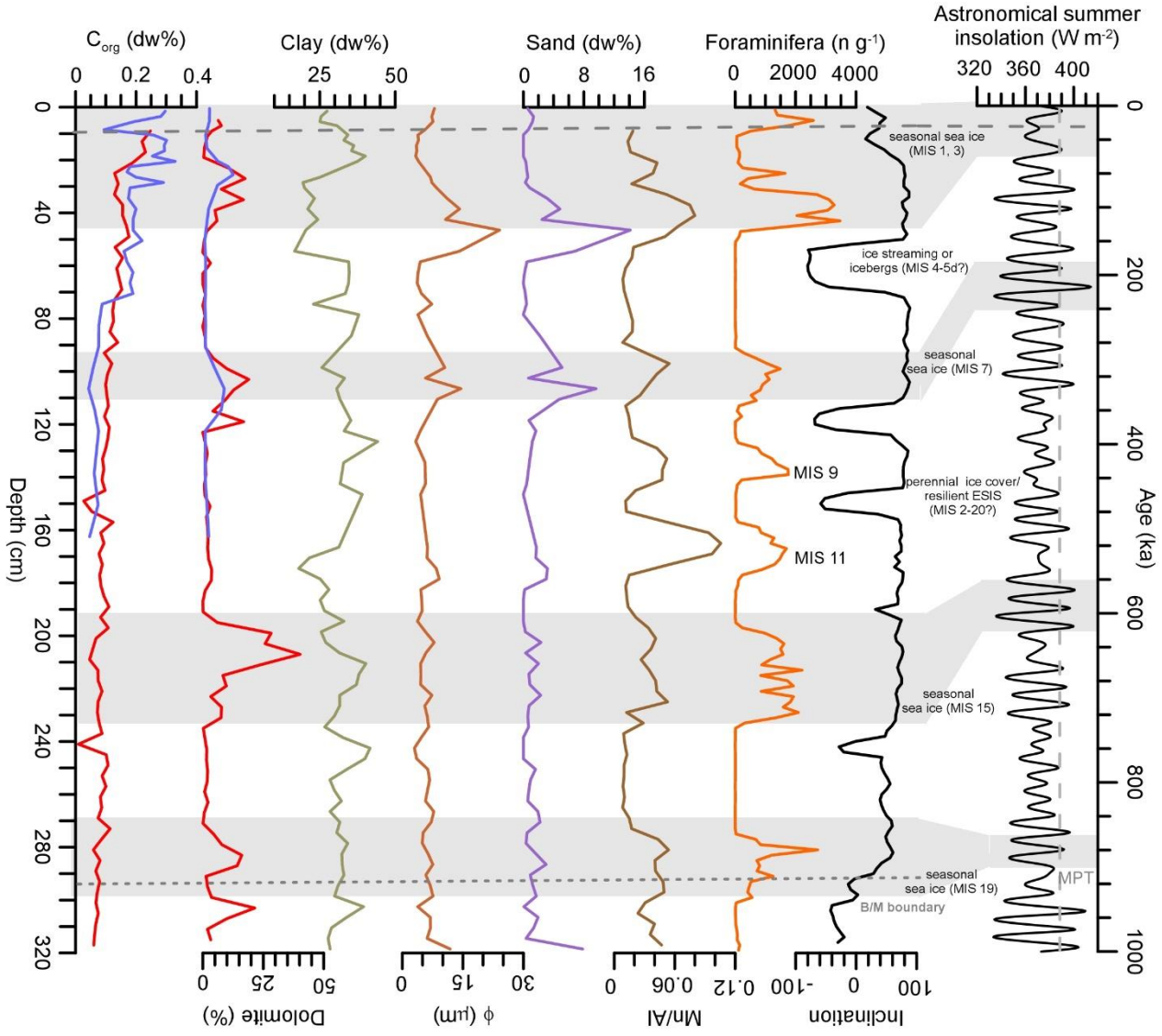

Figure 2-8 Sedimentology, geochemistry, foraminifer abundance, and magnetic inclination profiles in core E25 (C_{org}: personal communication of Zhao; other data: Zhao et al., 2022). Vertical dashed line: mean summer insolation at the middle Holocene Thermal Maximum; upper horizontal dashed line: LGM hiatus; lower horizontal dotted line: our interpretation of the Brunhes/Matuyama reversal boundary in the core. Excursions in the Brunhes epoch are interpreted here in relation to redox-driven diagenetic processes at the edge of Mn-rich layers (see Xuan and Channel, 2010; Wiers et al., 2020). Light grey shadowed layers correspond to interglacial/interstadials and/or late Ts likely covered by seasonal sea ice.

CHAPITRE 3

Cycling and behavior of ^{230}Th in the Arctic Ocean: Insights from sedimentary archives

Tengfei Song[1*], Claude Hillaire-Marcel[1], Yanguang Liu[2,3], Bassam Ghaleb[1], Anne de Vernal[1]

1 Geotop, Université du Québec à Montréal, C.P. 8888, Montréal, QC H3C 3P8, Canada;
2 Key Laboratory of Marine Geology and Metallogeny, First Institute of Oceanography, Ministry of Natural Resources, Qingdao 266061, China;
3 Laboratory for Marine Geology, Pilot National Laboratory for Marine Science and Technology, Qingdao 266061, China;

The article was in 2023 in the Journal of *Earth-Science Reviews*, https://doi.org/10.1016/j.earscirev.2023.104514.

Abstract

Some studies have used excesses of ^{230}Th ($^{230}Th_{xs}$) in marine cores from low sedimentation rate sites for the setting of a late Pleistocene stratigraphy, but the temporal and spatial variability of $^{230}Th_{xs}$ fluxes in the Arctic Ocean remains poorly understood. In this paper, we review all available ^{230}Th data from the Arctic Ocean to document the regional $^{230}Th_{xs}$ behavior within the geological time frame of the latest glacial/interglacial cycles. We evaluate the potential roles of bathymetry, sedimentological regimes, and geochemical properties of the sediment in relation to $^{230}Th_{xs}$ fluxes. The $^{230}Th_{xs}$ inventories in the sediment accumulated since the Last Glacial Maximum suggest that $^{230}Th_{xs}$ fluxes are linked to the sea-ice regime, brine production rate and sinking, organic carbon fluxes, ice-rafting pathways, seawater exchange between the Arctic, Atlantic, and Pacific oceans, nepheloid transportation, and possibly other unidentified factors. During "warm" intervals, the development of "ice factories" over shelves and enhanced detrital and organic matter fluxes related to high sea levels and high summer insolation conditions constitute major parameters governing $^{230}Th_{xs}$-records. During glacials, under a perennial ice cover or ice shelf, $^{230}Th_{xs}$ was partly exported through Fram Strait into the Nordic Seas, and possibly partly built up in the water column, depending on the ventilation rate of the deep-water masses. At the sea floor over slopes and ridges, the winnowing of fine fractions and brines-related compounds by deep currents leads to post-sedimentary redistributions of $^{230}Th_{xs}$. These features do not invalidate chronostratigraphic inferences

made using $^{230}Th_{xs}$-records in sediments but shed light on their use and limitations. Sedimentary profiles of $^{230}Th_{xs}$ allow the identification of interglacial-interstadial and glacial stages in low sedimentation rate settings. This remains valid for sediments encompassing from recent to Marine Isotope Stage 11 (MIS 11), with some reservations depending on the sedimentary characteristics of the site considered. The $^{230}Th_{xs}$ records have been initially proposed for the setting of an "extinction age" assigned to the final decay of the excess within the one-sigma uncertainty of its estimate. We show here that this extinction ages may vary between ~200 to ~420 kyr, mostly depending on the site-specific relationship between ^{230}Th deposition and sedimentary regime, and on any potential post-depositional effects, which may include redox-driven U mobility and $^{230}Th_{xs}$ losses linked to fine sediment fractions winnowing.

3.1 Introduction

Thorium-230 (^{230}Th) produced by dissolved and radioactive uranium (U) in the water column and accumulated into the sediment as an excess ($^{230}Th_{xs}$) over its fraction carried by detrital minerals, has often been used for normalizing sedimentary fluxes in the global oceans on the basis of a constant ^{230}Th flux model (Francois et al., 2004; Costa et al., 2020). Nonetheless, this constant model is incompatible in the Arctic Ocean mainly because i) ^{230}Th scavenging is highly constrained by the sea ice cover, especially during glacials (e.g., Ku and Broecker, 1965; Huh et al., 1997; Strobl, 1998; Not and Hillaire-Marcel, 2010; Gusev et al., 2013; Hillaire-Marcel et al., 2017; Geibert et al., 2021; Xu et al., 2021; Purcell et al., 2022); ii) boundary scavenging of ^{230}Th may occur in the context of the wide Arctic continental shelf areas (e.g., Edmonds et al., 2004; Valk et al., 2020); iii) potential ^{230}Th export toward the Nordic Seas through Fram Strait (e.g., Moran et al., 2005; Hoffmann et al., 2013; Luo and Lippold, 2015; Hillaire-Marcel et al., 2017; Kipp et al., 2021).

In parallel, some investigations addressed the potential use of $^{230}Th_{xs}$ in sedimentary records for the setting of a chronostratigraphy spanning the late Quaternary, starting with the pioneering work of Ku and Broecker (1965). Peaking values of $^{230}Th_{xs}$ in cored sequences were accordingly assigned to interglacial or interstadial intervals (e.g., Strobl, 1998; Not and Hillaire-Marcel, 2010; Gusev et al., 2013; Hillaire-Marcel et al., 2017; Purcell et al., 2022). In this respect, a striking feature of the $^{230}Th_{xs}$ distribution in sedimentary sequences is the widely observed “subsurface” $^{230}Th_{xs}$ peak (Huh et al., 1997), which was tentatively assigned to the last deglaciation by Hoffmann and McManus (2007), based on ^{14}C-derived chronologies

(Darby et al., 1997; Poore et al., 1999a,b). This peaking "subsurface" $^{230}Th_{xs}$-value is generally higher than that of the surface sample and was thought to be related to sediment focusing due to the rapid sea level rise at the end of the last deglaciation (Hoffmann and McManus, 2007) or some $^{230}Th_{xs}$ intensifications associated with an extremely low sedimentation rate (Geibert et al., 2022). Hoffmann and McManus (2007) concluded that $^{230}Th_{xs}$ sedimentary fluxes, as estimated from ^{14}C-based chronologies, had been in balance with the production of this isotope in the water column (henceforth the "^{230}Th-rain") since the Marine Isotope Stage 3 (MIS 3). In view of recent findings by Hillaire-Marcel et al. (2022a), which invalidates the ^{14}C-derived chronology used by Hoffmann and McManus (2007), this conclusion must now be revised. More recent studies suggest that the "subsurface" $^{230}Th_{xs}$ peak should be assigned to the early MIS 3 (Not and Hillaire-Marcel, 2010; Hillaire-Marcel et al., 2017; Purcell et al., 2022), possibly in relation to some build-up of ^{230}Th in the water column during the preceding MIS 5d–4 interval (Hillaire-Marcel et al., 2022b).

In some of these recent studies, the radioactive decay of $^{230}Th_{xs}$ to values within one sigma uncertainty of its calculation in sedimentary cores, was used for the setting of a "benchmark age" or "extinction age" (Not and Hillaire-Marcel, 2010; Hillaire-Marcel et al., 2017; Purcell et al., 2022). Purcell et al. (2022) also demonstrated that the correlation of $^{230}Th_{xs}$ peaks between marine sequences differing by as much as a factor 5 in their sediment accumulation rate, was sufficiently robust to set a $^{230}Th_{xs}$-based stratigraphy spanning the last few climatic cycles (see also Geibert et al., 2021).

This $^{230}Th_{xs}$-based chronostratigraphy disagrees with chronological schemes based on ecostratigraphic considerations (e.g., Backman et al., 2009) and the Mn-cyclostratigraphy proposed by Jakobsson et al. (2000). This issue falls beyond the scope of the present study, but has been discussed in several recent papers (e.g., Xiao et al., 2021, 2022; Hillaire-Marcel and de Vernal, 2022).

Aside from the above features of ^{230}Th-behaviour in the Arctic Ocean, the mechanism related to the low to near-nil $^{230}Th_{xs}$ accumulation in layers deposited during glacial stages is so far under debate. Geibert et al. (2021) assumed that near-nil $^{230}Th_{xs}$ accumulation resulted from the absence of ^{230}Th production due to the replacement of marine water by U-poor freshwater below a thick ice shelf. This assumption was challenged as several pieces of evidence show that seawater exchange between the Arctic and the Atlantic oceans continued during glacials (Spielhagen et al., 2022) and that the production of ^{230}Th was more certainly reduced but not suspended (Hillaire-Marcel et al., 2022b). Instead, for several other authors, the

very low burial rates of $^{230}Th_{xs}$ during glacial stages would result from a reduced production below thick ice shelves, thus a reduced marine water column, adding to reduced scavenging with the scarce and sporadic accumulation of coarse material during short ice streaming and iceberg-rafting events (Not and Hillaire-Marcel, 2010; Hillaire-Marcel et al., 2017, 2022b; Xu et al., 2021; Purcell et al., 2022).

The above summary of studies about $^{230}Th_{xs}$ in Arctic Ocean marine sequences illustrates that its behavior, in relation to the specific hydrography, ice conditions, and sedimentology features remains insufficiently documented. Some general features of ^{230}Th behavior in the world oceans are well established. The strongly particle-reactive ^{230}Th ensuing from the dissolved ^{234}U decay is rapidly removed from the water column by fine particles (Bacon and Anderson, 1982). In the central Arctic Ocean, where aeolian dust flux is low (cf. Stein, 2008), terrestrial and marine dissolved organic matter, as well as fine organic and inorganic particles delivered by seasonal sea ice, are major scavengers of trace metals, including ^{230}Th (e.g., Baskaran, 2005; Hillaire-Marcel et al., 2017; Charette et al., 2020; Liguori et al., 2021). At sites from the central Arctic Ocean, away from the continental margin, sedimentary fluxes linked to ice-rafting deposition (IRD) are low, the present interglacial being often represented by a few centimeters of partly sorted detrital and biogenic material (e.g., de Vernal et al., 2020). Other processes, such as lateral transportation (Chen et al., 2021), winnowing of fine particles by sinking brines (Osterkamp and Gosink, 2013) and turbidity or contour currents (cf. Mosher and Boggild, 2021), and early diagenetic ferromanganese coatings may also impact $^{230}Th_{xs}$ fluxes at the sea floor and its sedimentary fate (Hoffmann and McManus, 2007; Not and Hillaire-Marcel, 2010; Hillaire-Marcel et al., 2017). Analyses of soluble and particulate phases of ^{230}Th in the water column also indicate that other factors may interfere. They include isopycnal transportation in strongly stratified water masses (Pavia et al., 2020), ventilation rates of water masses (e.g, flux and residence time of the Atlantic Water in the Arctic Ocean; cf. Wefing et al, 2021; Richard et al., 2022), and hydrothermal plumes (e.g., Valk et al., 2018, 2020; Gdaniec et al., 2020).

Building on these earlier studies, we intend to further document the behavior of ^{230}Th in the context of the Arctic Ocean. Special attention will be paid to the distribution and inventory of $^{230}Th_{xs}$ in sedimentary sequences. Using all published $^{230}Th_{xs}$ records, we intend to demonstrate in particular that two robust benchmark ages can be retained: the inception of MIS 3 and the "extinction" age of $^{230}Th_{xs}$. At the time scale of the Last Glacial Maximum (LGM) to recent, we will examine the $^{230}Th_{xs}$ inventories vs the bathymetry, geochemistry, and other sedimentological features. We will also look deeper into ^{230}Th

scavenging in the Arctic Ocean, into its linkage to fine particle and organic compound fluxes, thus its relationship with sea ice production rates and subsequent brine fluxes. At last, at the Milankovitch time scale, we will explore how sea level and solar insolation changes govern $^{230}Th_{xs}$ fluxes at the sea floor, whereas its sedimentary fate might be further modified by the deep sea and diagenetic processes.

3.2 Background setting

The vast and shallow continental shelves (Jakobsson et al., 2012; Figure 3-1A) serve as an important source of terrestrial particles toward the deep Arctic Ocean. Under high sea levels, i.e., during interglacial and/or interstadial periods, coastal erosion, wind, wave, and tidal forces lead to the resuspension of fine particles over shelves. Likewise, part of the suspended particle matter is frozen in seasonal sea ice and redistributed along the surface circulation routes (Charette et al., 2020), mainly through the Transpolar Drift (TPD) towards the Fram Strait, and the Beaufort Gyre (BG) in the western Arctic Ocean (Figure 3-1A). The concentration of suspended particle matter in sea ice has been measured to range from 10 to 660 $mg.L^{-1}$, depending on the location and distance from the coast (Eicken, 2004, and reference therein).

The intermediate- and deep-water currents of the Arctic Ocean depict velocities generally below 6 $cm.s^{-1}$ (Galt, 1967; Hunkins et al., 1969), but could reach up to 20 $cm.s^{-1}$ in eddies extending from 100 m to at least 712 m on the Amundsen Basin side of the Lomonosov Ridge (Woodgate et al., 2001). Turbidity currents tend to be frequent, especially during glacials, leading to the potential winnowing of fine particles (Boggild and Mosher, 2021; Mosher and Boggild, 2021). Moreover, "katabatic flows of dense cold brines" (Osterkamp and Gosink, 2013) and high salinity water flow over ridges between the Amerasian basin and the Eurasian basin (Jones et al., 1995), may also contribute to the winnowing of fine particles.

As a result, large amounts of small-size particles (<51 µm; up to 60 $µg.L^{-1}$; Xiang and Lam, 2020) and of particulate organic carbon (POC; up to 4 $µmol.L^{-1}$), are laterally transported and redistributed basin-wide through sea ice rafting and deep currents. They are also displaced within the intermediate and benthic nepheloid layers toward deep basins (Benner et al., 2005; Vetrov and Romankevich, 2019a; Xiang and Lam, 2020; Schulz et al., 2021). The $\delta^{13}C$-value of POC is lower than -26‰ in the central Arctic Ocean, suggesting significant terrestrial supplies from river discharge (e.g., Xiang and Lam, 2020), whereas it averages ~ -24‰ in continental margin areas likely due to high marine primary productivity favored by seasonal sea ice opening (Bröder et al., 2016; Xiang and Lam, 2020). Lobbes et al. (2000) estimated that about 10^{13} g of

organic carbon (OC) was released annually into the Arctic Ocean by the 12 major Russian rivers, with the dissolved organic carbon (DOC) fraction accounting for more than 90% of the total OC. DOC concentrations are high in the surface waters of the Arctic Ocean, especially of the central Lomonosov Ridge area, with peaking values above 100 $\mu mol.L^{-1}$ (Vetrov and Romankevich, 2019b). In the intermediate and deep waters, DOC content ranges from ~54 to 64 $\mu mol.L^{-1}$ (Wheeler et al., 1996; Benner et al., 2005), except in the Canada Basin where mean DOC concentrations are ~20 $\mu mol.L^{-1}$ (Vetrov and Romankevich, 2019b). As a whole, the terrestrial DOC contributes to ~14 to 24% of the DOC budget of the Arctic Ocean (Benner et al., 2005). With the ongoing permafrost thawing and coastal erosion, terrestrial organic matter transport to the Arctic Ocean is expected to increase significantly (Abbott et al., 2014; Haugk et al., 2022).

The Arctic Ocean water masses are strongly stratified. Its surface layer, between 0 and ~50 m, the Polar Mixed Layer (Aagaard et al., 1981), is characterized by a low salinity related to sea ice melt in summer and freshwater discharge. The properties of the underlying halocline layer (50 to 200 m) are strongly influenced by seasonal sea ice formation and the subsequent brine production and sinking. The intermediate and deep waters in the Eurasian and Amerasian basins of the Arctic originate essentially from the Atlantic Ocean. However, dense water generated by the seasonal sea ice formation and brine production could also penetrate down to 300–400 m (Ivanov and Golovin, 2007). The mixture of Atlantic Water and sinking brines leads to the formation of an isopycnal layer within the 27.9–28.08 sigma theta (σ_θ) density range at a water depth of ~300 to 1500 m (Ivanov et al., 2004; Rogge et al., 2022) and possibly as deep as ~2000 m according to numerical models (Fu, 2022).

During glacial periods, under low sea levels, continental shelves were mostly exposed and/or glaciated. The northern margins of the two major ice sheets of the Northern Hemisphere, the Eurasian Ice Sheet and Laurentide Ice Sheet, directly impacted the Arctic Ocean (Stein et al., 2017). In addition, an East Siberian Ice Shelf/Ice Sheet, located in the East Siberian-Chukchi Sea Borderland, may have been active during several late Pleistocene glaciations (e.g., Niessen et al., 2013). This ice cover has produced scouring over the seafloor at water depths of up to 1 km (e.g., Polyak et al., 2001; Jakobsson et al., 2010; Niessen et al., 2013). Recently, it was hypothesized that, below such an ice shelf, freshwater would have replaced marine water in the deep Arctic basins and the Nordic Seas, at least during MIS 4 and 6 (Geibert et al., 2021). This hypothesis has been challenged (Spielhagen et al., 2022; Hillaire-Marcel et al., 2022b). Nonetheless, during glacials, more likely during ice advance and retreat intervals, sporadic and short sedimentary pulses

occurred, linked to iceberg-rafting/ice streaming (Purcell et al., 2022) or to downslope processes (Ye et al., 2020).

3.3 Dataset and source

This study is based on published datasets or datasets available in the PANGAEA archives. A summary of data available for each study site (sedimentology, geochemistry) is provided in the ANNEXE C Supplementary Material tables. A few sites have been discarded from this study due to i) the loss of core top sediments, thus the lack of data over an undefined time frame (e.g., site AF-00-07 from Gusev et al., 2013), ii) too-low numbers of U-Th measurements ($n < 10$; e.g, most sites from Somayajulu et al., 1989), iii) some large gaps in sampling intervals (e.g., up to 20 cm at site T3-63-1 of Ku and Broecker, 1965). The IRD contents are based on wet sieving, whereas clay contents are from laser diffraction measurements.

The conventional calculation of $^{230}Th_{xs}$ has been summarized by Costa et al. (2020). It consists in subtracting the lithologic and authigenic ^{230}Th fractions from the total based on the assumption that steady terrestrial particle supplies through time, thus a constant $^{232}Th/^{238}U$ ratio. However, significant variations of the $^{232}Th/^{238}U$ ratio were documented in sedimentary sequences from the Arctic Ocean, thus resulting in large uncertainties in the estimated $^{230}Th_{xs}$ (Geibert et al., 2021). Here, an approach recently proposed by Purcell et al. (2022) was used to calculate the $^{230}Th_{xs}$. It is summarized as follows:

$$A^{230}Th_{xs} = A^{230}Th - AU_{mean}.$$

where A = activity of the specific isotope and AU_{mean} = the mean ^{234}U activity, or if not applicable, the mean ^{238}U activity.

Because of minute uranium losses with the preferential departure of ^{234}U due to the oxidation of the sediment that increases through time (see ANNEXE C Supplementary Material section 2), calculating $^{230}Th_{xs}$ vs the mean ^{238}U activity may provide a better estimate of the ^{230}Th excess inherited from the initial ^{230}Th-rain downcore. However, considering the negligible offset between ^{234}U and ^{238}U activities in all records compiled ($= 0 \pm 0.08$ dpm.g^{-1}; 1σ; $n = 426$), using ^{238}U activity for estimating $^{230}Th_{xs}$ would not modify significantly the overall $^{230}Th_{xs}$ distribution reported here (see also Purcell et al., 2022 about this issue).

The dry bulk density (ρ_d; DBD) in core PS51/038-4, PS2185-3/6, PS2200-5, and PS2757-6/8 (hereafter named PS51, PS2185, PS2200, PS2757, respectively) has been calculated from bulk density (ρ_w) data, based

on porosity as follows: (ρ_d = (ρ_w - (porosity * $\rho_{seawater}$)). For core HLY0503-11MC (hereafter named MC11) and the top 25 cm of core PS87/030-1/3 (hereafter named M030), it was calculated from dry weight sediment versus initial sampling volume data. For the lower section of core M030, it was estimated from a logarithmic trendline based on the core top dataset: $\rho_d = 0.95 + 0.19 * \log(x)$; where x is the core depth in centimeters (see Hillaire-Marcel et al., 2017). This equation provides a density value at the high range of the available datasets (see Figure A.1). The ρ_d of cores 19-8, PL94-AR-BC 08–32, Arc5-MA01, HLY0503-12MC & 18MC (hereafter named 19-8, BC08–32, MA01, MC12, MC18, respectively) was then estimated using the mean DBD data of 1.09 ± 0.16 g. cm^{-3} (± 1σ; n = 2129; see Figure A.1).

The $^{230}Th_{xs}$ inventories were calculated as follows:

$$\sum^{230}Th_{xs} = \sum_i [(\rho_d)_i * Ai * \Delta Xi]$$

Where $\sum^{230}Th_{xs}$ is the total $^{230}Th_{xs}$ inventory, $(\rho_d)_i = \rho_d$ of i^{th} the depth interval; A_i = the activity of the interval; ΔX_i = the thickness of i^{th} depth interval.

When calculated from either ^{234}U or ^{238}U, $^{230}Th_{xs}$ inventories do not differ significantly (see Figure A.2).

The extinction depth of $^{230}Th_{xs}$ is reached when:

$\ln(A^{230}Th) - \ln(A^{234}U) \leq [(\sigma_{230})^2 + (\sigma_{234})^2]^{1/2}$

i.e., when $^{230}Th_{xs}$ falls within the quadratic sum of errors for its estimate.

The extinction age of $^{230}Th_{xs}$ at one sigma uncertainty could then be estimated based on the slope of the $\ln(A^{230}Th_{xs})$ line and the half-life of ^{230}Th (~75.6 kyr; Cheng et al. (2013)). Under interglacial conditions, the theoretical ^{230}Th-rain, which is its production in the water column, was estimated using the following equation after Suman and Bacon (1989): ^{230}Th-rain (dpm. cm^{-2}. kyr^{-1}): ~ [0.00263 * (D - 200)] + (200 * 0.00258), where D is the water depth in meters; dpm stands for disintegrations per minute.

The equation assumes a mean salinity of ~34.2 psu in the surface water layer (the upper 200 m) vs 34.9 in the deep waters of the Arctic Ocean, which is practically identical to the mean world ocean salinity (e.g., Fournier et al., 2020).

The production of ^{230}Th under full glacial conditions is based on the assumption that the Arctic Ocean was covered by an ~800 m-thick ice shelf with an ~130 m-thick freshwater layer during the peaking glacial intervals (Hillaire-Marcel et al., 2022b). Ice shelf thicknesses during distinct glacial spans were estimated proportionally to the LR04 benthic foraminifera oxygen isotope stack of Lisiecki and Raymo (2005). However, uncertainties about the relationship with global ice volume (e.g., Raymo et al., 2018) arise from the lack of any $\delta^{18}O$ stack for the Arctic Ocean. The mean glacial ^{230}Th production would then only account for approximately 60% of the interglacial production, using the international bathymetric chart of the Arctic Ocean (IBCAO; Jakobsson, 2002) corrected for sea level changes estimated from the LR04 stack (see Lisiecki and Stern, 2016).

Radiocarbon ages of large sets of foraminifer shells must be used with caution especially at sites with very low sediment accumulation rates, as documented by Hillaire-Marcel et al. (2022a). They nonetheless provide chronological boundaries within or beyond the radiocarbon time scale. All published ^{14}C ages of the study sites were recalibrated (see ANNEXE C Table A.2) using MARINE13 (Reimer et al., 2013), as MARINE20 is not recommended for polar oceans studies due to the large uncertainty of their marine radiocarbon concentration (Heaton et al., 2020). A large array of ΔR-values can be found in the literature about the Arctic Ocean. We use here the value of 440 ± 138, from MARINE13. It is compatible with estimates from Hanslik et al. (2010) for the Holocene and from Pearce et al. (2017) for the Chukchi Sea (~300 yr and 477 ± 60 yr, respectively). We did not use the larger value of 1000 yr proposed by Hanslik et al. (2010) for pre-Holocene samples as they could be biased by the benthic mixing of foraminifer shells between the MIS 3 and Holocene layers (Hillaire-Marcel et al., 2022a).

3.4 Results and discussion

3.4.1 $^{230}Th_{xs}$ inventories

Under steady-state conditions, with constant ^{230}Th fluxes to the sea floor and constant sediment accumulation rates, $^{230}Th_{xs}$ inventories should follow a logarithmic curve driven by the radioactive decay of the isotope. Significant departures from this theoretical pattern indicate that steady-state conditions are not fulfilled (Figure 3-2). Most sites show an increase in their $^{230}Th_{xs}$-inventory from the core top, with a slope well above that of a logarithmic function. This “acceleration” may be linked to a sedimentary hiatus

during MIS 2 and underlying peaking $^{230}Th_{xs}$ values during MIS 3 (Figure 3-2; e.g., Not and Hillaire-Marcel, 2010; Hillaire-Marcel et al., 2017).

On a longer time scale, most curves show a stepwise increase with plateaus likely corresponding to stadial and/or glacial stages (MIS 5d–4, MIS 6, and MIS 8 when recorded), and increases to interstadial/interglacial intervals (MIS 1, 3, 5e, and 7; Figure 3-2C, D). An asymptotic trend is finally depicted at sites where the $^{230}Th_{xs}$ "extinction depth" has been reached.

A closer look at sites along the TPD and BG tracks, where $^{230}Th_{xs}$-inventories have almost reached an asymptotic value (Figure 3-2C, D), i.e., when $^{230}Th_{xs}$ values fall within error bars of their estimate, shows inventories inversely proportional to the distance from the Russian shelves (Figure 3-3; see also Purcell et al., 2022). Site BC26 depicts a unique feature that will be discussed later in Chapter 3.4.5.

3.4.2 $^{230}Th_{xs}$ extinction depth and age

Estimates of $^{230}Th_{xs}$ extinction depths and ages in the Arctic Ocean are mentioned in very few studies (Not and Hillaire-Marcel, 2010; Hillaire-Marcel et al., 2017; Purcell et al., 2022), as they can only be calculated at sites where the $^{230}Th_{xs}$ inventory curve has reached its asymptotic value, thus, after three intervals with abrupt increases (see Figure 3-2C, D). So far, among the available $^{230}Th_{xs}$ records, only seven fulfill this condition. Their $^{230}Th_{xs}$ extinction ages vary from ~200 kyr to 420 kyr, depending on the uncertainties estimated from the deviation standard (one sigma) of the slope of the ln($A^{230}Th$) line and mean ^{234}U activity (Figure 3-4). Within glacial layers, due to the low $^{230}Th_{xs}$ values, often within the error bar of their calculation, the estimated ages depict large uncertainties, especially those based on low analytical precision (alpha counting) and with low sampling depth resolution (Figure 3-4; ANNEXE C Table A.1).

3.4.3 $^{230}Th_{xs}$ distribution as a chronostratigraphic tool

Following the approach of Not and Hillaire-Marcel (2010), Hillaire-Marcel et al. (2017), and Purcell et al. (2022), we tentatively assigned peaking $^{230}Th_{xs}$-values of all cores from the central Arctic Ocean low sedimentation sites (lower panel in Figure 3-5) to MIS 1, 3, 5e, 7, and also to MIS 9 and 11, where $^{230}Th_{xs}$ of these intervals are still measurable. The core top $^{230}Th_{xs}$ peak assigned to MIS 1 is difficult to distinguish from that of MIS 3 at several sites from the central Arctic Ocean due to sedimentary hiatuses during MIS

2 (Not and Hillaire-Marcel, 2010; Hillaire-Marcel et al., 2017), and because it might be reduced or missing when the sediment surface has not been perfectly recovered. The MIS 3 interval depicts the maximum $^{230}Th_{xs}$ value at all sites (the "subsurface maximum peak" of Huh et al., 1997). Deeper downcore, the MIS 5e $^{230}Th_{xs}$ values, when corrected for radioactive decay (i.e., multiplied by ~3), do not differ significantly from those of MIS 1 when it is distinguished from the MIS 3 peak, but seem lower than that of MIS 7 after correction for radioactive decay.

Using a ^{14}C-based age model, Hoffmann and McManus (2007) proposed that the subsurface $^{230}Th_{xs}$ maximum observed throughout all cores from the Arctic Ocean (Figure 3-5) was due to some sediment focusing during the rapid sea level rise of the last deglaciation. However, they also considered that their age model is questionable due to benthic mixing. Indeed, recent ^{14}C-measurements in fish otoliths from the Lomonosov Ridge demonstrate that ^{14}C-based chronostratigraphies can be biased by the mixing of MIS 3 or older fossil specimens with Holocene specimens at sites of low sedimentation rates (Hillaire-Marcel et al., 2022a). In addition to potential biological mixing, the winnowing of fine particles by contour and overflow density currents may have contributed to the merging of MIS 3 remains at the surface (Hillaire-Marcel et al., 2022a). Regardless of this feature, radiocarbon data below the impacted surface layer support the assignment of the sub-surface $^{230}Th_{xs}$ peak to MIS 3 (Hillaire-Marcel et al., 2017, 2022a).

Intervals with $^{230}Th_{xs}$ minimums are assigned to glacial/stadial stages. MIS 2 is characterized at many sites by a sedimentary hiatus, as does MIS 6 at some sites, notably along the Mendeleev and Lomonosov ridges (e.g., Not and Hillaire-Marcel, 2010; Hillaire-Marcel et al., 2017; Geibert et al., 2021, Figure 3-5). As documented in Hillaire-Marcel et al. (2022a) from the ^{14}C measurements in fish otoliths, such sites may also depict the mixing of Holocene and MIS 3 fossil remains. As substages 5a and 5c do not show significant $^{230}Th_{xs}$ peaking value in all sequences analyzed so far, we assigned the low $^{230}Th_{xs}$ layer between MIS 3 and MIS 5e to a "glacial" MIS 5d–4 interval (Figure 3-5).

Purcell et al. (2022) recently documented potential late diagenetic effects leading to a redistribution of U-isotopes (^{238}U, ^{234}U), thus impacting $^{230}Th_{xs}$ values, right below the extinction age of the initial $^{230}Th_{xs}$ at site PS2757 from the southeast Lomonosov Ridge. This fractionated U mobility seems governed by redox gradients between an organic carbon-rich layer and the over-underlying oxidized layers. Thus, much care must be taken to decipher ^{230}Th excesses linked to the initial ^{230}Th "rain" from the water column vs ^{230}Th

excesses due to the diagenetic relocation of its parent isotopes before the setting of any $^{230}Th_{xs}$-based stratigraphy. Here, as illustrated in Figure 3-5, a $^{230}Th_{xs}$ stratigraphy could be set with some confidence for most low sedimentation rate sites, and with some ambiguity in the case of core BC26 collected close to the North Pole.

3.4.4 The ^{230}Th production rate in the Arctic Ocean: glacials vs interglacials/interstadials

Since the work of Huh et al. (1997), low $^{230}Th_{xs}$ burial rates in the Arctic have been associated with the presence of a thick ice cover in the Arctic Ocean. However, the processes linking ice cover and $^{230}Th_{xs}$-fluxes at the sea floor remain unclear. Linkages with IRD during ice-sheet advances and retreats were proposed (e.g., Hillaire-Marcel et al., 2017, 2022b; Xu et al., 2021; Purcell et al., 2022). Extremely low $^{230}Th_{xs}$ during MIS 4 and 6 relate to the replacement of marine water by U-depleted freshwater, leading to negligible ^{230}Th production in the water column and $^{230}Th_{xs}$-fluxes at the sea floor, as hypothesized by Geibert et al. (2021), but challenged by Spielhagen et al. (2022) and Hillaire-Marcel et al. (2022b). Given the uncertainties about the processes involved, a reassessment of the ^{230}Th production, scavenging, and burial under distinct climate conditions seems thus needed.

Due to the relatively conservative behavior of the U/salinity ratio in oxygenated ocean water (3.22 ± 0.18 $ng.g^{-1}$ for a salinity of ~35 psu; Ku et al., 1977; see also Suman and Bacon, 1989; Not et al., 2012), the production rate of ^{230}Th in the water column of the Arctic Ocean should be proportional to salinity and depth. Following Suman and Bacon (1989), under the present-day mean bathymetry and salinity of the central Arctic Ocean (~2700 m; Jakobsson, 2002; ~34.9, Rudels and Carmack, 2022), the ^{230}Th-rain should average ~7.2 $dpm.cm^{-2}.kyr^{-1}$ (Figure 3-6). Based on $^{231}Pa/^{230}Th$ ratios in surface sediments of the modern Arctic Ocean, Moran et al. (2005) estimated that about 10% of this ^{230}Th production is exported through Fram Strait, suggesting $^{230}Th_{xs}$ fluxes at the sea floor of about 6.5 $dpm.cm^{-2}.kyr^{-1}$ (see also Kipp et al., 2021).

During glacials, with the development of ice shelves and under low sea levels, the ^{230}Th production in the glaciated Arctic Ocean was significantly changed. Under full glacial conditions, the global sea level was ~120 m below the modern one, and an ~800 m-thick ice overlying an ~130 m freshwater layer (Hillaire-Marcel et al., 2022b) could have characterized most of the Arctic Ocean. As documented by Spielhagen et al. (2022), there were exchanges between the deep Arctic Ocean and the Atlantic Ocean through Fram Strait, thus allowing for ^{230}Th export from the Arctic Ocean. Hence, the ^{230}Th-rain in the central Arctic Ocean

would have averaged ~4.5 dpm.cm^{-2}.kyr^{-1} under a saline water layer of about 1700 m thick (Figure 3-6). This would represent ~40 % reduction of the ^{230}Th-rain during glacials compared to interglacials. As coarse IRD is not an efficient scavenger of ^{230}Th, a significant part of the $^{230}Th_{xs}$ could have been exported through Fram Strait or partly build up in the water column, depending upon ventilation rates and seawater exchanges between the Arctic and Atlantic oceans (Figure 3-6; Hoffmann et al., 2013; Luo and Lippold, 2015; Kipp et al., 2021; Hillaire-Marcel et al., 2022b). This assumption, however, does not contradict the hypothesis of Geibert et al. (2021) as most studied sites are from relatively shallow ridges, close or within reach of the ice shelf and/or its accompanying freshwater lower boundary ridges. Hence, ^{230}Th flux at the sea floor may have been reduced at shallow sites such as that of core E25 (Figure 3-6).

3.4.5 Factors governing ^{230}Th fluxes from the water column and their sedimentary fate

The factors controlling $^{230}Th_{xs}$ scavenging rates and fluxes at the sea floor were examined based on studies of the water column (e.g., Bacon et al., 1989; Scholten et al., 1995; Edmonds et al, 1998) and sediments (e.g., Moran et al., 2005; Hoffman and McManus, 2007; Hoffman et al., 2013; Luo and Lippold, 2015; Hillaire-Marcel et al., 2017; Geibert et al., 2021). Water column investigations provide a snapshot of a modern-like situation, while sediment studies often used radiocarbon chronologies for flux calculation (e.g., Hoffmann and McManus, 2007; Hoffman et al., 2013; Luo and Lippold, 2015; Hillaire-Marcel et al., 2017), which may present intrinsic biases as documented by Hillaire-Marcel et al. (2022a). Other studies refer to surface sediments without any clear information about their temporal context (e.g., Moran et al., 2005). Further examination of factors controlling $^{230}Th_{xs}$ burial rates on well-constrained time frames and at large scale thus seems relevant.

3.4.5.1 ^{230}Th flux at the sea floor and its burial

Aside from a consensus about maximum $^{230}Th_{xs}$ values linked to MIS 3 and recent interglacial intervals, when Arctic shelves were submerged and the summer season insolation was peaking, not much is known about the variability of $^{230}Th_{xs}$ fluxes and burial rates during the late Quaternary and at the scale of the whole Arctic Ocean. Most studies published so far were based on a limited number of sedimentary sequences, thus yielding a partial view of the issue (e.g., Huh et al., 1997; Strobl, 1998; Not and Hillaire-Marcel, 2010; Gusev et al., 2013; Hillaire-Marcel et al., 2017; Purcell et al., 2022). Here, we try to confront

all published inventories of $^{230}Th_{xs}$ in post-LGM sediments with a few physical and chemical parameters, including water depth, sedimentation rate, clay and IRD fluxes, mean grain size (Φ-value), and OC flux.

Due to the difficulty of setting time boundaries in sedimentary records for time intervals older than MIS 3, we looked specifically at the post-LGM sedimentary layer, with the LGM set at the depth of the minimum $^{230}Th_{xs}$ value above the MIS 3 peak (Figures 2, 5). This post-LGM layer mostly records Holocene sedimentation, at least over ridges where it barely exceeds 1 or 2 cm (e.g., Not and Hillaire-Marcel, 2010; de Vernal et al., 2020), with maximum calibrated ^{14}C ages of 9 kyr and maximum sedimentary fluxes during the early to middle Holocene (Hillaire-Marcel et al., 2022a). In sequences recovered from box and multi-cores, this Holocene layer is generally well recovered (e.g., Poore et al., 1999a, b; ANNEXE C Table A.2), but its recovery is far from ascertained in gravity or piston cores where surface sediments may have been lost (e.g., Gusev et al., 2013). Thus, the total number of sites used for this part of the study was reduced to 17 or less, in cases when a physical or chemical parameter was missing (Figure 3-7). All cores illustrated in Figure 3-7 are from low sedimentation rate sites (<2 $cm.kyr^{-1}$). We will look at the two high sedimentation rate sites (PS2757; MC18) independently, later on. As most of the post-LGM sediment accumulation occurred during the last 9 ka (Not and Hillaire-Marcel, 2010; Hillaire-Marcel et al., 2022a), fluxes reported in Figure 3-7 have been estimated as representing 9 kyr interval, and not the last 21 kyr elapsed since the LGM.

Some features emerge from Figure 3-7. The post-LGM $^{230}Th_{xs}$ inventory correlates with the bathymetry of the coring site and the OC flux, whereas it anti-correlates with the coarse fraction content (Φ-value). In comparison with the ^{230}Th-rain, the $^{230}Th_{xs}$ burial rate is mostly in deficit, consistent with earlier assumptions about ^{230}Th export since the LGM (e.g., Moran et al., 2005; Hoffmann et al., 2013; Luo and Lippold, 2015). However, as documented in Hillaire-Marcel et al. (2022a), evidence of sediment winnowing over ridges by "katabatic flows of dense cold brines" (Osterkamp and Gosink, 2013), and/or turbidity, density-driven contour currents (Jones et al., 1995; Björk et al., 2007, 2010; Boggild and Mosher, 2021; Mosher and Boggild, 2021), could also account for some $^{230}Th_{xs}$-loss over these ridge sites. As discussed below, some deep intra-basin sites record relatively very high $^{230}Th_{xs}$ inventories likely due to re-sedimentation of winnowed sediments from ridges.

The weak correlation between $^{230}Th_{xs}$ and clay fluxes is based on a low number of observations and does not permit discarding the role of clay in scavenging. However, it seems reasonable to assume that in the "sediment-starved" Arctic Ocean, thorium scavenging is primarily controlled by organic compounds in part adsorbed onto fine particle surfaces (Baskaran et al., 2003; Zhang et al., 2021). For example, at a site such as that of core M030, the mean sedimentation rate is less than ~4 mm.kyr^{-1} (Hillaire-Marcel et al., 2017). Clays represent ~24% of the sediment (ANNEXE C Table A.4). The accumulation rate of fine scavenging mineral particles is low on a thousand-year time scale, which is significantly longer than the 20 to 40 yrs residence time of ^{230}Th in the Arctic Ocean as estimated by Scholten et al. (1995) and Trimble et al. (2004). The activity of $^{230}Th_{xs}$ value at the top of core M030 is ~12 dpm. g^{-1}. The ^{230}Th scavenger would be the DOC, in particular, specific fractions of colloids (Baskaran et al., 2003), which also play a substantial role in coagulating and transporting trace metals (e.g., Fe, Mn, Co, Ni; Guo et al., 2000; Pokrovsky et al., 2014; Krickov et al., 2019).

Beyond ^{230}Th production in the water column, the major parameter governing $^{230}Th_{xs}$ fluxes at the floor of the deep Arctic Ocean and its burial rates seems related to organic matter. Marine DOC is the major scavenger of trace metals in the western Arctic Ocean, whereas both marine and terrestrial DOC are effective carriers in the Eurasian basin (Williford et al., 2022). Under the influences of several physical and biological processes (e.g., coagulation, mixing, gravitational settling, ecosystem structure and food-web interactions; Roca-Martí, 2017), $^{230}Th_{xs}$-enriched organic matter aggregations would sink to the seafloor. The positive relationship between $^{230}Th_{xs}$ inventory and sedimentation rate, and OC flux in the TPD cluster relates to the riverine discharge and seasonal sea ice production on the Siberian continental shelf (Suman and Bacon, 1989; Wheeler et al., 1996; Benner et al., 2005; de Vernal et al., 2020; Fadeev et al., 2021; Rogge et al., 2022; Williford et al., 2022). On a long geological time scale, it could thus be related to high summer season insolation and high sea level conditions (Hillaire-Marcel et al., 2021).

In the BG cluster of the western Arctic Ocean (Figure 3-7), DOC concentrations are lower than those of the TPD area due to weak terrestrial discharge from the Mackenzie River compared to Russian rivers (Stein, 2008; Vetrov and Romankevich, 2019b). However, primary productivity over the Chukchi Sea shelf is important and constitutes the major contributor to the DOC budget of the western Arctic Ocean (Williford et al., 2022). The decreasing $^{230}Th_{xs}$ inventories from the continental margin to the central western Arctic Ocean (Figure 3-3) would thus be linked to the lateral transportation and progressive removal/decay of

the DOC along the intermediate and benthic nepheloid layers (e.g., Xiang and Lam, 2020; Chen et al., 2021; Schulz et al., 2021).

Brines play a complementary role as they carry most of the DOC produced by sea ice algae and microfauna. The organic contents of the brine promote organic ligand complexation (Becquevort et al., 2009; Ardiningsih et al., 2021). Brine could extract and release 60 to 70% of the labile trace metals (e.g., Fe, Mn, Cd) from the dirty sea ice (Grotti et al., 2005; Evans and Nishioka, 2018, 2019). Therefore, brines could re-distribute the soluble and leachate phases–$^{230}Th_{xs}$ along their advection and sinking into the central Arctic Ocean.

A few coring sites deserve specific attention. The cores MC18 and BC26 were raised ~24 nautical miles apart on the Lomonosov Ridge but at different water depths. Core BC26 is from ~1034 m on the ridge crest, and core MC 18 is from ~2500 m in an intra-basin of the ridge (Figure 3-1B). The post-LGM-inventories of $^{230}Th_{xs}$ in core MC18 is ~237 dpm.cm^{-2}, more than twice the ^{230}Th-rain. In opposition, the post-LGM peak is not distinguishable from that of MIS 3 in core BC26. Core BC26 depicts a highly compacted $^{230}Th_{xs}$ profile with an MIS 7 inception assigned at ~20 cm based on the distinction age of ^{230}Th, which corresponds to the depth of the MIS 3 peak in the deeper MC18 site. We see here evidence for proximal redeposition of fine sediments and their $^{230}Th_{xs}$ and will discuss it in subchapter 3.4.5.2.

Another site with particular features is that of core PS2757, which is characterized by relatively high sedimentation rates (~2.6 cm.kyr^{-1}; Figure A.4). Purcell et al. (2022) have well-documented the behavior of $^{230}Th_{xs}$ in this core. They highlighted the facts that sites with sedimentation rates exceeding a few cm.kyr^{-1} are characterized by dilution of the ^{230}Th from the water column by detrital ^{230}Th supplies and that the possible diagenetic U mobility would make the $^{230}Th_{xs}$ approach unsuitable for estimating extinction ages, as well as for the setting a $^{230}Th_{xs}$-based stratigraphy.

3.4.5.2 Post-depositional process impacting $^{230}Th_{xs}$ records

Aside from radioactive decay and vertical ^{230}Th rain, the post-depositional processes that could alter $^{230}Th_{xs}$ records include: i) late diagenetic processes along major redox boundaries linked to high organic carbon content layers, as documented from core PS2757 by Purcell et al. (2022); ii) supplies from glacial erosion

by thick ice shelves (e.g., Jakobsson et al., 2016); iii) sediment winnowing by deep currents and redeposition (Björk et al., 2007; Not and Hillaire-Marcel, 2010).

In the Lomonosov Ridge area, the post-LGM $^{230}Th_{xs}$-inventories at sites BC26 and 28 located on the crest of the ridge are close to equilibrium or in deficit with the corresponding ^{230}Th-rain values (Figure 3-8; ANNEXE C Table A.3). Comparatively, core MC18 raised from the Intra Basin of the ridge, and core PS2185 collected away from the deep-water exchange channel (Figure 1B) depict strong excesses in ^{230}Th-inventories. This feature may be associated with winnowing and redeposition processes driven by the active deep-water exchange between the Makarov and Amundsen basins (Björk et al., 2007, 2010), especially at site BC26 that is influenced by the Canadian Basin Deep Water (Björk et al., 2010). The $^{230}Th_{xs}$-enriched fine components of sites BC26 and BC28 would have been laterally transported toward deeper sites, such as MC18. Similar features are observed in the western Arctic Ocean. Sites MC11 and 12 are located at the northern tip of Mendeleev Ridge, in the pathway of the Canadian Basin Deep Water (Figure 3-1C; Rudels et al., 2012). They depict deficits in their post-LGM $^{230}Th_{xs}$ inventories vs the corresponding ^{230}Th-rain values (Figure 8; ANNEXE C Table A.3). In opposition, site BC20, lying deeper in the Makarov Basin, and the sheltered site BC19 show ^{230}Th-inventories in balance with the ^{230}Th-rain (Figures 3-1C, 8; ANNEXE C Table A.3). Unfortuanately, a quantitative assessment of the $^{230}Th_{xs}$ removal and redeposition relating to deep water exchanges is still out of reach, due to the rare datasets available, especially from the deep Arctic Basins.

3.4.6 Paleoclimatic and paleoceanographic implications from $^{230}Th_{xs}$ records

In contrast to the sediment-focusing model which has been used to interpret the subsurface $^{230}Th_{xs}$ peak (Hoffmann and McManus, 2007), Geibert et al. (2022) suggested that the subsurface $^{230}Th_{xs}$ peak might be linked to extremely low sedimentation rate by quoting Yang et al. (1986) "*Even fine particle fluxes generating sedimentation rates <1 mm/1000 yr lead to >100-fold ^{230}Th concentrations* ". However, this assumption is in contradiction with the thick sediment layer deposited during MIS 3 (>10 cm; Figure 3-5). In our view, the sub-surface $^{230}Th_{xs}$ peak indicates enhanced sea ice rafting deposition, thus seasonally open sea ice over largely submerged shelves (Xiao et al., 2015). Such conditions were met under i) the relatively high sea level (~ -40 m to -50 m) that was reached during MIS 3 (Pico et al., 2020; Dalton et al., 2022), ii) the high summer insolation of the ~54 to 49 kyr interval (Hillaire-Marcel et al., 2021), and iii) the

shrub tundra vegetation between 54 and 51 kyr that was reconstructed at the proximity of the Lena River delta by Zimmermann et al. (2017). However, all factors accounting for the maximum $^{230}Th_{xs}$ of this early MIS 3 interval still remain not fully elucidated. Hillaire-Marcel et al. (2022b) proposed that some build-up of ^{230}Th in the water column of the Arctic Ocean, under a resilient ice shelf spanning the MIS 5d–4 interval, may have contributed to the enhanced scavenging rates of $^{230}Th_{xs}$ during the early MIS 3. Enhanced DOC fluxes during this interval might have also played a role as DOC is an efficient scavenger of trace metals (e.g., Williford et al., 2022). Interestingly, the DOC contents in ice wedges from the Lena Delta by Wetterich et al. (2020) suggest that DOC concentrations in the MIS 3 layer (~367 mg. L^{-1}) were about one-order magnitude higher than those of the Holocene layer (~34 mg. L^{-1}), which is compatible with organic inputs from terrestrial vegetation (Zimmermann et al., 2017) through the Lena River that presently contributes ~50% of the DOC supplied by Russian rivers (Lobbes et al., 2000). Hence, a high terrestrial DOC flux toward the Arctic Ocean some 55-50 kyr ago might have greatly contributed to a high ^{230}Th-scavenging rate during this early MIS 3 interval.

A critical feature of all available records is the relatively low $^{230}Th_{xs}$ in sediments of the Last Interglacial (MIS 5e) compared to MIS 7. The longer duration of MIS 7 than MIS 5e, its high summer insolation, and its three high sea-level phases might explain a better recording of MIS 7 than MIS 5e in the Arctic Ocean sedimentary sequences as proposed by Hillaire-Marcel et al. (2021). Because of chronostratigraphic issues, as evoked in the introduction of the present paper, notably for the Last Interglacial (see also Kageyama et al., 2021; Hillaire-Marcel and de Vernal, 2022; West et al., 2022), there is no unequivocal information about the paleoceanography of MIS 5e for the central Arctic Ocean. Nevertheless, reliable stratigraphical schemes are available from the Nordic Seas, where all studies report a shorter, mostly cooler MIS 5e interval in comparison with the Holocene (Rasmussen et al., 2003; Oppo et al., 2006; Bauch and Erlenkeuser, 2008; Van Nieuwenhove and Bauch, 2008). On this basis, assuming a short and mostly cool Arctic Ocean during MIS 5e, a lesser $^{230}Th_{xs}$ recording of the interval is possible. According to Wetterich et al. (2016), "...*the isotopic composition ($d^{18}O$, dD) [and pollen content] of the Buchchagy ice-wedge [Laptev Sea cost] indicates [MIS 5] winter conditions colder than during the MIS 3 […], harsher summer conditions and rather similar vegetation as during the MIS 2 stadial*."

It is important to highlight the fact that, by itself, the low $^{230}Th_{xs}$ characterizing the MIS 5e in the Arctic Ocean, does not necessarily indicate a shorter or cooler interval in comparison with the Holocene. As

evoked above in reference to the study by Hillaire-Marcel et al. (2022a), the winnowing of fine $^{230}Th_{xs}$-barrier particles, by density-driven and contour currents, occurs over ridges. Therefore, active circulation and high rates of sea ice production and sinking brines could also result in low $^{230}Th_{xs}$ in sediments from the ridge summits. Under such a scenario, the low $^{230}Th_{xs}$ value of the interval assigned to MIS 5e could well point to warm conditions and high brine production rates during MIS 5e, in contradiction with what could be proposed solely based on some direct proportionality between ^{230}Th fluxes and climate conditions. Such a scenario involving the winnowing of fine particles by density-driven bottom currents can be supported by some arguments pointing to highly dynamic sea ice conditions during the Last Interglacial: i) the MIS 5e experienced a significantly higher sea level (up to ~9 m vs the Present; Kopp et al., 2009; Dutton et al., 2015; ii) thus, the flux of relatively "warm" and low salinity Pacific waters through Bering Strait was potentially higher by ~50% than at present (Song et al., 2022b), with impact on the freshwater budget and sea ice regime in the Arctic Ocean (Karami et al., 2021). Enhanced circulation and higher brine production rates could then account for a loss of $^{230}Th_{xs}$ and of its fine carrier particles and compounds through winnowing processes. Thus, we suggest keeping open the debate about paleoclimate conditions in the Arctic Ocean during MIS 5e until more direct evidence from proxies is available.

3.4.7 Overview of the glacial vs interglacial ^{230}Th cycling in the Arctic Ocean

In addition to the main parameters governing the fate of ^{230}Th production in the Arctic Ocean discussed above, a large array of other processes may also interfere with its scavenging, fluxes within the basin and at the sea floor, effective burial, and post-depositional evolution. They range from land erosion and river runoff, coastal erosion, sea ice and brine dynamics, slope processes, isopycnal transportation, reversible scavenging, deep currents, deep ocean circulation and exchanges with other oceans, hydrothermal plumes (e.g., Valk et al., 2018, 2020; Gdaniec et al., 2020; Pavia et al., 2020; Chen et al., 2021), aside from other potential factors not yet documented. An overview of major processes so far identified, which may have variable impacts in time and space, is provided in Table 3.1 and illustrated in Figure 3-9.

3.4.7.1 The submerged continental margin during interglacials/interstadials

Aside from the direct linkages between ^{230}Th production and shelf water salinity, primary productivity, river runoff, terrestrial DOC, and fine particle fluxes, shallow currents control the dispersal of fine particles and colloids, thus ^{230}Th-boundary scavenging processes (e.g., Nozaki et al., 1981; Roy-Barman, 2009; Kuzyk

et al., 2013). Coastal and shelf processes also include permafrost thawing, groundwater discharge, coastal erosion, and sediment resuspension induced by tidal, wave, and wind forces (Holmes et al., 2002; Abbott et al., 2014; Wegner et al., 2015; Haugk et al., 2022). In fine, ^{230}Th-scavenging particles and compounds are dispersed toward the central Arctic Ocean through sea ice-rafting, eddies, and currents (Figure 3-9; Roy-Barman, 2009; Kipp et al., 2018; Xiang and Lam, 2020; Rogge et al., 2022). Due to the large shelf area of the Arctic Ocean, boundary scavenging is a critical parameter, especially under high sea levels, when shelves are submerged (cf. Edmonds et al., 2004; Moran et al., 2005; Gdaniec et al., 2020). Seasonal sea ice production also interferes as fragile sea ice dwelling from the sea surface down to 25 m, could capture suspended particles (Ito et al., 2019, 2021; Drits et al., 2021). At last, brines related to sea ice formation sink on the shelf floor (down to ~300–400 m in the Laptev shelf; e.g., Ivanov and Golovin, 2007), leading to the mixing of trace metals over the shelf and their redistribution downslope (Evans and Nishioka, 2018, 2019).

3.4.7.2 The exposed continental margin during glacials/stadials

Under the low sea levels of glacial/stadial intervals, continental shelves were mostly exposed (Jakobsson et al., 2010, 2012), and the Bering Strait was closed (Jakobsson et al., 2017). Thus, several parameters mentioned above, such as shallow shelf currents related to the Pacific and Atlantic waters inflows, sediment resuspension, boundary scavenging, and seasonal sea ice-related processes, including primary productivity, were either strongly reduced or nil (Figure 3-9; Table 3.1). Besides, river and continental DOC discharges were impeded by the existence of ice sheets/shelves surrounding the Arctic (Polyak et al., 2001; Jakobsson et al., 2010; Stein et al., 2017), whereas large lakes developed southward over northern Siberia (Krinner et al, 2004). Glacial advance over shelves would then carry unsorted, relatively coarse particles toward the deep basins (Purcell et al., 2022). Combining all these features, ^{230}Th scavenging on the continental shelves was practically stopped, with quasi-nil transportation of ^{230}Th-bearing particles and compounds towards the central Arctic Ocean (Figure 3-9).

3.4.7.3 The cycling of ^{230}Th in the deep Arctic Ocean during interglacials/interstadials

^{230}Th distribution in the Arctic Ocean is influenced by the sea ice-generated brines, as it does around Antarctica (Grotti et al., 2005; Becquevort et al., 2009; Ardiningsih et al., 2021). With a penetration depth of ~300–400 m, brines depict high concentrations of soluble and adsorbed phases of ^{230}Th as discussed

above. They are partly mixed with the intruding Atlantic Water, forming an isopycnal layer ~300–1000 m deep (Ivanov et al., 2004). The intrusion of Atlantic Water was observed to be stronger over the past ten years, leading to the deepening of the isopycnal layer to ~1500 m, occasionally down to 2000 m (Figure 3-9; Gdaniec et al., 2020; Valk et al., 2020; Fu, 2022; Rogge et al., 2022). Thus, isopycnal transportation must be considered as an important player in the redistribution of ^{230}Th in the high-latitude ocean (Pavia et al., 2020). The Arctic deep water also depicts a high soluble ^{230}Th concentration as a result of the reversible scavenging (Gdaniec et al., 2020). Hence, ^{230}Th speciation and concentration are heterogeneous within the different water layers of the Arctic Ocean.

Another important process that influences the ^{230}Th distribution in the deep Arctic Ocean is the lateral transportation within the intermediate and bottom nepheloid layers (Figure 3-9; e.g., Chen et al., 2021; Schulz et al., 2021; Gardner et al., 2022; Williford et al., 2022). Following the fine particle concentration gradients from the continental slope to the central Arctic Ocean (Xiang and Lam, 2020; Williford et al., 2022), decreasing trace metal concentrations (e.g., Fe, Co, Nd) in the water column are observed (Charette et al., 2020; Liguori et al., 2021).

It has been reported that hydrothermal plumes from the Gakkel Ridge could contribute to ^{230}Th scavenging in the deep Nansen Basin (Valk et al., 2018). However, the relatively slow spreading rate and low overall hydrothermal activity (Jean-Baptiste and Fourré, 2004) lead to inferring low influence on ^{230}Th cycling at the scale of the whole Arctic Ocean.

3.4.7.4 $^{230}Th_{xs}$ burial in the deep Arctic Ocean during glacials

During glacial periods, turbulent mixing was mostly paused below the severe ice cover, resulting in reduced lateral transportation (Rippeth and Fine, 2022). The deep circulation might have been similarly reduced (e.g., Hillaire-Marcel et al., 2022b). Whereas, due to their low velocity (2 to 6 cm.s^{-1}; Galt, 1967; Hunkins et al., 1969), bottom currents should generally be of minor impact on the $^{230}Th_{xs}$-rain dispersal. However, they cannot be overlooked where boundary currents are active (Woodgate et al., 2001). Such turbidity and contour currents were apparently active during glacials in the Lomonosov Ridge and Canadian Basin (Weigelt et al., 2020; Boggild and Mosher, 2021), especially under low sea levels (Mosher and Boggild, 2021). This might have led to the resuspension and removal of fine particles deposited during earlier interglacial/interstadial intervals.

3.5 Conclusion

One major conclusion that may be drawn from this synthesis work is that there is no simple proportionality between time and sediment or $^{230}Th_{xs}$ deposition in the deep Arctic Ocean. No realistic time interpolation or time estimate can be made aside from the stratigraphic assignment of peaking $^{230}Th_{xs}$-values to specific "warm" intervals and the calculation of $^{230}Th_{xs}$ extinction ages.

Without more information on $^{230}Th_{xs}$ in deep depocenter, ^{230}Th-budgets are difficult to set, especially for glacial intervals. Overall, one may infer reduced ^{230}Th deposition during such episodes, in particular at shallow sites within reach of ice shelves or of their underlying freshwater layer (Hillaire-Marcel et al., 2022b). This would be partly compatible with the hypothesis of a "freshwater-filled" Arctic Ocean by Geibert et al. (2021). The strongest evidence for some ^{230}Th-export, at least during MIS 2, may be derived from $^{231}Pa/^{230}Th$ activity ratios as documented by Moran et al. (2005) or Hillaire-Marcel et al. (2017). This would imply a possibly reduced, but still active deep water circulation and exchanges with the Nordic Seas and Atlantic Ocean (Spielhagen et al., 2022).

The compilation of $^{230}Th_{xs}$ distributions and inventories in cored sequences published so far allows us to reassess the usefulness of $^{230}Th_{xs}$ as a stratigraphic tool as proposed in earlier papers (e.g., Strobl, 1998; Not and Hillaire-Marcel, 2010; Hillaire-Marcel et al., 2017; Geibert et al., 2021; Purcell et al., 2022). Two benchmark ages could be reasonably set: i) that of the subsurface $^{230}Th_{xs}$ peak (~53 kyr), and ii) the $^{230}Th_{xs}$ extinction age downcore (~220 to 420 kyr). They lead to paleoceanographic inferences about the Arctic Ocean quite distinct from those using biostratigraphic markers and Mn-based cyclostratigraphy (see also Hillaire-Marcel and de Vernal, 2022) and even, radiocarbon (Hillaire-Marcel et al., 2022a). However, in some cases, the $^{230}Th_{xs}$-based stratigraphy should be used with some caution, notably when the MIS 1 $^{230}Th_{xs}$ peak is not distinguishable from that of MIS 3, or when the redox-driven diagenetic processes interfere (Purcell et al., 2022).

This review highlights the importance of solar insolation and sea level in governing the cycling and sedimentation of trace metals in the Arctic Ocean, through the critical role of seasonal sea ice production and melting over submerged continental shelves (Hillaire-Marcel et al., 2021). It also documents post-depositional processes related to brine-driven deep current exchanges between the Canadian, Amundsen and Eurasian basins resulting in some $^{230}Th_{xs}$ redistribution from the ridges to the deep basins. At last, it

confirms the major role of DOC, either produced by marine algae or discharged by the rivers (particularly the Lena River), in ^{230}Th-scavenging processes.

Future work could be focused on deep basins and continental margins as their inventories in ^{230}Th and ^{231}Pa could help constrain better the budgets of these isotopes during recent glacials and the MIS 3 and 5e, in particular.

3.6 Acknowledgment

This work was supported by the Natural Sciences and Engineering Research Council (NSERC) of Canada, the Fonds de Recherche du Québec Nature et Technologies (FQRNT), and the National Natural Science Foundation of China [grant number: 41876070]. Thanks to Dr. Yufen Rong for her assistance with drawing the figures. The financial support from the China Scholarship Council is highly appreciated by T.-F. Song. Three anonymous reviewers provided many helpful suggestions. Their input has been highly appreciated.

3.7 Data availability

All the data used in this study are referenced in Table S1 of the ANNEXE C Supplementary Material.

3.8 Reference

Aagaard, K., Coachman, L. K. and Carmack, E., 1981. On the halocline of the Arctic Ocean. Deep Sea Res. Part I Oceanogr. Res. Pap. 28(6), 529–545. https://doi.org/10.1016/0198-0149(81)90115-1.

Abbott, B. W., et al., 2014. Elevated dissolved organic carbon biodegradability from thawing and collapsing permafrost. J. Geophys. Res. Biogeosci. 119(10), 2049–2063. https://doi.org/10.1002/2014JG002678.

Ardiningsih, I., et al., 2021. Fe-binding organic ligands in coastal and frontal regions of the western Antarctic Peninsula. Biogeosciences 18(15), 4587–4601. https://doi.org/10.5194/bg-18-4587-2021.

Backman, J., Fornaciari, E. and Rio, D., 2009. Biochronology and paleoceanography of late Pleistocene and Holocene calcareous nannofossil abundances across the Arctic Basin. Mar. Micropaleontol. 72(1-2), 86–98. https://doi.org/10.1016/j.marmicro.2009.04.001.

Bacon, M. P. and Anderson, R. F., 1982. Distribution of thorium isotopes between dissolved and particulate forms in the deep sea. J. Geophys. Res. Oceans 87(C3), 2045–2056. https://doi.org/10.1029/JC087iC03p02045.

Bacon, M. P., Huh, C. and Moore, R. M., 1989. Vertical profiles of some natural radionuclides over the Alpha Ridge, Arctic Ocean. Earth Planet. Sci. Lett. 95(1-2), 15–22. https://doi.org/10.1016/0012-821X(89)90164-7.

Baskaran, M., Swarzenski, P. W. and Porcelli, D., 2003. Role of colloidal material in the removal of ^{234}Th in the Canada basin of the Arctic Ocean. Deep Sea Res. Part I Oceanogr. Res. Pap. 50(10-11), 1353–1373. https://doi.org/10.1016/S0967-0637(03)00140-7.

Baskaran, M., 2005. Interaction of sea ice sediments and surface sea water in the Arctic Ocean: Evidence from excess ^{210}Pb. Geophys. Res. Lett. 32(12), L12601. https://doi.org/10.1029/2004GL022191.

Bauch, H. A. and Erlenkeuser, H., 2008. A "critical" climatic evaluation of last interglacial (MIS 5e) records from the Norwegian Sea. Polar Res. 27(2), 135–151. https://doi.org/10.1111/j.1751-8369.2008.00059.x.

Becquevort, S., et al., 2009. Biogeochemistry and microbial community composition in sea ice and underlying seawater off East Antarctica during early spring. Polar Biol. 32(6), 879–895. https://doi.org/10.1007/s00300-009-0589-2.

Benner, R., Louchouarn, P. and Amon, R. MW., 2005. Terrigenous dissolved organic matter in the Arctic Ocean and its transport to surface and deep waters of the North Atlantic. Glob. Biogeochem. Cycles 19(2), GB2025. https://doi.org/10.1029/2004GB002398.

Björk, G., et al., 2007. Bathymetry and deep-water exchange across the central Lomonosov Ridge at 88–89 N. Deep Sea Res. Part I Oceanogr. Res. Pap. 54(8), 1197–1208. https://doi.org/10.1016/j.dsr.2007.05.010.

Björk, G., et al., 2010. Flow of Canadian basin deep water in the Western Eurasian Basin of the Arctic Ocean. Deep Sea Res. Part I Oceanogr. Res. Pap. 57(4), 77–586. https://doi.org/10.1016/j.dsr.2010.01.006.

Boggild, K. and Mosher, D. C., 2021. Turbidity currents at polar latitudes: A case study of NP-28 channel in the Amundsen Basin, Arctic Ocean. Mar. Geol. 440, 106571. https://doi.org/10.1016/j.margeo.2021.106571.

Bröder, L., et al., 2016. Fate of terrigenous organic matter across the Laptev Sea from the mouth of the Lena River to the deep sea of the Arctic interior. Biogeosciences 13(17), 5003–5019. https://doi.org/10.5194/bg-13-5003-2016.

Charette, M. A., et al., 2020. The Transpolar Drift as a source of riverine and shelf-derived trace elements to the central Arctic Ocean. J. Geophys. Res. Oceans 125(5), e2019JC015920. https://doi.org/10.1029/2019JC015920.

Chen, S. Y. S., et al., 2021. On the cycling of ^{231}Pa and ^{230}Th in benthic nepheloid layers. Deep Sea Res. Part I Oceanogr. Res. Pap. 177, 103627. https://doi.org/10.1016/j.dsr.2021.103627.

Cheng, H., et al., 2013. Improvements in ^{230}Th dating, ^{230}Th and ^{234}U half-life values, and U–Th isotopic measurements by multi-collector inductively coupled plasma mass spectrometry. Earth Planet. Sci. Lett. 371, 82–91. https://doi.org/10.1016/j.epsl.2013.04.006.

Costa, K. M., et al., 2020. ^{230}Th normalization: New insights on an essential tool for quantifying sedimentary fluxes in the modern and Quaternary ocean. Paleoceanogr. Paleoclimatol. 35(2), e2019PA003820. https://doi.org/10.1029/2019PA003820.

Darby, D. A., Bischof, J. F. and Jones, G. A., 1997. Radiocarbon chronology of depositional regimes in the western Arctic Ocean. Deep Sea Res. Part II Top. Stud. Oceanogr. 44(8), 1745–1757. https://doi.org/10.1016/S0967-0645(97)00039-8.

Dalton, A. S., et al., 2022. The marine δ^{18}O record overestimates continental ice volume during Marine Isotope Stage 3. Glob. Planet. Change 212, 103814. https://doi.org/10.1016/j.gloplacha.2022.103814.

Drits, A. V., et al., 2021. Influence of riverine discharge and timing of ice retreat on particle sedimentation patterns on the Laptev Sea shelf. J. Geophys. Res. Oceans 126(10), e2021JC017462. https://doi.org/10.1029/2021JC017462.

Dutton, A., et al., 2015. Sea-level rise due to polar ice-sheet mass loss during past warm periods. Science, 349(6244), aaa4019. https://doi.org/10.1126/science.aaa4019.

Edmonds, H. N., et al., 1998. Protactinium-231 and thorium-230 abundances and high scavenging rates in the western Arctic Ocean. Science 280(5362), 405–407. https://doi.org/10.1126/science.280.5362.405.

Edmonds, H. N., et al., 2004. ^{230}Th and ^{231}Pa in the Arctic Ocean: implications for particle fluxes and basin-scale Th/Pa fractionation. Earth Planet. Sci. Lett. 227(1-2), 155–167. https://doi.org/10.1016/j.epsl.2004.08.008.

Eicken, H., 2004. The role of Arctic sea ice in transporting and cycling terrestrial organic matter. In Stein, R. and Macdonald, R. W. (eds): The organic carbon cycle in the Arctic Ocean: present and past. 45–53, Springer-Verlag, Berlin. https://doi.org/10.1007/978-3-642-18912-8_4.

Evans, L. K. and Nishioka, J., 2018. Quantitative analysis of Fe, Mn and Cd from sea ice and seawater in the Chukchi Sea, Arctic Ocean. Polar Sci. 17, 50–58. https://doi.org/10.1016/j.polar.2018.07.002.

Evans, L. K. and Nishioka, J., 2019. Accumulation processes of trace metals into Arctic sea ice: distribution of Fe, Mn and Cd associated with ice structure. Mar. Chem. 209, 36–47. https://doi.org/10.1016/j.marchem.2018.11.011.

Fadeev, E., et al., 2021. Sea ice presence is linked to higher carbon export and vertical microbial connectivity in the Eurasian Arctic Ocean. Commun. Biol. 4(1), 1–13. https://doi.org/10.1038/s42003-021-02776-w.

Fournier, S., et al., 2020. Sea surface salinity as a proxy for Arctic Ocean freshwater changes. J. Geophys. Res. Oceans 125(7), e2020JC016110. https://doi.org/10.1029/2020JC016110.

Francois, R., et al., 2004. ^{230}Th normalization: An essential tool for interpreting sedimentary fluxes during the late Quaternary. Paleoceanography 19(1), PA1018. https://doi.org/10.1029/2003PA000939.

Fu, C., 2022. Modelling the Atlantic Water along its poleward pathway into and through the Arctic Ocean. MSc Thesis, University of Alberta, Edmonton. https://doi.org/10.7939/r3-gadk-ny91.

Galt, J. A., 1967. Current measurements in the Canadian Basin of the Arctic Ocean, summer, 1965. Tech. Rep. No. 184. Dept. of Oceanography, Univ. of Washington, Seattle.

Gardner, W. D., et al., 2022. Distribution, Sources, and Dynamics of Particulate Matter Along Trans-Arctic Sections. J. Geophys. Res. Oceans 127(6), e2021JC017970. https://doi.org/10.1029/2021JC017970.

Geibert, W., et al., 2021. Glacial episodes of a freshwater Arctic Ocean covered by a thick ice shelf. Nature 590(7844), 97–102. https://doi.org/10.1038/s41586-021-03186-y.

Geibert, W., et al., 2022. Reply to 'Challenging the hypothesis of an arctic ocean lake during recent glacial episodes' by Hillaire-Marcel, et al. J. Quat. Sci. 37(4), 568–571. https://doi.org/10.1002/jqs.3431.

Gdaniec, S., et al., 2020. ^{231}Pa and ^{230}Th in the Arctic Ocean: Implications for boundary scavenging and ^{231}Pa/^{230}Th fractionation in the Eurasian Basin. Chem. Geol. 532, 119380. https://doi.org/10.1016/j.chemgeo.2019.119380

Grotti, M., et al., 2005. Trace metals distributions in coastal sea ice of Terra Nova Bay, Ross Sea, Antarctica. Antarct. Sci. 17(2), 289–300. https://doi.org/10.1017/S0954102005002695.

Guo, L., Santschi, P. H. and Warnken, K. W., 2000. Trace metal composition of colloidal organic material in marine environments. Mar. Chem. 70(4), 257–275. https://doi.org/10.1016/S0304-4203(00)00031-1.

Gusev, E. A., et al., 2013. Stratigraphy of bottom sediments in the Mendeleev Ridge area (Arctic Ocean). Dokl. Earth Sci. 450, 602–606.

Hanslik, D. M., et al., 2010. Quaternary Arctic Ocean sea ice variations and radiocarbon reservoir age corrections. Quat. Sci. Rev. 29(25-26), 3430–3441. https://doi.org/10.1016/j.quascirev.2010.06.011.

Haugk, C., et al., 2022. Organic matter characteristics of a rapidly eroding permafrost cliff in NE Siberia (Lena Delta, Laptev Sea region). Biogeosciences 19(7), 2079–2094. https://doi.org/10.5194/bg-19-2079-2022.

Heaton, T. J., et al., 2020. Marine20—the marine radiocarbon age calibration curve (0–55,000 cal BP). Radiocarbon 62(4), 779–820. https://doi.org/10.1017/RDC.2020.68.

Hillaire-Marcel, C. and de Vernal, A., 2022. A comment about" A sedimentary record from the Makarov Basin, Arctic Ocean, reveals changing middle to Late Pleistocene glaciation patterns"(Quat. Sci. Rev., 270 (2021), p. 107176) from W. Xiao, L. Polyak, R. Wang, C. Not, L. Dong, Y. Liu, T. Ma, T. Zhang. Quat. Sci. Rev. 279, 107239. https://doi.org/10.1016/j.quascirev.2021.107239.

Hillaire-Marcel, C., et al., 2017. A new chronology of late Quaternary sequences from the central Arctic Ocean based on “extinction ages” of their excesses in ^{231}Pa and ^{230}Th. Geochem. Geophys. Geosystems 18(12), 4573–4585. https://doi.org/10.1002/2017GC007050.

Hillaire-Marcel, C., et al., 2022a. Challenging radiocarbon chronostratigraphies in central Arctic Ocean sediment. Geophys. Res. Lett. 49, e2022GL100446. https://doi.org/10.1029/2022GL100446.

Hillaire-Marcel, C., et al., 2022b. Challenging the hypothesis of an Arctic Ocean lake during recent glacial episodes. J. Quat. Sci. 37(4), 559–567. https://doi.org/10.1002/jqs.3421.

Hillaire-Marcel, C., de Vernal, A. and Crucifix, M., 2021. Sea-level and summer season orbital insolation as drivers of Arctic sea-ice. arXiv preprint arXiv:2102.02067. https://doi.org/10.48550/arXiv.2102.02067.

Hoffmann, S. and McManus, J., 2007. Is there a ^{230}Th deficit in Arctic sediments?. Earth Planet. Sci. Lett. 258(3-4), 516–527. https://doi.org/10.1016/j.epsl.2007.04.011.

Hoffmann, S., et al., 2013. Persistent export of ^{231}Pa from the deep central Arctic Ocean over the past 35,000 years. Nature 497(7451), 603–606. https://doi.org/10.1038/nature12145.

Holmes, R. M., et al., 2002. A circumpolar perspective on fluvial sediment flux to the Arctic Ocean. Glob. Biogeochem. Cycles 16(4), 1098. https://doi.org/10.1029/2001GB001849.

Huh, C. A., et al., 1997. Natural radionuclides and plutonium in sediments from the western Arctic Ocean: sedimentation rates and pathways of radionuclides. Deep-Sea Res. II: Top. Stud. Oceanogr. 44(8), 1725–1743. https://doi.org/10.1016/S0967-0645(97)00040-4.

Hunkins, K., Thorndike, E. M. and Mathieu, G., 1969. Nepheloid layers and bottom currents in the Arctic Ocean. J. Geophys. Res. 74(28), 6995–7008. https://doi.org/10.1029/JC074i028p06995.

Ito, M., et al., 2019. Favorable conditions for suspension freezing in an Arctic coastal polynya. J. Geophys. Res. Oceans 124(12), 8701–8719. https://doi.org/10.1029/2019JC015536.

Ito, M., et al., 2021. Underwater frazil ice and its suspension depth detected from ADCP backscatter data around sea ice edge in the Sea of Okhotsk. Cold Reg. Sci. Technol. 192, 103382. https://doi.org/10.1016/j.coldregions.2021.103382.

Ivanov, V. V., et al., 2004. Dense water cascades around the World Ocean. Prog. Oceanogr. 60, 47–98. https://doi.org/10.1016/j.pocean.2003.12.002.

Ivanov, V. V. and Golovin, P. N., 2007. Observations and modeling of dense water cascading from the northwestern Laptev Sea shelf. J. Geophys. Res. Oceans 112(C9), C09003. https://doi.org/10.1029/2006JC003882.

Jakobsson, M., 2002. Hypsometry and volume of the Arctic Ocean and its constituent seas. Geochem. Geophys. Geosystems 3(5), 1–18. https://doi.org/10.1029/2001GC000302.

Jakobsson, M., et al., 2000. Manganese and color cycles in Arctic Ocean sediments constrain Pleistocene chronology. Geology 28(1), 23–26. https://doi.org/10.1130/0091-7613(2000)28%3C23:MACCIA%3E2.0.CO;2.

Jakobsson, M., et al., 2010. An Arctic Ocean ice shelf during MIS 6 constrained by new geophysical and geological data. Quat. Sci. Rev. 29(25-26), 3505–3517. https://doi.org/10.1016/j.quascirev.2010.03.015.

Jakobsson, M., et al., 2012. The international bathymetric chart of the Arctic Ocean (IBCAO) version 3.0. Geophys. Res. Lett. 39(12), L12609. https://doi.org/10.1029/2012GL052219.

Jakobsson, M., et al., 2016. Evidence for an ice shelf covering the central Arctic Ocean during the penultimate glaciation. Nat. Commun. 7(1), 10365. https://doi.org/10.1038/ncomms10365.

Jakobsson, M., et al., 2017. Post-glacial flooding of the Bering Land Bridge dated to 11 cal ka BP based on new geophysical and sediment records. Clim. Past 13(8), 991–1005. https://doi.org/10.5194/cp-13-991-2017.

Jones, E. P., Rudels, B. and Anderson, L. G., 1995. Deep waters of the Arctic Ocean: origins and circulation. Deep Sea Res. Part I Oceanogr. Res. Pap. 42(5), 737–760. https://doi.org/10.1016/0967-0637(95)00013-V.

Kageyama, M., et al., 2021. A multi-model CMIP6-PMIP4 study of Arctic sea ice at 127 ka: sea ice data compilation and model differences. Clim. Past 17(1), 37–62. https://doi.org/10.5194/cp-17-37-2021.

Karami, M. P., et al., 2021. The role of Arctic gateways on sea ice and circulation in the Arctic and North Atlantic Oceans: a sensitivity study with an ocean-sea-ice model. Clim. Dyn. 57(7), 2129–2151. https://doi.org/10.1007/s00382-021-05798-6.

Krickov, I. V., et al., 2019. Colloidal transport of carbon and metals by western Siberian rivers during different seasons across a permafrost gradient. Geochim. Cosmochim. Acta 265, 221–241. https://doi.org/10.1016/j.gca.2019.08.041.

Kipp, L. E., et al. 2018. Increased fluxes of shelf-derived materials to the central Arctic Ocean. Sci. Adv. 4(1), eaao1302. https://doi.org/10.1126/sciadv.aao1302.

Kipp, L. E., McManus, J. F. and Kienast, M., 2021. Radioisotope constraints of Arctic deep water export to the North Atlantic. Nat. Commun. 12(1), 3658. https://doi.org/10.1038/s41467-021-23877-4.

Kopp, R. E., et al., 2009. Probabilistic assessment of sea level during the last interglacial stage. Nature, 462(7275), 863–867. https://doi.org/10.1038/nature08686.

Krinner, G., et al., 2004. Enhanced ice sheet growth in Eurasia owing to adjacent ice-dammed lakes. Nature, 427(6973), 429–432. https://doi.org/10.1038/nature02233.

Kuzyk, Z. Z. A., Gobeil, C. and Macdonald, R. W., 2013. ^{210}Pb and ^{137}Cs in margin sediments of the Arctic Ocean: Controls on boundary scavenging. Glob. Biogeochem. Cycles 27(2), 422–439. https://doi.org/10.1002/gbc.20041.

Ku, T. L. and Broecker, W. S., 1965. Rates of sedimentation in the Arctic Ocean. Prog. Oceanogr. 4, 95–104. https://doi.org/10.1016/0079-6611(65)90043-1.

Ku, T. L., Mathieu, G. G. and Knauss, K. G., 1977. Uranium in open ocean: concentration and isotopic composition. Deep Sea Res. 24(11), 1005–1017. https://doi.org/10.1016/0146-6291(77)90571-9.

Lobbes, J. M., Fitznar, H. P. and Kattner, G., 2000. Biogeochemical characteristics of dissolved and particulate organic matter in Russian rivers entering the Arctic Ocean. Geochim. Cosmochim. Acta 64(17), 2973–2983. https://doi.org/10.1016/S0016-7037(00)00409-9.

Liguori, T. P. B., et al., 2021. The Transpolar Drift Influence on the Arctic Ocean Silicon Cycle. J. Geophys. Res. Oceans 126(11), e2021JC017352. https://doi.org/10.1029/2021JC017352.

Lisiecki, L. E. and Raymo, M. E., 2005. A Pliocene-Pleistocene stack of 57 globally distributed benthic δ^{18}O records. Paleoceanography 20(1), PA1003. https://doi.org/10.1029/2004PA001071.

Lisiecki, L. E. and Stern, J. V., 2016. Regional and global benthic δ^{18}O stacks for the last glacial cycle. Paleoceanography, 31(10), 1368–1394. https://doi.org/10.1002/2016PA003002.

Luo, Y. and Lippold, J., 2015. Controls on ^{231}Pa and ^{230}Th in the Arctic Ocean. Geophys. Res. Lett. 42(14), 5942–5949. https://doi.org/10.1002/2015GL064671.

Moran, S. B., et al., 2005. ^{231}Pa and ^{230}Th in surface sediments of the Arctic Ocean: Implications for ^{231}Pa/^{230}Th fractionation, boundary scavenging, and advective export. Earth Planet. Sci. Lett. 234(1-2), 235–248. https://doi.org/10.1016/j.epsl.2005.02.016.

Mosher, D. C. and Boggild, K., 2021. Impact of bottom currents on deep water sedimentary processes of Canada Basin, Arctic Ocean. Earth Planet. Sci. Lett. 569, 117067. https://doi.org/10.1016/j.epsl.2021.117067.

Niessen, F., et al., 2013. Repeated Pleistocene glaciation of the East Siberian continental margin. Nat. Geosci. 6(10), 842–846. https://doi.org/10.1038/ngeo1904.

Nozaki, Y., Horibe, Y. and Tsubota, H., 1981. The water column distributions of thorium isotopes in the western North Pacific. Earth Planet. Sci. Lett. 54(2), 203–216. https://doi.org/10.1016/0012-821X(81)90004-2.

Not, C. and Hillaire-Marcel, C., 2010. Time constraints from ^{230}Th and ^{231}Pa data in late Quaternary, low sedimentation rate sequences from the Arctic Ocean: an example from the northern Mendeleev Ridge. Quat. Sci. Rev. 29(25-26), 3665–3675. https://doi.org/10.1016/j.quascirev.2010.06.042.

Not, C. and Hillaire-Marcel, C., 2012. Enhanced sea-ice export from the Arctic during the Younger Dryas. Nat. Commun. 3(1), 647. https://doi.org/10.1038/ncomms1658.

Not, C., et al., 2012. Conservative behavior of uranium vs. salinity in Arctic sea ice and brine. Mar. Chem. 130, 33–39. https://doi.org/10.1016/j.marchem.2011.12.005.

Osterkamp, T. S. and Gosink, J. P., 2013. Observations and analyses of sediment-laden sea ice. In Barnes, P. W., Schell, D. M. and Reimnitz, E. (eds.): The Alaskan Beaufort Sea: Ecosystems and Environments. 82, Academic Press, London. https://doi.org/10.1016/C2013-0-10332-7.

Oppo, D. W., McManus, J. F. and Cullen, J. L., 2006. Evolution and demise of the Last Interglacial warmth in the subpolar North Atlantic. Quat. Sci. Rev. 25(23-24), 3268–3277. https://doi.org/10.1016/j.quascirev.2006.07.006.

Pavia, F. J., et al., 2020. Isopycnal transport and scavenging of ^{230}Th and ^{231}Pa in the Pacific Southern Ocean. Glob. Biogeochem. Cycles 34(12), e2020GB006760. https://doi.org/10.1029/2020GB006760.

Pearce, C., et al., 2017. The 3.6 ka Aniakchak tephra in the Arctic Ocean: a constraint on the Holocene radiocarbon reservoir age in the Chukchi Sea. Clim. Past 13(4), 303–316. https://doi.org/10.5194/cp-13-303-2017.

Jean-Baptiste, P. and Fourré, E., 2004. Hydrothermal activity on Gakkel Ridge. Nature, 428(6978), 36. https://doi.org/10.1038/428036a.

Pico, T., et al., 2020. Recent constraints on MIS 3 sea level support role of continental shelf exposure as a control on Indo-Pacific hydroclimate. Paleoceanogr. Paleoclimatology 35(8), e2020PA003998. https://doi.org/10.1029/2020PA003998.

Pokrovsky, O. S., et al., 2014. Fate of colloids during estuarine mixing in the Arctic. Ocean Sci. 10(1), 107–125. https://doi.org/10.5194/os-10-107-2014.

Polyak, L., et al., 2001. Ice shelves in the Pleistocene Arctic Ocean inferred from glaciogenic deep-sea bedforms. Nature 410(6827), 453–457. https://doi.org/10.1038/35068536.

Poore, R. Z., et al., 1999a. Late Pleistocene and Holocene meltwater events in the western Arctic Ocean. Geology 27(8), 759–762. https://doi.org/10.1130/0091-7613(1999)027%3C0759:LPAHME%3E2.3.CO;2.

Poore, R. Z., Ostermann, D. R. and McGeehin, J., 1999b. Stable isotope data and AMS ^{14}C dates from Arctic Ocean Section 1994 surface sediment transect and box core samples from the Mendeleyev Ridge area. US Department of the Interior, US Geological Survey.

Purcell, K., et al., 2022. Potential and limitation of ^{230}Th-excess as a chronostratigraphic tool for late Quaternary Arctic Ocean sediment studies: An example from the Southern Lomonosov Ridge. Mar. Geol. 448, 106802. https://doi.org/10.1016/j.margeo.2022.106802.

Rasmussen, T. L., et al., 2003. Late warming and early cooling of the sea surface in the Nordic seas during MIS 5e (Eemian Interglacial). Quat. Sci. Rev. 22(8-9), 809–821. https://doi.org/10.1016/S0277-3791(02)00254-8.

Raymo, M. E., et al., 2018. The accuracy of mid-Pliocene δ^{18}O-based ice volume and sea level reconstructions. Earth-Sci. Rev. 177, 291–302. https://doi.org/10.1016/j.earscirev.2017.11.022.

Reimer, P. J., et al., 2013. IntCal13 and Marine13 radiocarbon age calibration curves 0–50,000 years cal BP. Radiocarbon 55(4), 1869–1887. https://doi.org/10.2458/azu_js_rc.55.16947.

Richards, A.E., et al., 2022. Spatial and temporal variability of Atlantic Water in the Arctic from 40 years of observations. Geophys. Res. Oceans 127, e2021JC018358. https://doi.org/10.1029/2021JC018358.

Rippeth, T. and Fine, E., 2022. Turbulent mixing in a changing Arctic Ocean. Oceanography 35(2). https://doi.org/10.5670/oceanog.2022.103.

Roca Martí, M., 2017. Carbon export from the upper water column of the polar oceans by using natural radionuclides. PhD Thesis, Universitat Autònoma de Barcelona, Cerdanyola del Vallès.

Rogge, A., et al., 2022. Carbon dioxide sink in the Arctic Ocean from cross-shelf transport of dense Barents Sea water. Nat. Geosci. 16, 82–88. https://doi.org/10.1038/s41561-022-01069-z.

Roy-Barman, M., 2009. Modelling the effect of boundary scavenging on Thorium and Protactinium profiles in the ocean. Biogeosciences, 6(12), 3091–3107. https://doi.org/10.5194/bg-6-3091-2009.

Rudels, B., 2011. Arctic Ocean circulation and variability-advection and external forcing encounter constraints and local processes. Ocean Sci. Discuss. 8(2), 261–286. https://doi.org/10.5194/os-8-261-2012.

Rudels, B., et al., 2012. Observations in the ocean. In Lemke, P. and Jacobi, HW. (eds.): Arctic Climate Change. 43, 117–198, Springer, Dordrecht. http://dx.doi.org/10.1007/978-94-007-2027-5_4.

Rudels, B. and Carmack, E., 2022. Arctic Ocean water mass structure and circulation. Oceanography 35(3/4), 52–65.

Scholten, J. C., Van Der Loeff, M. M. R. and Michel, A., 1995. Distribution of ^{230}Th and ^{231}Pa in the water column in relation to the ventilation of the deep Arctic basins. Deep-Sea Res. II: Top. Stud. Oceanogr. 42(6), 1519–1531. https://doi.org/10.1016/0967-0645(95)00052-6.

Schulz, K., et al., 2021. Turbulent mixing and the formation of an intermediate nepheloid layer above the Siberian continental shelf break. Geophys. Res. Lett. 48(9), e2021GL092988. https://doi.org/10.1029/2021GL092988.

Somayajulu, B. L. K., Sharma, P. and Herman, Y., 1989. Thorium and uranium isotopes in Arctic sediments. In Herman, Y. (eds.): The Arctic Seas. 571–579, Springer, Boston, MA. https://doi.org/10.1007/978-1-4613-0677-1_22.

[dataset]Song, T., et al., 2022a. Sedimentology, mineralogy, and geochemistry results of core Arc7-E25 from southern Mendeleev Ridge, Arctic Ocean. PANGAEA. https://doi.org/10.1594/PANGAEA.949846.

Song, T., et al., 2022b. A reassessment of Nd-isotopes and clay minerals as tracers of the Holocene Pacific water flux through Bering Strait. Mar. Geol. 443, 106698. https://doi.org/10.1016/j.margeo.2021.106698.

Spielhagen, R. F., et al., 2022. No freshwater-filled glacial Arctic Ocean. Nature 602 (7895), E1–E3. https://doi.org/10.1038/s41586-021-04089-8.

Stein, R., 2008. Arctic Ocean sediments: processes, proxies, and paleoenvironment. In Chamley, H. (eds.): Developments in Marine Geology. 82–83, Elsevier, Oxford.

Stein, R., et al., 2017. Arctic Ocean sea ice cover during the penultimate glacial and the last interglacial. Nat. Commun. 8(1), 373. https://doi.org/10.1038/s41467-017-00552-1.

Strobl, C., 1998. Datierung von Sedimentkernen und Rekonstruktion der Transportwege der Radionuklide ^{10}Be, ^{230}Th und ^{231}Pa in hohen nördlichen Breiten. PhD Thesis, Ruprecht-Karls-Universität, Heidelberg.

Suman, D. O. and Bacon, M. P., 1989. Variations in Holocene sedimentation in the North American Basin determined from ^{230}Th measurements. Deep Sea Res. Part I Oceanogr. Res. Pap. 36(6), 869–878. https://doi.org/10.1016/0198-0149(89)90033-2.

Trimble, S. M., Baskaran, M. and Porcelli., D., 2004. Scavenging of thorium isotopes in the Canada Basin of the Arctic Ocean. Earth Planet. Sci. Lett. 222(3-4), 915–932. https://doi.org/10.1016/j.epsl.2004.03.027.

Valk, O., et al., 2018. Importance of hydrothermal vents in scavenging removal of ^{230}Th in the Nansen Basin. Geophys. Res. Lett. 45(19), 10539–10548. https://doi.org/10.1029/2018GL079829.

Valk, O., et al., 2020. Decrease in ^{230}Th in the Amundsen Basin since 2007: far-field effect of increased scavenging on the shelf?. Ocean Sci. 16(1), 221–234. https://doi.org/10.5194/os-16-221-2020.

Van Nieuwenhove, N. and Bauch, H. A., 2008. Last interglacial (MIS 5e) surface water conditions at the Vøring Plateau (Norwegian Sea), based on dinoflagellate cysts. Polar Res. 27(2), 175–186. https://doi.org/10.1111/j.1751-8369.2008.00062.x.

de Vernal, A., et al., 2020. Natural variability of the Arctic Ocean sea ice during the present interglacial. Proc. Natl. Acad. Sci. U.S.A. 117(42), 26069–26075. https://doi.org/10.1073/pnas.2008996117.

Vetrov, A. A. and Romankevich, E. A., 2019a. Distribution, Fluxes, and Balance of Particulate Organic Carbon in the Arctic Ocean. Oceanology, 59(4), 491–499. https://doi.org/10.1134/S0001437019040180.

Vetrov, A. A. and Romankevich, E. A., 2019b. Distribution and fluxes of dissolved organic carbon in the Arctic Ocean. Polar Res. 38, 3500. https://doi.org/10.33265/polar.v38.3500.

Wefing, A.M., et al., 2020. Circulation timescales of Atlantic Water in the Arctic Ocean determined from anthropogenic radionuclides. Ocean Sci. 17(1), 111–129. https://doi.org/10.5194/os-17-111-2021.

Wegner, C., et al., 2015. Variability in transport of terrigenous material on the shelves and the deep Arctic Ocean during the Holocene. Polar Res. 34(1), 24964. https://doi.org/10.3402/polar.v34.24964.

Weigelt, E., Jokat, W. and Eisermann, H., 2020. Deposition History and Paleo-Current Activity on the Southeastern Lomonosov Ridge and its Eurasian Flank Based on Seismic Data. Geochem. Geophys. Geosystems 21(11), e2020GC009133. https://doi.org/10.1029/2020GC009133.

West, G., et al., 2023. Amino acid racemization in Neogloboquadrina pachyderma and Cibicidoides wuellerstorfi from the Arctic Ocean and its implications for age models. Geochronology 5(1), 285–299. https://doi.org/10.5194/gchron-5-285-2023.

Wetterich, S., et al., 2016. Ice complex permafrost of MIS5 age in the Dmitry Laptev Strait coastal region (East Siberian Arctic). Quat. Sci. Rev. 147, 298–311. https://doi.org/10.1016/j.quascirev.2015.11.016.

Wetterich, S., et al., 2020. The cryostratigraphy of the Yedoma cliff of Sobo-Sise Island (Lena delta) reveals permafrost dynamics in the central Laptev Sea coastal region during the last 52 kyr. The Cryosphere 14(12), 4525–4551. https://doi.org/10.5194/tc-14-4525-2020.

Wheeler, P. A., et al., 1996. Active cycling of organic carbon in the central Arctic Ocean. Nature, 380(6576), 697–699. https://doi.org/10.1038/380697a0.

Williford, T., et al., 2022. Spatial complexity in dissolved organic matter and trace elements driven by hydrography and freshwater input across the Arctic Ocean during 2015 Arctic GEOTRACES expeditions. J. Geophys. Res. Oceans 127, e2022JC018917. https://doi.org/10.1029/2022JC018917.

Woodgate, R. A., et al., 2001. The Arctic Ocean boundary current along the Eurasian slope and the adjacent Lomonosov Ridge: Water mass properties, transports and transformations from moored instruments. Deep Sea Res. Part I Oceanogr. Res. Pap. 48(8), 1757–1792. https://doi.org/10.1016/S0967-0637(00)00091-1.

Xiang, Y. and Lam, P. J., 2020. Size-Fractionated Compositions of Marine Suspended Particles in the Western Arctic Ocean: Lateral and Vertical Sources. J. Geophys. Res. Oceans 125(8), e2020JC016144. https://doi.org/10.1029/2020JC016144.

Xiao, X., Stein, R. and Fahl, K., 2015. MIS 3 to MIS 1 temporal and LGM spatial variability in Arctic Ocean sea ice cover: Reconstruction from biomarkers. Paleoceanography, 30(7), 969–983. https://doi.org/10.1002/2015PA002814.

Xiao, W., et al., 2021. A sedimentary record from the Makarov Basin, Arctic Ocean, reveals changing middle to Late Pleistocene glaciation patterns. Quat. Sci. Rev. 270, 107176. https://doi.org/10.1016/j.quascirev.2021.107176.

Xiao, W., et al., 2022. Reply to comment by Hillaire-Marcel and de Vernal on "A sedimentary record from the Makarov Basin, Arctic Ocean, reveals changing middle to late Pleistocene glaciation patterns"[Quat. Sci. Rev., 270 (2021), p. 107176]. Quat. Sci. Rev. 276, 107298. https://doi.org/10.1016/j.quascirev.2021.107298.

Xu, Q., et al., 2021. Driving Mechanisms of Sedimentary ^{230}Th and ^{231}Pa Variability in the Western Arctic Ocean Through the Last Glacial Cycle. Paleoceanogr. Paleoclimatol. 36(7), e2020PA004039. https://doi.org/10.1029/2020PA004039.

Yang, H. S., et al., 1986. The distribution of ^{230}Th and ^{231}Pa in the deep-sea surface sediments of the Pacific Ocean. Geochim. Cosmochim. Acta 50(1), 81–89. https://doi.org/10.1016/0016-7037(86)90050-5.

Ye, L., et al., 2020. Ice events along the East Siberian continental margin during the last two glaciations: Evidence from clay minerals. Mar. Geol. 428, 106289. https://doi.org/10.1016/j.margeo.2020.106289.

Zhang, X., et al., 2021. Adsorption of Th and Pa onto particles and the effect of organic compounds in natural seawater. J. Oceanol. Limnol. 39(6), 2209–2219. https://doi.org/10.1007/s00343-021-0297-5.

Zimmermann, H. H., et al., 2017. Sedimentary ancient DNA and pollen reveal the composition of plant organic matter in Late Quaternary permafrost sediments of the Buor Khaya Peninsula (north-eastern Siberia). Biogeosciences, 14(3), 575–596. https://doi.org/10.5194/bg-14-575-2017.

Table 3.1 Overview of factors influencing ^{230}Th cycling in the Arctic Ocean.

Parameter	Effective role	Status		Reference
		Glacial	Interglacial	
River discharge	Fine particule and DOC supplies		√	Holmes et al., 2002
Coastal erosion	Particulate supply		√	Wegner et al., 2015
Boundary scavenging	^{230}Th burial & resuspension over continental shelves	on slopes?	√	Edmonds et al., 2004; Moran et al., 2005; Kuzyk et al., 2013
Sediment resuspension over shelves	Entrainment into fragile sea ice and lateral transportation		√	Baskaran, 2005; Charette et al., 2020; Drits et a., 2021
Brines	Coagulation of organic matter with ^{230}Th adsorption		√	Evans and Nishioka, 2016; Ito et al., 2019, 2021
Seasonal sea-ice melting	Fine particle release and phytoplankton blooms		√	Kipp et al., 2018; Fadeev et al., 2020;
Ice streaming	Glacial erosion and unsorted detrital supplies	√		Polyak et al., 2001; Jakobsson et al., 2010, 2016; Purcell et al., 2022
Isopycnal transportatioon	Brines mixing with Atlantic Water		√	Pavia et al., 2020
Hydrothermal fluid	Sporadic scavenging	√	√	Valk et al., 2018; Gdaniec et al., 2020
Pacific Water inflow	Chukchi Sea role		√	Kuzyk et al., 2013
Atlantic water inflow and deep water export	Export of ^{230}Th	√	reduced	Moran et al., 2005; Hoffmann et al., 2013; Gdaniec et al., 2020; Valk et al., 2020
Deep overflowing currents	Fine particle and compound winnowing on ridge crests		√	Björk et al., 2007, 2010
Reversible scavenging	Desorption at the water-sediment interface	√	√	Trimble et al., 2004; Gdaniec et al., 2020; Valk et al., 2020
Intermediate and bottom currents	Re-suspension of scavenged particles and compounds	reduced	√	Xiang and Lam, 2020; Schulz et al., 2021; Gardner et al., 2022;
Turbidity and contour currents	Winnowing of fine particles and compounds	Enhanced?	√	Mosher and Boggild, 2021

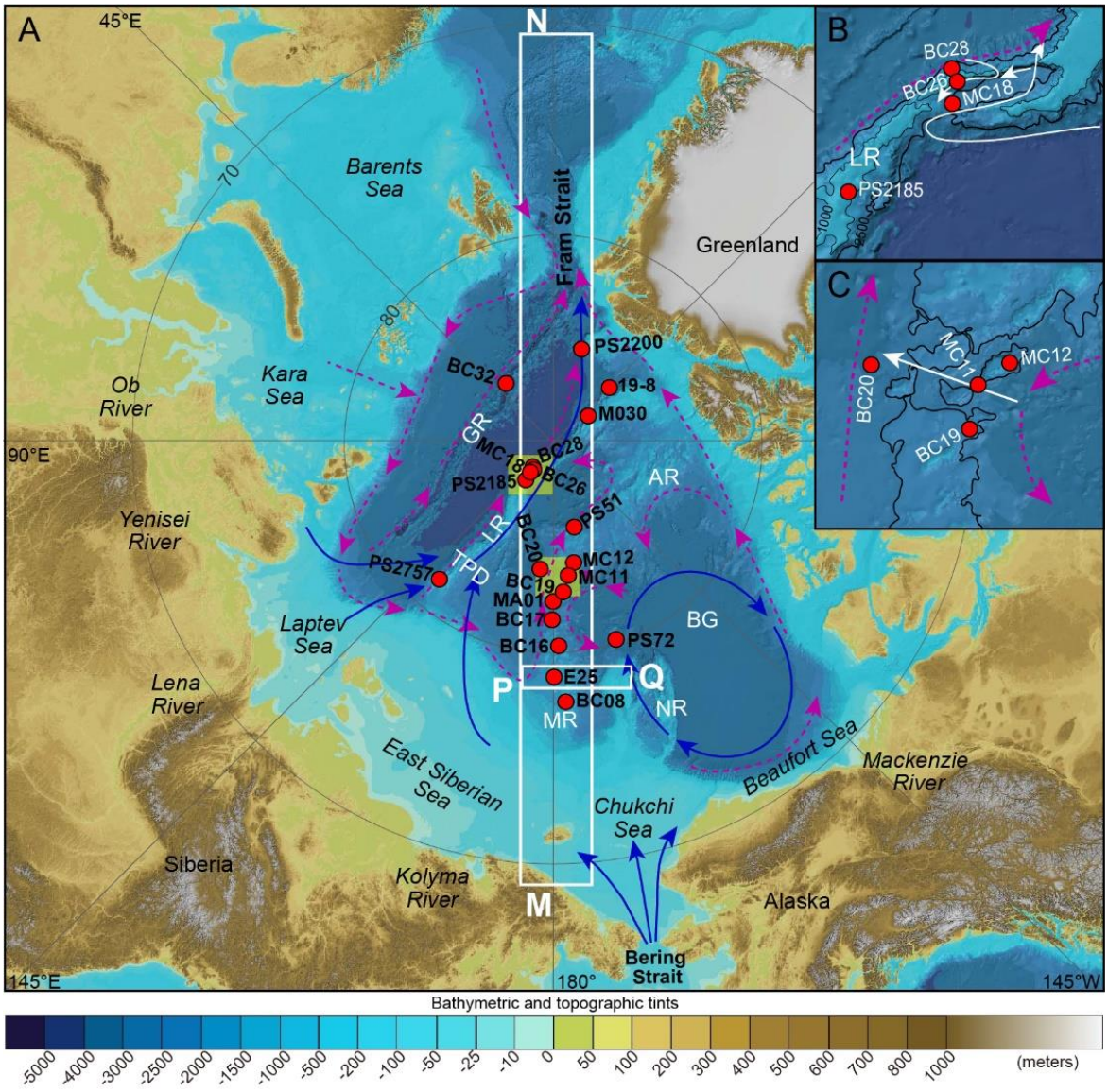

Figure 3-1 A) Bathymetric map of the Arctic Ocean and major circulation features. Red dots: location of all cited cores (from Somayajulu et al., 1989; Huh et al., 1997; Strobl, 1998; Hoffmann and McManus, 2007; Not and Hillaire-Marcel, 2010, 2012; Hoffmann et al., 2013; Hillaire-Marcel et al., 2017; Geibert et al., 2021; Xu et al., 2021; Purcell et al., 2022; Song et al., 2022a); blue arrows: major surface circulation pathways; purple dashed arrows: intermediate and deep currents pathways (Rudels, 2011; Mosher and Boggild, 2021); AR: Alpha Ridge; BG: Beaufort Gyre; GR: Gakkel Ridge; LR: Lomonosov Ridge; MR: Mendeleev Ridge; NR: Northwind Ridge; TPD: Transpolar Drift. B) Closer view of sites from the Lomonosov Ridge, central Arctic Ocean, with intermediate currents paths (white arrows) based on Björk et al. (2007, 2010). C) Closer view of sites from northern Mendeleev Ridge, with the Canadian Basin Deep Water path in white arrows (Rudels et al., 2012). M-N: section along 180˚E; P-Q: cross-section over core Arc7-E25 (hereafter named E25). The names of the cited cores are abbreviated in the map. The full names are provided in the main text.

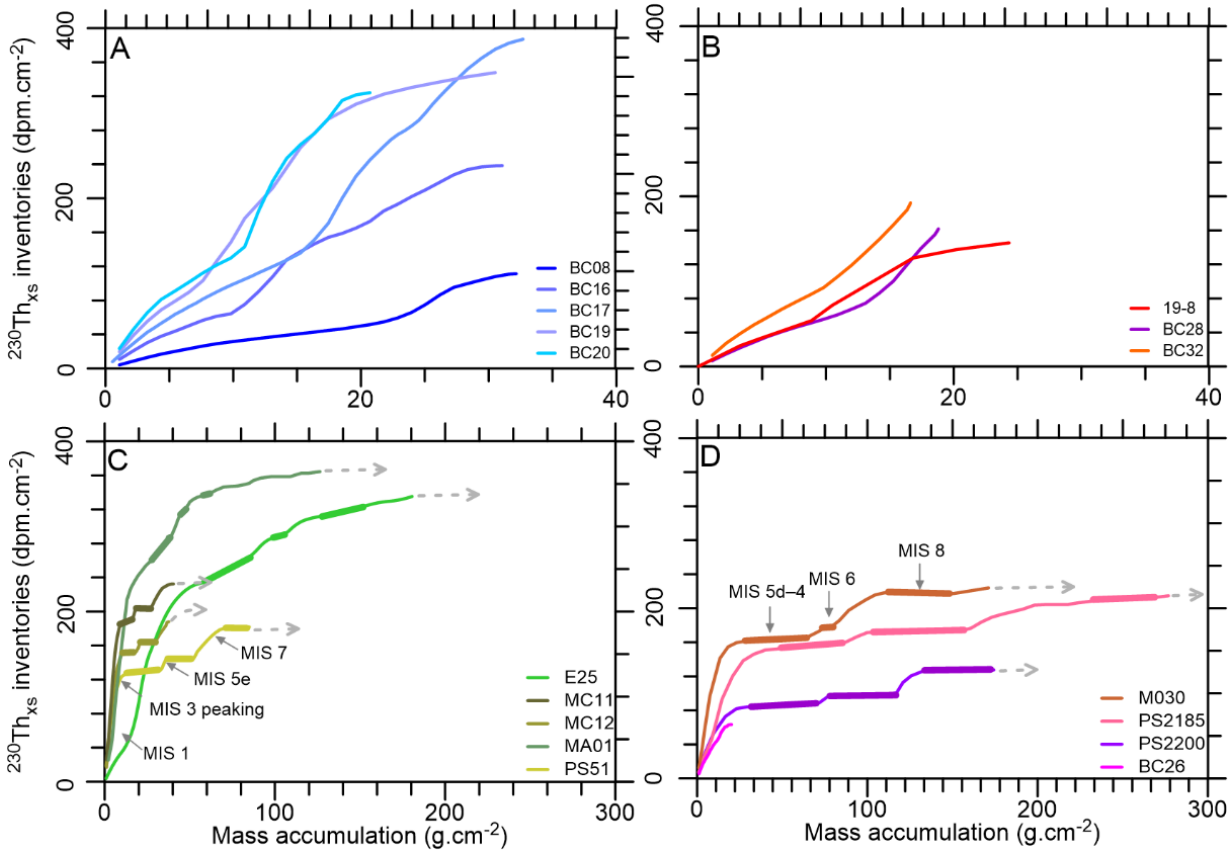

Figure 3-2 $^{230}Th_{xs}$ inventories vs sediment mass accumulation at low sedimentation rate sites (<2 cm.kyr^{-1}). Here, sediment mass accumulation is used as the x-axis to avoid $^{230}Th_{xs}$ inventory biases related to the variability of sediment density downcore. Upper graphs A and B: sequences spanning MIS 3–1; lower graphs C and D: low accumulation rate sites with sequences spanning several climatic cycles; left graphs A and C: sites from the western Arctic Ocean mainly influenced by the BG; right graphs B and D: sites from the eastern Arctic Ocean influenced by the TPD. Line thickenings illustrate gaps or reduced $^{230}Th_{xs}$ burial rates during glacial intervals. Sites PS2757 and MC18 are not illustrated here as they depict significantly higher accumulation rates (>2.5 cm.kyr^{-1}) and $^{230}Th_{xs}$ inventories (>500 dpm.cm^{-2}) (see ANNEXE C Figures A.3 and A.4).

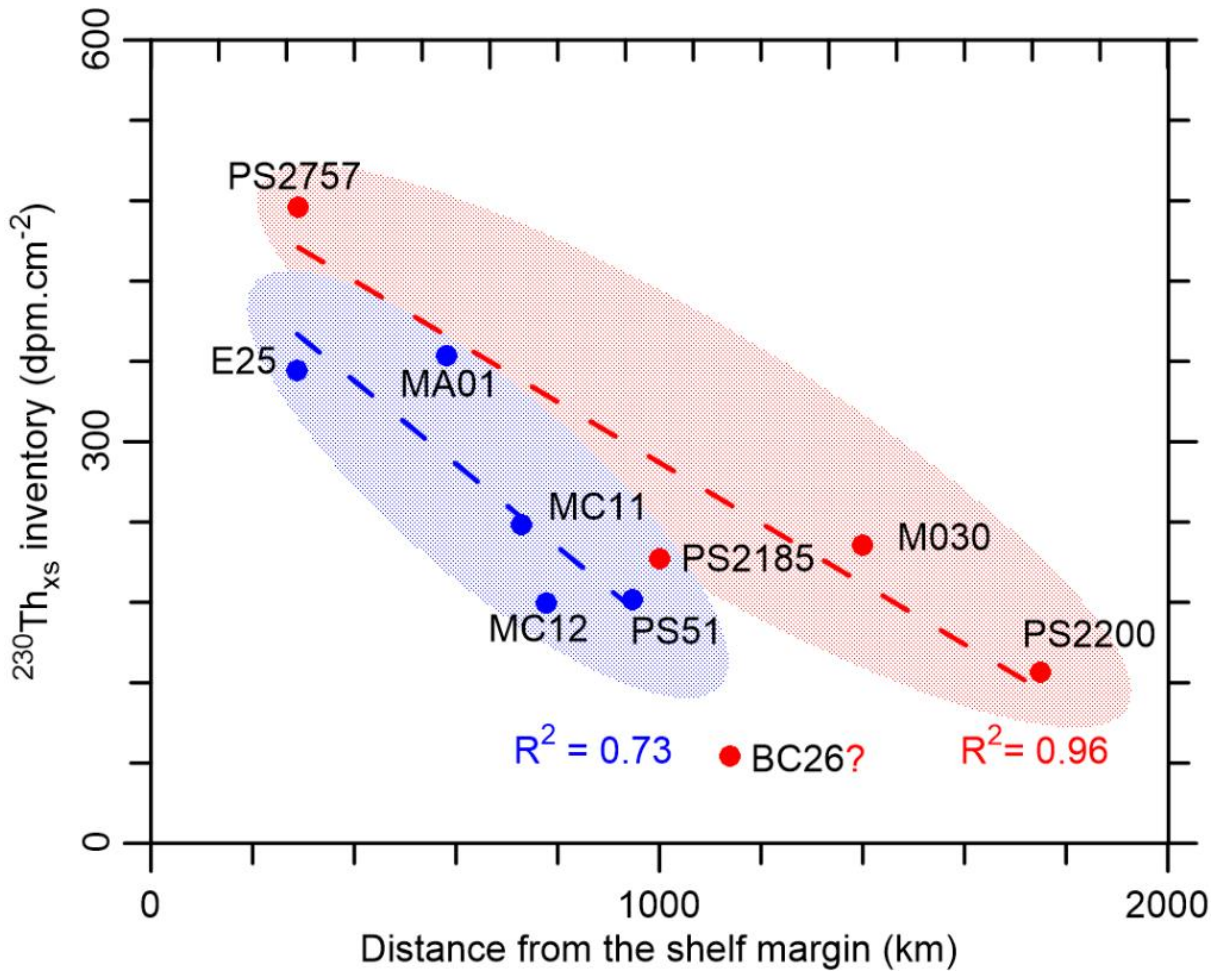

Figure 3-3 $^{230}Th_{xs}$ inventories at sites where an asymptotic value has been approximately reached vs the distance from the Russian margin. Two clusters can be identified along the surface circulation patterns: BG-cluster (in blue) and TPD-cluster (in red).

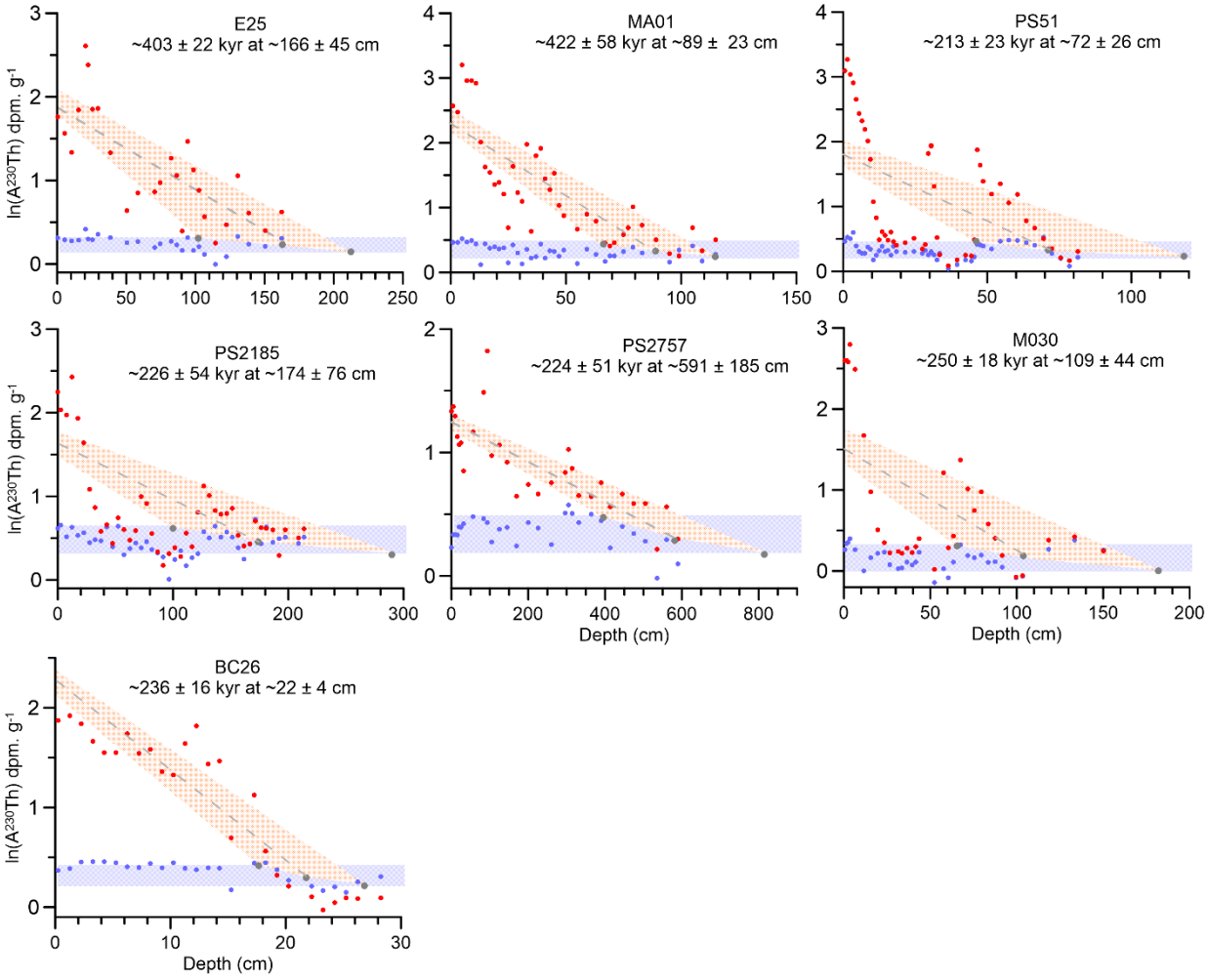

Figure 3-4 ^{230}Th extinction age and depth estimates using a constant decay model for the seven sequences with suitable resolution and time span (data from Strobl, 1998; Not and Hillaire-Marcel, 2010; Hoffmann et al., 2013; Hillaire-Marcel et al., 2017; Geibert et al., 2021; Xu et al., 2021; Purcell et al., 2022; Song et al., 2022a). Blue dot: ln($A^{234}U$); blue shadow area: supported ln($A^{230}Th$) estimated based on the standard deviation of ln($A^{234}U$); red dot: ln($A^{230}Th$); grey dashed line: linear regression of ln($A^{230}Th$); orange shadow area: standard deviation of the linear regression line. ^{230}Th extinction ages and their depths uncertainties are indicated below core numbers.

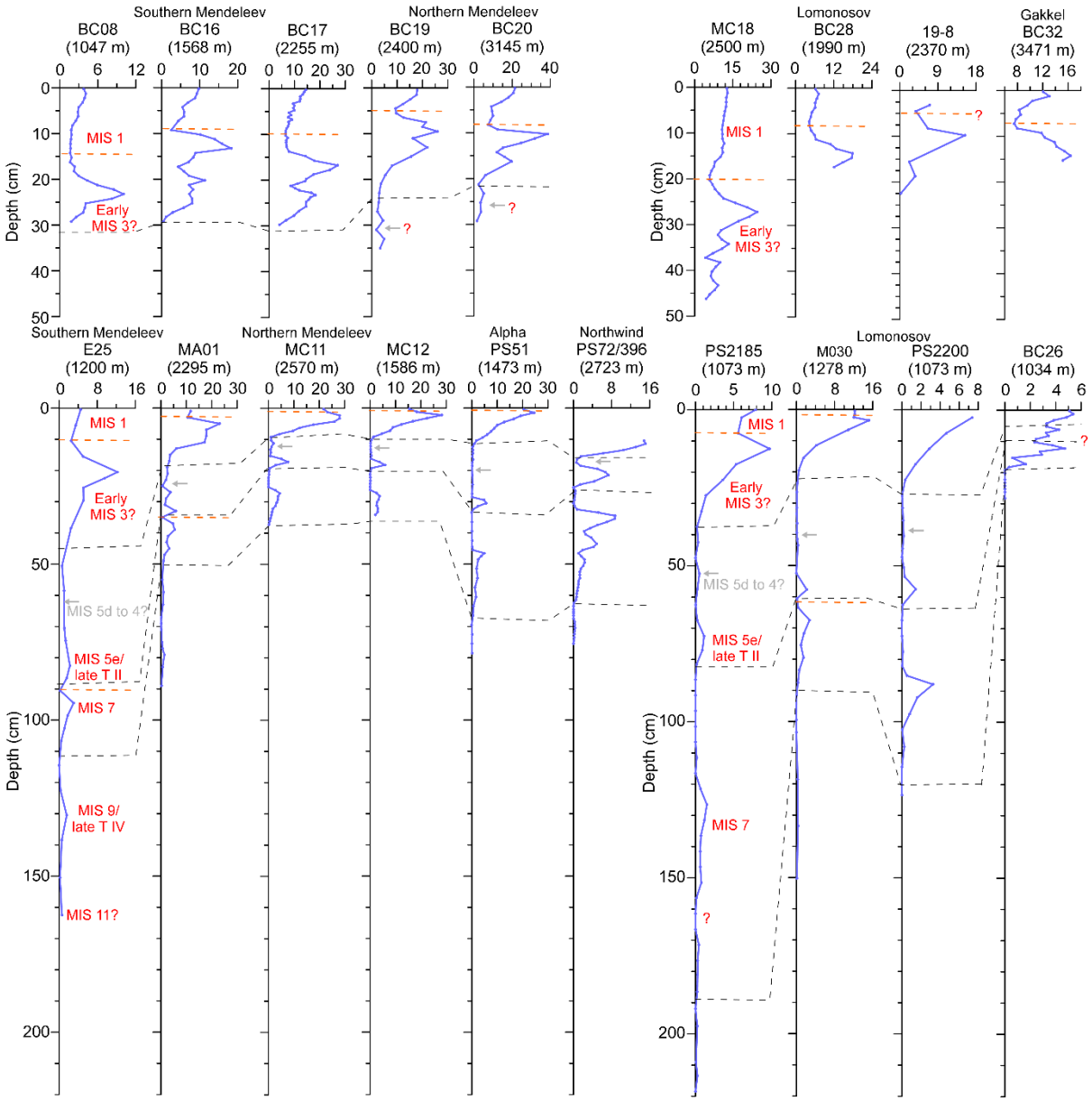

Figure 3-5 $^{230}Th_{xs}$ (in dpm.g^{-1}) distribution in sedimentary sequences of the Arctic Ocean. Below core names, the water depths of the coring sites are indicated. The records in the upper part of the figure encompass MIS 3 to 1. The records in the lower part of the figure span a longer time interval. The orange dashed lines point to the MIS 2 hiatus and locally recorded MIS 6 hiatus; the black dashed lines correspond to tentative depth estimates of the MIS 4/3 transition, MIS 5e/late Termination II, and MIS 7/late termination III.

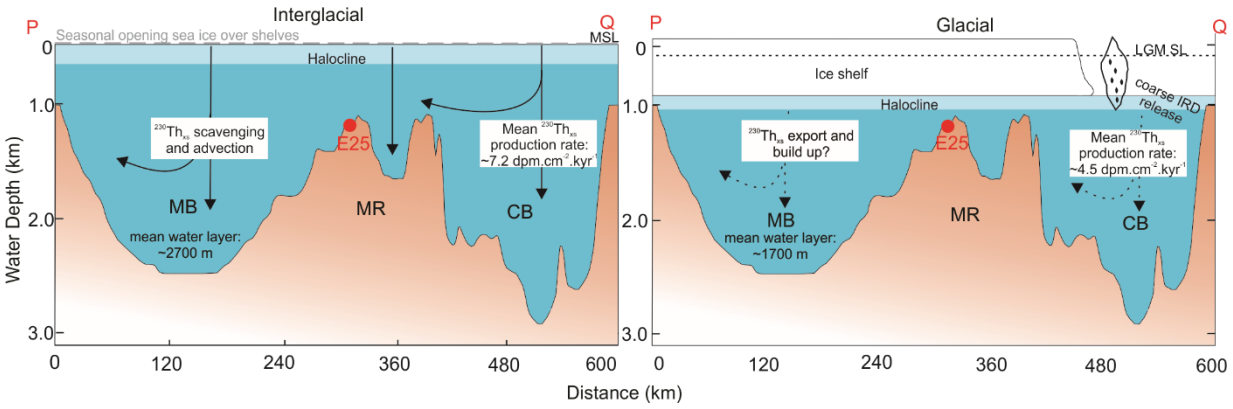

Figure 3-6 Sketch of the 230Thxs production in the Arctic Ocean during interglacial and glacial intervals. The location of section P-Q could be seen in Figure 1A. Red dot: location of core E25. CB: Canadian Basin; MB: Makarov Basin; MR: Mendeleev Ridge; MSL: Modern Sea Level; SL: sea level.

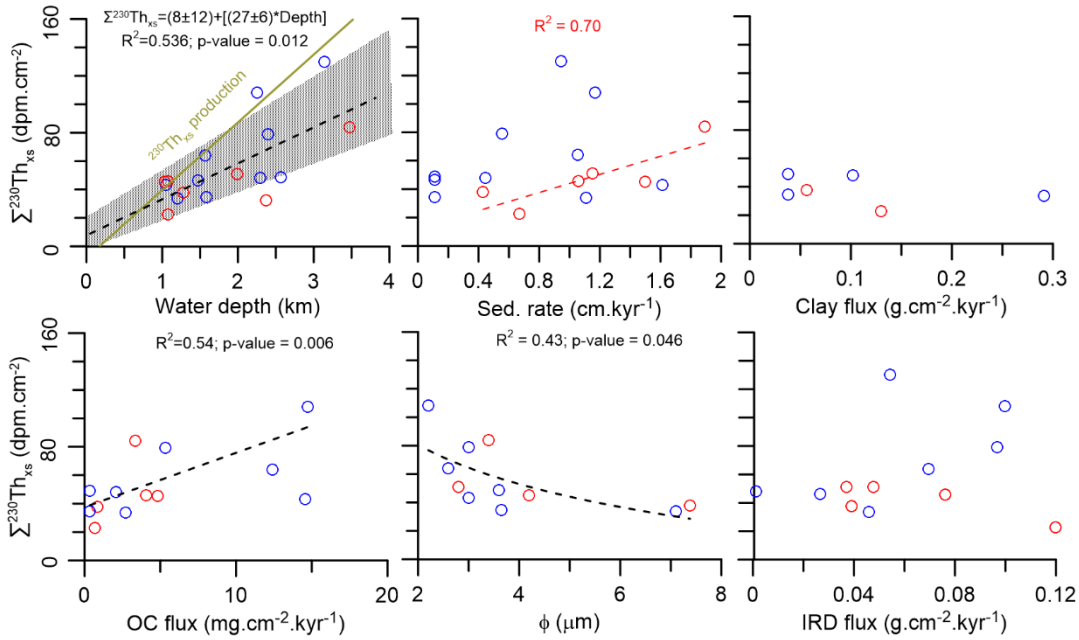

Figure 3-7 The post-LGM $^{230}Th_{xs}$ inventories vs physical and chemical parameters in low sediment accumulation rate sites. Correlation coefficients and p-values are reported when significant. Blue circles: datasets from the BG cluster; red circles: datasets from the TPD cluster; black line: regression trend based on both datasets; olive line: estimated ^{230}Th production over the past 21 kyr; red dashed line: linear regression based on the TPD dataset; Φ: mean grain size; IRD: larger than 63 μm fractions. The sedimentation rate and all fluxes have been set assuming that the post-LGM layer mostly includes sediments deposited since 9 cal. kyr BP (see text in subchapter 3.4.5.1).

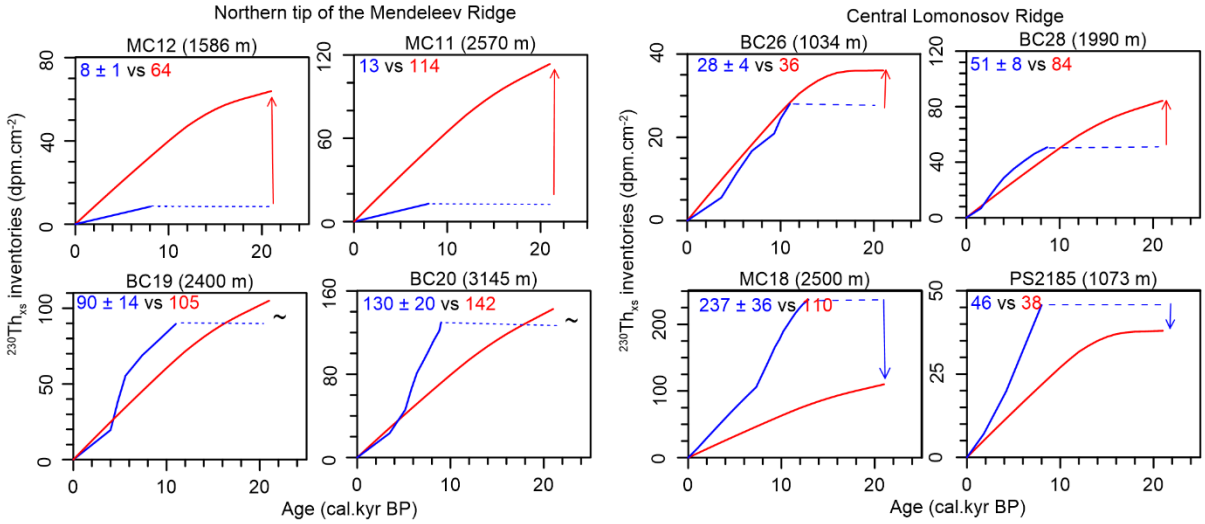

Figure 3-8 Post-LGM $^{230}Th_{xs}$ inventories vs ^{230}Th production in the overlying water column (^{230}Th-rain) in cores from Lomonosov and Mendeleev ridge areas. Inventories are estimated to mostly represent sediment and $^{230}Th_{xs}$ accumulation during the last 9 kyr; the ^{230}Th-rain is calculated since the end of the LGM (21 kyr). Blue lines and numbers: $^{230}Th_{xs}$ inventory in cores; red lines and numbers: ^{230}Th-rain; blue arrows: $^{230}Th_{xs}$ inventory above the ^{230}Th-rain; red arrows: $^{230}Th_{xs}$ inventory below the ^{230}Th-rain.

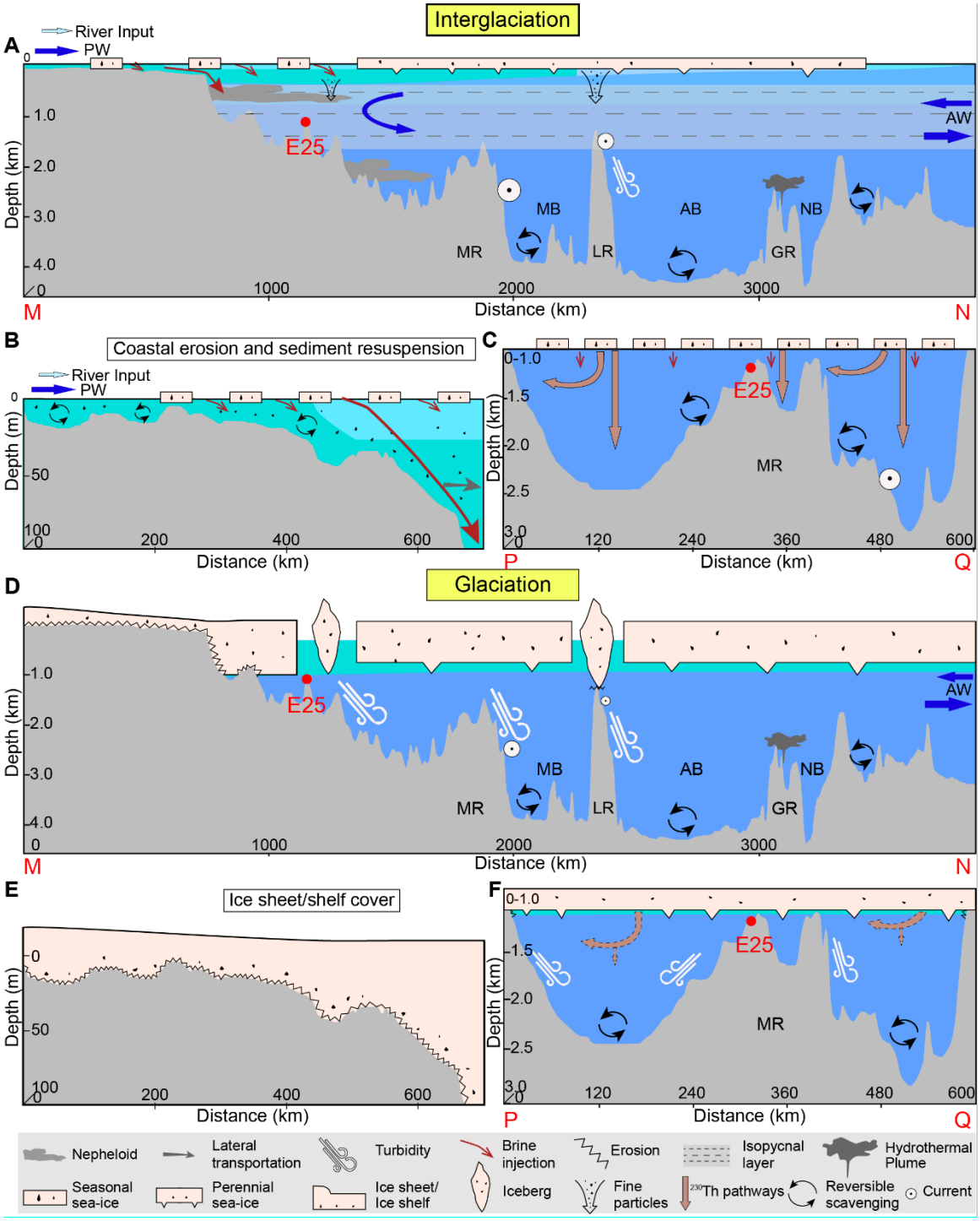

Figure 3-9 Sketch of the cycling of ^{230}Th in the water column of the Arctic Ocean under different climate conditions. A, B, C): interglacial/interstadial; D, E, F) glacial/stadial; A, D): along the 180º transect of the Arctic Ocean; B, E): Siberian continental shelf; C, F): cross-section through site E25 from the southern Mendeleev Ridge. The red dot marks the location of core E25.

CONCLUSION

The Arctic Ocean has experienced significant paleoceanographic and sedimentological changes at the Milankovitch time scale in response to driving parameters, such as insolation and sea level changes in particular. It has varied from a semi-enclosed basin during glacials, with the development of ice shelves, reduced exchanges with the North Atlantic (e.g., Geibert et al., 2021; Hillaire-Marcel et al., 2022b), and nil exchange with the Pacific Ocean due to the closure of Bering Strait (Jakobsson et al., 2017), to a major player in the exchanges with the Pacific to Atlantic oceans during interglacials (de Vernal et al., 2020), whereas the dynamics of its sea-ice/ice cover has governed the albedo of the high latitude Northern Hemisphere (Stein et al., 2017b).

Despite many paleoceanographic studies, attempts at reconstructing the recent glacial/interglacial history of the Arctic Ocean from deep-sea archives have been hampered by conflictual geochronologies (e.g., Spielhagen et al., 1997, 2004) and, more importantly, by the fact that these archives present major discontinuities through time (Purcell et al., 2022).

As a consequence, the temporal and spatial variations of sea ice and their impact on sedimentation processes have not been fully elucidated. Similarly, studies concerning the estimation of Pacific Water flux through the Bering Strait in the past are sparse.

The present thesis has thus been undertaken to use relatively new tools for the analysis of sedimentary sequences that would provide a fresh look at the sedimentary processes involved and their temporal variability. $^{230}Th_{xs}$ records have been used to shed light on sedimentary processes, as well as to put constraints on radioactivity-based time estimates, whereas Nd-isotopes and, to a lesser extent, clay mineralogy, were used to document the fluxes and role of Pacific Water during warm intervals.

More specific objectives were: i) to evaluate the role that sea ice production over the submerged continental shelves played in governing sediment fluxes to the central Arctic Ocean, ii) to reconstruct the Pacific Water inflow history during the present Interglacial, and iii) to infer deep sedimentary processes from $^{230}Th_{xs}$ records.

The results obtained so far further illustrate sporadic sedimentation episodes relating to seasonal open sea ice conditions over shelves, i.e., under high sea level and peaking summer season insolation, during warm intervals (interglacials and possibly some interstadials) when Bering Strait was opened allowing "warm" but relatively freshwater fluxes from the Pacific Ocean to impact freshwater budgets as far as the North Atlantic deep convection sites, governing the Atlantic Meridional Overturning Circulation, aside from boosting significantly primary productivity in the western Arctic Ocean. Sedimentation in the central Arctic Ocean is then discontinuous and no time interpolations could be made for a specific time span to establish "high-resolution" paleoceanographic reconstructions.

Due to the difficulty in defining high-resolution time frames for the warm intervals, investigations about the impact of a progressive increase in Pacific Water fluxes accompanying the progressive rise in sea level have been focused on the present interglacial, with records supported by a robust radiocarbon chronology (first chapter). Our findings here illustrate the late attainment of maximum Pacific Water flux during the present interglacial, at ~4 ka BP, i.e., several thousand years after the insolation peak, at a time when the trend towards the Neoglacial started (de Vernal et al, 2020). The major factors governing the millennial variability of sea ice in the western Arctic Ocean are then more complicated than previously expected. Besides the heat flow through Pacific Water input (Stein et al., 2017a), other factors, such as solar radiation, atmospheric circulation patterns, and river discharge, could also exert an important role (Deschamps et al., 2019; Dong et al., 2022).

Thorium-230 has been used as a normalization tool for the estimation of sedimentation fluxes in global oceans based on a constant ^{230}Th flux model (e.g., Costa et al., 2020). Unlike in the open ocean, sedimentary fluxes in the deep Arctic Ocean are closely linked to sea ice-rafting deposition, resulting in drastically distinct ^{230}Th sedimentation regimes under glacial vs interglacial conditions. The peaking $^{230}Th_{xs}$ contents in the interglacial/interstadial layers are linked to i) sea ice production over the submerged continental shelves (Hillaire-Marcel et al., 2017), ii) enhanced fine particle fluxes, iii) high organic matter fluxes relating to high primary production and to continental dissolved organic matter supplies from river discharge, and iv) brine sinking and deep currents, as documented in our third chapter. During glacial, we have estimated an average 40% reduction in ^{230}Th production in the water column, relating to the presence of a ~ 1 km-thick ice shelf, low sea levels, and coarse particles sporadically supplied by icebergs (e.g., Xu et

al., 2021; Hillaire-Marcel et al., 2022b). Under such conditions, very low to even nil $^{230}Th_{xs}$ contents mark glacial layers (e.g., Not and Hillaire-Marcel, 2010; Geibert et al., 2021).

In combination with the ^{230}Th extinction age, the $^{230}Th_{xs}$ distribution downcore could provide a reliable chronostratigraphic frame (Purcell et al., 2022), up to MIS 11, for sites with low sedimentation rates. As illustrated in chapters 2 and 3, $^{230}Th_{xs}$ records, mainly from the Mendeleev, Lomonosov, and Northwind ridges, indeed point to low mean sedimentation rates, of the order of ~2 to 4 $mm.kyr^{-1}$, rates similar to those proposed by Clark et al. (1980) from paleomagnetic records. This leads to challenging the high sedimentation rate scenario, mostly based on ecostratigraphic markers (e.g., Backman et al., 2009), correlations between sites using the Mn-oxide cyclostratigraphy proposed by Jakobsson et al. (2000), and therefore, the re-interpretation of paleomagnetic records proposed in these studies. As a result, most of the Arctic paleoceanographic reconstructions published over the past 20 years should be carefully revised as their age models are much younger than expected (see also Smith et al., 2022; West et al., 2023).

Comparisons of the $^{230}Th_{xs}$ inventories between sites from the northern Mendeleev Ridge and central Lomonosov Ridge, suggest that winnowing by sinking brines and through the overflow of deep high salinity waters from the western Arctic Ocean towards the Eurasian basin, results in sediment removal over ridges and its deposition in deep basins. Such processes further mix the residual sediment and fossils over ridges up to tens of thousands of years, limiting the usage of radiogenic carbon-14 ages and microfossils as unequivocal age assignments and paleoceanographic reconstruction tools in the deep Arctic Ocean (Hillaire-Marcel et al., 2022a). Special attention should then be paid to the interpretation of sedimentary archives of the Arctic Ocean as they may represent a mixture of temporal and spatial components. In addition, sedimentation hiatuses at MIS 2 (Not and Hillaire-Marcel, 2010), possibly MIS 6 (Hillaire-Marcel et al., 2017) and older intervals (this thesis) documented in some sites of the central Arctic Ocean may be attributed to either negligible sediment fluxes under severe ice cover or to fine particle winnowing relating to active deep currents. If the latter played an important role, sedimentary sequences from deep Arctic basins may preserve more marine deposits than ridges and would be more suitable for paleoceanographic and sedimentological reconstructions, although possibly recording temporally reversed reworked sediments from ridges.

In the second chapter, a closer look was paid to the history of a glacier or a thick-ice shelf over and/or off the East Siberian Sea, proposed in earlier studies (e.g., Niessen et al., 2013), based on a detailed sedimentological and geochemical analysis of a sequence from the southernmost Mendeleev Ridge. Our findings strongly suggest a glaciated Arctic Ocean, over most of the late Pleistocene, probably spanning the MIS 14 to MIS 4 interval, marked by the presence of a resilient East Siberian Ice Shelf/Ice Sheet anchored over the East Siberian-Chukchi Plateau areas, only interrupted during short interglacial time windows. This assumption is consistent with the low maximums in summer season insolation following MIS 15 (Hillaire-Marcel et al., 2021). If the occurrence of seasonally open sea ice conditions linked to these maximum insolation/high sea level intervals cannot be discarded, distinct sediment features still suggest the resilience of an ice cover. Whereas sea ice-rafting depositions appear to be the dominant sedimentation process during some "warm" intervals (MIS 7, MIS 3, and MIS 1), fine particles transported by bottom currents are observed during the MIS 11, MIS 9, and MIS 5e episodes, thus not necessarily discarding the possibility of the presence of some resilient ice cover in the area. At last, under full glacial conditions, sporadic sedimentation relating to ice advance or retreat intervals may have occurred.

More evidence from other sea ice proxies, such as the sterol biomarker-IP_{25} and microfossil abundances, would be helpful to further document sea ice conditions in the Arctic Ocean during the late Pleistocene. However, the utilization of such proxies as environmental tools, requires some care as lateral transportation of organic compounds and microfossils from open sea ice areas, either along the strong halocline or due to bottom currents as mentioned above, do occur.

Summing up, the present study adds to our understanding of the cycling of ^{230}Th in the Arctic Ocean, at a geological time scale, and further documented the use of $^{230}Th_{xs}$ as a reliable chronostratigraphic tool. It also pointed to difficulties in interpreting sequences linked to sporadic sedimentation and deep current activity. At last, it suggests that the use of radiogenic isotopes or clay minerals as tracers of sediment sources might well be restricted to relatively specific settings, such as the southern Chukchi Sea, where Pacific Water fluxes during high sea level intervals, when Bering Strait is open, are well recorded.

ANNEXE A

Supplementary Material of Chapter 1

Nd-extraction (sediment leachates)

The chemical procedure for the recovery of Nd-leachable fractions from sediments may vary depending upon the composition of the sediment (e.g., Gutjahr et al., 2007; Asahara et al., 2012; Chen et al., 2012; Maccali et al., 2013; Wilson et al., 2013; Blaser et al., 2016; Deschamps et al., 2019; Huang et al., 2021; cf. Table below). Here, we provide details about our analytical protocol.

Comparison of Nd leaching methods

Leaching Procedure	Gutjahr et al., 2007	Asahara et al., 2012	Chen et al., 2012	Maccali et al., 2013	Wilson et al., 2013	Blaser et al., 2016	Deschampset al., 2019	Huang et al., 2021	This study
Decarbonatation	1M Na-acetate buffer	20% acetic acid	No	1M Na-acetate buffer	0.44M Na-acetate buffer	0.1M Na-acetate buffer	No	No	1M Na-acetate Buffer
Solution: HH AA Na-EDTA	0.05M +15% +0.03M	1M +25% +N/A	0.005M +1.5% +0.03M	0.05M +15% +0.03M	0.02M +4.4M +N/A	0.005M +1.5% +0.03M	0.005M +1.5% +0.03M	0.005M +1.5% +0.001M	0.005M +1.5% +0.03M
Reaction time	24 hrs	3 hrs	1 hr	24 hrs	1 hr	1 hr	1 hr	10"	3 hrs

Na-Acetate buffer = sodium acetate + acetic acid in a ratio of 1:1; HH = hydroxylamine hydrochloride; AA = acetic acid; Na-EDTA = Ethylenediaminetetraacetic acid disodium salt

The dissolution of carbonates represents a major issue, as they may include syn-sedimentary biogenic carbonates as well as detrital carbonates (calcite, dolomite). This step may be omitted if the carbonate content of the sediment is negligible (Chen et al., 2012; Deschamps et al., 2019), or when biogenic carbonates are dominant (Wilson et al., 2013; Blaser et al., 2016). Over-leaching may occur with extreme leaching times and/or highly concentrated solutions (Gutjahr et al., 2007). A diluted leaching solution was thus developed by Chen et al. (2012) and followed by Blaser et al. (2016), then Deschamps et al. (2019), which we adopted. Chen et al. (2012) also shortened the leaching time from 24 hours to 1 hour. The 1 hour leaching time was also used by Wilson et al. (2013) and Blaser et al. (2016), who proposed that labile volcanic materials might be over-leaching with a longer leaching time. However, we followed Asahara et al. (2012) with a leaching time set to approximately three hours to extract as much exchangeable-Nd fraction as possible. Data from the Bering Sea shelf surface samples showed that contaminations from

residues remained negligible with a 3 hours-leaching time and using a 1M Hydroxylamine Hydrochloride (HH) and 25% acetic acid solution (Asahara et al., 2012). Recently, a 10-seconds leaching time process was applied on Southern Ocean sediments by Huang et al. (2021). They also used a more diluted solution, with 0.001M EDTA that appeared sufficient to extract enough exchangeable Nd for isotopic measurements. However, experiments with different sediment compositions are needed to assess this extraction method, in particular with hemipelagic muds.

Biogenic carbonates are generally assumed to be a reliable recorder of the ambient water masses (Elmore et al., 2011). Nd isotopic measurements on such carbonates from surface sediments of the northern Bering Sea shelf (site MC18; main text Figure 1) yielded an εNd value of ~ -2.0±0.6 (1σ; n=4) that can be considered representative of water masses at the entry of the Bering Strait (Asahara et al., 2012). This value is consistent with the εNd values of the exchangeable fraction at the southern sites of the present study (SR03 and R03), where εNd values range -1.3 to -2.4. Nearly similar values (-1.8 to -2.2) were reported by Hadley and Polyak (2013) in sediments from the southern Chukchi Sea. εNd values of leachates from all sediment fractions in our studied surface samples depict similar south to north trends (main text, Figure 6). This seems a fair indication of the reliability of the extraction method and the representativity of the εNd values of leachates. Overall, Nd isotopes in leachates from clay fractions from core R09 are considered a good recorder of Pacific Water supplies.

Supplementary Table 1 Sedimentology, clay mineral and geochemistry properties of R09.

Depth (cm)	Age (kyr)	Sedimentology				Nd isotopes				Clay mineral relative abundances and fluxes (g. cm^{-2}. kyr^{-1})										
		Clay (%)	Silt (%)	Sand (%)	SS (μm)	εNd-L	± 2σ	εNd-R	± 2σ	S (%)	I (%)	C (%)	K (%)	(C+K)/I	C/I	SR	S flux	I flux	C flux	K flux
1	0.04	11	85	4	25	-3.00	0.07	-9.36	0.08	16	61	14	8	0.37	0.23	38.5	0.9	3.5	0.8	0.5
25	0.59	11	87	2	25	-2.77	0.08	-9.51	0.09	-	-	-	-	-	-	38.5	-	-	-	-
50	1.25	13	76	11	25	-2.79	0.05	-9.40	0.06	7	71	18	4	0.32	0.26	38.5	0.5	5.0	1.3	0.3
66	1.67	11	87	3	26	-2.91	0.05	-9.70	0.06	14	69	12	6	0.25	0.17	26.1	0.5	2.7	0.4	0.2
90	2.38	9	86	5	28	-2.85	0.07	-9.34	0.07	4	76	14	7	0.27	0.19	26.1	0.1	2.5	0.5	0.2
110	3.13	9	87	4	28	-3.55	0.06	-9.42	0.05	13	67	11	9	0.30	0.17	26.4	0.5	2.3	0.4	0.3
130	3.91	8	87	5	29	-3.33	0.07	-9.52	0.07	15	65	14	5	0.30	0.22	26.4	0.5	2.0	0.4	0.2
150	4.88	9	82	9	30	-3.45	0.07	-8.93	0.06	10	69	13	9	0.32	0.19	15.2	0.2	1.2	0.2	0.2
154	5.18	9	82	9	29	-3.95	0.06	-9.45	0.09	9	70	17	3	0.29	0.24	15.2	0.2	1.4	0.3	0.1
158	5.45	8	84	8	30	-4.01	0.07	-9.49	0.07	8	69	16	7	0.34	0.24	15.2	0.1	1.2	0.3	0.1
162	5.74	8	83	9	29	-3.99	0.06	-9.52	0.08	8	72	12	8	0.28	0.17	15.2	0.1	1.3	0.2	0.1
166	6.05	8	83	9	29	-4.22	0.06	-9.42	0.08	15	65	15	6	0.32	0.22	15.2	0.3	1.1	0.3	0.1
170	6.36	7	82	11	30	-4.52	0.05	-9.50	0.13	18	63	13	7	0.31	0.20	15.2	0.3	1.1	0.2	0.1
174	6.63	8	79	13	30	-4.61	0.07	-9.46	0.11	6	70	17	8	0.35	0.24	15.2	0.1	1.2	0.3	0.1
178	6.93	8	79	13	29	-4.85	0.04	-9.38	0.09	13	65	16	6	0.34	0.25	15.2	0.2	1.2	0.3	0.1
182	7.19	8	81	12	30	-5.25	0.09	-9.42	0.10	8	74	12	6	0.24	0.16	15.2	0.1	1.3	0.2	0.1
186	7.43	8	78	14	30	-5.29	0.06	-9.43	0.13	5	76	14	5	0.25	0.19	15.2	0.1	1.3	0.2	0.1
190	7.69	9	75	16	29	-5.73	0.05	-9.08	0.17	3	73	19	5	0.34	0.26	15.2	0.1	1.4	0.4	0.1
194	7.85	9	75	16	30	-4.66	0.05	-9.06	0.10	5	73	15	7	0.30	0.20	15.2	0.1	1.5	0.3	0.1
198	8.02	9	75	16	32	-5.85	0.05	-9.63	0.09	9	73	12	6	0.25	0.17	32.1	0.4	3.4	0.6	0.3
202	8.15	10	75	15	32	-4.84	0.05	-9.04	0.18	2	77	13	8	0.27	0.17	32.1	0.1	4.0	0.7	0.4
222	8.63	10	70	19	33	-5.36	0.06	-9.58	0.08	10	68	13	9	0.32	0.20	43.9	0.7	5.0	1.0	0.6
242	9.07	7	65	28	40	-5.53	0.06	-9.57	0.12	3	76	12	8	0.27	0.16	43.9	0.2	3.7	0.6	0.4
262	9.84	9	74	17	41	-5.90	0.06	-9.44	0.12	2	78	12	8	0.26	0.16	43.9	0.1	4.8	0.8	0.5

Supplementary Table 2 ^{226}Ra in surface sediment samples from eastern Chukchi Sea (from Baskaran and Naidu, 1995).

Site	Latitude (N)	Longitude (W)	Water depth (m)	Interval (cm)	^{226}Ra (dpm. g^{-1})
CH-13	72º31.1'	164˚8.0'	48	0-1	0.82±0.01
CH-21	71º12.2'	164˚12.0'	42	0-1	1.00±0.02
CH-25	72º37.6'	167˚4.5'	51	0-1	1.16±0.02
CH-38	70º42.0'	167˚22.9'	52	0-2	1.09±0.02
CH-39	71º52.2'	168˚15.4'	48	0-2	1.28±0.03
CH-40	70º16.7'	167˚54.3'	45	0-1	0.94±0.02
SU-5	67º2.0'	169˚0.0'	50	0-1	1.29±0.11
SU-11	67º2.3'	165˚44.7'	28	0-1	0.85±0.02
KS-1	66º37.0'	163˚0.3'	13	0-1	0.96±0.02
84-12	71º29.0'	165˚7.0'	41	0-1	1.35±0.02

Supplementary Table 3 Grain-size and Nd-isotope data of the five surface samples.

Site	Size fraction (μm)	Percentage (%)	Leachates				Residues			
			$^{143}Nd/^{144}Nd$	±2σ	εNd	±2σ	$^{143}Nd/^{144}Nd$	±2σ	εNd	±2σ
SR03	0-2	11	0.512522	0.000004	-2.27	0.08	0.512245	0.000014	-7.67	0.27
R03		9	0.512524	0.000003	-2.23	0.05	0.512220	0.000009	-8.16	0.17
SR09		10	0.512481	0.000004	-3.06	0.08	0.512243	0.000013	-7.70	0.25
SR11		23	0.512475	0.000003	-3.18	0.07	0.512224	0.000010	-8.09	0.19
SR14		3	0.512288	0.000003	-6.82	0.06	0.512068	0.000008	-11.10	0.16
SR03	2-10	23	0.512530	0.000003	-2.11	0.05	0.512279	0.000003	-7.00	0.07
R03		22	0.512517	0.000005	-2.36	0.11	0.512260	0.000005	-7.37	0.09
SR09		23	0.512491	0.000003	-2.87	0.07	0.512231	0.000006	-7.95	0.11
SR11		52	0.512498	0.000004	-2.73	0.09	0.512218	0.000008	-8.20	0.15
SR14		49	0.512052	0.000004	-7.34	0.08	0.512052	0.000017	-11.40	0.33
SR03	10-63	34	0.512569	0.000004	-1.34	0.08	0.512360	0.000004	-5.41	0.07
R03		32	0.512543	0.000003	-1.86	0.05	0.512322	0.000004	-6.16	0.08
SR09		30	0.512483	0.000003	-3.02	0.07	0.512275	0.000004	-7.07	0.07
SR11		14	0.512431	0.000004	-4.05	0.07	0.512244	0.000012	-7.68	0.22
SR14		28	0.512227	0.000004	-8.03	0.08	0.511998	0.000010	-12.50	0.20
SR03	>63	32	0.512520	0.000004	-2.31	0.07	0.512338	0.000004	-5.86	0.08
R03		38	0.512529	0.000003	-2.12	0.06	0.512272	0.000007	-7.14	0.14
SR09		37	0.512480	0.000003	-3.09	0.06	0.512300	0.000006	-6.60	0.11
SR11		11	0.512436	0.000004	-3.94	0.07	0.512285	0.000012	-6.88	0.23
SR14		21	0.512220	0.000004	-8.16	0.08	0.512071	0.000005	-11.10	0.10

Supplementary Table 4 Clay mineral abundances in clay fraction of surface samples.

Site	Lat.	Long.	Smectite (%)	Illite (%)	Chlorite (%)	Kaolinite (%)
SR03	67°40.122'N	168°55.509'W	13	64	16	7
SR09	70°59.706'N	168°51.247'W	9	60	21	10
SR11	72°59.920'N	168°58.568'W	17	63	11	9
SR14	78°00.588'N	168°58.642'W	8	66	13	13

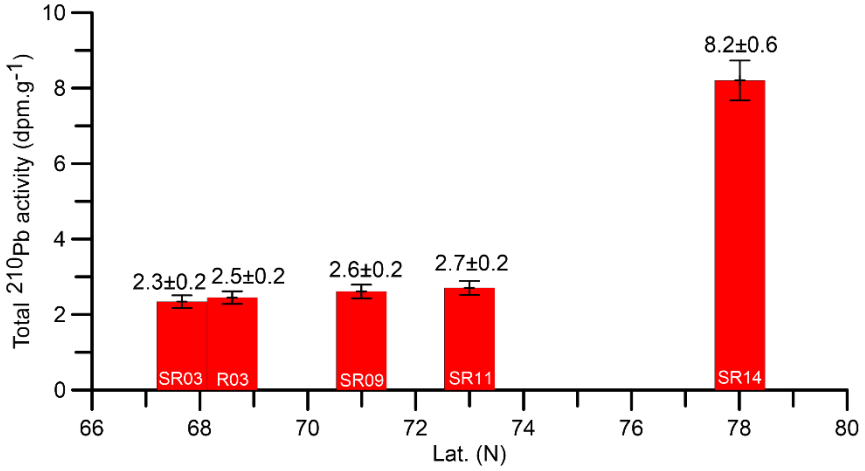

Supplementary Figure 1 Total ^{210}Pb activities in surface samples with their 1σ errors.

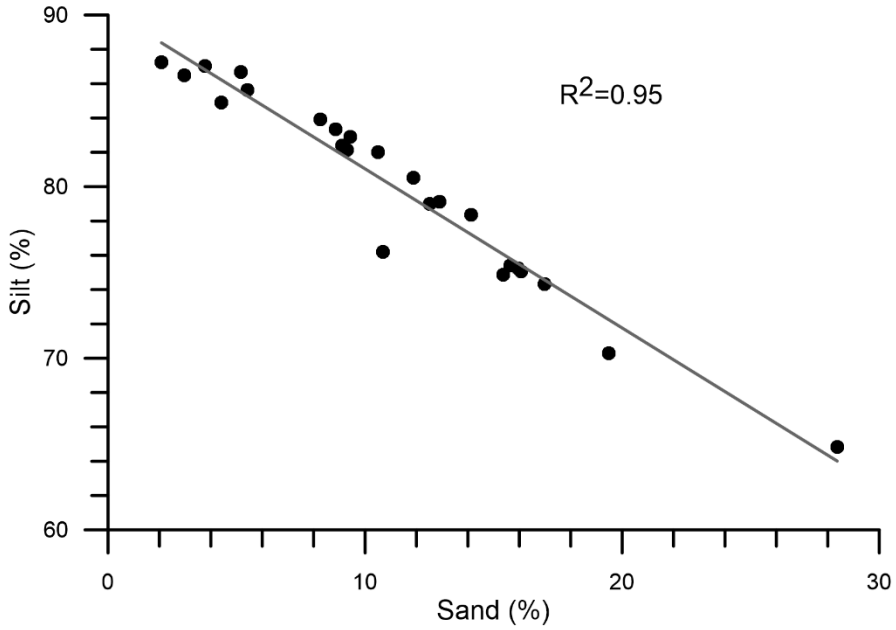

Supplementary Figure 2 Silt *vs* sand contents in core R09. The silt content is anticorrelated with the sand content, with a correlation coefficient of ~ 0.95.

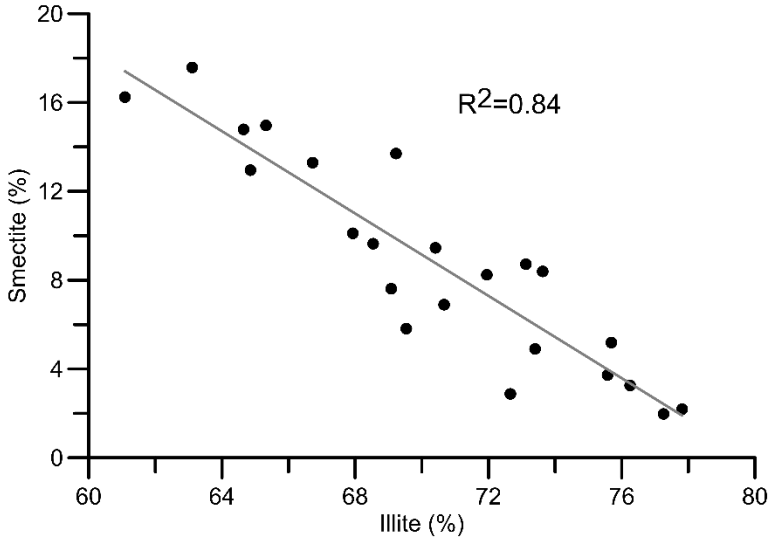

Supplementary Figure 3 Illite *vs* smectite abundances in core R09. Illite abundance is anticorrelated with the smectite abundance, with a correlation coefficient of ~ 0.84. As illite is the dominant clay mineral in core R09, the smectite abundance is highly influenced by the illite flux.

ANNEXE B

Supplementary Material of Chapter 2

Supplementary Table S1 ^{226}Ra and ^{210}Pb activities of the core top 10 cm samples.

Interval (cm)	Depth (cm)	$A^{210}Pb$ (dpm. g^{-1})	Uncertainty (±1σ)	$A^{226}Ra$ (dpm. g^{-1})	Uncertainty (±1σ)
0-1	0.5	3.98	0.26	4.11	0.48
1-2	1.5	3.57	0.23	/	/
2-3	2.5	3.33	0.22	4.07	0.41
3-4	3.5	3.62	0.24	/	/
4-5	4.5	3.77	0.25	4.67	0.42
5-6	5.5	2.93	0.20	/	/
6-8	7	2.72	0.19	4.02	0.44
8-9	8.5	2.36	0.16	/	/
9-10	9.5	2.49	0.18	2.89	0.29

Supplementary Table S2 Bulk mineralogy data of core E25.

Depth (cm)	Smectite	Illite	Clinochlore	Kaolinite	Hornblende	Quartz	Albite	Microcline	Calcite	Dolomite	Pyrite	Pyroxene	Halite
0.5	0.4	9.5	4.4	1.6	2.1	45.6	16.7	6.2	10.4	2.8	0.3	nil	nil
5.5	0.3	9.0	4.2	1.5	2.0	48.5	15.8	5.8	9.9	2.7	0.3	nil	nil
10.5	0.4	10.7	4.1	1.8	2.3	51.4	18.8	7.0	2.0	1.2	0.3	nil	nil
15.5	0.4	15.2	5.9	1.7	2.1	47.2	17.3	6.4	1.8	1.7	0.3	nil	nil
20.5	0.4	13.3	5.6	1.6	2.0	44.7	17.5	6.1	2.2	6.3	0.3	nil	nil
22.5	0.3	11.6	5.4	1.5	1.9	42.7	16.7	5.8	3.2	10.6	0.3	nil	nil
25.5	0.3	11.5	4.6	1.5	1.9	42.0	16.5	5.7	3.1	12.6	0.3	nil	nil
29.5	0.3	13.2	5.0	1.3	1.7	45.1	17.1	7.2	2.8	6.1	0.2	nil	nil
38.5	0.4	10.4	6.7	1.8	1.6	45.8	17.3	6.8	6.5	2.4	0.3	nil	nil
50.5	0.3	13.4	8.6	1.2	1.1	51.6	14.2	7.0	1.6	0.8	0.2	nil	nil
58.5	0.4	18.1	7.1	1.6	1.6	39.4	19.9	8.2	2.2	1.2	0.3	nil	nil
70.5	0.3	16.6	6.5	1.5	1.5	45.1	18.3	7.5	1.4	1.1	0.3	nil	nil
74.5	0.3	12.8	7.3	1.4	1.4	42.8	23.4	8.2	1.3	0.9	0.2	nil	nil
82.5	0.4	11.3	4.0	1.8	1.8	42.5	24.3	10.8	1.7	1.2	0.3	nil	nil
90.5	0.3	8.8	3.1	1.4	1.4	54.8	19.1	8.4	1.3	1.0	0.3	nil	nil
98.5	0.4	9.7	4.5	1.6	1.2	42.5	20.9	6.2	7.9	4.8	0.3	nil	nil
106.5	0.3	12.2	5.6	1.5	1.1	40.1	16.3	8.7	5.0	8.9	0.3	nil	nil
114.5	0.3	13.7	8.5	1.5	1.2	41.7	17.0	6.4	1.7	7.7	0.3	nil	nil
122.5	1.5	11.1	5.3	3.1	2.1	41.9	22.7	6.6	2.3	1.0	0.3	1.4	0.7
138.5	1.3	8.2	3.1	1.9	1.0	52.5	19.0	5.7	2.9	0.9	0.2	1.2	2.1
150.5	1.4	12.7	6.0	2.6	2.0	38.6	20.1	7.9	1.4	1.7	0.2	2.2	3.2
162.5	1.0	11.0	4.7	2.0	2.0	46.3	15.0	6.3	5.5	2.5	0.2	1.6	1.9

Supplementary Table S3 Sedimentology data of core E25.

Depth (cm)	Clay (dw%)	Silt (dw%)	Sand (dw%)	f (mm)
1.5	27.4	72.0	0.6	7.9
3.5	25.5	73.2	1.3	7.3
5.5	25.1	73.7	1.2	7.6
7.0	30.7	68.6	0.7	5.6
10.5	34.4	65.6	0.0	3.9
12.5	33.0	67.0	0.0	4.0
14.5	36.3	63.7	0.0	3.5
16.5	35.5	64.5	0.0	3.6
18.5	40.1	59.9	0.0	3.3
20.5	37.5	62.2	0.3	4.0
26.5	25.1	74.3	0.6	7.0
28.5	19.5	80.2	0.3	7.3
30.5	20.0	79.2	0.8	8.5
34.5	23.3	73.5	3.2	11.1
38.5	21.1	74.1	4.8	14.2
42.5	24.4	73.1	2.5	10.7
46.5	20.4	65.4	14.2	24.1
54.5	16.7	76.5	6.8	14.1
58.5	34.6	64.9	0.5	4.4
62.5	34.8	65.0	0.2	3.9
66.5	34.6	65.4	0.0	3.7
70.5	33.5	66.2	0.3	4.7
74.5	22.9	76.7	0.4	7.3
78.5	37.9	62.1	0.0	3.9
86.5	35.5	62.3	2.2	6.2
98.5	25.7	69.2	5.1	10.5
102.5	33.2	66.1	0.7	5.7
106.5	30.6	59.8	9.6	14.5
110.5	31.7	63.5	4.8	8.7
118.5	35.3	64.0	0.7	5.8
122.5	33.1	65.2	1.7	4.4
126.5	44.2	54.6	1.2	3.3
134.5	32.9	66.3	0.8	5.6
142.5	31.8	67.7	0.5	5.7
146.5	39.1	60.9	0.0	4.5
166.5	31.3	67.0	1.7	6.2
170.5	21.6	76.7	1.6	6.1
174.5	18.1	78.8	3.2	8.4
178.5	25.2	71.8	3.1	9.2

182.5	28.1	71.8	0.2	4.6
186.5	25.2	74.8	0.0	4.8
190.5	26.6	73.4	0.0	4.9
194.5	33.1	67.0	0.0	3.7
198.5	25.5	74.3	0.3	5.7
202.5	27.0	70.7	2.3	7.9
206.5	31.6	68.1	0.3	5.8
210.5	40.3	57.7	2.0	4.5
214.5	38.0	61.3	0.7	4.6
218.5	37.2	62.0	0.9	4.5
222.5	31.6	66.1	2.3	7.3
226.5	31.6	67.6	0.7	5.6
230.5	29.8	69.6	0.6	6.2
234.5	26.7	72.6	0.7	6.5
238.5	32.7	67.3	0.0	4.7
242.5	41.7	58.3	0.0	3.0
246.5	40.0	60.0	0.0	3.6
250.5	34.0	64.4	1.6	6.3
254.5	28.4	70.7	0.9	6.8
258.5	29.9	69.4	0.7	6.2
262.5	32.2	67.2	0.6	5.7
266.5	28.4	69.6	1.9	7.8
270.5	31.7	66.1	2.2	7.2
274.5	30.6	68.9	0.5	5.1
278.5	34.3	65.4	0.4	4.9
282.5	32.3	66.0	1.7	6.4
286.5	32.4	64.6	3.0	7.6
290.5	33.0	66.1	0.9	5.8
294.5	31.1	67.7	1.3	6.9
298.5	29.9	68.3	1.7	7.6
302.5	39.5	60.4	0.1	3.8
306.5	34.0	64.1	2.0	6.9
310.5	28.9	69.7	1.4	7.0
314.5	27.8	71.9	0.4	6.1
318.5	28.46	63.7	7.84	11.8

Supplementary Table S4 Geochemistry data of core E25.

Depth (cm)	OC (dw%)	$\delta^{13}C$	^{238}U (ppm)	error (±2σ)	^{232}Th (ppm)	error (±2σ)	AR ($^{234}U/^{238}U$)	error (±2σ)	^{230}Th (dpm. g^{-1})	error (±2σ)	$^{230}Th_{xs}$ (dpm. g^{-1})	error (±2σ)
1.5	0.30	-22.5	1.78	0.02	8.86	0.07	1.03	0.02	5.80	0.04	4.52	0.12
3.5	0.28	-22.3	/	/	/	/	/	/	/	/	/	/
5.5	0.19	-23.6	1.78	0.01	9.27	0.08	1.01	0.01	4.78	0.05	3.49	0.12
8.5	0.09	-24	/	/	/	/	/	/	/	/	/	/
10.5	0.26	-23.1	1.77	0.02	10.83	0.09	1.00	0.01	3.80	0.03	2.52	0.12
12.5	0.30	-23.7	/	/	/	/	/	/	/	/	/	/
14.5	0.29	-23.6	/	/	/	/	/	/	/	/	/	/
15.5	/	/	1.79	0.02	11.11	0.11	1.00	0.01	6.32	0.05	5.03	0.12
16.5	0.29	-23.5	/	/	/	/	/	/	/	/	/	/
18.5	0.25	-23.2	/	/	/	/	/	/	/	/	/	/
20.5	0.33	-23	1.98	0.02	12.21	0.11	1.03	0.01	13.55	0.11	12.26	0.16
22.5	0.18	-22.6	1.75	0.02	10.12	0.11	1.03	0.02	10.80	0.12	9.51	0.17
24.5	0.17	-22.7	/	/	/	/	/	/	/	/	/	/
25.5	/	/	1.74	0.02	10.70	0.10	1.03	0.01	6.38	0.07	5.09	0.13
26.5	0.20	-22.8	/	/	/	/	/	/	/	/	/	/
28.5	0.29	-24.3	/	/	/	/	/	/	/	/	/	/
29.5	/	/	1.88	0.02	10.62	0.11	1.02	0.01	6.42	0.06	5.13	0.12
30.5	0.18	-23.3	/	/	/	/	/	/	/	/	/	/
34.5	0.17	-23.3	/	/	/	/	/	/	/	/	/	/
38.5	0.20	-22.8	1.77	0.02	8.81	0.12	1.04	0.01	3.78	0.05	2.50	0.12
42.5	0.19	-22.6	/	/	/	/	/	/	/	/	/	/
46.5	0.19	-22.8	/	/	/	/	/	/	/	/	/	/
50.5	0.22	-23.7	1.82	0.01	8.43	0.07	0.95	0.01	1.90	0.03	0.61	0.12
54.5	0.16	-22.9	/	/	/	/	/	/	/	/	/	/
58.5	0.17	-22.9	1.81	0.02	11.22	0.10	0.97	0.01	2.34	0.02	1.05	0.11
62.5	0.19	-23.6	/	/	/	/	/	/	/	/	/	/
66.5	0.18	-23.5	/	/	/	/	/	/	/	/	/	/
70.5	0.19	-23.1	1.64	0.01	10.31	0.09	1.00	0.01	2.37	0.02	1.09	0.11
74.5	0.09	-22.7	1.70	0.01	9.59	0.08	1.00	0.00	2.64	0.02	1.36	0.11
82.5	0.08	-23.7	1.77	0.01	11.52	0.09	0.99	0.00	3.55	0.03	2.26	0.11

86.5	/	/	1.75	0.01	10.21	0.07	0.96	0.00	2.89	0.02	1.60	0.11
90.5	0.08	-24.9	1.64	0.01	7.81	0.06	0.96	0.01	1.48	0.01	0.20	0.11
94.5	/	/	1.79	0.01	9.90	0.09	1.02	0.00	4.34	0.02	3.05	0.11
98.5	0.06	-23.2	1.63	0.01	9.36	0.09	1.04	0.01	3.08	0.03	1.80	0.11
102.5	/	/	1.63	0.01	9.21	0.06	1.01	0.00	2.41	0.01	1.12	0.11
106.5	0.04	-25.1	1.50	0.01	8.64	0.07	1.00	0.01	1.76	0.02	0.47	0.11
114.5	0.06	-25.3	1.38	0.01	9.05	0.07	0.97	0.01	1.29	0.02	0.00	0.11
122.5	0.08	-24.5	1.53	0.01	10.05	0.09	0.96	0.00	1.60	0.01	0.31	0.11
130.5	/	/	1.85	0.01	11.01	0.07	1.01	0.01	2.87	0.01	1.59	0.11
138.5	0.06	-24.0	1.66	0.01	9.80	0.16	1.03	0.01	1.84	0.01	0.56	0.11
150.5	0.07	-25.0	1.77	0.01	11.07	0.10	0.93	0.00	1.49	0.01	0.20	0.11
162.5	0.05	-24.7	1.63	0.01	9.31	0.08	1.12	0.00	1.86	0.01	0.58	0.11

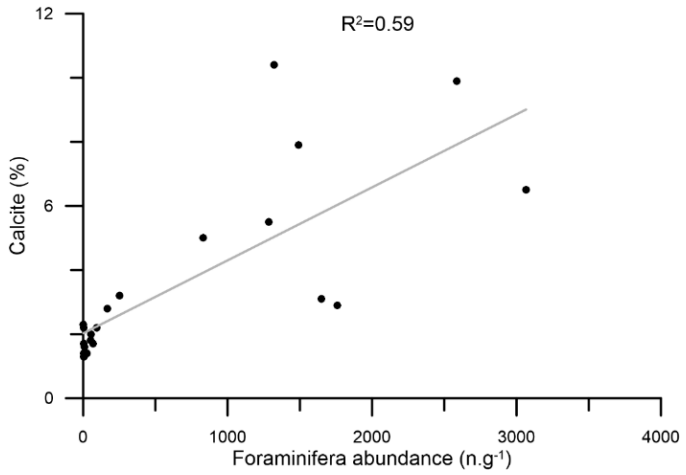

Supplementary Figure S1 Correlation between calcite content and foraminifera abundance in core E25.

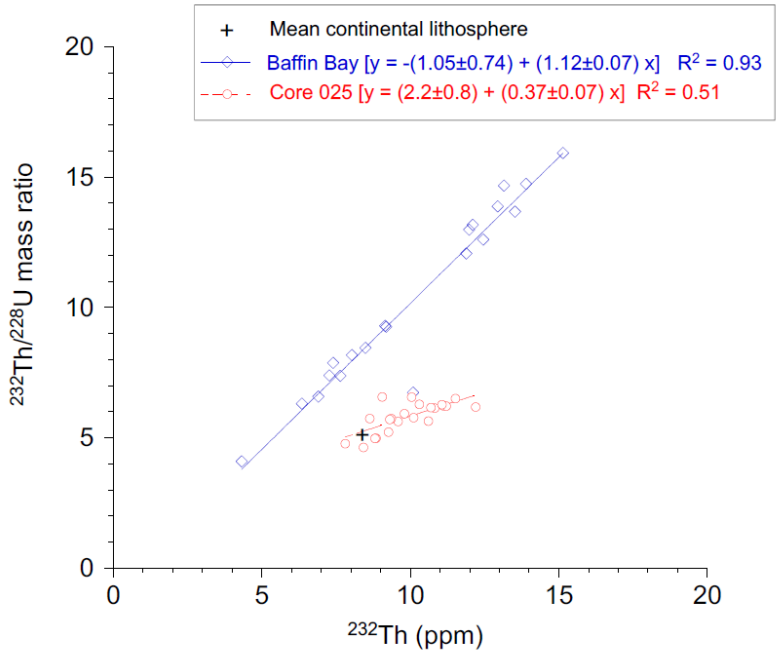

Supplementary Figure S2 $^{238}U/^{232}Th$ ratio vs ^{232}Th content. Red dots: our studied core E25; Blue squares: site HU2008-029-016PC from Nuttin and Hillaire-Marcel, 2015; Black cross: mean continental lithosphere from Wedepohl, (1995).

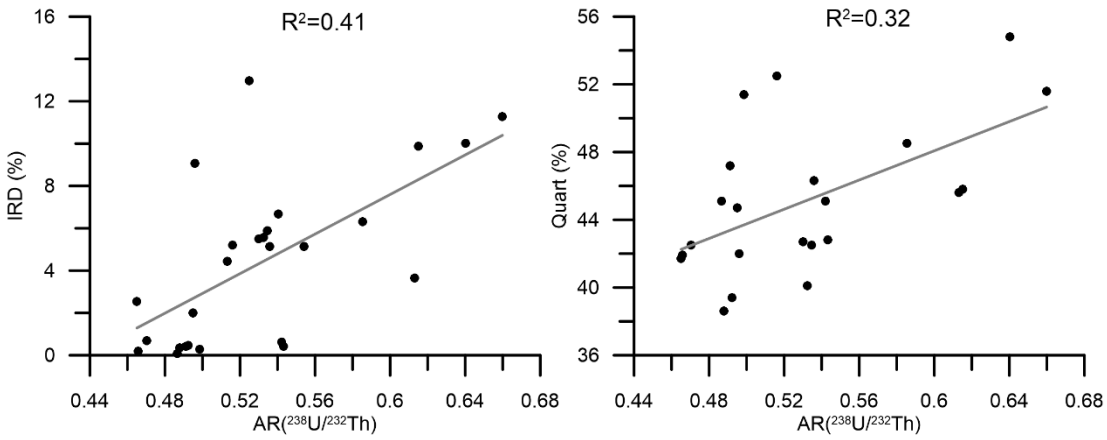

Supplementary Figure S3 AR($^{238}U/^{232}Th$) value versus IRD and quartz contents.

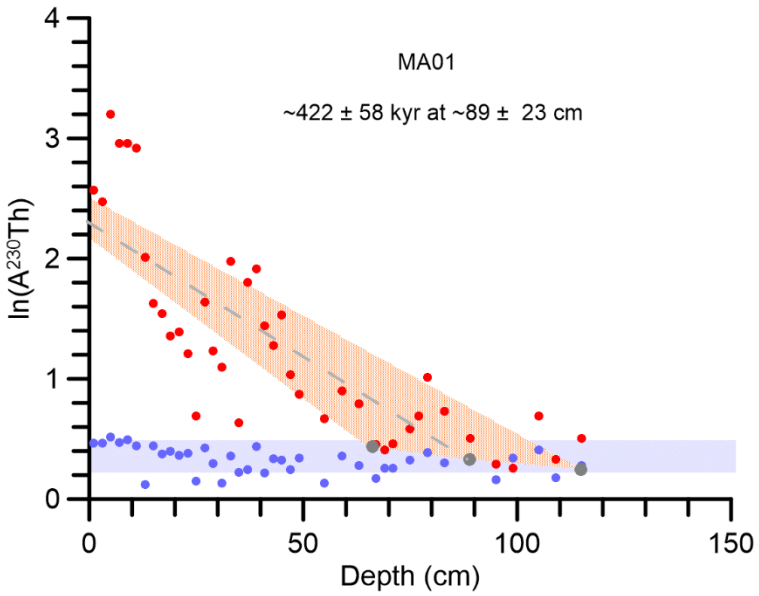

Supplementary Figure S4 Linear correlation of Ln ($A^{230}Th$) and core depth of site MA01 from Xu et al. (2021). Red dots: Ln ($A^{230}Th$); Blue dots: Ln ($A^{234}U$). The calculation of extinction depth and age of $^{230}Th_{xs}$ could be found in the main text. The $^{230}Th_{xs}$ decay downcore illustrates an age of ~422 ± 58 kyr at the core depth of ~89 ± 23 cm, suggesting that the $^{230}Th_{xs}$ peak at ~80 cm should be assigned to MIS 11 (see fig. 2-6 in chapter 2).

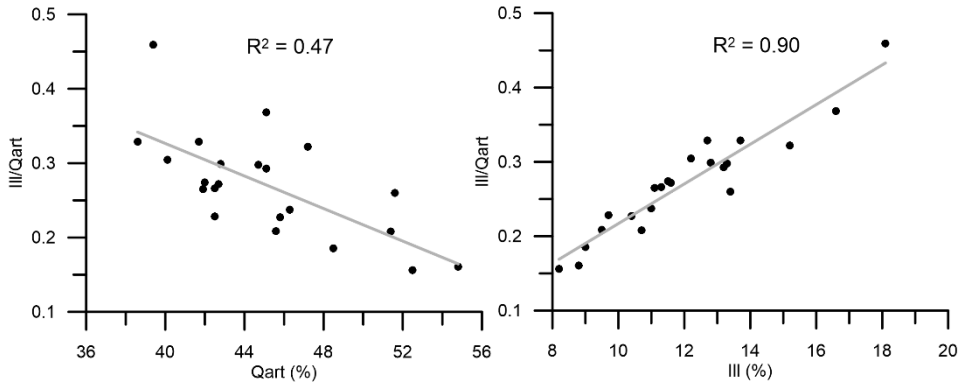

Supplementary Figure S5 Quartz content vs illite/quartz ratio (left) and illite content vs illite/quartz ratio (right).

ANNEXE C

Supplementary Material of Chapter 3

Estimating the dry bulk density

The dry bulk density (DBD) data of cores used in the present study were not always available (e.g., BC series). A rough DBD of 0.85 g.cm^{-3} was previously used by Xu et al. (2021) to calculate the $^{230}Th_{xs}$ inventory. However, this value is lower than those measured in most sites (e.g., Not and Hillaire-Marcel, 2010; Hillaire-Marcel et al., 2017; Song et al., 2022). Thus, a better estimate of mean DBD values was needed.

We used here all available DBD data (seven sites) and plotted them in Figure A.1. There is no clear depth trend within the upper 6 m of the available data sets. An average value of 1.09 ± 0.16 g.cm^{-3} (n = 2129; ±1σ) was obtained, thus an estimate with a relative uncertainty of ~15%, which we carried into calculations requiring DBD value.

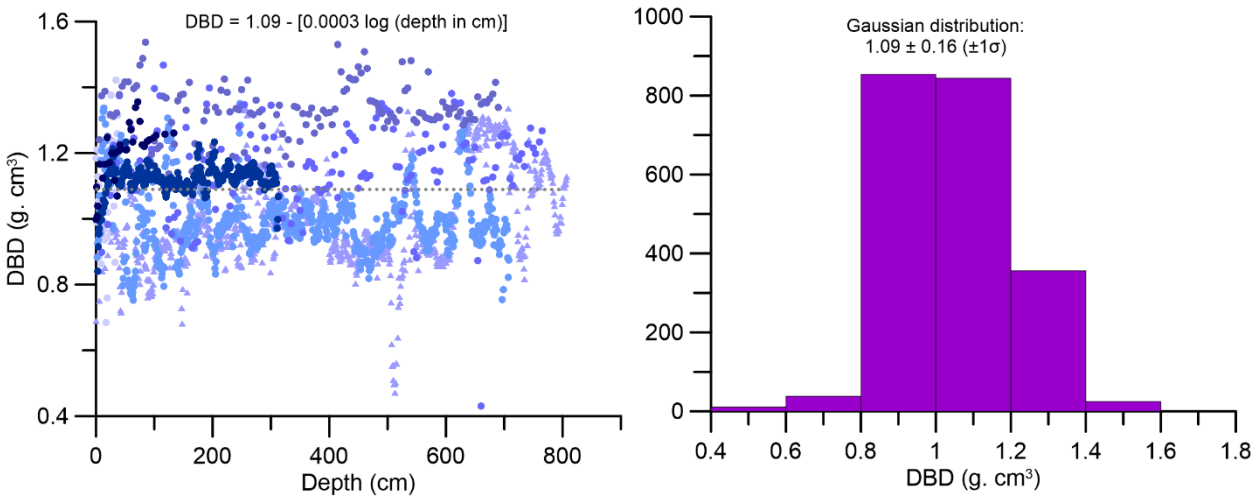

Figure A.1. Dry bulk density (DBD) vs core depth (left) and DBS distribution pattern (right). Datasets are from sites E25, M030, MC11, PS51, PS2185, PS2200, and PS2757; Sources are indicated Table A.1.

The $^{230}Th_{xs}$ inventory

Estimating $^{230}Th_{xs}$ in cored sequences from the Arctic Ocean is based on the subtraction of detrital ^{230}Th either from ^{234}U (Geibert et al., 2021) or ^{238}U (Hillaire-Marcel et al., 2017). As illustrated in Figure A.2, the comparison

of the cumulative $^{230}Th_{xs}$ inventories from these two distinct methods shows minor differences in the nine cited long-term cores but for a trend towards a few percent larger cumulative excess in ^{230}Th vs ^{234}U, in comparison with that calculated vs ^{238}U, back in time.

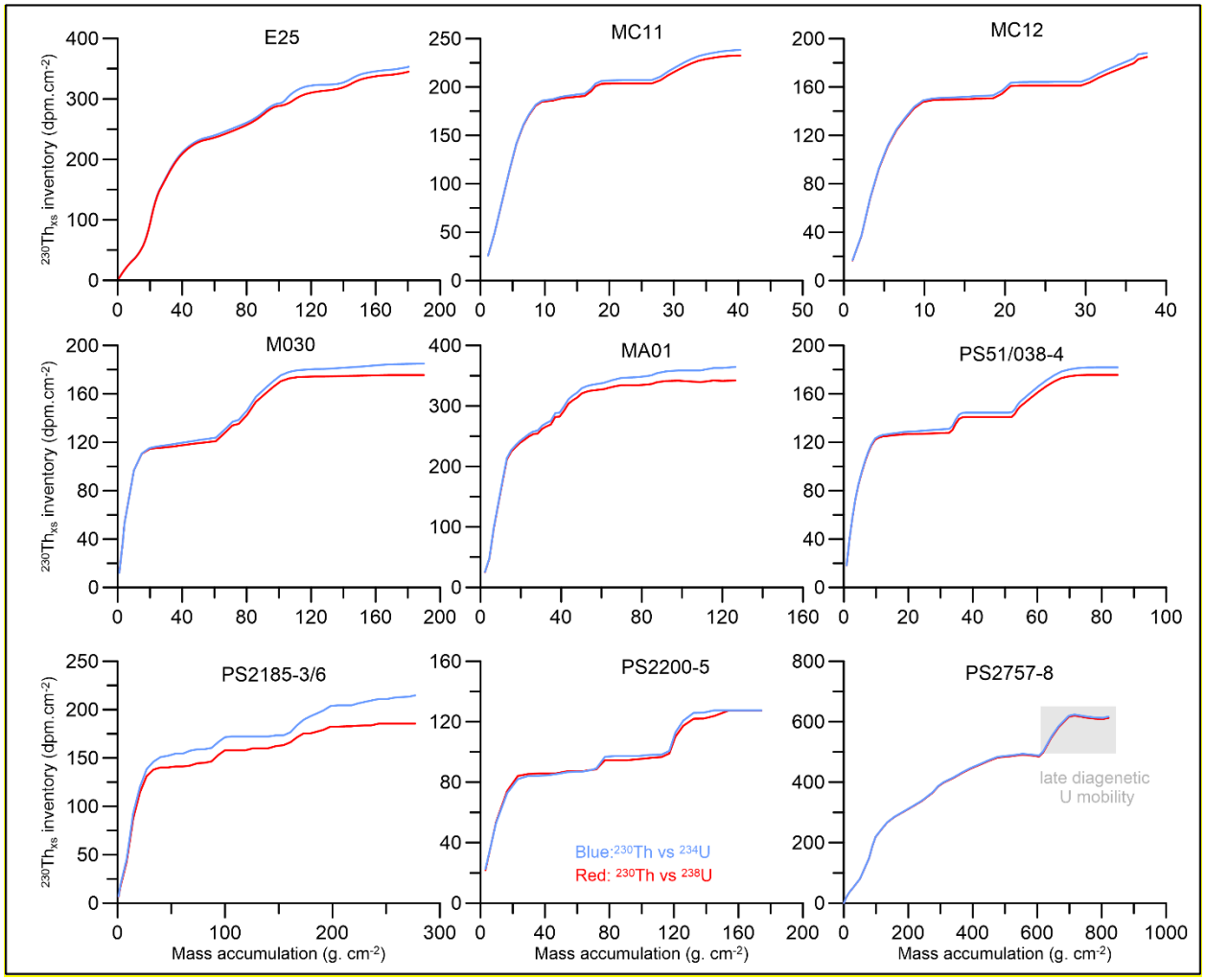

Figure A.2. The cumulative $^{230}Th_{xs}$ inventory vs mass accumulation in sites spanning several glacial/interglacial cycles. Blue curve: inventory of $^{230}Th_{xs}$ vs ^{234}U; red curve: inventory of $^{230}Th_{xs}$ vs ^{238}U. Source of datasets: see Table A.1.

The only process that would explain this pattern relates to U-losses from detrital minerals under the oxidizing conditions of the Arctic Ocean sediments, which would be increasing through time (see a similar process in the Labrador Sea; Fig. 2.5 in Vallières, 1997). Due to recoil effects, the uranium lost into pore waters is enriched in

^{234}U, leading to ^{234}U-depleted residual mineral fractions (Figure A.3), thus to apparent larger excesses in ^{230}Th vs ^{234}U, than vs ^{238}U (see another example of enhanced redox-driven diagenetic effects in Purcell et al., 2022).

A consequence of these diagenetic effects is that the "extinction ages" of $^{230}Th_{xs}$ (Figure 4, main text), should be seen as maximum ages, due to a diagenetically induced residual excess in ^{230}Th when calculated against ^{234}U. However, considering the large uncertainty in the extinction age estimate, correcting for the long-term diagenetic loss in uranium does not move the effective extinction age of the initial $^{230}Th_{xs}$ much away from the estimates illustrated in Figure 4 (main text). Indeed, Purcell et al. (2022) calculated that the ^{234}U/^{238}U activity ratio of the U lost by detrital minerals was about 1.49. Assuming a similar value for the U lost in sites illustrated in Figure A.2, all but PS2185, likely experienced minor diagenetic effects and negligible U-losses (Figure A.3).

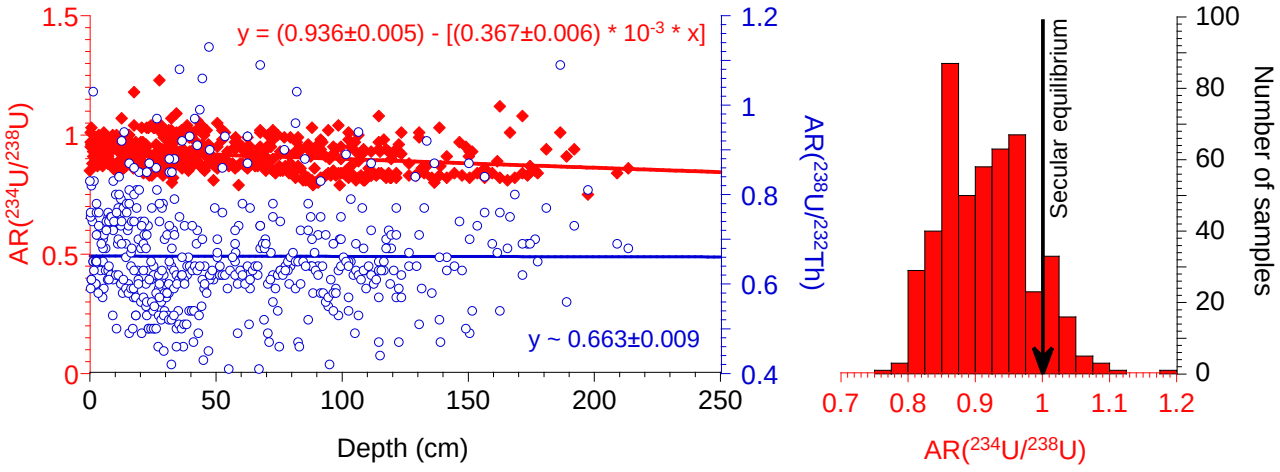

Figure A.3. Long-term diagenetic evolution of uranium in sequences spanning several climatic cycles. Left: Activity ratios ^{234}U/^{238}U and ^{238}U/^{232}Th illustrating a progressive depletion in ^{234}U (vs ^{238}U) through time without significant loss in uranium, thus pointing to the loss of a highly fractionated uranium (with high ^{234}U excess). Right: histogram of ^{234}U/^{238}U activity ratios illustrating the general trend for fractionated U-losses under the relatively oxidizing conditions of the central Arctic Ocean sediments.

Nonetheless, the calculation of $^{230}Th_{xs}$ vs ^{234}U seems is the most intuitive way of calculating the effective excess in ^{230}Th, whereas, in the long term, the calculation of $^{230}Th_{xs}$ vs ^{238}U might well provide a better estimate due to the observed diagenetic evolution of the sediment uranium. This is notably illustrated by the better achievement of asymptotic values of inventories based on ^{238}U than those based on ^{234}U (e.g., sites PS2185, MC11, M030,

MA01, PS51, Figure A.2). Of course, these diagenetic effects do not impact significantly the $^{230}Th_{xs}$-based stratigraphies discussed in the main text and illustrated in Figure 5.

The $^{230}Th_{xs}$ distribution and inventory in core PS2757

Unlike cores from the central Arctic Ocean, core PS2757 collected from the southern Lomonosov Ridge near the Siberian continental margin depicts a comparatively high mean sedimentation rate of ~2.6 cm.kyr^{-1} (Figure A.4; Purcell et al., 2022). Aside from the stepwise increasing trend in its $^{230}Th_{xs}$ inventory (main text Figure 2), this core also depicts some uranium relocation at a depth of ~ 6 m linked to redox processes driven by peaking values in terrestrial organic carbon at this depth (Purcell et al., 2022). Moreover, this core depicts low $^{230}Th_{xs}$-values, in comparison with those from the central Arctic Ocean sequences, where mean sedimentation rates are generally below ~1 cm.kyr^{-1}, thus where the ^{230}Th-rain is less diluted in sediments (see discussions in the main text). Core PS2757 thus represents borderline conditions for using the $^{230}Th_{xs}$-dating approach.

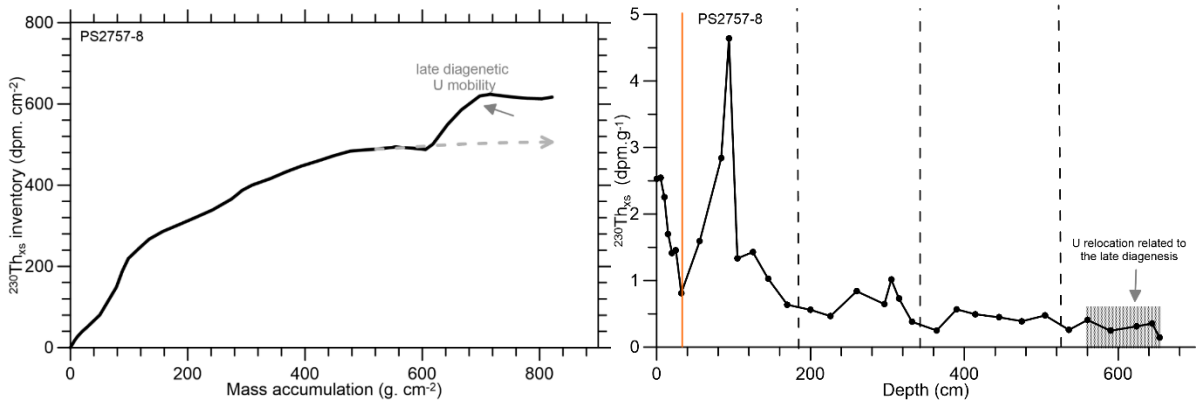

Figure A.4. $^{230}Th_{xs}$ inventory vs mass accumulation (left) and its distribution (right) in core PS2757. Orange line: MIS 2 hiatus; black dashed line: inception depths of MIS 3, 5e, and 7; grey dashed arrow: the estimated $^{230}Th_{xs}$ inventory trend without the influence of late diagenetic processes. Data from Purcell et al. (2022).

The $^{230}Th_{xs}$ inventory in core MC18

The $^{230}Th_{xs}$ distribution in core MC18 has been previously discussed in Not and Hillaire-Marcel (2012). This core is characterized by high $^{230}Th_{xs}$ and high sedimentary fluxes since MIS 3, despite the LGM hiatus (Figure 5 in the main text; Figure A.5). They are associated with fine particle redistribution from the Lomonosov Ridge crest to

the Intra Basin (driven by the intermediate and deep currents from the Makarov Basin to the Amundsen Basin (Figure A.6; see details in the main text).

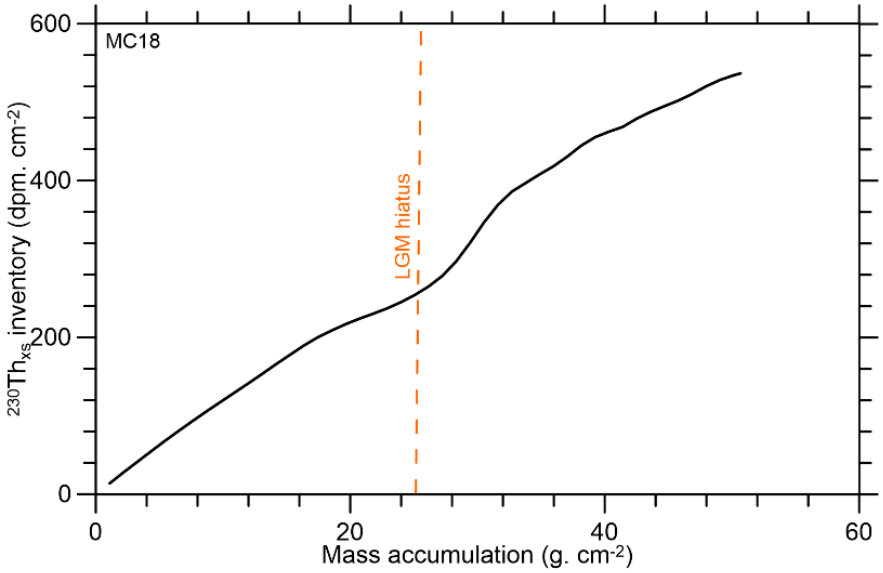

Figure A.5. $^{230}Th_{xs}$ inventory vs mass accumulation in core MC18 (Data from Not and Hillaire-Marcel, 2012)

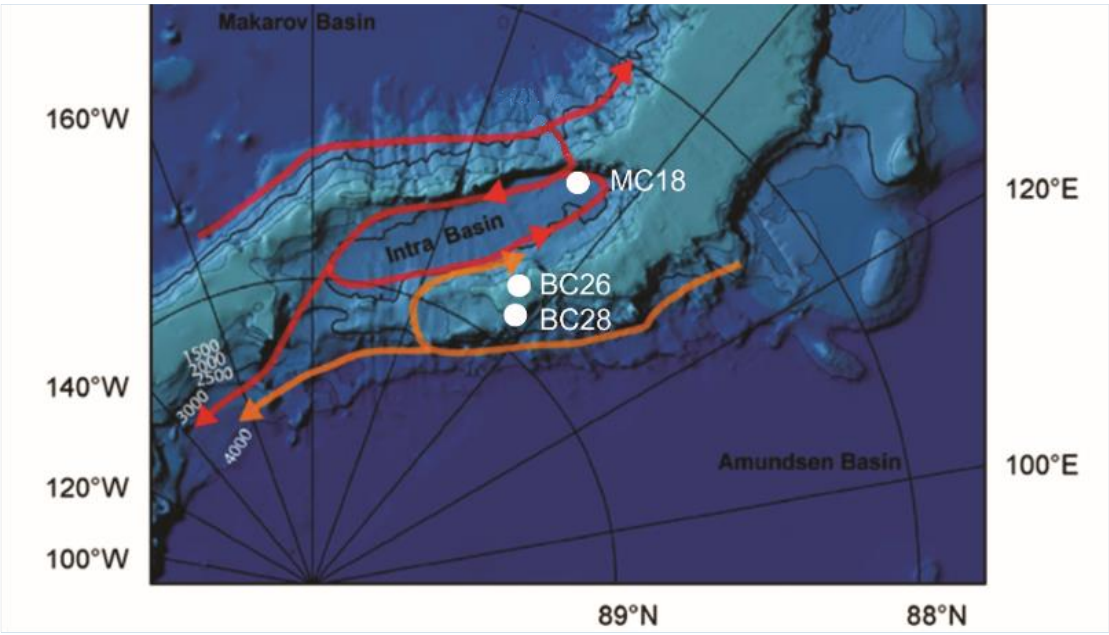

Figure A.6. Blow up of the bathymetric map of the central Lomonosov Ridge with the intermediate and deep currents routes (from Björk et al., 2007). The positions of the sheltered site MC18, in the deep intra basin vs. those of BC26 and BC28, from the ridge crest bathed by overflowing waters from the Makarov Basin, are reported. Significantly higher sedimentation rates characterize site MC18.

Table A.1 Cores used in the present study.

Site	Long. (˚E)	Lat. (˚N)	Depth (m)	^{14}C data	U-Th series analyses	Grain size	OC	References (earlier studies of the cored sequences)
19-8	-48.175	87.257	2370	N	α-counting	N	N	Somayajulu et al., 1989
E25	-179.261	78.573	1200	Y	MC-ICP-MS	Y	Y	Zhao et al., 2022; Song et al., 2022
MA01	178.960	82.031	2295	Y	MC-ICP-MS	Y	N	Xiao et al., 2020; Xu et al., 2021; Park et al., 2022
MC11	-174.693	83.129	2570	Y	MC-ICP-MS	Y	Y	Not and Hillaire-Marcel, 2010
MC12	-171.917	83.297	1586	N	MC-ICP-MS	Y	Y	Not and Hillaire-Marcel, 2010
MC18	146.683	88.433	2500	Y	MC-ICP-MS	Y	Y	Hanslik et al., 2010; Not and Hillaire-Marcel, 2012
BC08	-176.883	78.133	1047	Y	α-counting	N	Y	Clough et al., 1997; Huh et al., 1997; Poore et al., 1999b; Hoffmann and McManus, 2007
BC16	-178.717	80.333	1568	Y	α-counting	N	Y	Clough et al., 1997; Darby et al., 1997; Huh et al., 1997; Poore et al., 1999a; Hoffmann and McManus, 2007
BC17	178.867	81.267	2255	Y	α-counting	N	Y	Clough et al., 1997; Darby et al., 1997; Huh et al., 1997; Poore et al., 1999a; Hoffmann and McManus, 2007
BC19	-175.758	82.447	2400	Y	α-counting	N	Y	Clough et al., 1997; Huh et al., 1997; Poore et al., 1999a; Hoffmann and McManus, 2007
BC20	174.106	83.170	3145	Y	α-counting	N	N	Darby et al., 1997; Huh et al., 1997; Poore et al., 1999b; Hoffmann and McManus, 2007
BC26	142.982	88.810	1034	Y	α-counting	N	Y	Clough et al., 1997; Huh et al., 1997; Poore et al., 1999b; Hoffmann et al., 2013
BC28	140.180	88.873	1990	Y	α-counting	N	N	Darby et al., 1997; Huh et al., 1997; Poore et al., 1999b; Hoffmann et al., 2013
BC32	37.742	85.717	3471	Y	α-counting	N	Y	Clough et al., 1997; Huh et al., 1997; Poore et al., 1999b; Hoffmann et al., 2013
PS51	-171.442	85.135	1473	N	MC-ICP-MS	Y	N	Spielhagen et al., 2004; Stein et al., 2004; Geibert et al., 2021
PS72/396	-162.318	80.578	2723	N	MC-ICP-MS	N	N	Geibert et al., 2021
M030	-61.426	88.657	1278	Y	MC-ICP-MS	Y	Y	Hillaire-Marcel et al., 2017
PS2185	144.166	87.529	1073	Y	α-counting	Y	Y	Strobl, 1998; Spielhagen et al., 1997, 2004
PS2200	-14.022	85.328	1073	Y	α-counting	Y	Y	Uwe, 1996; Strobl, 1998; Spielhagen et al., 2004
PS2757	140.200	81.163	1241	N	MC-ICP-MS	Y	Y	Niessen, 1996; Müller and Stein, 2000; Purcell et al., 2022

References in red: reporting U-series measurements. OC = organic carbon data.

Table A.2 ^{14}C ages data.

Core	Depth interval (cm)	Conventional Age (yr)	Error (±σ)	Calibrated Age (yr BP; 2σ)		
				minimiun	maximum	median
E25	0-1	3277	76	2167	2939	2600
	2-3	6578	29	6274	6899	6580
	6-8	8670	30	8401	9115	8760
	18-20	12540	40	13279	13872	13540
	24-26	34500	260	36992	38717	38250
	32-34	37460	400	40338	41929	41300
	38-40	39230	420	41876	43066	42450
	44-46	40020	430	42326	43758	42900
MA01	0-2	5170	20	4593	5333	4860
	2-4	9905	25	9933	10661	10260
	4-6	12795	30	13481	14136	13820
	6-8	28170	30	31010	31424	31200
	8-10	33380	270	35738	37498	36400
	10-12	37610	450	40388	42080	41400
	12-14	39470	630	41924	43880	42850
	14-16	40580	730	42379	44722	43350
	16-18	40960	670	42695	44925	43600
	18-20	41270	700	42855	45212	44100
	20-22	38360	550	40974	42702	41900
	22-24	42470	810	43475	46450	45000
PS2185	surface	2680	65	1505	2253	1840
	1-2	3105	65	1994	2730	2360
	2-3	4555	60	3747	4576	4160
	4-5	5290	60	4800	5529	5180
	6-7	6740	75	6409	7144	6780
	7-8	7975	75	7682	8316	7960
	8-9	8370	85	8023	8804	8360
	9-10	10310	85	10423	11188	10800
	10-11	16730	150	18741	19648	19150
	10-11	16130	140	18065	18918	18550
	11-12	13950	160	15100	16303	15750
	11-12	13250	210	13791	15340	14450
	12-13	15560	110	17486	18341	17900
	13-14	18110	190	20230	21498	20800
	14-15	23250	230	26092	27279	26600
	15-16	25500	250	28045	29347	28700
	16-17	30380	530	32245	34685	33650
	19-20	33670	550	35667	38439	36800
PS2200	surface	5215	60	4670	5444	5050
	3-4	11050	85	11300	12470	11950
	6-7	19720	150	22361	23297	22700
	8-9	26620	280	29233	30741	29950

	10-11	32060	460	34245	36099	35050
MC11	0-0.5	8525	35	8291	8975	8560
	4-4.5	32630	510	34579	36846	35650
	8-8.5	27010	250	29677	30947	30550
	12-12.5	33550	540	35556	38355	36850
MC18	0.9	2690	70	1514	2266	1880
	7.7	7220	80	6938	7578	7300
	11.2	8795	90	8508	9362	8860
	15.2	10240	100	10301	11138	10700
	17.7	11480	110	12001	12897	12600
	21.7	11890	120	12621	13278	12900
	25.7	11720	120	12444	13196	12720
	27.7	12535	110	13221	13942	13500
	29.7	23250	350	25964	27406	26600
	31.2	26100	600	28140	30737	29400
M030	0-1	7792	59	7548	8130	7840
	1-2	7636	33	7423	7933	7640
	2-3	14085	85	15348	16331	15900
	3-4	16568	63	18675	19391	18860
	4-5	15700	77	17679	18453	18060
	7-8	19110	76	21760	22460	22180
	8-9	21800	137	24642	25707	25300
	9-10	26175	116	28889	29900	29400
	10-11	29518	219	31832	33484	32300
	12-13	21998	392	24362	26174	25500
	14-15	34341	311	36725	38624	38050
BC08	0-1	4130	50	3241	3987	3580
	2-3	5580	50	5125	5854	5540
	6-7	7700	50	7458	8000	7700
	8-9	7760	50	7506	8076	7780
	12-13	7960	50	7684	8289	7880
	14-15	10630	50	10783	11755	11150
	21-22	10960	50	11215	12286	11780
	24-25	21740	100	24617	25615	25220
	26-27	33110	280	35407	36940	36150
	34-35	35580	350	38493	40091	39200
BC16	0-0.5	3780	40	2825	3528	3180
	2-3	4680	50	3958	4774	4360
	4-5	7750	50	7495	8060	7780
	6-7	10050	50	10160	10886	10500
	10-11	11300	60	11830	12669	12440
	13-14	12250	60	12929	13584	13280
	16-17	29680	170	32251	33619	32950
	17.5-18	41250	850	42672	45418	44050
	19-20	33810	350	36196	38269	36900

	19-21	31930	280	34388	35668	34950
	20-21	36610	480	39257	41422	40400
	21-22	36890	570	39405	41753	40700
	23-24	37770	580	40287	42334	41550
	26-27	42310	980	43119	46601	44950
BC17	0-0.5	3150	-	2053	2755	2380
	5-6	7150	50	6889	7500	7240
	10-11	11690	50	12512	13084	12740
	12-13	12250	50	12937	13574	13280
	16-17	13040	50	13745	14807	14140
	20-21	29400	110	31828	33173	32650
	27-28	36970	280	40063	41433	40650
	34-35	41480	460	43270	45053	44300
BC19	2-3	5680	50	5282	5915	5560
	5-6	12120	60	12809	13431	13180
	7-8	12570	60	13293	13916	13560
	10-11	25410	190	28025	29110	28650
	12-13	35120	410	37623	39855	38700
BC20	0-0.5	3880	25	2930	3643	3340
	4-4.5	9580	35	9525	10215	9900
	8-8.5	10550	40	10686	11565	11140
	12-12.5	27700	140	30713	31225	30950
	16-16.5	43000	500	44543	46415	45450
BC26	0-0.5	4020	35	3123	3845	3440
	2-2.5	6720	40	6405	7099	6720
	6-6.5	14500	70	16049	16981	16400
	8-8.5	22100	150	25151	25947	25600
	10-10.5	23800	120	26837	27626	27320
	12.12.5	24400	110	27414	27963	27680
	15-15.5	38600	320	41566	42568	42100
BC28	0-1	2250	50	1052	1696	1360
	3-4	4400	50	3585	4371	3960
	12-13	10480	60	10588	11360	11080
	15-17	16810	60	18898	19617	19240
	18-19	25970	140	28715	29621	29150
BC32	0-1*	/	/	/	/	5260*
	1-2	5680	50	5282	5915	5550
	4-5	7330	50	7113	7669	7400
	7-8	8790	50	8523	9307	8960
	10-11	11300	50	11846	12663	12440
	12-13	15700	70	17686	18446	18040
	15-16	36210	470	38831	41029	39950

*: missing conventional information; A ΔR-value of 440 ± 138 yrs was applied (see details in main text); ^{14}C-ages in red: conventional ^{14}C ages beyond 35 kyr possibly relating to secondary carbonate precipitation (cf. Broecker et al., 2006; Haynert et al., 2011).

Table A.3 Calculated $^{230}Th_{xs}$ inventory in (in dpm.cm^{-2}) vs "^{230}Th-rain" (see main text for details about calculations).

Core	Post-LGM inventory	Post-LGM ^{230}Th-rain	MIS 3 inventory	MIS 3 ^{230}Th-rain	Long-term inventory	~ 400 kyr ^{230}Th-rain	Post-LGM sedimentary budget vs ^{230}Th-rain	MIS 3 sedimentary budget vs ^{230}Th-rain	Long-term sedimentary budget vs ^{230}Th-rain
BG cluster (western Arctic Ocean)									
BC08*	43	37	111	65	/	/	116%	171%	/
E25	34	43	231	83	353	208	79%	278%	170%
BC16*	64	59	238	127	/	/	108%	187%	/
BC17*	108	90	382	208	/	/	120%	184%	/
MA01*	48	91	259	213	364	516	53%	122%	71%
BC19*	79	96	345	225	/	/	82%	153%	/
BC20*	130	138	324	314	/	/	94%	103%	/
MC11	49	103	187	246	238	593	48%	76%	40%
MC12	35	60	137	129	180	317	58%	106%	57%
PS51	46	55	128	115	182	285	84%	111%	64%
TPD cluster (eastern Arctic Ocean)									
PS2757	50	45	311	88	475	220	111%	353%	216%
PS2185	46	38	155	68	213	173	121%	227%	123%
BC26*	45	36	63	63	/	/	125%	100%	/
BC28*	51	78	162	177	/	/	65%	92%	/
MC18*	237	100	537	189	/	/	237%	284%	/
M030	38	47	161	92	224	230	81%	175%	97%
PS2200	23	38	84	68	128	173	61%	124%	74%

Sites with stars: $^{230}Th_{xs}$ inventory with 15% uncertainty due to the estimated dry bulk density (see main text). BG: Beaufort Gyre; TPD: TransPolar Drift.

Table A.4 The post-LGM $^{230}Th_{xs}$ inventory and parameters related to the ^{230}Th scavenging of available sites. The post-LGM $^{230}Th_{xs}$ inventory ($^{230}Th_{xs}$ invent.) in dpm.cm^{-2}; Water depth (WD) in km; Sedimentation rate (Sed. rate) in cm.kyr^{-1}; Clay, OC, IRD (>63 μm) contents in percentage (%); Clay and IRD flux in g.cm^{-2}.kyr^{-1}; OC flux in mg.cm^{-2}.kyr^{-1}; Mean grain size (Φ) in μm; distance from the adjacent shelf (Distance) in km. Sites with stars: $^{230}Th_{xs}$ inventory, clay, OC, and IRD fluxes with 15% uncertainty limited by the estimated DBD.

Site	$^{230}Th_{xs}$ invent.	WD	Sed. rate	Clay	Clay flux	OC	OC flux	IRD	IRD flux	Φ	Distance
BG cluster (western Arctic Ocean)											
BC08*	43	1.0	1.6	/	/	0.8	14.6	/	/	3.0	270
E25	34	1.2	1.1	27	0.29	0.3	2.7	4.5	0.05	7.1	320
BC16*	64	1.6	1.1	/	/	1.1	12.4	7.5	0.09	2.6	289
BC17*	108	2.3	1.2	/	/	1.2	14.8	6.1	0.08	2.2	371
MA01*	48	2.3	0.4	21	0.10	0.4	2.1	0.3	0.00		428
BC19*	79	2.4	0.6	/	/	0.9	5.3	7.1	0.04	3.0	515
MC11	49	2.6	0.1	30	0.04	0.3	0.4	/	/	3.6	583
MC12	35	1.6	0.1	30	0.04	0.3	0.4	/	/	3.6	597
BC20*	130	3.1	0.9	/	/	/	/	7.7	0.08		541
PS51	46	1.5	0.1	/	/	/	/	12.1	0.01		802
TPD cluster (eastern Arctic Ocean)											
PS2757	50	1.2	2.9	48	1.18	0.5	11.5	3.8	0.09	/	412
PS2185	46	1.1	1.0	/	/	0.4	4.1	7.4	0.07	/	1083
BC26*	45	1.0	1.2	/	/	0.4	4.8	/	/	4.2	1196
BC28*	51	2.0	0.8	/	/	/	/	3.8	0.04	2.8	1220
BC32*	84	3.5	0.8	/	/	0.4	3.4	/	/	3.4	1420
MC18*	237	2.5	1.8	27	0.52	0.6	12.4	2.9	0.06	3.1	1185
M030	38	1.3	0.2	24	0.06	0.4	0.9	8.7	0.02	7.4	1544
PS2200	23	1.1	0.2	50	0.13	0.3	0.7	15.3	0.04	/	1766
19-8*	32	2.4	0.6	/	/	/	/	/	/	/	1708

Sites with stars: $^{230}Th_{xs}$ inventory with 15% uncertainty due to the estimated dry bulk density (see main text). BG: Beaufort Gyre; TPD: TransPolar Drift.

RÉFÉRENCES

Anderson, R. F., Bacon, M. P. and Brewer, P. G. (1983). Removal of ^{230}Th and ^{231}Pa at ocean margins. Earth and Planetary Science Letters, 66, 73–90.

Andersson, P. S., et al. (2008). Neodymium isotopes in seawater from the Barents Sea and Fram Strait Arctic–Atlantic gateways. Geochimica et Cosmochimica Acta, 72.12, 2854–2867.

Asahara, Y., et al. (2012). Provenance of terrigenous detritus of the surface sediments in the Bering and Chukchi Seas as derived from Sr and Nd isotopes: Implications for recent climate change in the Arctic regions. Deep Sea Research Part II: Topical Studies in Oceanography, 61, 155–171.

Astakhov, A. S., et al. (2019). Reconstruction of ice conditions in the northern Chukchi Sea during recent centuries: Geochemical proxy compared with observed data. Quatanary International, 522, 23–37.

Backman, J., Fornaciari, E. and Rio, D. (2009). Biochronology and paleoceanography of late Pleistocene and Holocene calcareous nannofossil abundances across the Arctic Basin. Marine Micropaleontology, 72(1-2), 86–98.

Björk, G., et al. (2007). Bathymetry and deep-water exchange across the central Lomonosov Ridge at 88–89 N. Deep Sea Research Part I: Oceanographic Research Papers, 54(8), 1197–1208.

Blaser, P., et al. (2016). Extracting foraminiferal seawater Nd isotope signatures from bulk deep sea sediment by chemical leaching. Chemical Geology, 439, 189–204.

Broecker, W. S., et al. (2006). Anomalous radiocarbon ages for foraminifera shells. Paleoceanography, 21(2), PA2008.

Chen, T., et al. (2012). Variations of North Atlantic inflow to the central Arctic Ocean over the last 14 million years inferred from hafnium and neodymium isotopes. Earth and Planetary Science Letters, 353, 82–92.

Clark, D. L., et al. (1980). Stratigraphy and Glacial-Marine Sediments of the Amerasian Basin, Central Arctic Ocean. Special paper of the Geological Society of America, 181.

Clough, L. M., et al. (1997). Infaunal density, biomass and bioturbation in the sediments of the Arctic Ocean. Deep-Sea Research Part II: Topical Studies in Oceanography, 44.8, 1683–1704.

Costa, K. M., et al. (2020). ^{230}Th normalization: New insights on an essential tool for quantifying sedimentary fluxes in the modern and Quaternary ocean. Paleoceanography and Paleoclimatology, 35(2), e2019PA003820.

Darby, D. A., Bischof, J. F. and Jones, G. A. (1997). Radiocarbon chronology of depositional regimes in the western Arctic Ocean. Deep-Sea Research Part II: Topical Studies in Oceanography, 44(8), 1745–1757.

Darby, D. A., et al. (2009). The role of currents and sea ice in both slowly deposited central Arctic and rapidly deposited Chukchi–Alaskan margin sediments. Global and Planetary Change, 68(1-2), 58–72.

Deschamps, C. E., Montero-Serrano, J. C. and St-Onge, G. (2018). Sediment provenance changes in the western Arctic Ocean in response to ice rafting, sea level, and oceanic circulation variations since the last deglaciation. Geochemistry, Geophysics, Geosystems, 19(7), 2147–2165.

Deschamps, C. E., et al. (2019). Holocene changes in deep water circulation inferred from authigenic Nd and Hf isotopes in sediment records from the Chukchi-Alaskan and Canadian Beaufort margins. Paleoceanography and Paleoclimatology, 34(7), 1038–1056.

Dong, J., et al. (2022). Enhanced Arctic sea ice melting controlled by larger heat discharge of mid-Holocene rivers. Nature Communications, 13(1), 5368.

Elmore, A. C., et al. (2011). Testing the extraction of past seawater Nd isotopic composition from North Atlantic deep sea sediments and foraminifera. Geochemistry, Geophysics, Geosystems, 12.9, 2011GC003741.

Farmer, J. R., et al. (2021). Arctic Ocean stratification set by sea level and freshwater inputs since the last ice age. Nature Geoscience, 14(9), 684–689.

Geibert, W., et al. (2021). Glacial episodes of a freshwater Arctic Ocean covered by a thick ice shelf. Nature, 590(7844), 97–102.

Ghaleb, B. (2009). Overview of the methods for the measurement and interpretation of short-lived radioisotopes and their limits. In IOP conference series: Earth and environmental science 5(1), 012007. IOP Publishing.

Grebmeier, J. M., et al. (2006). Ecosystem dynamics of the Pacific-influenced northern Bering and Chukchi Seas in the Amerasian Arctic. Progress in Oceanography, 71(2-4), 331–361.

Gusev, E. A., et al. (2013). Stratigraphy of bottom sediments in the Mendeleev Ridge area (Arctic Ocean). In Doklady Earth Sciences 450(2), 602. Springer Nature BV.

Gutjahr, M., et al. (2007). Reliable extraction of a deepwater trace metal isotope signal from Fe–Mn oxyhydroxide coatings of marine sediments. Chemical Geology, 242, 351–370.

Haley, B. A. and Polyak, L. (2013). Pre-modern Arctic Ocean circulation from surface sediment neodymium isotopes. Geophysical Research Letters, 40(5), 893–897.

Haynert, K., et al. (2011). Biometry and dissolution features of the benthic foraminifer Ammonia aomoriensis at high pCO2. Marine Ecology Progress Series, 432, 53–67.

Hoffmann, S. and McManus, J. (2007). Is there a ^{230}Th deficit in Arctic sediments?. Earth and Planetary Science Letters, 258(3-4), 516–527.

Hoffmann, S. S., et al. (2013). Persistent export of ^{231}Pa from the deep central Arctic Ocean over the past 35,000 years. Nature, 497(7451), 603–606.

Hillaire-Marcel, C. and de Vernal, A. (2022). A comment about" A sedimentary record from the Makarov Basin, Arctic Ocean, reveals changing middle to Late Pleistocene glaciation patterns"(Quat. Sci. Rev., 270 (2021), p. 107176) from W. Xiao, L. Polyak, R. Wang, C. Not, L. Dong, Y. Liu, T. Ma, T. Zhang. Quaternary Science Reviews, 279, 107239.

Hillaire-Marcel, C., et al. (2017). A new chronology of late Quaternary sequences from the central Arctic Ocean based on “extinction ages” of their excesses in ^{231}Pa and ^{230}Th. Geochemistry, Geophysics, Geosystems, 18(12), 4573–4585.

Hillaire-Marcel, C., de Vernal, A. and Crucifix, M. (2021). Sea-level and summer season orbital insolation as drivers of Arctic sea-ice. arXiv preprint arXiv:2102.02067.

Hillaire-Marcel, C., de Vernal, A., Rong, Y., Roberge, P. and Song, T. (2022a). Challenging radiocarbon chronostratigraphies in central Arctic Ocean sediment. Geophysical Research Letters, 49(21), p.e2022GL100446.

Hillaire-Marcel, C., et al. (2022b). Challenging the hypothesis of an Arctic Ocean lake during recent glacial episodes. Journal of Quaternary Science, 37(4), 559–567.

Huang, H., et al. (2021). Efficient extraction of past seawater Pb and Nd isotope signatures from Southern Ocean sediments. Geochemistry, Geophysics, Geosystems, 22.3, e2020GC009287.

Hu, A., et al. (2015). Effects of the Bering Strait closure on AMOC and global climate under different background climates. Progress in Oceanography, 132, 174–196.

Huh, C. A., et al. (1997). Natural radionuclides and plutonium in sediments from the western Arctic Ocean: sedimentation rates and pathways of radionuclides. Deep-Sea Research Part II: Topical Studies in Oceanography, 44(8), 1725–1743.

Jakobsson, M., et al. (2000). Manganese and color cycles in Arctic Ocean sediments constrain Pleistocene chronology. Geology, 28(1), 23–26.

Jakobsson, M. (2002). Hypsometry and volume of the Arctic Ocean and its constituent seas. Geochemistry, Geophysics, Geosystems, 3(5), 1–18.

Jakobsson, M., et al. (2016). Evidence for an ice shelf covering the central Arctic Ocean during the penultimate glaciation. Nature Communications, 7.1, 10365.

Jakobsson, M., et al. (2017). Post-glacial flooding of the Bering Land Bridge dated to 11 cal ka BP based on new geophysical and sediment records. Climate of the Past, 13(8), 991–1005.

Joe, Y. J., et al. (2020). Late Quaternary depositional and glacial history of the Arliss Plateau off the East Siberian margin in the western Arctic Ocean. Quaternary Science Reviews, 228, 106099.

Kang, H. S., et al. (2007). Organic carbon and nitrogen composition in the sediment of the Kara Sea, Arctic Ocean during the Last Glacial Maximum to Holocene times. Geophysical Research Letters, 34(12), L12607.

Khim, B. K., et al. (2018). Surface water productivity and sediment transport by Bering Strait throughflow in the Chukchi Shelf (the western Arctic Ocean) during the Holocene. The Holocene, 28(5), 814–826.

Kobayashi, D., et al. (2016). Distribution of detrital minerals and sediment color in western Arctic Ocean and northern Bering Sea sediments: Changes in the provenance of western Arctic Ocean sediments since the last glacial period. Polar Science, 10(4), 519–531.

Lewis, K. M., Van Dijken, G. L. and Arrigo, K. R. (2020). Changes in phytoplankton concentration now drive increased Arctic Ocean primary production. Science, 369(6500), 198–202.

Maccali, J., et al. (2013). Geochemical signatures of sediments documenting Arctic sea-ice and water mass export through Fram Strait since the Last Glacial Maximum. Quaternary Science Reviews, 64, 136–151.

Myers, W. B. and Darby, D. A. (2022). A compilation of the silt and clay mineralogy from coastal and shelf regions of the Arctic Ocean. Marine Geology, 454, 106948.

Müller, C. and Stein, R. (2000). Sedimentology of core PS2757-8. PANGEA.

Naidu, A. S., Creager, J. S. and Mowatt, T. C. (1982). Clay mineral dispersal patterns in the north Bering and Chukchi Seas. Marine geology, 47(1-2), 1–15.

Niessen, F., et al. (2013). Repeated Pleistocene glaciation of the East Siberian continental margin. Nature Geoscience, 6(10), 842–846.

Niessen, F. (1996). Physical properties of sediment core PS2757-8. PANGEA.

Not, C. and Hillaire-Marcel, C. (2010). Time constraints from ^{230}Th and ^{231}Pa data in late Quaternary, low sedimentation rate sequences from the Arctic Ocean: an example from the northern Mendeleev Ridge. Quaternary Science Reviews, 29(25-26), 3665–3675.

Not, C., et al. (2008). ^{210}Pb–^{226}Ra–^{230}Th systematics in very low sedimentation rate sediments from the Mendeleev Ridge (Arctic Ocean). Canadian Journal of Earth Sciences, 45.11, 1207–1219.

Not, C. and Hillaire-Marcel, C. (2012). Enhanced sea-ice export from the Arctic during the Younger Dryas. Nature Communication, 3(1), 647.

Nuttin, L. and Hillaire-Marcel, C. (2015). U-and Th-series isotopes in deep Baffin Bay sediments: tracers of detrital sources and of contrasted glacial/interglacial sedimentary processes. Marine Geology, 361, 1–10.

O'Regan, M., et al. (2017). The De Long Trough: a newly discovered glacial trough on the East Siberian continental margin. Climate of the Past, 13(9), 1269–1284.

Park, K., et al. (2022). Increased terrigenous input from North America to the northern Mendeleev Ridge (western Arctic Ocean) since the mid-Brunhes Event. Scientific Reports, 12(1), 15189.

Polyak, L., et al. (2016). Holocene sea-ice conditions and circulation at the Chukchi-Alaskan margin, Arctic Ocean, inferred from biomarker proxies. The Holocene, 26(11), 1810-–1821.

Poore, R. Z., et al. (1999a). Late Pleistocene and Holocene meltwater events in the western Arctic Ocean. Geology, 27(8), 759–762.

Poore, R. Z., Ostermann, D. R. and McGeehin, J. (1999b). Stable isotope data and AMS ^{14}C dates from Arctic Ocean Section 1994 surface sediment transect and box core samples from the Mendeleyev Ridge area. US Department of the Interior, US Geological Survey.

Porcelli, D., et al. (2009). The distribution of neodymium isotopes in Arctic Ocean basins. Geochimica et Cosmochimica Acta, 73(9), 2645–2659.

Purcell, K., et al. (2022). Potential and limitation of ^{230}Th-excess as a chronostratigraphic tool for late Quaternary Arctic Ocean sediment studies: An example from the Southern Lomonosov Ridge. Marine Geology, 448, 106802.

Smith, J. M., 2022. Amino acid geochronology of foraminifera from the central Arctic Ocean and Nordic Seas. Msc. Thesis, Northern Arizona University, Arizona.

Smith, J. N., et al. (2003). Shelf–basin interactions in the Arctic Ocean based on ^{210}Pb and Ra isotope tracer distributions. Deep Sea Research Part I: Oceanographic Research Papers, 50.3, 397–416.

Somayajulu, B. L. K., Sharma, P. and Herman, Y. (1989). Thorium and uranium isotopes in Arctic sediments. In: The Arctic Seas. Springer, Boston, MA. pp. 571–579.

Song, T., et al. (2022). Sedimentology, mineralogy, and geochemistry results of core Arc7-E25 from southern Mendeleev Ridge, Arctic Ocean. PANGAEA.

Spielhagen, R. F., et al. (1997). Arctic Ocean evidence for late Quaternary initiation of northern Eurasian ice sheets. Geology, 25(9), 783–786.

Spielhagen, R. F., et al. (2004). Arctic Ocean deep-sea record of northern Eurasian ice sheet history. Quaternary Science Reviews, 23(11-13), 1455–1483.

Stein, R., 2008. Arctic Ocean sediments: processes, proxies, and paleoenvironment. In Chamley, H. (eds.): Developments in Marine Geology. Elsevier, Oxford.

Stein, R., et al. (2017a). Holocene variability in sea ice cover, primary production, and Pacific-Water inflow and climate change in the Chukchi and East Siberian Seas (Arctic Ocean). Journal of Quaternary Science, 32(3), 362–379.

Stein, R., et al. (2017b). Arctic Ocean sea ice cover during the penultimate glacial and the last interglacial. Nature communications, 8(1), 373.

Stein, R., Usbeck, R. and Polozek, K. (2004). Physical properties of sediment core PS51/038-4. PANGAEA.

Strobl, C. (1998). Datierung von Sedimentkernen und Rekonstruktion der Transportwege der Radionuklide ^{10}Be, ^{230}Th und ^{231}Pa in hohen nördlichen Breiten. Ph.D. Thesis, Ruprecht-Karls-Universität, Heidelberg.

Swärd, H., et al. (2018). Sedimentary proxies for Pacific water inflow through the Herald Canyon, western Arctic Ocean. arktos, 4(1), 1–13.

Uwe, B. (1996). Physical properties of sediment core PS2200-5. PANGAEA.

Vallières, S. (1997). Flux d'uranium et excès de ^{230}Th dans les sédiments de la mer du Labrador: relation avec les conditions paléocéanographiques et la paléoproductivité du bassin. Ph.D. Thesis, Université du Québec à Chicoutimi.

Wasserburg, G. J., et al. (1981). Precise determination of SmNd ratios, Sm and Nd isotopic abundances in standard solutions. Geochimica et Cosmochimica Acta, 45(12), 2311–2323.

Wedepohl, K. H. (1995). The composition of the continental crust. Geochimica et Cosmochimica Acta, 59.7, 1217–1232.

West, G., et al. (2023). Amino acid racemization in Neogloboquadrina pachyderma and Cibicidoides wuellerstorfi from the Arctic Ocean and its implications for age models. Geochronology, 5(1), 285–299.

Wilson, D. J., et al. (2013). Reactivity of neodymium carriers in deep sea sediments: Implications for boundary exchange and paleoceanography. Geochimica et Cosmochimica Acta, 109, 197–221.

Woodgate, R. A. and Aagaard, K. (2005). Revising the Bering Strait freshwater flux into the Arctic Ocean. Geophysical Research Letters, 32.2, L02602.

Woodgate, R. and Peralta-Ferriz, C. (2021). Warming and Freshening of the Pacific Inflow to the Arctic from 1990 ‐ 2019 implying dramatic shoaling in Pacific Winter Water ventilation of the Arctic water column. Geophysical Research Letters, 48.9, e2021GL092528.

Woodgate, R. A., Weingartner, T. and Lindsay, R. (2010). The 2007 BS oceanic heat flux and anomalous Arctic sea-ice retreat. Geophysical Research Letters, 37.1, L01602.

Xiao, W., et al. (2020). Middle to Late Pleistocene Arctic paleoceanographic changes based on sedimentary records from Mendeleev Ridge and Makarov Basin. Quaternary Science Reviews, 228, 106105.

Xu, Q., et al. (2021). Driving Mechanisms of Sedimentary ^{230}Th and ^{231}Pa Variability in the Western Arctic Ocean Through the Last Glacial Cycle. Paleoceanography and Paleoclimatology, 36.7, e2020PA004039.

Yamamoto, M., et al. (2017). Holocene dynamics in the Bering Strait inflow to the Arctic and the Beaufort Gyre circulation based on sedimentary records from the Chukchi Sea. Climate of the Past, 13(9), 1111-1127.

Ye, L., et al. (2020). Ice events along the East Siberian continental margin during the last two glaciations: Evidence from clay minerals. Marine Geology, 428, 106289.

Zhao, S., et al. (2022). Sedimentary record of glacial impacts and melt water discharge off the East Siberian Continental Margin, Arctic Ocean. Journal of Geophysical Research: Oceans, 127(1), e2021JC017650.